UNIVERSITY OF SOUTHAMPTON

FACULTY OF NATURAL AND ENVIRONMENTAL SCIENCES

School of Ocean and Earth Science

MEASUREMENT AND PARAMETERISATION OF THE AIR-SEA CO_2 FLUX IN HIGH WINDS

by

John Prytherch

Thesis for the degree of Doctor of Philosophy

May 2011

UNIVERSITY OF SOUTHAMPTON

ABSTRACT

FACULTY OF NATURAL AND ENVIRONMENTAL SCIENCES
SCHOOL OF OCEAN & EARTH SCIENCE

Doctor of Philosophy

MEASUREMENT AND PARAMETERISATION OF THE AIR-SEA CO2 FLUX IN HIGH WINDS

by John Prytherch

During a three year occupation of Station Mike (66°N 2°E), the Norwegian Ocean Weather Ship *Polarfront* was equipped with a range of meteorological and seastate measuring instruments, including the autonomous air-sea flux system "AutoFlux" (Yelland et al., 2009) and an underway ΔpCO_2 system. An extensive set of direct, eddy covariance measurements of momentum, latent heat, sensible heat and CO_2 flux was obtained over a wide range of open ocean conditions. The maximum recorded 20-minute mean wind speed was 25 $m.s^{-1}$. The maximum significant wave height was 11 m.

The initial CO_2 flux results were subject to a large, commonly observed humidity cross-sensitivity error. A novel iterative correction procedure was developed, tested against an independent data set and proved to be robust (Prytherch et al., 2010a). Open-path sensors may now be used for air-sea CO_2 flux measurement, greatly increasing the number of measurements available for analysis.

There are large differences between existing gas transfer to wind speed relationships, particularly at high wind speeds, and there is significant uncertainty over the form (quadratic or cubic) of the relationship. From the 3938 direct CO_2 flux measurements made onboard *Polarfront*, a new relationship between gas transfer velocity, k_{660}, and wind speed, U_{10n} has been obtained:

$$k_{660} = -0.51 + 0.095U_{10n}^{2.7} \qquad 0 \le U_{10n} \le 20 \text{ m.s}^{-1}$$

The motion corrected fluxes were found to have a large signal at frequencies associated with platform motion. This signal is also apparent in results from previous air-sea experiments from both fixed and moving platforms. The cause of this signal, whether error or real wind-wave interaction, remains unknown. The gas transfer relationship obtained after removal of this signal is:

$$k_{660} = -0.09 + 0.02U_{10n}^{3.1} \qquad 2 \le U_{10n} \le 20 \text{ m.s}^{-1}$$

demonstrating that the observed near cubic dependence on wind speed, also reported in some previous experiments over a more limited wind speed range (McGillis et al., 2001a), is a robust result. This suggests a significant role for wave breaking and bubble-mediated exchange in air-sea gas transfer.

TABLE OF CONTENTS

LIST OF FIGURES

LIST OF TABLES

DECLARATION OF AUTHORSHIP

I, John Prytherch,

declare that the thesis entitled

Measurement and parameterisation of the air-sea CO_2 flux in high winds

and the work presented in the thesis are both my own, and have been generated by me as the result of my own original research. I confirm that:

- this work was done wholly or mainly while in candidature for a research degree at this University;
- where I have consulted the published work of others, this is always clearly attributed;
- where I have quoted from the work of others, the source is always given. With the exception of such quotations, this thesis is entirely my own work;
- I have acknowledged all main sources of help;
- where the thesis is based on work done by myself jointly with others, I have made clear exactly what was done by others and what I have contributed myself;
- parts of this work have been published as: Prytherch et al., (2010a) and Prytherch et al., (2010b).

Signed:……

Date:……

ACKNOWLEDGEMENTS

I would especially like to thank my supervisors, Margaret J. Yelland and Meric A. Srokosz (NOCS), for providing invaluable guidance. I'm grateful to Robin W. Pascal (NOCS) and Ben I. Moat (University of Southampton) for their assistance and suggestions, Peter K. Taylor for his thoughtful input, and Neil C. Wells (University of Southampton), my panel chair. I'd also like to thank the crew of *Polarfront*, the Norwegian Meteorological Institute for use of the ship, Ingunn Skjelvan (BCCR) for providing the ΔpCO_2 measurements, and Jeff Hare (UEA) for his motion correction algorithms. Funding was provided by the National Environment Research Council (grants NE/F007442/1, NE/C001826/1, NE/C001869/1, NE/C001834/1, NE/G000115/1, NE/G000123/1, NE/ G003696/1, and Oceans 2025). This work would not have been possible without the support, patience and wisdom of my wife Amy.

I was inspired and encouraged to take this path by my friend Geri Lambert. This thesis is dedicated to her.

1. Background and literature review

1.1. Introduction

The air-sea boundary forms the interface between two dynamic fluids that cover the majority of the Earth's surface. Transfer of properties such as momentum, heat, moisture, and gases between the ocean and the atmosphere are important factors in the dynamics of the Earth system. The ocean acts as a net sink for a significant proportion of the atmospheric anthropogenic CO_2, acting to mitigate the greenhouse effect. Different parts of the world's oceans act as both sinks and sources of CO_2, and the direction of flux at a particular location can vary during the course of a year. Quantifying air-sea gas exchange is thus important for understanding and modeling the climate system, and is essential for predicting future climate change, especially with coupled ocean-atmosphere models. Air-sea gas exchange is also important in studies of pollution, ocean acidification and biogeochemical cycling.

Transfer is primarily driven by turbulent fluctuations in the atmospheric boundary layer and the upper layers of the ocean and an exact mathematical model is usually not possible. The transfer velocity, k, is commonly parameterised in terms of wind speed. Proposed gas transfer to wind speed relationships differ significantly, particularly at high wind speeds. At winds of 7 $m.s^{-1}$ published relationships differ by 50%, and at 15 $m.s^{-1}$ the relationships differ by 100% (e.g.: Woolf, 2005). Wind speeds of 15 $m.s^{-1}$ or more occur infrequently over the global ocean but due to the non-linear dependence of k on wind speed, they have a significant effect on the global gas flux (e.g.: Takahashi et al., 2002). There are very few measurements of k obtained at wind speeds above 15 $m.s^{-1}$, and the derived relationships are extrapolated to higher wind speed values. Large uncertainties in gas transfer measurements make determining the form of the wind speed dependence difficult without measurements at high wind speeds.

The work presented in this thesis seeks to address the large uncertainty in the air-sea gas transfer parameterisation through a new, long term set of direct air-sea CO_2 flux measurements obtained in the North Atlantic onboard the Weathership *Polarfront*. The measurements were obtained in a region that experiences a large air-sea CO_2 concentration difference and frequent storms. CO_2 flux measurements were made at higher wind speeds than have previously been reported.

Some proportion of the variability in transfer velocity is due to the dependence of gas transfer on kinetic factors other than wind speed. Simultaneous measurement was made of forcing variables including directional seastate and whitecap fraction. Some theories and some CO_2 flux measurements suggest a significant role for bubble-mediated transfer in enhancing air-sea gas transfer but until now such theories could not be tested due to a lack of concurrent flux and seastate data.

This chapter examines the physical process of gas transfer and the models used to describe it. Section 1.2 describes the theory of air-sea gas transfer. The various techniques used to determine the transfer are described in Section 1.3, with a focus on the most direct technique, Eddy Correlation (EC), the method employed for the majority of the research in this thesis (Section 1.3.2). Previously published transfer velocity parameterisation are described in Section 1.4, with particular attention given to wind speed and the potential role of bubble-mediated transfer (Section 1.4.3).

Chapter 2 of this thesis describes the experimental setup: location, platform, instrumentation and initial processing relevant to the results presented. Chapter 3 describes the development and testing of a correction to a long-standing humidity cross-sensitivity error in air-sea CO_2 measurements made using open-path instruments. Chapter 4 describes the CO_2 flux measurements obtained onboard *Polarfront* and derives a "classic" gas transfer parameterisation. Chapters 5, 6 and 7 address the various sources of uncertainty in ship based EC measurements; in particular Chapter 6 examines platform motion and quantifies the wave scale signal apparent in air-sea flux cospectra for the first time. Finally, Chapter 8 gives the conclusions of the thesis and contains suggestions for future areas of study.

A glossary of parameters (and their units) can be found after the Appendices.

1.2. Air-sea gas transfer theory

1.2.1 Stagnant film model

The air-sea interface experiences exchange of momentum, heat, water and gases, including CO_2. In its simplest form we can consider the interface to be an unbroken surface separating the two fluids. The effects of wave breaking, bubbles and sea spray will be considered later.

There are numerous models of air-sea exchange across the interface. The simplest is the stagnant film model (e.g.: Broecker and Peng, 1982). For a thin

interfacial sub-layer (~ 100 μm: Jähne et al., 1987b) on either side of the interfacial layer, turbulent motion is suppressed and the transport of material and properties occurs through molecular diffusion. Molecular diffusion is usually orders of magnitude smaller than turbulent transfer. Hence, diffusion through the sub-layers is the rate-limiting step in the transfer of constituents between the bulk air and sea. In this model the air-sea exchange of gas can be considered to consist of: the transfer between the bulk water and the water-side interfacial layer; the transfer between the water-side and air-side interfacial layers and; the transfer between the air-side interfacial layer and the bulk air:

$$F_n = \delta_{na} \frac{C_{n0} - C_{na}}{z_a} = \delta_{nw} \frac{C_{nw} - C_{n0}}{z_w} \tag{1.1}$$

Here, F (typical units: mols.m^{-2}.s^{-1}), is the mass flux of a particular gas species denoted by the subscript n, C_n is the (assumed constant) concentration (mols.m^{-3}) of the gas in the air and water at, above and below the interface, denoted by the subscripts O, a and w respectively. The thicknesses of the air-side and water-side interfacial sub-layers are z_a and z_w respectively, and δ_{na} and δ_{nw} (m^2.s^{-1}) are the diffusivities of the gas species n in the air and water. The unknown gas concentration at the interface, C_{n0}, can be eliminated:

$$F_n = \frac{\delta_{nw}\delta_{na}}{\delta_{na} z_w + \delta_{nw} z_a}(C_{nw} - C_{na}) \tag{1.2}$$

For a poorly soluble trace gas such as CO_2, $\delta_{na} \gg \delta_{nw}$ i.e. the exchange rate is controlled by the diffusivity in water of the gas in question and the thickness of the oceanic interfacial layer. Eqn. (1.2) can thus be simplified to Fick's law of diffusion:

$$F_n = \frac{\delta_{nw}}{z_w}(C_{nw} - C_{na}) \tag{1.3}$$

The model assumes the interface thickness is proportional to ν_w (m^2.s^{-1}), the kinematic seawater viscosity, and inversely proportional to the friction velocity, u_* (m.s^{-1}), defined as:

$$u_* = \left[\overline{(u'w')}^2 + \overline{(v'w')}^2 \right]^{1/4} \equiv \left(\left| \frac{\tau}{\rho} \right| \right)^{1/2} \tag{1.4}$$

where τ (kg.s^{-2}m^{-1}) is the surface wind stress and ρ (kg.m^{-3}) is the air density. The wind vector (m.s^{-1}: along wind component *u*, crosswind component *v*, vertical component *w*) is denoted using standard Reynolds decomposition: the turbulent parts are designated by accents and an overbar indicates an average (in practice, a time average). The flux can thus be represented as:

$$F_n \propto u_* Sc^{-1} (C_{nw} - C_{na}) \tag{1.5}$$

with the non-dimensional Schmidt number, *Sc*, defined as:

$$Sc \equiv \frac{\nu_w}{\delta_{nw}} \tag{1.6}$$

The exchange is driven by the concentration difference in a manner analogous with electrical potential. The rate of this exchange (in electrical analogy, equivalent to the inverse resistance) is commonly termed the transfer velocity, *k* (m.s^{-1}). Note that *k* is frequently given in units of cm/hr. For the stagnant film model *k* is:

$$k \propto u_* Sc^{-1} \tag{1.7}$$

Whilst this model is appealing due to its simplicity, in conditions of widespread wave breaking it is often impossible to identify an interface and the model assumptions break down.

1.2.2 Surface renewal model

A more physically realistic representation of gas transfer is the surface renewal model (e.g.: Danckwerts, 1951; Krauss and Businger, 1994). In addition to molecular diffusion, the surface renewal model assumes that parcels of fluid at the interface are intermittently replaced by parcels of fluid from the turbulent layers away from the interface. This conceptual model is supported by observations of convergence and divergence in the interfacial layer (e.g.: Jähne et al., 1987b). The transfer velocity in the surface renewal model is proportional to the square root of the Schmidt number (c.f. Eqn. (1.7)):

$$k \propto u_* Sc^{-0.5} \tag{1.8}$$

1.2.3 Transfer velocity theory

In addition to surface renewal models, there are a large number of other conceptual models of air-sea gas transfer that feature dynamic surface layers (e.g.: Harriott, 1962; Deacon, 1977; Brumley and Jirka, 1988). A detailed description of each is beyond the scope of this review. It is sufficient for the purposes of this study to state that a typical representation of the transfer velocity from dynamic surface layer models (including surface renewal models) is:

$$k \propto u_* Sc^{-n} \tag{1.9}$$

Where the exponent of the Schmidt number depends on the model and lies between $1/2 \le n \le 2/3$. Laboratory measurements indicate that an interface of constant thickness, and the resulting $n = 1$, as predicted by stagnant film models of gas exchange, is unrealistic (e.g.: Jähne et al., 1987b). Measurements in laboratories and in the field instead support a range of exponent values similar to that determined in dynamic surface models, with $n = 1/2$ thought appropriate for rough surfaces and $n = 2/3$ thought appropriate for smooth surfaces (Jähne et al., 1987b; Watson et al., 1991; Jähne and Haubecker, 1998; Nightingale et al., 2000b).

The presence of surfactants, resulting from biological or geochemical processes, can modify the transport processes at the interfacial layer (Frew et al., 1997; Asher and Wanninkhof, 1998b). Modeling of a film-covered surface also leads to predictions of $n = 2/3$, and modeling a clean surface, $n = 1/2$ (e.g.: Asher and Wanninkhof, 1998b). A fully clean or fully film covered water surface is rarely found in nature. Hence, this theoretical approach suggests that the value of n lies somewhere in between. This is supported by laboratory measurements of gas transfer through surfactant-contaminated surfaces (e.g.: Asher et al., 1996). However, there is some experimental evidence to suggest that surfactants do not significantly modify open ocean gas transfer (Nightingale et al., 2000a). The uncertainty in the value of n remains a significant source of uncertainty for calculations of k (Sections 1.3.3 and 1.3.5).

In experimental usage, the flux equation of a poorly soluble gas such as CO_2, which is rate limited by the water side diffusive layer, is commonly defined as:

$$F_n = k\,(C_{nw} - C_{na}/\alpha) \tag{1.10}$$

where α is the Henry's law constant (atm.m^3.mol^{-1}):

$$\alpha = pn_a / C_{nw} \tag{1.11}$$

C_w and C_a are the gas concentrations in the bulk water and air respectively and pn_a (atm) is the partial pressure of the gas *n* in air (e.g.: Liss and Merlivat, 1986). The Henry's law constant is the equilibrium ratio of the partial pressure of a gas in air to the concentration of the gas dissolved in water. There are many different forms of the constant specified in the literature.

The gas flux can also be expressed in terms of fugacities. Due to the small difference when measured in normal environmental temperature ranges, the fugacity is often approximated by the partial pressure (Appendix A), and the flux represented as:

$$F_{CO_2} = k\,K_{0CO_2}\,(pCO_{2w} - pCO_{2a}) \tag{1.12}$$

where K_{0CO2} is the solubility of CO_2 in seawater (mol.m^{-3}.atm^{-1}), pCO_{2w} is the partial pressure of CO_2 (atm) in water and pCO_{2a} (atm) is the partial pressure of CO_2 in air. In this form, an invasive flux from the atmosphere into water is negative and an evasive flux into the atmosphere is positive. The partial pressure form of the flux equation (Eqn. (1.12)) will be most often used in the remainder of this thesis. The solubility is often given in non-dimensional form as the Ostwald solubility coefficient, α_{on}, defined as $\alpha_{on} = K_{0n} R T_w$ where *R* is the universal gas constant (m^3.atm.mols^{-1}.K^{-1}) and T_w is the water temperature (K). The temperature dependence of K_{0CO2} is shown in Figure 1.1.

The transfer velocity is usually assumed dependent on the Schmidt number (Eqn. (1.9)). Both ν_w and δ_{nw} are dependent on temperature, and the Schmidt number variation with temperature and salinity is shown in Figure 1.2. The gas transfer velocity thus strongly increases with increasing temperature.

Both K_{0n} and *Sc* are dependent on the water temperature (Figure 1.2; Figure 1.1). To a lesser extent both are also dependent on the salinity. Whilst it is the temperatures and salinity of the sub-layer close to the sea surface that directly affects the transfer process, in situ measurements obtained from ships or buoys are usually obtained at depths of a metre or more. The calculations can therefore be subject to

errors introduced by near surface temperature gradients such as those from diurnal warming (Prytherch et al., 2011) or cool skin effects (Robertson and Watson, 1992). The temperature dependence of K_{0CO2} and $Sc_{CO_2}^{0.5}$ or $Sc_{CO_2}^{0.66}$ are similar, and hence, when considering only direct transfer (without bubble-mediated exchange), the flux of CO_2 has a smaller dependence on water temperature (Figure 1.3).

There are relatively few trace gases for which measurement of the air-sea flux is currently possible. To enable the transfer velocities of poorly soluble trace gases of different diffusivities to be compared, and to account for the seawater temperature of a particular measurement, transfer velocity measurements are usually normalised to some Schmidt number value, often either Sc = 660 (CO_2 in seawater with salinity of 35 psu at 20°C) or Sc = 600 (CO_2 in freshwater at 20°C) via:

$$k_{660} = k \times (660/Sc)^{-n} \tag{1.13}$$

If the Schmidt number exponent, n, is known and assumed constant then Eqn. (1.13) enables a measured gas transfer velocity of one gas to be applied to another of interest. An exponent of 2/3 is thought appropriate for a smooth surface, and is observed to change from 2/3 to approximately 1/2 with the onset of waves (at wind speeds of approximately 3-4 $m.s^{-1}$; e.g.: Jähne et al., 1987b). For moderate wind conditions, laboratory and field results show that assuming that n = 1/2 is reasonable (e.g.: Holmen and Liss, 1984; Watson et al., 1991; Nightingale et al., 2000b). The exact value of n in both rough and smooth conditions also remains uncertain, and is dependent on factors affecting the interfacial dynamics such as surfactants (e.g.: Asher and Wanninkhof, 1998b). Assumption of a constant value for n implies that gas transfer rates for different gases are only dependent on the diffusivity across the molecular interfacial layer. In the presence of bubbles caused by wave breaking, a transfer velocity dependence on gas solubility is introduced (Section 1.4.3; e.g.: Woolf, 1997) and different gases cannot be related using the simple formula Eqn. (1.13).

For more soluble gases (e.g.: DMS), the transfer is governed by the water-side and air-side transfer terms (e.g.: Liss, 1983; Johnson, 2010). The transfer velocities of such gas species have an explicit dependence on solubility, and hence cannot be simply compared using Eqn. (1.13).

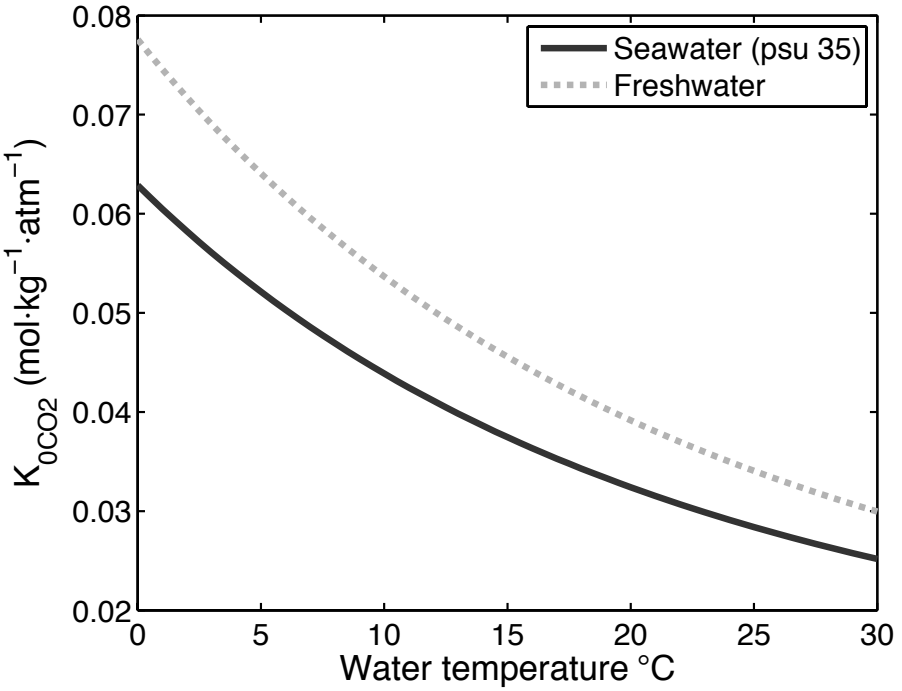

Figure 1.1. CO_2 solubility dependence on water temperature for seawater (psu 35) and freshwater. Solubility calculated from the measurements detailed in Weiss (1974).

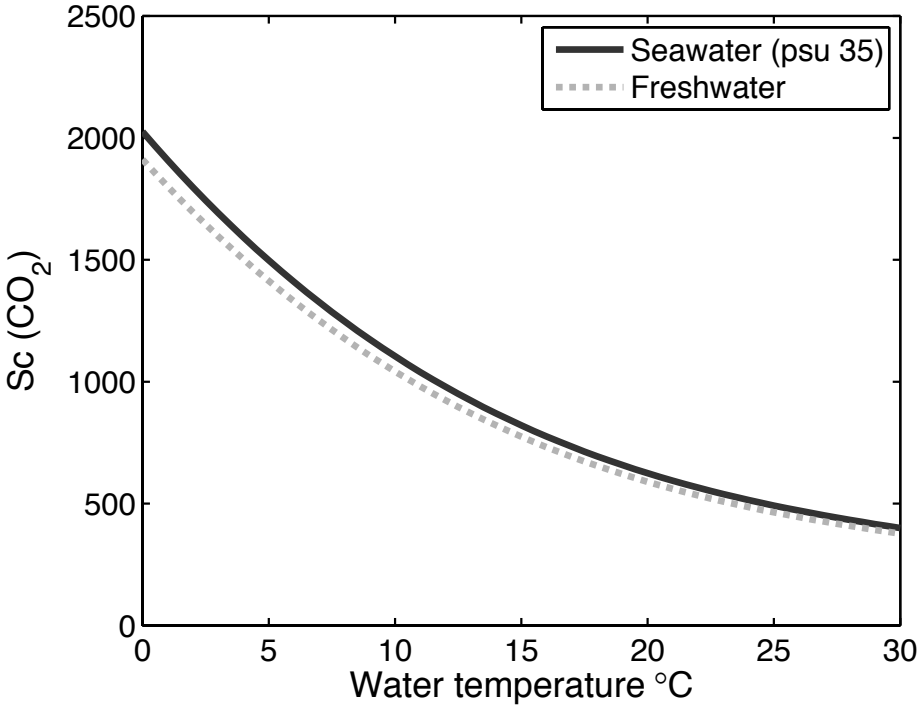

Figure 1.2. CO_2 Schmidt number dependence on temperature and salinity. The relationship shown here was determined using a least squares third order fit to the measurements reported in Jähne et al., (1987a).

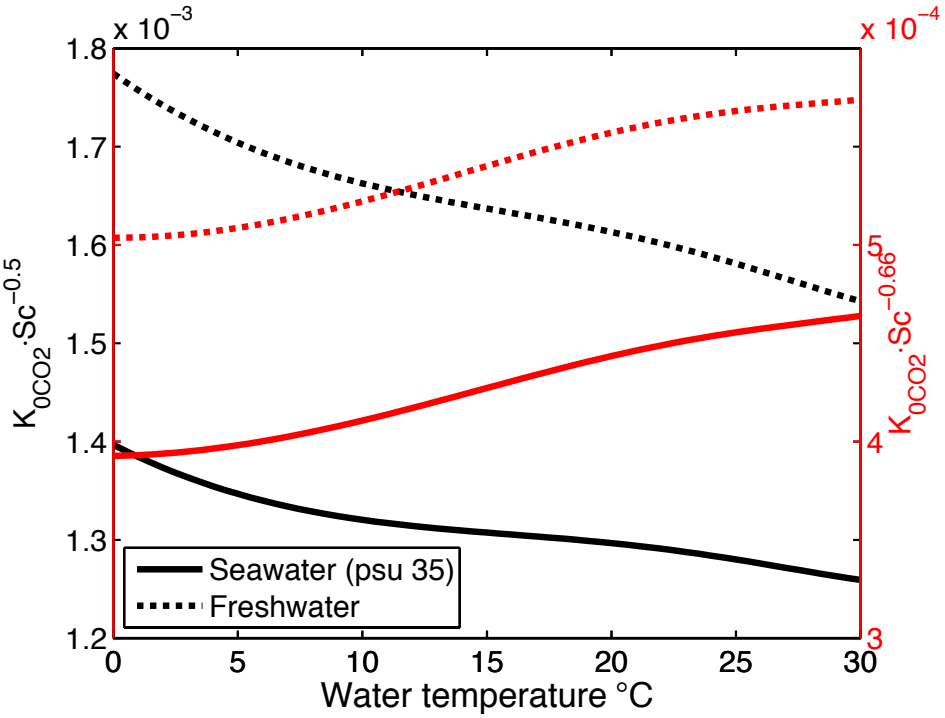

Figure 1.3. Temperature dependence of direct air-sea CO_2 flux.

1.3. Measurement techniques

1.3.1 Inertial dissipation

1.3.1.a. Theory

The Inertial Dissipation (ID) technique (e.g.: Edson et al., 1991) obtains an indirect measurement of flux from the balance between the high frequency sink and lower frequency source terms of turbulence. Spectral measurement in the inertial subrange (turbulent scales smaller than the energy containing eddies but larger than the viscous eddies) is used to determine the dissipation rates of energy, ε ($m^2.s^{-2}$) (or, for heat fluxes, the heat dissipation). A common interval for measurement of the inertial subrange is 2-4 Hz (Figure 1.4). The dissipation rate is used to close the turbulent kinetic energy (TKE) or heat-variance budget. The ID method relies on assumptions implicit in Monin-Obukhov Similarity Theory (MOST). MOST assumes that the parameters describing mean and turbulent flow in the atmospheric surface layer (approximately the lowest 10% of the atmospheric boundary layer) can be expressed as dimensionless universal functions, ξ, with:

$$\xi = \frac{z}{L} \tag{1.14}$$

where z is height and L is the Obukhov length (m). The Obukhov length, a measure of the balance between turbulent production and buoyancy production (or dissipation) of turbulence, is defined as:

$$L = -\frac{Tu_*^3}{g\kappa_v \overline{T_v' w'}} \tag{1.15}$$

where κ_v is the von Karman constant (= 0.4), g is acceleration due to gravity (m.s^{-2}), T is the absolute air temperature (K), T_v is virtual temperature (K), w is the vertical wind velocity (m.s^{-1}), primes indicate a fluctuation from the mean and an overbar a time average. The term $\overline{T_v' w'}$ is thus a kinematic virtual temperature flux.

Within the inertial subrange, the power spectral density of the wind speed, $S_u(f)$, measured at frequency f (Hz) and height z, is proportional to $f^{-5/3}$ (Figure 1.4):

$$S_u(f) = K\varepsilon^{2/3} f^{-5/3} \left(\frac{U_{rel}}{2\pi} \right)^{2/3} \tag{1.16}$$

where U_{rel} (m.s^{-1}) is the relative wind speed at the anemometer and K is the Kolmogorov constant (in the range 1.53-1.68: Stull, 1988). The expression $f^{5/3} . S_u(f)$ has units of m^2.s^{-2}. The inertial dissipation technique obtains ε from spectral measurements and Eqn. (1.16), which is used to determine ϕ_ε, the non-dimensional dissipation function as defined by Yelland and Taylor (1996). By making some assumptions about divergence and storage terms (Yelland and Taylor, 1996), the turbulent kinetic energy budget can then be rearranged to give the friction velocity u_* (Eqn. (1.4)):

$$u_*^2 = \frac{f^{5/3} S_u(f)}{K} \left[\frac{2\pi}{U_{rel}} \frac{\kappa_v z}{(\phi_\varepsilon)} \right] \tag{1.17}$$

MOST and its application to gas fluxes is covered in detail elsewhere (e.g.: Fairall et al., 2000). However, for trace gases such as CO_2 the high frequency sensor response (at up to about 10 Hz) required for ID calculations is beyond current sensor

capabilities, making the method currently impractical, though some initial studies have been performed (Iwata et al., 2005).

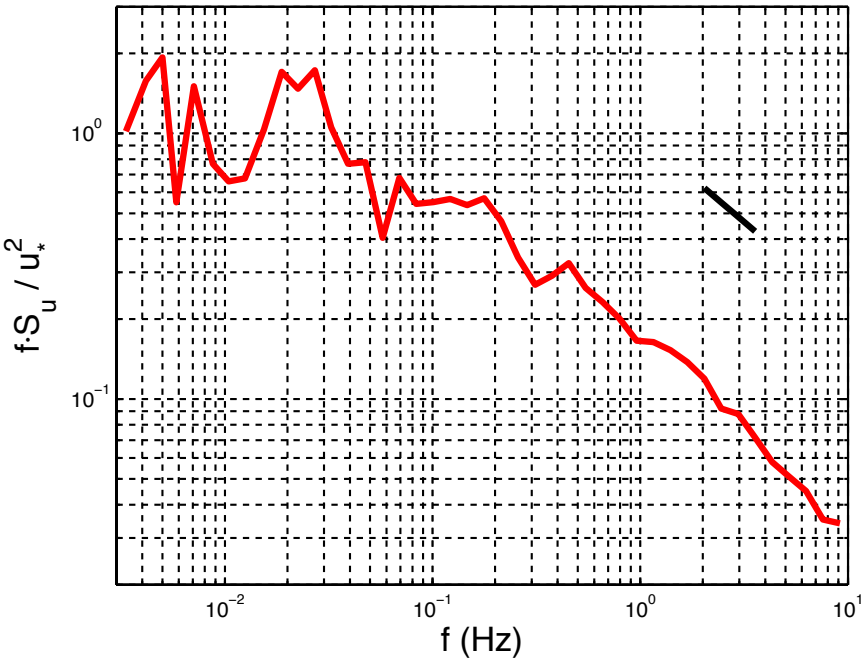

Figure 1.4. Example spectrum (red line) of the along wind component of the wind vector measured onboard *Polarfront* in September 2006. The spectrum has been normalised by the frequency and the friction velocity. The black line shows the $f^{-2/3}$ line over part of the inertial subrange (here, 2-4 Hz).

1.3.1.b. Sources of uncertainty in ID measurements

The ID technique assumes conditions of isotropy and stationarity. In addition, several poorly known terms of the budgets are assumed to be negligible (Yelland et al., 1994). The ID technique has been successfully used to measure ocean wind stress (e.g.: Yelland et al., 1994; Yelland et al., 1998) and heat fluxes (e.g.: Dupuis et al., 1997). Despite the assumptions made in ID theory, the technique is appealing for marine measurements.

ID measurements use the high frequency portion of the turbulence spectrum which is unaffected by low frequency platform motion (Yelland et al., 1998) unlike the eddy covariance flux measurements (Section 1.3.2). Additionally, the high frequency turbulence is thought to be minimally affected by flow distortion (e.g.: Edson et al., 1991). Despite this, flow distortion must still be considered when making ID measurements. The platform structure can distort the mean flow by inducing a change in flow velocity and/or a vertical displacement of the flow (e.g.: Yelland et al., 1998). If

the airflow is raised, as would be expected to happen when the flow field passes over a large structure such as a research vessel, then the air measured at the anemometer height will have originated closer to the sea surface where the turbulence is more intense. For example, flow distortion on one exposed instrument site has been shown to cause overestimation of the drag coefficient by 60% (Yelland et al., 1998). In addition the superstructure can alter the angle of the flow streamlines and introduce apparent vertical mean flow in the wind field (e.g.: Dupuis et al., 2003). The flow angle effect has been found to be small relative to other flow distortion effects (Yelland et al., 2002).

Numerical modeling of wind flow over a structure using computational fluid dynamics (CFD) techniques can enable the effects of flow distortion on the mean flow to be quantified for that structure (Yelland et al., 2002). Whilst this technique does allow corrections to be applied to mean flow components and ID flux measurements (e.g.: Yelland et al., 1998), a dependence on relative wind direction is apparent in both momentum and scalar fluxes (Dupuis et al., 2003). Comparison with more simple flow distortion corrections not derived from numerical modeling techniques (e.g.: Hare et al., 1999) show that these corrections may only be valid for a very limited range of wind directions. The strong relative wind direction dependence of the flow distortion means that a correction determined from modeling a particular wind direction correction is likely to be valid for a limited range of wind direction (approximately ±10°; Yelland et al., 2002). Additionally, for situations with large variation in flow height (approximately 4m or more) there remains uncertainty in the correction due to uncertainty in the time scale for the turbulent fluctuations to adjust to the flow height (Yelland et al., 2002).

1.3.2 Eddy covariance

1.3.2.a. Theory

Measurement of the turbulent fluctuations of wind and gas concentration allows the gas transfer velocity to be determined directly via the Eddy Covariance (EC) technique (e.g.: Krauss and Businger, 1994). The method relies on several assumptions about the turbulence in the near surface layer. To correctly measure turbulent fluctuations, an ensemble average of many identical experiments is desired. This is not normally possible when making field measurements. Turbulence measurements are commonly made using time averages of measurements made from a single point. When the turbulence field is homogenous and stationary (statistics not changing with time)

then time averages are equivalent to ensemble averages (the ergodic condition; e.g.: Stull, 1988).

In the conditions typically encountered over the oceans, we can utilize Taylor's theorem and assume that the turbulence field is "frozen" as it is advected past the measurement point, allowing the turbulence to be measured and wave number, κ (m^{-1}), related to frequency, f via (e.g.: Stull 1988):

$$\kappa = f / U \tag{1.18}$$

EC measurements also require that the flux is essentially constant with height from the surface up to the level of measurement. For a scalar quantity *s,* this implies that the vertical gradient ϕ_s (e.g.: Geernaert, 1990):

$$\frac{\kappa_v z}{s_*}\frac{\partial \bar{s}}{\partial z} = \phi_s \tag{1.19}$$

be a constant. The scale variable s_* is defined with reference to the flux of *s* and the velocity scale (friction velocity) such that $s_* u_* = \overline{s'w'}$.

For the EC method, the mass flux of a scalar quantity such as CO_2, F_{CO2} (typical units $mol.m^{-2}.s^{-1}$), is simply:

$$F_{CO2} = \overline{w'c'} + \overline{w}\,\overline{c} \tag{1. 20}$$

The first term on the right hand side of Eqn. (1. 20) is the covariance of the fluctuations of the quantity of interest with the turbulent component of the vertical wind speed. The second term represents a mean flow contribution and for trace gases this can be significant (Section 1.3.2.b).

Calculation of fluxes via the EC technique requires measurement of the variable and the wind at a frequency sufficient to include the high frequency turbulent motion, and averaged over a time period long enough to include the low frequency turbulence. To avoid signal aliasing, measurements must be made at a frequency twice that of the highest frequency that is required to be resolved. The ideal measurement period depends on factors such as the mean speed at which eddies are advected past the measurement point and the amount of inhomogeneity and stationarity in the spatial and

temporal field of the quantity in question. EC assumes a homogenous and stationary turbulent field in order to be able to apply Taylor's theorem (Eqn. (1.18)); homogeneity being equivalent to stationarity through the use of Taylor's theorem). A longer averaging period may introduce errors into the EC flux through variation in the turbulence or scalar fields, whilst too short a period may omit the contributions to the flux of the largest eddies. The measurement uncertainty of an individual measurement is inversely proportional to the length of the measurement period (Fairall et al., 2000). EC CO_2 flux measurements are typically made at frequencies of 10 Hz and averaged over periods from 10-60 minutes. In order to capture all of the turbulent motion that contributes to the flux, the frequencies that need to be resolved are usually up to about 1 Hz (Figure 1.5). Hence good sensor response up to about 2 or 3 Hz is required (e.g.: Burba and Anderson, 2007).

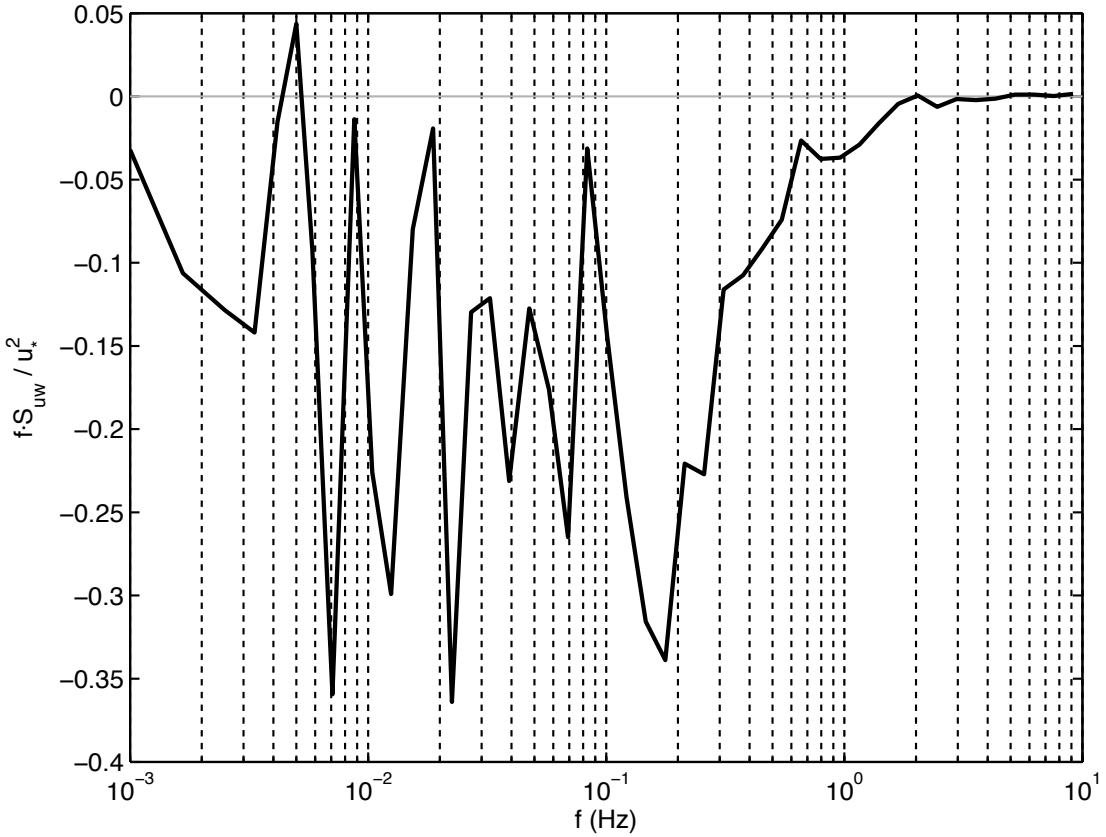

Figure 1.5. Example cospectrum of the along wind momentum flux measured onboard *Polarfront* in September 2006, U_{10n} = 15 m.s^{-1}. The spectrum has been normalised by the frequency and the friction velocity. The measurements have been corrected for platform motion.

1.3.2.b. Density correction

The second term in Eqn. (1. 20) represents a mean vertical velocity contribution to the flux and is usually assumed to be zero. However, in the presence of temperature or humidity fluxes, the density variations caused by the humidity or temperature variation will cause an apparent vertical mean mass flux for all atmospheric components (Webb et al., 1980). Hence, a correction, referred to here as the Webb et al. (1980) density correction, must be applied to either the flux or the concentration measurements (e.g.: Fairall et al., 2000). Note that a correction is only required if the atmospheric measurement is of the concentration or density. If the mixing ratio is measured (the ratio of the mass of the constituent in a particular air parcel with the mass of dry air in the air parcel) then no density correction is required.

For moisture, the effect of density variation on the measured flux can be 10% of the true flux. For CO_2, the effect can be larger than the true flux (Webb et al., 1980). As an example, mean CO_2 fluxes obtained from two different infrared instruments as part of the 1996 Air-Sea Gas Transfer and Marine Aerosol Generation (ASGAMAGE; Oost, 1998) study were -7.9 mols.m^{-2}.yr^{-1} and -26.5 mols.m^{-2}.yr^{-1} before density correction. The magnitude of the Webb et al. (1980) density correction determined for these fluxes was +32.3 mols.m^{-2}.yr^{-1} (Fairall et al., 2000).

Recently there has been debate over the true form of the Webb et al. (1980) density correction, with suggestions that important fluctuations in the air volume had been omitted (Liu, 2005). Subsequent analysis has confirmed that the original form of the Webb et al. (1980) density correction was correct (Leuning, 2007). Application of the Webb et al. (1980) density correction is discussed in detail in Chapter 4.

1.3.2.c. Signal measurement

Sensors capable of measuring CO_2 in the field at the necessary frequency for EC calculations first became available in the late 1970s. Over land, the EC method has become the standard for flux measurements of CO_2 (e.g.: Baldocchi, 2003) and other variables of interest such as heat and moisture. For CO_2 in particular the small size of the signal means that careful attention must be applied to reducing or quantifying numerous sources of error in the measurement (e.g.: Foken and Wichura, 1996; Burba and Anderson, 2007).

There are significant additional sources of error when making EC measurements in a marine environment. Firstly the air-sea concentration differences of CO_2 are often

small. Typical absolute air-sea fluxes of carbon are of the order 0-8 $mol.m^{-2}.yr^{-1}$ (Takahashi et al., 2009) whilst absolute air-land fluxes of carbon are of the order 2.5-50 $mol.m^{-2}.yr^{-1}$ (Baldocchi, 2003). Hence, locations and times of air-sea experiments must be carefully selected to ensure that the size of the signal is as large as possible compared to the precision of the measurements. The air-sea CO_2 flux signal to noise problem is increased by additional sources of error from platform motion, airflow distortion, surfactant effects and environmental contamination, which are introduced below, and discussed in detail in subsequent chapters.

1.3.2.d. Platform motion

The EC method requires measurement of fluctuations in the vertical wind speed relative to the surface through which the flux is occurring. Wind speed measurements for use in EC flux calculations are made in 3 dimensions using an instrument such as a sonic anemometer. If a flux-determining anemometer is fixed on a moving platform such as a ship at sea, then the instruments will be subject to the motion of the platform. The motion signal will often dwarf the size of the wind fluctuations (Edson et al., 1998). Whilst the method for correcting the effect of platform motion on EC measurements at sea is well established, uncertainty remains from for example, the digital filtering that must be applied to the motion signals, and the vertical movement of the measurement location through the air column. Chapter 2 describes the problem and correction method in detail, and the results of applying the platform motion correction are analysed in Chapter 6.

1.3.2.e. Instrument alignment

In order to minimize the linear velocity imposed on the measured wind at the point of measurement by the rotation of the anemometer around the platform motion sensor, it is desirable to locate the anemometer and motion instruments close together (Nilsson et al., 2010). The vector offset between the two instruments (specifically, the offset between the centre of the anemometer's measurement volume and the centre of the motion instrument) should be determined to a degree of accuracy better than the required wind velocity accuracy. Taking the resolution of the anemometer as 0.01 $m.s^{-1}$ (as for the Gill R3 Sonic Anemometer used in the experiments here) and a typical rotation rate of $10^{o}.s^{-1}$, the required vector offset accuracy is 0.057 m, an accuracy that necessitates the instruments being positioned near to one another (Brooks, 2008).

Uncertainty in the alignment of the anemometer's measurement axis with the axis of the motion instrument will cause error in the determination of the vertical wind speed and thus error in the EC momentum and scalar fluxes. A recent analysis of alignments between platform motion and anemometer instruments determined that the error in the along wind momentum flux is 3.2% for a pitch misalignment of 1°, 3.7% for a roll misalignment of 1°, and 0.7% for a yaw misalignment of 1° (Brooks, 2008). Note that the relative importance of the pitch, roll and yaw offsets shown here is likely a result of the particular platform motion experienced during the experiment. An analysis of the flux instrumentation alignment on *Polarfront* found the uncertainties in the alignments to be small (pitch and roll less than 0.1°, yaw less than or equal to 1.2°; Prytherch et al., 2010c).

1.3.2.f. Flow distortion

The distortion of the wind field by the superstructure of large measurement platforms such as research ships can be a significant source of error in EC measurements even for instruments well sited in exposed locations. In addition to the effect of flow distortion on the mean flow height and speed (Section 1.3.1.b), flow distortion affects the turbulence carried by the mean wind. It is commonly assumed that the high frequency portion of the turbulent spectrum used in ID calculations is minimally affected by flow distortion (Section 1.3.1; Yelland et al., 1998; Dupuis et al., 2003). In contrast, EC measurements utilise a much wider range of frequencies and the influence of flow distortion on the turbulence cannot be neglected.

The effect of flow distortion on the turbulent flow can be significant, with estimates of the effect on EC momentum fluxes of 15-20% (Pedreros et al., 2003; Edson et al., 1998). The effect is usually smaller for scalar fluxes as they are dependent on only the vertical component of the wind vector (Pedreros et al., 2003).

Flow distortion effects have been shown to be strongly dependent on relative wind direction, even for well-exposed sites (Popinet et al., 2004). CFD modeling, as applied to flow over structures, provides no information about flow distortion effects on the turbulent flow. The CFD corrections are therefore of most use to ID measurements as opposed to EC measurements. It is not currently possible to correct the turbulent flow for the effects of flow distortion (e.g.: Oost et al., 1994). Hence, care must be taken over instrument positioning and relative wind direction during measurement to minimize EC flow distortion errors. The effects of flow distortion are discussed in detail in Chapter 7.

1.3.2.g. Environmental contamination

The most commonly used instruments for EC CO_2 flux measurement are Infra-Red Gas Analysers (IRGAs). The instruments measure absorption of Infra-Red radiation by CO_2 molecules within a measurement volume. IRGAs are either open-path, with the measurement volume open to the environment, or closed path, where tubing is used to draw a sample from the measurement point to the enclosed analyser. Open-path IRGA instruments (e.g.: LICOR 7500) are ideally situated close to the anemometer instrument to minimize spatial error in the EC measurement. Closed path sensors draw the air from the measurement point down a tube to the instrument. The air parcel is dried and heated to a uniform temperature before measurement, eliminating the need for a large density correction. The sensors are capable of operating in rainy conditions and are less prone to environmental contamination than open path sensors. Closed path sensors introduce uncertainties into the EC CO_2 flux measurement from: attenuation of the high frequency signal in the sample tube; pressure fluctuations due to induction pump noise; time lag between sample and measurement and; heat fluctuations in the measurement volume (McGillis et al., 2001a; Marandino et al., 2007).

Over land, open-path infrared CO_2/H_2O sensors have generally been considered the standard against which closed-path sensors are evaluated, for example to determine the effects of lag due to the sampling tube required by the closed-path system (e.g.: Leuning and King, 1992). However, since the first oceanic deployments, open-path sensors have given significantly higher flux values than were obtained by other sensors or techniques and this disparity has persisted until the present. Sensor testing suggests that the error in the CO_2 flux often observed with open-path sensors could result from a cross-sensitivity to water vapor caused by contamination of the sensor lens with hydroscopic particles such as salt (Kohsiek, 2000). The effect is intermittent and highly variable, making a straightforward calibration correction problematic. Chapter 3 of this thesis addresses this source of error and describes the testing and development of a similarity theory based correction procedure (Prytherch et al., 2010a).

1.3.3 Mass inventory and dual tracer techniques

Estimates of gas transfer on large timescales (days to years) and spatial scales (kilometer to global) have been obtained using various mass balance techniques. The first estimates of gas transfer velocity were obtained using isotopes with known activity

such as radon (R^{222}). The disequilibrium in the surface ocean of R^{222} from its parent, R^{226} is due to loss to the atmosphere, allowing k to be calculated (Peng et al., 1979; Liss, 1983; Bender et al., 2011). On global scales, bomb radiocarbon, ^{14}C, released into the stratosphere during nuclear weapon testing and subsequently taken up by the ocean, provides a constraint on gas transfer (Broecker and Peng, 1974; Broecker et al., 1985).

For the last two decades, the simultaneous release of two carefully chosen tracers (often sulfur hexafluoride, SF_6 and helium isotope ^3He) in Dual Tracer Experiments (DTEs) has become a widespread technique for estimating k (Watson et al., 1991). Following release into the ocean, the concentration change of inert chemicals will be due to i) advection and dispersion away from the area of release and ii) flux into the atmosphere. By assuming that i) is the same for both chemicals, the ratio of the concentration change of the two chemicals with time is then a factor of the ratio of their transfer velocities. The difference in the concentrations will be a factor of the inverse square root of the ratio of the two chemical Sc numbers (e.g.: Wanninkhof et al., 1993):

$$k_a = h\frac{\partial}{\partial t}\left(\ln(C_a / C_b) / \left(1 - (Sc_b / Sc_a)^{-n}\right)\right) \tag{1.21}$$

where the subscripts a and b denote the two chemicals in question and h is the tracer mixed layer depth. The method requires that chemicals with significantly different Sc numbers must be selected (at 20°C and psu 35, $Sc_{SF6} = 992$, $Sc_{3He} = 144$) and strongly depends on the Schmidt number exponent whose exact value remains uncertain (Section 1.2.3). If the true value of n is assumed to lie within $1/2 \leq n \leq 2/3$ then the error in k_{CO2} (calculated in Eqn. (1.21)) associated with the uncertainty in n is of order 10-20% (Asher and Wanninkhof, 1998b). Care must be taken in relating gas transfer measurements obtained on larger scales to wind speed measurements because of the likely non-linear dependence of k on wind speed. Additionally these techniques do not provide any information on variation on gas transfer at shorter time scales than their averaging period (typically one day or longer). The technique also requires determination of the mixed layer depth within the experiment site in order to constrain the measurement volume. The measurements used to determine the depth may not fully capture the spatial and temporal structure of the layer and hence further uncertainty is introduced into the gas transfer calculation.

1.3.4 Other measurement techniques

The profile method utilizes simultaneous measurements of the quantity in question at two or more different heights. The gradient of the concentration profile then enables the flux to be calculated with MOST used to determine the atmospheric stability. The method offers a significant advantage for trace gas fluxes over other "direct" methods in that the measurements do not have to be made at high frequency (McGillis et al., 2001b). Whilst the stability corrections, developed over land, have been shown to be valid in marine settings (Edson et al., 2004) there are other significant problems in applying the profile method at sea. The parameterisations used become invalid when surface waves influence the near surface atmosphere; ship motion adversely affects the measurements due to the non-linearity of the gradient; the small concentration gradients of trace gases can be below detection limits of current sensors and making measurements close to a wavy surface is challenging. Measurements close to the surface on large platforms such as ships can also be subject to increased effects of flow distortion (Yelland et al., 2002).

Whereas EC gas flux measurements are usually made some distance above the air-sea interface, some initial attempts have been made to measure water-side EC. The vertical velocity of a neutrally buoyant LagGrangian drifter floating a short distance below the surface has been used to measure O_2 fluxes in hurricane conditions (D'Asaro and McNeil, 2007; McNeil and D'Asaro, 2007). A significant challenge to water-side EC measurements is that wave orbital velocities are orders of magnitude larger than the turbulent velocities required to calculate the fluxes.

1.3.5 Laboratory measurements

It is noteworthy that the results of gas transfer measurements made in laboratory conditions in wind/wave tanks are often hard to translate to oceanic conditions. The wave field in even the largest tanks is severely restricted compared with the open ocean and the seastate dependence on mean wind speed is significantly different (e.g.: Hasse, 1990). Bubble size and spectra also differ in laboratory conditions in comparison with the open ocean. A particular cause of the observed differences between wave tanks and natural conditions are wall effects and the limited fetch of wave tanks. For example in wind-wave tunnel experiments a clear relationship has been found between tank size and k, with smaller tanks showing smaller values of gas transfer velocity (Ocampo-

Torres et al., 1994). The more developed wave field of a larger tank may explain the difference.

Measurements of heat at the air-sea interface using infrared thermographic imaging allow the dispersion rates of heat, and thus the transfer velocity of heat, k_{heat}, to be measured. This method has been used for the study of gas transfer based on the assumption that k_{heat} can be related to gas using a Schmidt number relation as per Eqn. (1.13) (Jähne et al., 1987b, Haußecker et al., 1995). The Schmidt number for heat is very low (~6) in comparison to most gases of interest, and thus the method relies strongly on the accuracy to which the Schmidt number and exponent are determined. If the true value of n is unknown and assumed to lie within $1/2 \leq n \leq 2/3$ then the uncertainty in k_{CO2} derived from heat transfer is of order 200% (Asher and Wanninkhof, 1998b). The accuracy to which heat measurements can be used to quantify gas exchange has been called into further question by recent studies showing significant differences in determined fluxes (for example, in one experiment k_{heat} was found to be 2.5 times greater than k_{gas} : Zappa et al., 2004).

1.4. Transfer velocity parameterisation

1.4.1 Wind speed and wind stress parameterisation

Evaluating the air-sea flux of CO_2 is an essential part of understanding climate. The flux of a trace gas such as CO_2 is parameterised in terms of a transfer velocity coefficient (Eqn. (1.12)). In order to estimate the gas flux on regional and global scales, the transfer velocity itself must be parameterised in terms of some widely measured variable. Wind speed is commonly used due to its dominant influence on near-interfacial turbulence and the availability of global coverage datasets. Wind speed in the surface layer can be represented as having a logarithmic dependence on height above the surface:

$$U_z = \left(\frac{u_*}{\kappa_v}\right)\ln\left(\frac{z}{z_0}\right) \tag{1.22}$$

where U_z is the wind speed at a height z, and z_0 is the aerodynamic roughness length, defined as the height above the surface at which the wind speed goes to zero. The roughness length is dependent on the characteristics of the surface. Over the ocean it is

of order 10^{-3} to 10^{-4} m (Stull, 1988), though its dependence on seastate remains uncertain (e.g.: Taylor and Yelland, 2001; Lange et al., 2004; Drennan et al., 2005). To account for the effect of measurement height and atmospheric stability, wind speed measurements are usually normalised to conditions of neutral stability and a common measurement height of 10 m. The normalization is indicated by the subscripts *10n*.

Proposed gas transfer to wind speed relationships differ significantly, particularly at high wind speeds (Figure 1.6; Table 1.1). At winds of 7 $m.s^{-1}$ published relationships differ by 50%, and at 15 $m.s^{-1}$ the relationships differ by 100% (Figure 1.7). Wind speeds of 15 $m.s^{-1}$ or more occur infrequently over the global ocean but due to the non-linear dependence of k on wind speed, they have a significant effect on the global flux (e.g.: Takahashi et al., 2002). There are very few measurements of k obtained at wind speeds above 15 $m.s^{-1}$, and the derived relationships are extrapolated to higher wind speed values.

There are numerous reported parameterisations of the transfer velocity, derived from various types of experiment. A selection are described here, and summarized in Figure 1.6 and Table 1.1. For clarity, some of the most widely used parameterisations (within this thesis and in other studies) are shown in Figure 1.7.

One of the earliest widely accepted parameterisations of k , that of Liss and Merlivat, (1986) was based on a combination of data obtained from a tracer release (SF_6) into a lake (Wanninkhof et al., 1985) and wind tunnel measurements (Broecker and Siems, 1984). The relationship had three distinct regimes, corresponding to a relatively smooth ocean surface, a rough surface following the formation of significant waves, and a high wind speed regime incorporating wave breaking:

$$\begin{aligned} k_{600} &= 0.17U_{10} \qquad for\, U_{10} \le 3.6\, m/s \\ k_{600} &= 2.85U_{10} - 9.65 \quad for\, 3.6 < U_{10} \le 13\, m/s \\ k_{600} &= 5.9U_{10} - 49.3 \quad for\, U_{10} > 13\, m/s \end{aligned} \tag{1.23}$$

Estimates of k obtained via DTEs (e.g.: Nightingale et al., 2000a) and from the bomb radiocarbon inventory (e.g.: Wanninkhof, 1992) are in good agreement following a reanalysis of the radiocarbon inventory (Sweeney et al., 2007). The dependence of transfer velocity on wind speed from DTEs is found to be quadratic, with, for instance, the two relationships of Nightingale et al (2000a):

$$k_{600} = 0.24U_{10}^2 + 0.061U_{10} \tag{1.24}$$

and Sweeney et al (2007):

$$k_{660} = 0.27U_{10}^2 \qquad (1.25)$$

giving very similar values for wind speeds up to 15 m.s^{-1} (Figure 1.6; Figure 1.7). A quadratic dependence of gas transfer has a theoretical justification if the gas transfer is considered to scale with wind stress (Eqn. (1.4)). However, it should be noted that the relationship determined from the radiocarbon budget implicitly assumes both a quadratic dependence, which is fit to one data point (determined from the global radiocarbon budget), and that $n = 1/2$. It is also dependent on the choice of wind speed product used (e.g.: Naegler et al., 2006).

The various DTEs include wind speeds up to 16 m.s^{-1}, but are highly scattered. For example, two separate experiments in the Southern Ocean (SoFex: Wanninkhof et al., 2004; and SAGE: Ho et al., 2006) obtained significantly different results (Figure 1.6; Table 1.1). DTEs also rely strongly on the uncertain Schmidt number exponent (Section 1.3.3; Eqns. (1.9),(1.13) and (1.21)). Some studies suggest that a constant value of n is not appropriate due to the solubility dependence of bubble mediated gas transfer, with resulting errors for CO_2 transfer velocity of around 20-30% (Asher and Wanninkhof, 1998a). Other studies have found that $n = 1/2$ is appropriate even under wave breaking conditions (Nightingale et al., 2000b). Around 50% of the difference between the DTE results appears to be inherently due to experimental uncertainty (Asher, 2009). The coastal locations used for some DTEs (e.g.: Nightingale et al., 2000b, which summarized the results of various North Sea coastal experiments; Wanninkhof et al., 1993; Wanninkhof et al., 1997) may have had less developed wave fields and different surfactant concentrations to that of the open ocean, which raises further questions about the general applicability of these results. Some recent open ocean DTEs (e.g.: Nightingale et al., 2000a; Ho et al., 2006) are in reasonable agreement with the coastal DTE results whilst others (Wanninkhof et al., 2004) suggest a different dependence on wind speed.

Direct measurement of the turbulent CO_2 flux using Eddy Covariance (EC) techniques allows the flux to be measured on shorter timescales similar to the variability of the various forcing factors. EC measurements are challenging to perform at sea due to a small signal, platform motion (Section 1.3.2.d; Edson et al., 1998), distortion of the

wind flow by platform superstructure (Section 1.3.2.f; Yelland et al., 1998) and environmental sensor contamination (Section 1.3.2.g; Prytherch et al., 2010a). The first successful open ocean EC measurements were made during the Interdisciplinary Air-Sea Gas Exchange Experiment (GasEx-98) in the North Atlantic in June, 1998. The experiment found a stronger, cubic dependence of k on wind speed (McGillis et al., 2001a):

$$k_{660} = 3.3 + 0.026U_{10}^3 \quad (1.26)$$

The non-zero intercept observed in this experiment was ascribed to buoyancy related flux at low wind speeds. A cubic dependence was also suggested by Monahan and Spillane (1984) who hypothesized that k scales with the fractional whitecap coverage (Section 1.4.3), which scales approximately with U^3. A cubic relationship of k with wind speed has been observed in other open-ocean EC experiments (McGillis et al., 2004; Table 1.1). This experiment, in the equatorial pacific, experienced strong solar heating and weak to moderate winds. The resulting daytime near surface stratification in the ocean suppressed convective mixing and was found to significantly impact the air-sea CO_2 flux through changes to the water-side partial pressure. The combination of near surface stratification and surfactants suppressed daytime flux values by approximately 40% relative to night time fluxes. An experiment using a dedicated near surface profiler examined the dependence of CO_2 flux on near surface temperature gradients and determined the maximum flux biases in low winds were approximately ± 4% (Ward et al., 2004).

A cubic dependence of gas transfer on wind speed is able to satisfy the radiocarbon budget constraint (Wanninkhof and McGillis, 1999). Whilst the increased transfer at higher winds is supposed to be due to the influence of wave breaking and bubbles, the smaller transfer at low to moderate winds in a cubic dependence is hypothesized to be due to the influence of surfactants (Wanninkhof and McGillis, 1999). Whilst most DTEs observe a quadratic wind speed relationship, an experiment in the Southern Ocean found results that could be best explained with a cubic wind speed fit, though the difference in correlation coefficients between the quadratic and cubic fits was minimal (Wanninkhof et al., 2004).

There have been relatively few reported open ocean EC gas flux measurements, especially at high wind speeds (> 15 $m.s^{-1}$). Some air-sea EC experiments have found quadratic wind speed dependence. One such experiment (Weiss et al., 2007) reported

results for average wind speeds of up to 17.5 $m.s^{-1}$, from a coastal location with low salinity (less than 9 psu) and relatively short fetch (order 100 Km). Hence, the result obtained from these measurements:

$$k_{660} = 0.365U_{10}^2 + 0.46U_{10} \tag{1.27}$$

may not be directly applicable to the open ocean.

It is noteworthy that many of wind speed parameterisations of k go to zero at zero wind speed, whilst the parameterisations of McGillis et al., 2001a (Eqn. (1.26)) and McGillis et al., 2004 (Table 1.1) have a positive contribution at zero wind speed. Zero mean wind gusts and effects independent of mean wind such as buoyancy convection would likely give rise to a small flux, though a significant flux would only be likely in tropical areas with a large diurnal cycle in near surface temperature (Jeffery et al., 2007; Jeffery et al., 2008).

The transfer velocity represents the numerous kinetic factors that influence gas exchange. The thermodynamic factors are represented by the fugacity difference across the interface. Some proportion of the variability in the proposed parameterisations of k (Table 1.1) is due to unaccounted-for kinetic factors. These include varying wave fields (e.g.: Jähne et al., 1987b), rain effects (e.g.: Turk et al., 2010) and surfactants (e.g.: Frew et al., 1997). Wind stress at the sea surface drives much of the surface dynamics (although not all, i.e. surfactants), which suggests that the friction velocity should be a good choice for parameterising the gas transfer velocity (e.g.: Eqn. (1.9)). Surface renewal theory suggests that the dependence of k on u_* should be linear. A linear relationship has been observed in some field experiments (Huebert et al., 2010; McGillis et al., 2001a) but others have found considerable scatter and a non-linear dependence (Frew et al., 2004). Some laboratory measurements found that gas transfer was not well described by u_* (Jähne et al., 1987b). Huebert et al. (2010) suggest that the lack of a linear relationship in the Frew et al. (2004) measurements may be due to the presence of surfactants, and that when the low wind speed measurements are removed from the analysis, a linear dependence is observed. Direct measurements of the friction velocity are routinely made using micrometeorological sensors, for instance in EC experiments. However, they are not routinely available. In order to obtain friction velocities from wind speed measurements, either the roughness length (Eqn. (1.22)) or an equivalent empirical coefficient termed the drag coefficient, C_D, is utilized, defined as:

$$C_{D10n} = \frac{u_*^2}{U_{10n}^2} \tag{1.28}$$

where the subscript *10n* indicates a normalization to a 10 metre measurement height and neutral atmospheric stability.

An example of a parameterisation of the drag coefficient determined from ID measurements (Section 1.3.1) following a correction for the effects of flow distortion (Section 1.3.2), is (Yelland et al., 1998):

$$1000 \cdot C_{D10n} = 0.50 + 0.071 U_{10n} \quad (6 \le U_{10n} \le 26\, m \cdot s^{-1}) \tag{1.29}$$

In addition to the simple wind based parameterisations detailed above, more complex physical models of gas transfer have been developed (e.g.: National Atmospheric and Oceanic Administration / Coupled-Ocean Atmospheric Response Experiment: NOAA / COARE, Fairall et al., 1996; Fairall et al., 2000). These models have the advantage of being able to represent gas transfer in a wider variety of situations. They can incorporate numerous physical effects, for instance, COARE incorporates bubble mediated transfer model (Woolf, 1997). However, the COARE model contains several tunable parameters that must be determined with experimental data, and are thus influenced by the variability between different data sets (e.g.: Hare et al., 2004, who tuned the model to flux measurements obtained in GAS-EX 98). The most recent development of the NOAA / COARE model is probably Jeffery et al. (2010), who utilized an extensive model run to obtain coefficients that give a reasonable fit with a variety of different data sets.

Table 1.1. A selection of reported wind speed parameterisations of the gas transfer velocity. The location used to obtain the measurements that the parameterisation was derived from (if appropriate) and brief details of the experiment are given. *W* is the fractional coverage of whitecaps. Further information is given in the stated references.

Reference	Relationship	Location	Method and comments
Liss & Merlivat, 1986	$k_{600} = 0.17U_{10}$ $for U_{10} \le 3.6 m/s$ $k_{600} = 2.85U_{10} - 9.65$ $for\, 3.6 < U_{10} \le 13 m/s$ $k_{600} = 5.9U_{10} - 49.3$ $for U_{10} > 13 m/s$	Laboratory and Lake	Theory, wind tunnel measurements and lake tracer (Sf_6) release. Tracer winds 1.2 – 6.1 m.s^{-1}.
Wanninkhof, 1992	$k_{660} = 0.31U_{10}^2$ (Short -term winds) $k_{660} = 0.39U_{10}^2$ (long-term winds)	Global	Global ^{14}C constraint. Quadratic fit to one data point (7.4 m.s^{-1}).
Woolf, 1997	$k_{600} = 56.52u_* + 3.84 \times 10^{-6} U_{10n}^{3.41}$	-	Laboratory measurements and theory. Whitecaps parameterised as per Monahan and Muircheartaigh, 1980.
Asher and Wanninkhof, 1998a	$k = \left[\left(AU_{10} - B\right) + W\left(A_T - \left(AU_{10} - B\right)\right)\right] Sc^{-1/2} + W\left(\frac{a_1}{\alpha_o} + b_1 \alpha_o^{-m} Sc^{-n1}\right)$	-	Laboratory measurements. Coefficients differ for invasion and evasion (Asher et al., 1996).
Wanninkhof & McGillis, 1999	$k_{660} = 0.0283U_{10}^3$ (short -term) $k_{660} = 1.09U_{10} - 0.333U_{10}^2 + 0.078U_{10}^3$ (long-term)	Global	Global ^{14}C constraint. Cubic fit to one data point (7.4 m.s^{-1}).
Nightingale et al., 2000a	$k_{600} = 0.24U_{10}^2 + 0.061U_{10}$	Coastal and open ocean	DTE summary result. Addition of one open ocean result to North Sea coastal results. Open ocean wind 5.5 – 7.3 m.s^{-1}.
Nightingale et al., 2000b	$k_{600} = 0.222U_{10n}^2 + 0.333U_{10n}$	Coastal	DTE summary result. North Sea coastal studies. Wind speeds 5.9 – 14.7 m.s^{-1}.
McGillis et al., 2001a	$k_{660} = 3.3 + 0.026U_{10}^3$	North Atlantic (GasEx-98)	EC (closed-path). Wind speeds 0.9 - 16.3 m.s^{-1}. Invasion only.
McGillis et al., 2004	$k_{660} = 8.2 + 0.014U_{10n}^3$	Equatorial Pacific (GasEx-2001)	EC (closed-path). Wind speeds 2.5 – 11 m.s^{-1}. Evasion only.
Wanninkhof et al., 2004	$k_{660} = 0.027U_{10}^3$	Southern Ocean (SoFex).	DTE. Wind speeds 7.8 – 11.3 m.s^{-1}.
Woolf, 2005	$k_{600} = 56.52u_* + 2 \times 10^{-5} \frac{u_* 0.0163 X^{1/2} U_{10}}{\nu_w}$	-	Bubble mediated transfer theoretically parameterised using a fetch model (Carter, 1982).
Ho et al., 2006	$k_{600} = 0.266U_{10}^2$	Southern Ocean (SAGE).	DTE. Wind speeds 7.4 -16 m.s^{-1}.
Naegler et al., 2006	$k_{660} = 0.38U_{10}^2$	Global	Reanalysis of the ^{14}C inventory. NCEP short-term (daily) winds. Quadratic fit to one data point (6.6 m.s^{-1}).
Sweeney et al., 2007	$k_{660} = 0.27U_{10}^2$	Global	Reananalysis of Global ^{14}C constraint. NCEP short -term winds. Quadratic fit to one data point (6.9 m.s^{-1}).
Weiss et al., 2007	$k_{660} = 0.365U_{10}^2 + 0.46U_{10}$	Baltic sea	EC measurements (open-path). Fetch ~ 100km, psu ~ 9. Wind speeds 0-17.5 m.s^{-1}. Mainly Invasive.
Wanninkhof et al., 2009	$k_{660} = 3 + 0.1U_{10} + 0.064U_{10}^2 + 0.011U_{10}^3$	-	Theoretical considerations.

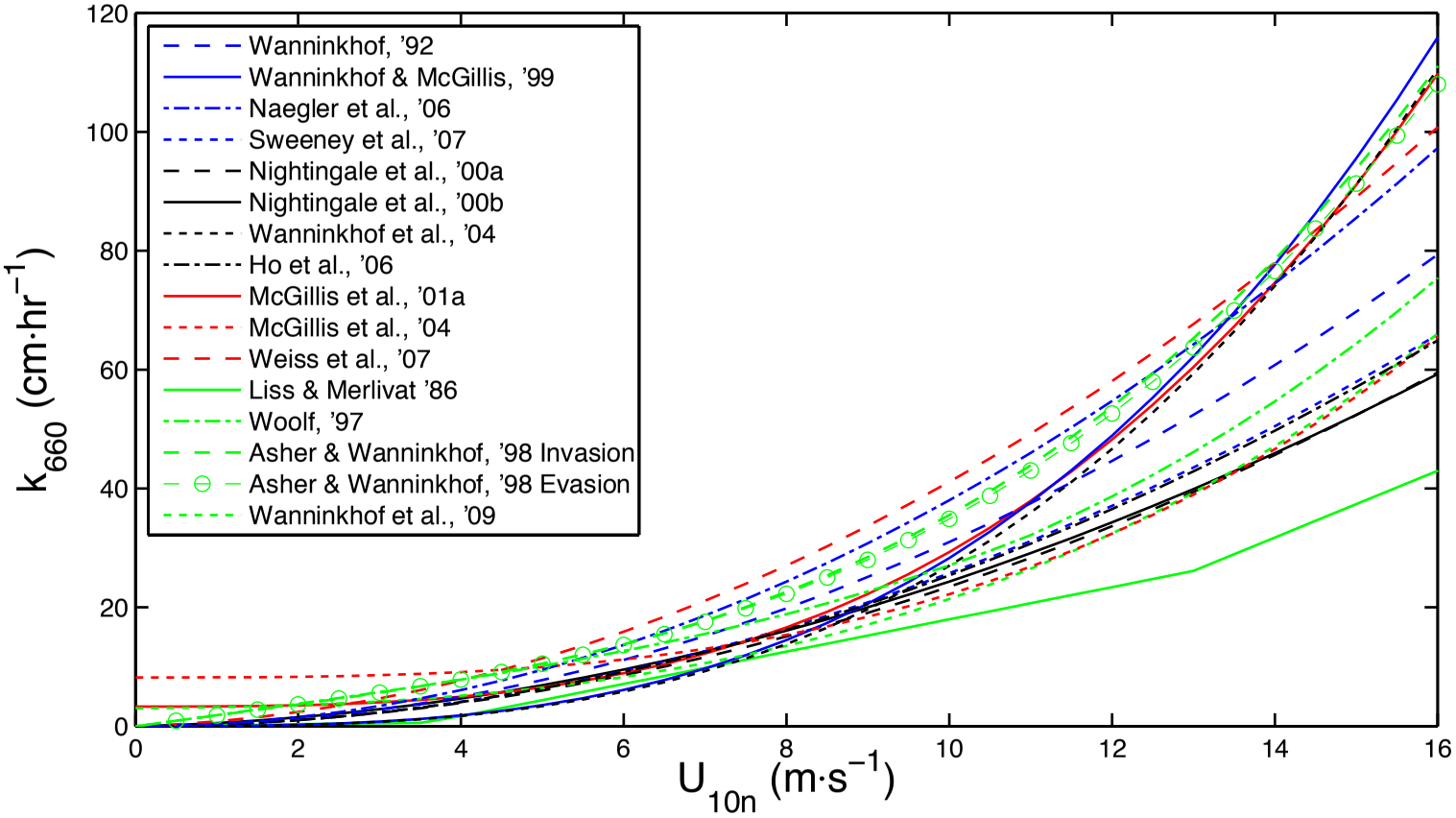

Figure 1.6. A selection of *k* parameterisations normalised to a *Sc* of 660. Relationships are described in the text, listed in Table 1.1 and detailed in the references listed in the key. Blue lines indicate parameterisations derived from the global C14 inventory. Black lines indicate parameterisations obtained from DTEs. Red lines indicate parameterisations obtained from direct EC measurements and green lines indicate other (laboratory and theoretical) methods were used. Relationships corresponding to short-term (steady on a timescale of order 1 hour) winds have been used.

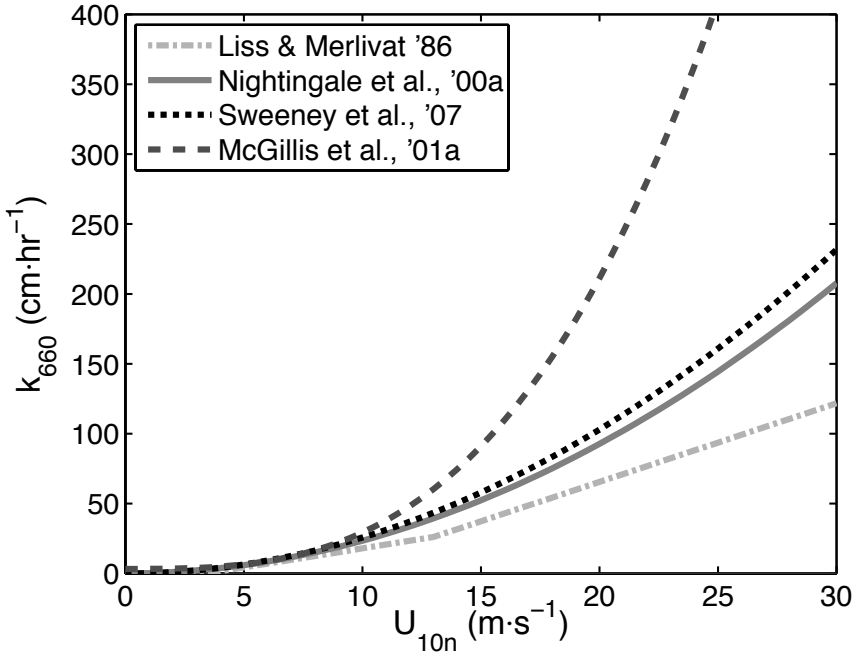

Figure 1.7. A selection of current wind speed based parameterisations of *k,* normalised to a *Sc* of 660. Relationships are described in the text, listed in Table 1.1 and detailed in the references listed in the key.

1.4.2 Mean square slope

The formation of waves at the surface of the air-water boundary significantly impacts the rate of gas transfer across the boundary. Laboratory measurements have shown that in changing from a relatively flat interface to a rough, wavy one, the Schmidt number dependence of the transfer velocity (Eqn. (1.9)) changes from $n = 2/3$ to $n = 1/2$ (Jähne et al., 1987b). The change is ascribed to two main processes associated with the formation of waves. Firstly, local convergences and divergences, directly related to the conceptually modeled surface renewal events (Section 1.2) begin to occur at the boundary (e.g.: Csanady, 1990). This serves to thin the diffusive layer, increasing the gas transfer rate. Secondly, energy from the wind is transferred via wave-wave interactions and turbulent dissipation into interfacial turbulence, also increasing the gas transfer rate. This process was found in laboratory measurements to be best described by the total mean square slope of the wave field, $\langle S^2 \rangle$, (Jähne et al., 1987b). Field measurements using heat transfer as a proxy for gas transfer also found a stronger correlation between $\langle S^2 \rangle$ and *k* than for wind speed or wind stress (for wavenumbers in the range 40-800 rad.m^{-1}; Frew et al*.,* 2004).

At lower wind speeds, microbreaking (defined as the breaking of steep, wind-forced waves without air entrainment, where the waves are *O*(0.1-1m) in length and

O(0.01-0.1 m) in amplitude) has been shown to exert a significant influence on gas transfer through modification of the aqueous interfacial layer. A dependence of *k* on micro breaking has been theorised (Csanady, 1990) and observed in laboratory measurements using IR imaging to detect the disruption to the boundary layer in the presence of microbreaking (Zappa et al., 2001; Zappa et al*.,* 2004). Some laboratory results suggest that waves of any size should influence gas transfer (Jähne et al., 1987b). Other laboratory experiments support the significance of micro breaking, with a dependence of *k* on mean square slope, $<S^2>$, shown to be primarily due to relatively small waves (wavelength <= 3 cm; Bock et al., 1999). However, there remain significant uncertainties over the applicability of heat as a proxy for gas transfer (Section 1.3.5).

At low wind speeds gas transfer rates may be complicated by the presence of surface films. Surface films impede gas transfer by creating an additional barrier through which the gas must transfer. Surfactants also act to suppress relatively small waves and surface roughness, whilst having little effect on larger gravity waves (wavelengths >= 30 cm; Bock et al., 1999). Hence, measurement of gas transfer in the presence of films provides information about the relative importance of different sized waves.

Measurement of gas transfer in the presence of surface films result in reductions of *k* of as much as 60% (Bock et al., 1999). Laboratory (Frew et al., 1997) and field (Frew et al., 2004) measurements suggest that parameterising *k* in terms of $<S^2>$ removes the dependence of gas transfer on surfactants apparent in measurements of wind speed. This may be due to the suppression of smaller waves by the surfactants, reducing both *k* and $<S^2>$ and implying a dominant role for smaller waves in gas transfer.

Information on wave slope can be obtained from satellite-based instruments and hence wave slope provides a possible alternative to wind speed as a forcing in global flux products. Both altimeters and scatterometers (e.g.: QuikSCAT) provide information on wave slope. For scatterometers, the observed upwind Normalized Radar Cross-Section (NRCS), is related to mean square slope. Wave slope is inferred from NRCS through a wave scattering model. Altimeters provide good measurements but have narrower swaths and take longer to achieve global coverage (typically 10-day repeat passes). Hence, they do not capture short timescale variability as well as scatterometers. Scatterometers have better coverage, but the larger footprint means that wave variability

may be lost through averaging. Work is ongoing to develop parameterisations of k from the dependence of $<S^2>$ on observations of NRCS made by QuikSCAT using in situ gas transfer measurements (Bogucki et al., 2010). The current analysis is based on relatively few data points and further validation of the technique using in situ measurements over a larger range of wind speeds is required. It is not currently clear that $<S^2>$ will prove a better global parameterisation of k than does wind speed.

1.4.3 Whitecapping and seastate parameterisation

Bubbles are another factor that have been shown to exert a significant influence on gas transfer (e.g., Farmer et al, 1993; Asher et al., 1996) by both providing an additional medium through which transfer can occur, and by disrupting the interfacial layer at the sea surface. There are two main, distinct models of bubble-mediated gas transfer (Woolf, 1993; Memery and Merlivat, 1985). Both models imply that the presence of bubbles will increase both invasive (downwards) and evasive gas transfer, with the increase in transfer inversely proportional to the solubility of the gas species (e.g.: Woolf, 1997). The effect is asymmetric, with an unequal contribution to invasive (from air into water) and evasive fluxes. Gas transfer measurements in a whitecapping tank show that k is larger for invasive fluxes (Figure 1.6; Asher and Wanninkhof, 1998a; Asher et al., 1996). Whilst the transfer coefficients derived from the whitecapping tank measurements for a typical range of wind speeds (5-15 $m.s^{-1}$) suggested that the invasive gas transfer rate is 2% higher than the evasive rate, two experiments making open-ocean EC measurements of the CO_2 flux found that the invasive rate was 25% higher than the evasive rate for the same wind speed range (McGillis et al., 2001a; McGillis et al., 2004).

In the open ocean, bubbles are primarily the result of wave breaking. Wave breaking affects gas transfer through both bubble injection and by enhancing near surface turbulence, increasing the rate of surface renewal events and disrupting the molecular skin that controls the rate of gas transfer. Bubble-mediated transfer has a complicated dependence on bubble size, bubble depth, bubble lifetime, near surface turbulence and properties of the particular gas species (e.g.: Woolf, 1993). Hydrostatic pressure and surface tension can increase the partial pressure of gases within a bubble so that transfer into the ocean occurs from bubbles even in conditions of super saturation (Woolf, 1997).

The presence of surfactants (Section 1.4.2) will also affect bubble-mediated transfer through modification of bubbles reaching the water surface (Asher et al., 1996). Whilst surfactants are generally thought to have a smaller influence on gas exchange at higher wind speeds, the presence of surfactants may strongly influence bubble-mediated exchange by their presence on bubble skins (Woolf, 1997). The effect may be significant, potentially reducing the transfer through bubble surfaces by a factor of five (Memery and Merlivat, 1985). It is not yet understood how to best parameterise this effect.

The seastate can be described through a number of different variables such as wave height, wave steepness, wave age, wave development and mean square slope (e.g.: Tucker and Pitt, 2001). Wave height is a complicated function of the wind forcing history both locally and at distance. Wave height can be parameterised in terms of wind speed and fetch (Carter, 1982). Whilst the seastate itself has a dependence on wind speed, wind speed alone does not dully describe seastate due to the particular combination of wind sea and swell at the measurement point, the relative directions of the swell to the mean wind and the influence of numerous other factors affecting the wave field (fetch and wave age, wind stress and wind history, current interactions, surface films and boundary layer stability). The relationship between wind speed or seastate and the amount of wave breaking is very uncertain.

The concentration of bubbles near to the sea surface is commonly described in terms of fractional coverage of whitecaps, W (e.g.: Monahan and Muicheartaigh, 1980). Whitecap coverage can be measured through still or video imaging and image processing routines (e.g.: Callaghan and White, 2009). There have been numerous attempts to relate W to wind speed, and W has often been shown to scale as the cube of the wind speed (e.g.: Monahan and Spillane, 1984). A scarcity of available W data (to date in excess of 30 relationships have been published comprising approximately 800 data points) and experimental uncertainty has led to extremely large variation (> 2 orders of magnitude) between currently proposed parameterisations (Anguelova and Webster, 2006; Figure 1.8). In addition, there may also be a significant dependence of the measurements on experimental factors such as orientation of the vessel and camera to the wind and wave direction (pers. comm., Dr Ben I Moat, NOCS, 2011).

The influence of bubbles on gas transfer is also suggested by experiments measuring the transfer of gases with different solubilities. For a particular gas species, both models (Woolf, 1993) and laboratory measurements (Liss and Merlivat, 1986;

Asher et al., 1996) have shown that the bubble gas transfer rate is highly dependent on the solubility of the gas in question. Hence the enhancement to gas transfer will vary between gas species based on both the diffusivity of the gas and the solubility. An influence of bubbles implies an inverse dependence of gas transfer on gas solubility. EC field measurements of DMS, a gas species with a solubility approximately an order of magnitude larger than CO_2, have shown a lower transfer velocity than that sometimes obtained making EC CO_2 measurements, as might be expected due to the lesser influence of bubbles on the transfer (Huebert et al., 2010). However, the quality of these results are somewhat questionable due to the extremely high scatter in the EC momentum fluxes obtained on the cruise, which resulted in ID momentum fluxes obtained from other instruments being used in the analysis of the DMS flux results. Other existing EC measurements of air-sea DMS flux comprise too few measurements, and are at too low wind speeds to be able to make definitive conclusions on the possible influence of bubble mediated transfer (Miller et al., 2009; Marandino et al., 2007).

Bubble-mediated gas transfer velocity is dependent on the gas solubility, with the transfer velocity expected to be higher for less soluble gases (Woolf, 1997). This solubility dependence was proposed as a means to explain differences in gas transfer velocity measured in different DTEs (Wanninkhof et al., 1993; Asher and Wanninkhof, 1998a). Their results showed that whilst bubbles did not significantly affect the results of DTEs (made using two similarly insoluble gases, SF_6 and ^3He), they would be significant when using the DTE measurements to infer transfer velocities for more soluble gases such as CO_2. A reanalysis of all the DTE made at sea, including those discussed in Asher and Wanninkhof (1998a), concluded that a variable Schmidt exponent (Wanninkhof et al., 1993) was not necessary for agreement between the studies, and that the remaining differences could be explained by other factors such as varying wind speeds (Nightingale et al., 2000b).

Parameterisations of gas transfer which incorporate wave breaking effects have been developed from radiocarbon invasion rates and wave tank studies (Asher and Wanninkhof, 1998a), and from wave tank studies and a theoretical dependence of wave breaking on fetch (Woolf, 2005). The model of Asher and Wanninkhof (1998a) includes a dependence on both wind speed and the fractional whitecap coverage W:

$$k = \left[\left(AU_{10} - B \right) + W \left(A_T - \left(AU_{10} - B \right) \right) \right] Sc^{-1/2} + W \left(\frac{a_1}{\alpha_o} + b_1 \alpha_o^{-m} Sc^{-n} \right) \qquad (1.30)$$

where the coefficients A, A_T, B, a_1, b_1, m and n are different for gas invasion and evasion and were determined in a wave/whitecapping tank (Figure 1.6; Asher et al., 1996).

The model was applied to a relatively small sample of open ocean whitecap measurements for which coincident, EC measurements of CO_2 k were also available (GasEx-98 measurements; Asher et al., 2002). The model incorporating whitecaps predicted similar transfer velocities to the EC measurements, showing a slightly higher dependence on wind speed than the cubic relationship obtained from the EC k measurements. Variability in the W measurements in the experiment was high, and whilst clearly indicating an influence of bubbles on gas transfer, the relative importance of solubility-dependent bubble processes in determining the total transfer velocity using the model was found to be no more than 25% at the wind speeds encountered (up to around 16 $m.s^{-1}$). This proportional effect of bubble-mediated exchange would not be enough to explain the disparity between published quadratic and cubic parameterisations of k. It should also be noted that the model is sensitive to the value of W, and use of some commonly used W parameterisations (e.g.: Monahan and Muircheartaigh, 1980) leads to unrealistically high transfer velocities.

A different k model, incorporating wave-breaking effects via a fetch dependence, was tuned to encompass the spread of published parameterisations (Figure 1.9; Woolf, 2005):

$$k_{600} = 56.52u_* + 2 \times 10^{-5} \frac{u_* 0.0163 X^{1/2} U_{10}}{\nu_w} \qquad (1.31)$$

where X is the fetch (km), which is used in the model as a representation of seastate (Woolf, 2005; Carter, 1982).

The Woolf model is suggestive: some experiments making in situ measurements in relatively short fetch conditions (e.g.: Liss and Merlivat, 1986; Nightingale et al., 2000b) find a weaker dependence of gas transfer on wind speed than other experiments that made in situ measurements in locations with large fetches (e.g.: McGillis et al., 2001a). However, the model was derived from several untested parameterisations of seastate parameters (relating fetch and whitecap coverage to gas transfer) and then tuned to give reasonable results. Simultaneous measurements of fluxes, seastate and whitecapping are required to allow the assumptions of these models (Eqns. (1.30) and (1.31)) to be properly tested.

An enhancement of wind stress due to seastate at a particular wind speed could also impact gas transfer through the dependence of k on u_* (Eqn. (1.9)). However variation in the drag coefficient has been shown to be more attributable to flow distortion effects than to seastate (Yelland et al., 1998) and there is still considerable debate about the impacts of seastate on wind stress (e.g.: Drennan et al., 2005; Lange et al., 2004; Taylor and Yelland, 2001).

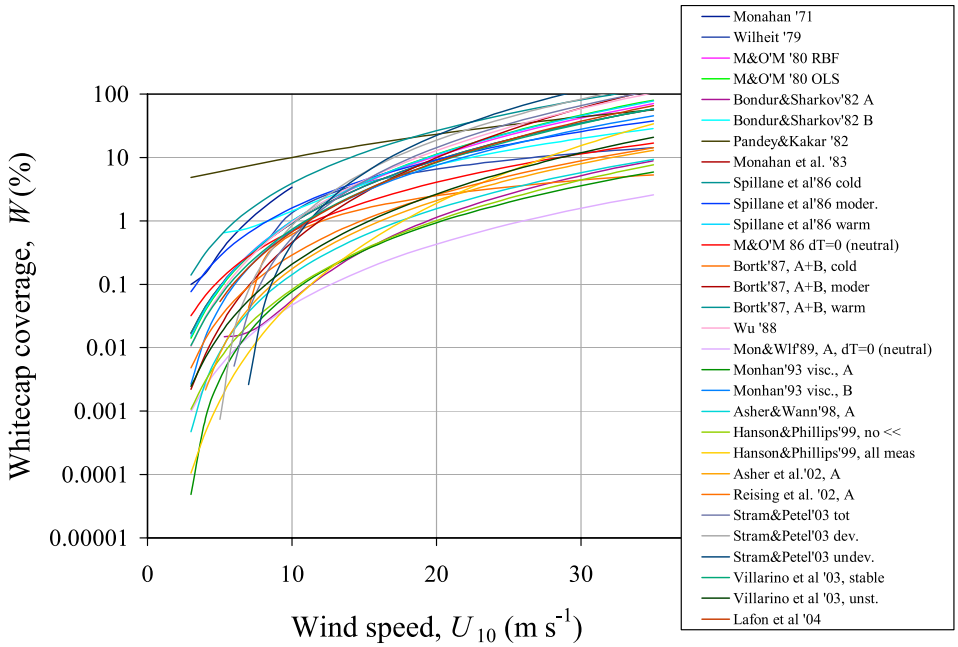

Figure 1.8. Copy of Figure 1 from Anguelova and Webster (2006). Original caption: "Various parameterizations for $W(U_{10})$ relation".

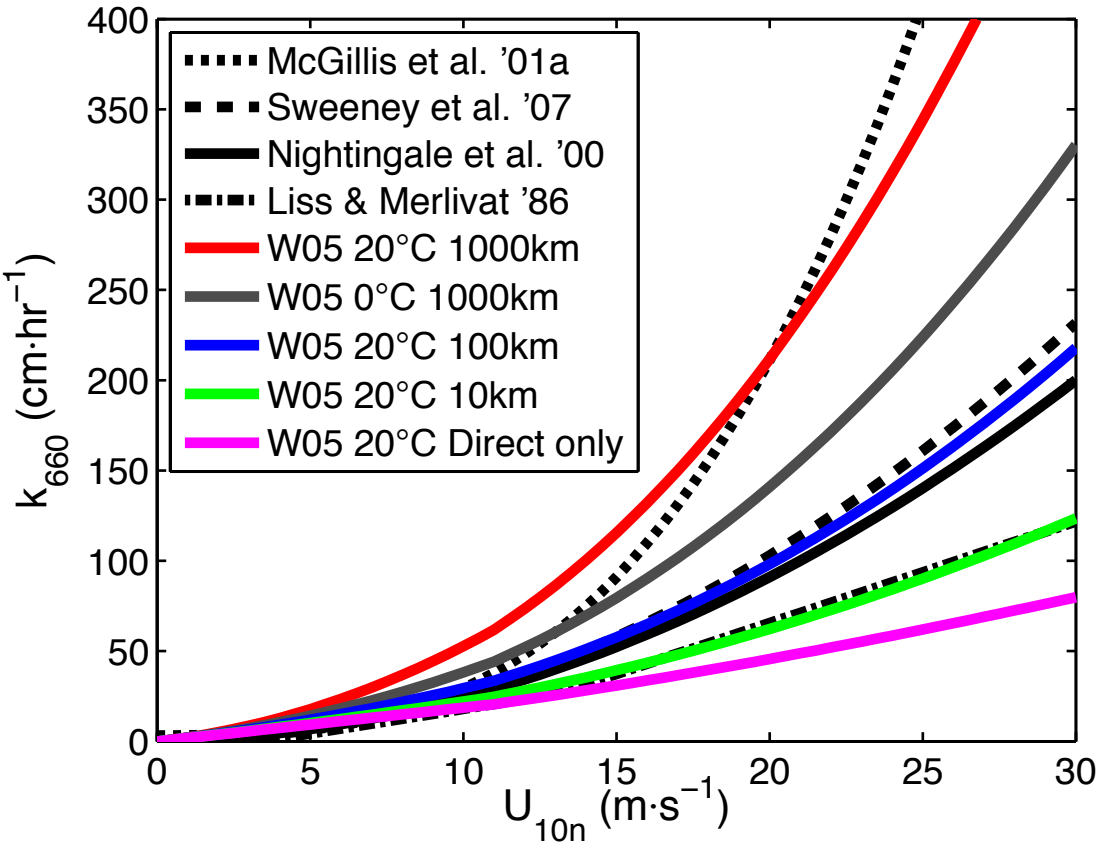

Figure 1.9. Variation of the Woolf (2005) gas transfer model with fetch (representing seastate and wave breaking effects). Also shown are wind speed based parameterisations for reference.

1.4.4 Gas transfer results summary

Several techniques have been successfully used to measure open ocean gas transfer velocity. Indirect DTEs have been carried out in a variety of oceanic locations since the early 1990s (Section 1.3.3). Many of the DTE results are in reasonable agreement with one another and suggest an approximately quadratic relationship of gas transfer to wind speed. Other DTE results however suggest that a stronger dependence is appropriate. Direct measurements of gas transfer via the eddy covariance technique have been challenging to perform in ocean conditions (Section 1.3.2). Several experiments have been successfully completed since the late 1990s. EC results suggest that the wind speed dependence of gas transfer could be in a range that includes quadratic and cubic dependences. Laboratory experiments allow influencing factors to be more easily controlled but are difficult to scale to the open ocean.

A summary of air-sea gas transfer results to date is shown in Figure 1.6. The results span a wide range of possible gas transfer to wind speed relationships, from

lower than quadratic to higher than cubic. The results from each type of experiment, such as DTE or EC, also span much of this range.

There have been a number of theories put forward to explain the large variation between experiments measuring air-sea gas transfer. The dependence of gas transfer on factors other than wind speed may explain some of the variation in wind speed based relationships. Mean square wave slope has been shown in some experiments to better account for the variation between flux measurements than wind speed (e.g.: Jähne et al., 1987b). Other experiments suggest that the fluxes are influenced by diurnal temperature variations (e.g.: McGillis et al., 2004), rain (e.g.: Turk et al., 2010) or surfactants (e.g.: Nightingale et al., 2001).

At higher wind speeds, bubble mediated exchange may significantly contribute to gas exchange. Bubble concentrations are dependent on seastate variations, which are not solely correlated with wind speed (e.g.: as a result of fetch; Woolf, 2005). Some experiments however, suggest that bubble mediated exchange can only account for a relatively small fraction of the observed gas transfer rate (e.g.: ~ 25 %, Asher et al., 2002). Laboratory measurements of gas transfer also suggest that invasive bubble mediated exchange will be greater than evasive by approximately 2% (Asher and Wanninkhof, 1998a; Asher et al., 1996). Two separate open ocean EC experiments, one observing invasive and one observing evasive fluxes, found invasive transfer rate larger than the evasive rate by approximately 25%, suggesting that bubble mediated exchange may explain only a small proportion of the difference between experimental results (McGillis et al., 2001a; McGillis et al., 2004).

All gas transfer measurement techniques are challenging to perform in oceanic conditions. Whilst several different research groups have successfully performed DTEs, the error resulting from experimental uncertainty (e.g.: mixed layer depth or bubble-mediated transfer) in each measurement is approximately 50% (Asher, 2009). EC measurements are subject to numerous sources of error as described in Section 1.3.2 and examined in detail in this thesis. These sources of error can sum to substantially more than the magnitude of the flux, and must be carefully addressed.

1.5. Summary and conclusions

Increased understanding of gas transfer across the air-sea interface through improved parameterisation will advance studies of climate, biogeochemical cycling and ocean acidification and improve forecasts of future climate change.

The rate of transfer, driven by the air-sea concentration difference of the gas in question, is represented by the gas transfer velocity (Eqn. (1.12)). The gas transfer velocity, k, represents the numerous kinetic factors modifying the air-sea interfacial layer and thus influencing the air-sea exchange of gases. Its exact functional form is uncertain (Eqn. (1.9)). In order to calculate gas flux on large spatial-temporal scales, k is parameterised in terms of some widely measured parameter . Wind speed is commonly used (Section 1.4.1) due to its influence on interfacial turbulence and availability of global data sets.

Existing gas transfer to wind speed relationships differ significantly (Figure 1.6; Table 1.1), particularly at high wind speeds (Figure 1.7). High wind speeds (> 15 $m.s^{-1}$) occur infrequently over the global ocean but due to the non-linear dependence of k on wind speed, they have a significant effect on the global flux (e.g.: Takahashi et al., 2002). There are very few measurements of k obtained at wind speeds above 15 $m.s^{-1}$, and the differences between parameterisations at these wind speeds are great (> 100%). Large uncertainties in transfer velocity measurements mean that measurements at high wind speeds where the transfer velocities are high, may be best suited for determining the form (quadratic or cubic) of the gas transfer wind speed dependence.

A quadratic dependence of k on U has been suggested (Wanninkhof, 1992), which has subsequently been observed by several different DTEs (Section 1.3.3; Nightingale et al, 2000a; Nightingale et al., 2000b; Ho et al., 2006). Direct measurements of gas transfer using the EC technique (Section 1.3.2) have been challenging to perform at sea. Some EC experiments have found a stronger, cubic dependence of k on U (McGillis et al., 2001a; McGillis et al., 2004). A cubic dependence on wind speed was also observed in a DTE experiment in the Southern Ocean (Wanninkhof et al., 2004). Either a cubic or a quadratic wind speed relationship satisfies the constraint imposed on gas transfer by the radiocarbon budget (Wanninkhof and McGillis, 1999). All of the methods used show a similar spread of results among one experiment/analysis and another.

Some portion of the uncertainty in k (Figure 1.6) results from experimental uncertainty (Asher, 2009; Yelland et al., 1998) and some is due to the influence of kinetic factors not represented in wind speed based parameterisations such as seastate (Section 1.4.2; Jähne et al., 1987b), bubble-mediated transfer (1.4.3; Woolf, 1997) and surfactants (Frew et al., 1997). The uncertainty is compounded by a paucity of direct measurements and a lack of measurements in high wind speeds. In addition, few

experiments have measured all the variables that influence gas exchange (e.g.: heat fluxes, meteorological conditions, seastate, whitecapping and surfactants). Several models that include the influence of bubble mediated transfer and seastate have been proposed (Asher and Wanninkhof, 1998a; Woolf, 2005), but require verification from in situ measurements.

1.6. Thesis aims

The aim of this thesis is to use direct flux measurements to increase the understanding of air-sea trace gas flux, and to improve the parameterisation of the air-sea gas transfer velocity. This thesis will focus on moderate to high wind speeds and in particular on wind speeds over 15 $m.s^{-1}$ where there is a paucity of existing measurements and where the differences between existing gas transfer parameterisations are largest (Figure 1.6). The specific goals of the work described in this thesis are thus:

- To obtain direct measurements of the open ocean CO_2 flux, especially at high wind speeds (> 15 $m.s^{-1}$).
- To analyse and quantify the various sources of error affecting air-sea EC gas flux measurement.
- To examine the influence of seastate and wave breaking on air-sea gas transfer.

The measurements presented in this thesis were obtained as part of the High Winds Air-Sea Exchanges (HiWASE) experiment. The aim of the HiWASE experiment was to improve the understanding and parameterisations of the turbulent air-sea fluxes in high wind speeds. The HiWASE experiment, and in particular the components of relevance to this thesis, is described in detail in Chapter 2. Due to the focus on flux measurement in high winds, factors that influence gas transfer at low wind speeds (buoyancy flux, surfactants and rain) were not directly investigated and will not be discussed in detail in this thesis.

The open path IRGAs widely used to measure fast response CO_2 concentration (and used during HiWASE) have been subject to a long-standing humidity cross-sensitivity error when deployed at sea. A novel correction for this error has been developed and is described in Chapter 3. The HiWASE gas transfer results, with the

humidity cross-sensitivity correction applied, are presented in Chapter 4, and a "classical" parameterisation of gas transfer in terms of wind speed is derived.

Chapter 5 examines several sources of uncertainty in air-sea EC flux measurement, including sensor accuracy, IRGA head deformation and statistical measurement uncertainty. The uncertainty due to platform motion is examined in Chapter 6, and Chapter 7 examines the effect of flow distortion on the CO_2 flux, as well as presenting preliminary results of the momentum, latent heat and sensible heat flux measurements performed during HiWASE.

The errors in flux measurement that result from platform motion and flow distortion effects are strongly dependent on relative wind direction. As such these two different effects are challenging to distinguish from one another. Upper and lower bounds on the size of platform motion error determined in Chapter 6 are used throughout Chapter 7 to allow the combined effect of platform motion and flow distortion errors to be examined. Chapter 8 summarises the thesis, presents the conclusions and gives a discussion of possible areas of future work.

2. The HiWASE experiment

This chapter focuses on the experimental details that are especially relevant to the turbulent flux results presented in Chapters 4, 6 and 7. Section 2.1 describes the ship from which the measurements were made. Section 2.2 provides a description of the instrumentation used to measure the fluxes and the various forcing variables analysed in this thesis, and the initial processing applied prior to flux calculation. Section 2.3 describes the location at which the measurements were made and the mean atmospheric and oceanic conditions during the course of the experiment.

Further details on the initial instrument installation for the HiWASE project are given in the associated mobilisation cruise report (Yelland and Pascal, 2010). Instrument and experimental details, including changes to the instrumentation during the three years of the project, are given in the HiWASE metadata report (Moat et al., 2010). An overview of the HiWASE project and some initial momentum and latent heat flux results are presented in Yelland et al. (2009). Additional information about HiWASE and details of some of the other components of UK-SOLAS is provided in Brooks et al. (2009).

2.1. Measurement platform

The measurements analysed in this thesis were obtained onboard the Norwegian Ocean Weather Ship (OWS) *Polarfront* (Figure 2.1) between September 2006 and December 2009. The *Polarfront* was a dedicated meteorological platform. It occupied Station Mike (66°N 2°E; Figure 2.2) in the North Atlantic year round from 1976 to the end of 2009. Station Mike was part of an international network of ocean weather stations, established in 1948. Prior to 1976, the station was occupied by the *Polarfront's* predecessors: *Polarfront I* and *Polarfront II*. In December 2009 the continuous year-round monitoring of Station Mike was discontinued and the *Polarfront's* occupation of the station ended. The *Polarfront* was owned and operated by Misje Rederi AS, under contract to the Norwegian Meteorological Institute (DNMI).

The *Polarfront* was particularly suited as a platform for making air-sea flux measurements. For the majority of its time on-station, the *Polarfront* drifted with its main engines off and oriented with the starboard beam-on to the mean wind. The *Polarfront* would drift until approximately 20 nautical miles away from 66°N, 2°E. It would then steam slowly back to the station at approximately 6 knots (Yelland and Pascal, 2010). For some wind directions, the ship would be oriented with the port beam facing the wind to improve performance of some ship-based communication systems. For higher wind speeds (above 15-20 $m.s^{-1}$, depending on sea sate) the ship turned bow-on to the wind. For the three years of HiWASE, the mean wind was on the starboard beam (± 30°) 31 % of the time, port beam (± 30°) 16 % of the time and on the bow (± 30°) 18 % of the time (Figure 2.3). For high wind speeds (> 15 $m.s^{-1}$), the mean wind was on the starboard beam (± 30°) 18 % of the time, port beam (± 30°) 11 % of the time and on the bow (± 30°) 56 % of the time (Figure 2.3).

Turbulent flux measurements are strongly affected by airflow distortion. CFD modeling of the airflow over the *Polarfront* (Moat and Yelland, 2009) found that the flow was least disrupted when the wind was on the bow. Hence, the flux instruments were installed on the foremast with maximum exposure to winds from the bow and starboard beam (Chapter 7).

The *Polarfront* visited port in Ålesund, Norway every four weeks to resupply and rotate crew. During the port visits the *Polarfront* was typically docked for a period of eight hours. On average, the *Polarfront* spends 25 out of every 28 days on-station, with the other three days spent either docked or in transit to and from port. A longer refit lasting approximately one week was performed once per year in Maloy, north of Bergen, usually in early September. Port visits and refit dates are shown in Table 2.5. Further details are available in the metadata report (Moat et al., 2010).

Figure 2.1. OWS *Polarfront* in port in Ålesund, Norway in January 2008.

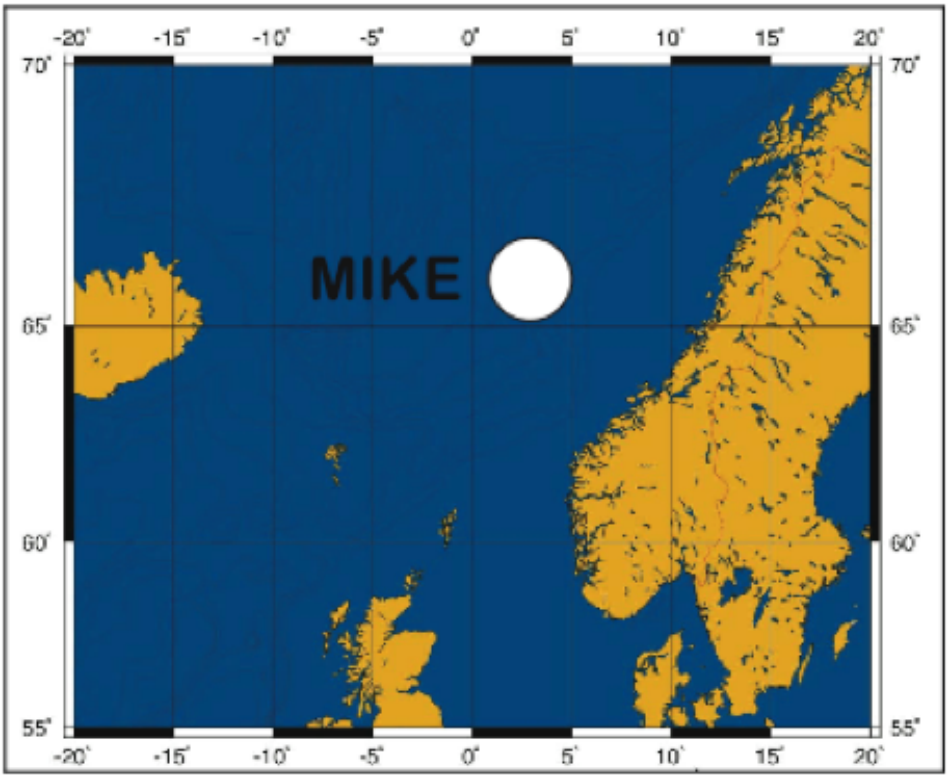

Figure 2.2. Map showing the location of Station Mike (66°N 2°E), an ocean weather monitoring station in the North Atlantic.

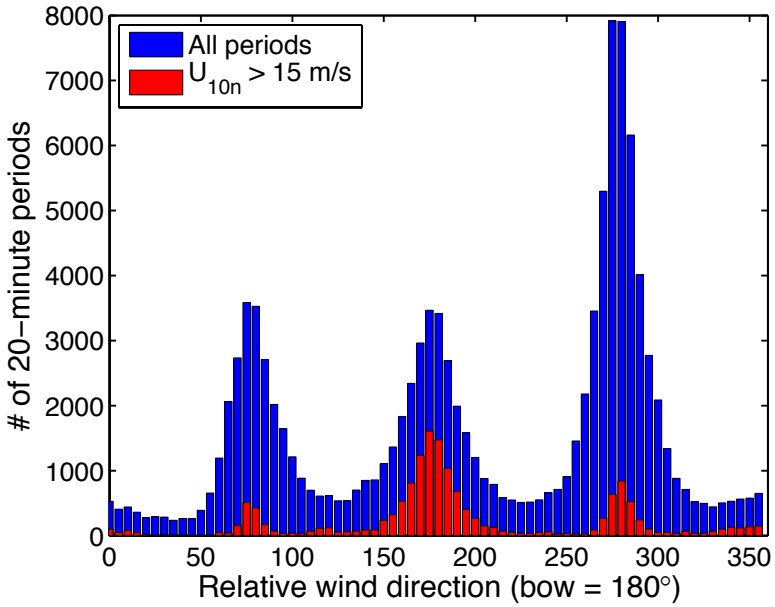

Figure 2.3. Relative wind directions measured onboard *Polarfront* at Station Mike during the HiWASE project. Values are 20-minute averages. Relative wind directions were measured using the Gill R3 sonic anemometer (Table 2.1).

2.2. Instrumentation and initial processing

2.2.1 Introduction

For the HiWASE project the *Polarfront* was equipped by NOCS personnel with an autonomous turbulent flux measurement system and an extensive set of high quality meteorological and oceanographic instrumentation. Following the installation, NOCS personnel remained on board for an evaluation cruise lasting one month (Yelland and Pascal, 2010). The *Polarfront* was a working weather ship and as such, also carried high quality meteorological instrumentation operated by the Norwegian meteorological office (DNMI). This section provides details of the instrumentation relevant to this thesis. Summary information of the principal flux instrumentation and the main sources of flux measurement error addressed in this thesis is given in Table 2.1. Summary information of the other instrumentation used during HiWASE is given in Table 2.2.

During HiWASE, the data processing required for the calculation of EC fluxes was performed post cruise. The EC calculation itself, and the experimental details relating to this calculation (e.g.: detrending, despiking, density dilution correction) are not described in this chapter but are detailed subsequently in Chapter 4. A detailed description of the processing steps preceding the EC calculation is provided in Appendix B, and summarized in Section 2.2.3. The wind measurements are corrected in

pre-processing to remove the effects of platform motion. The method used is closely based on that described by Edson et al. (1998) and is described in detail in Section 2.2.8. The results of applying the motion correction are analysed in Chapter 6.

ID measurements made during HiWASE were calculated in near real time. The near real-time processing is briefly described in Appendix B. A full description of the ID flux calculation can be found in Yelland et al. (1994), Yelland (1997), Yelland et al. (1998) and Taylor and Yelland (2000).

2.2.2 Flux instrumentation

An autonomous turbulent flux measurement system, "AutoFlux" (Yelland et al., 2009) and a range of related instrumentation all owned and operated by NOCS, were installed on the *Polarfront's* foremast (Figure 2.4) in September 2006 by NOCS personnel. Prior to installation on *Polarfront*, AutoFlux operated successfully for a period of 20 months onboard *RRS Discovery*. AutoFlux, developed at NOCS, automatically calculates momentum and latent heat fluxes via the ID technique. Fluxes of CO_2, sensible heat, latent heat and momentum are calculated via EC post cruise. The system is designed to work continuously with minimal maintenance.

The primary components of the AutoFlux system are described here and summarized in Table 2.1. A Solent R3A sonic anemometer (hereafter Sonic; Gill Instruments Ltd, U.K.) provides three-axis measurements of wind velocity. Additionally, the Sonic automatically infers an air temperature ("sonic temperature"; approximately equivalent to virtual temperature) via measurement of speed-of-sound between the three transducers (e.g.: Kaimal and Gaynor, 1991). A Systron Donner MotionPak (hereafter MotionPak; BEI technologies Inc, USA) measures platform motion via three orthogonal angular rate sensors and three orthogonal accelerometers. The motion measurements are used to remove the platform motion signal from the wind velocity measurements and rotate the wind vector into the required frame of reference.

Two LICOR-7500 Infrared Gas Analysers (hereafter IRGAs; LI-COR Inc, USA) each measure H_2O and CO_2 concentration in situ. The concentration is determined through measurement of the absorption of radiation at wavelengths centred on 4.26 μm (CO_2) and 2.59 μm (H_2O). A reference signal is measured at a wavelength centred on 3.95 μm. The absorption is measured over an optical path exposed to the environment ("open path"). An internal chopper wheel alternates a measurement window with a

blanking plate, enabling "null" measurements to be made alternately with the optical path measurements for internal calibration.

One of the IRGAs was usually operated with a shroud in place, sealing it from the environment in order to determine error caused by deformation of the sensor head and various other motion effects (Chapter 5.5; Yelland et al., 2009). The shroud was swapped between the two IRGAs at regular intervals, usually during port visits (Moat et al., 2010). The IRGAs were changed periodically to allow the instruments to be sent to the manufacturer for routine calibration and servicing. In total, 5 different IRGAs were used during HiWASE (Table 2.5). Replacement of the internal H_2O and CO_2 scrubbing chemicals was carried out at a frequency equal to, or greater than, the minimum frequency recommended by the manufacturer (Moat et al., 2010).

The four fast response instruments (Sonic, MotionPak and two IRGAs) were mounted close to one another on the foremast of the *Polarfront.* To minimize the effects of airflow distortion on the sensors (Section 2.1), the flux instruments were mounted on the front starboard corner of the foremast (Figure 2.4; Figure 2.5; Figure 2.6). The exact positioning of the flux instruments was changed on several occasions during the project (Table 2.5; Moat et al., 2010) to enable more accurate determination of instrument alignment (Prytherch et al., 2010c) or to minimise the obstruction to the *Polarfront* crew's sightlines from the bridge.

2.2.3 Flux instrumentation processing

Data from the flux instruments were logged automatically by an onboard UNIX workstation (SUN Fire V210 server). The onboard system has the capacity to store in excess of six months of data from all the logged instruments. Visits by NOCS personnel occurred typically every two months, during which data were backed up and transferred to land based systems. Maintenance tasks were performed during ship visits as required. The UNIX workstation internal clock was automatically checked against GPS time to ensure the correct time stamp was applied to the data. The workstation was connected to an Uninterruptible Power Supply (UPS) to allow a clean shut down in the event of power failure. Separate programs logged and monitored each of the main data streams. The monitoring programs automatically re-launched any program that crashed, helping to minimize protracted periods of data loss. Summary data, including meteorological data, calculated fluxes and diagnostic parameters were transmitted to NOCS on an hourly basis via Iridium satellite. A summary of output was displayed in real-time on

the project website (http://www.noc.soton.ac.uk/ooc/CRUISES/HiWASE/OBS/data_intro.php). The satellite link also allowed monitoring and limited control over the software. All instruments except for the MotionPak and whitecap cameras could be monitored by this method.

As described in Appendix B, measurements from the Sonic, IRGAs and MotionPak are merged together and synchronized using an asymmetric square wave synchronization signal input to the analogue channels of the Sonic and IRGAs. Ship's navigation data are then merged and synchronized with the fast response data by obtaining the maximum correlation between the MotionPak rotation rate measurement about the vertical axis, and the rate of change of the ship's heading from the ship's gyro.

The motion correction procedure, described below (Section 2.2.8), is applied to correct the wind velocity measurements. After motion correction, each 58.3-minute long file is split into three slightly overlapping 23.5-minute files. These are subsequently shortened to 20-minute files to remove any transient signal that may result from the motion correction filtering procedures. The wind speeds after motion correction are relative to the ship. Finally, the motion corrected wind speeds are rotated into alongwind, crosswind and vertical wind speeds in the true wind speed frame of reference.

Table 2.1. Summary of the fast response (20 Hz) flux instrumentation comprising the AutoFlux system onboard *Polarfront*.

Instrument	Model	Manufacturer	Location	Measures	Sources of measurement error
Sonic anemometer (Sonic)	Solent R3a	Gill Instruments Ltd, U.K.	Foremast	Wind speed vector Sonic temperature	Flow distortion (Chapter 6).
Infrared Gas Analyser (IRGA)	LICOR-7500	LI-COR Inc, USA	Foremast	CO_2 concentration H_2O concentration	Hygroscopic particles (Chapter 3). Head deformation (Section 5.5). Webb et al. (1980) density correction (Section 4.2.2). Low CO_2 signal size (Section 5.2).
Motion measurement (MotionPak)	Systron-Donner MotionPak	BEI technologies Inc, USA	Foremast	3-axis acceleration 3-axis rotation	Platform motion (Chapter 6).

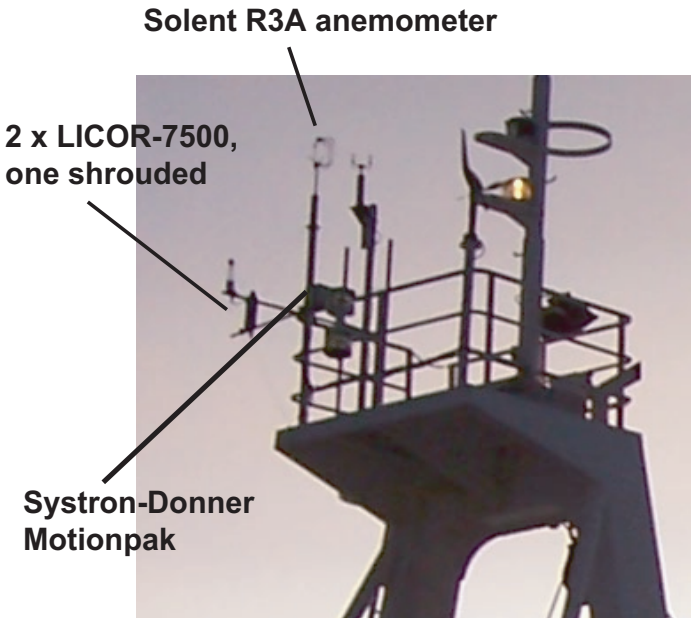

Figure 2.4. Components of the AutoFlux turbulent flux system installed on the *Polarfront's* foremast. The instrument configuration shown here (and in Figure 2.5) was in place from September 2006 to September 2007, when the anemometer was rotated 60° to starboard. In January 2008 the configuration was changed substantially (Table 2.5). The photograph was taken from the port-fore direction, looking towards the starboard-aft side of the ship.

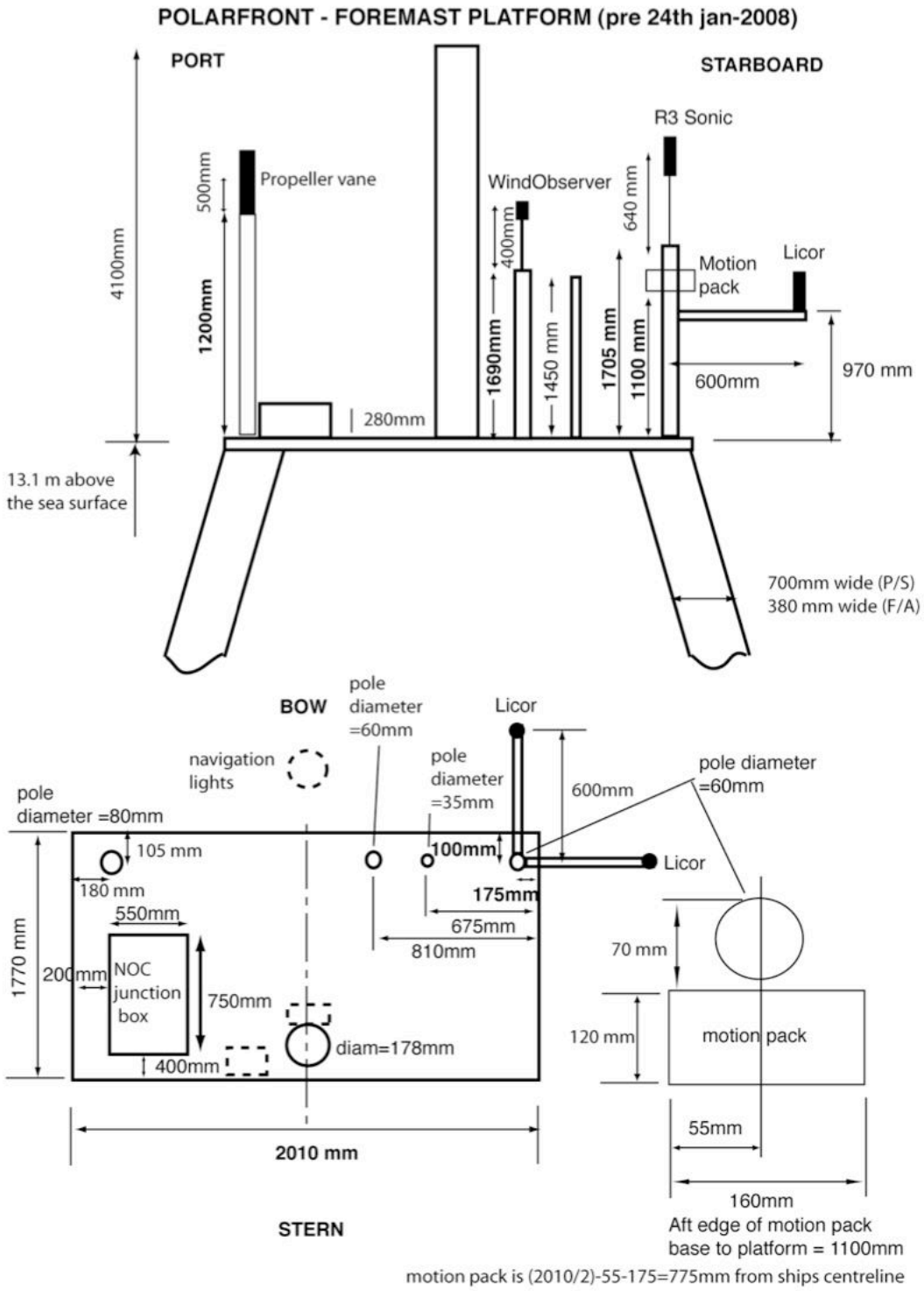

Figure 2.5. Layout of the foremast instrumentation from September 3rd 2006 to 24th January 2008 (from Yelland and Pascal, 2010). The top panel shows the view from the bridge looking forward and the lower shows the plan view. The drawing on the bottom right shows the dimensions of the MotionPak. Relative instrument locations were changed during the course of the HiWASE project (Moat et al., 2010). Height above sea level refers to the mean sea level, and may vary depending on ship loading.

Figure 2.6. Components of the AutoFlux turbulent flux system installed on the *Polarfront's* foremast. The instrument configuration shown here was in place from January 2008 to December 2009 (Table 2.5). The photograph was taken from the aft-starboard side of the ship, looking towards the fore of the ship. The right-hand IRGA is shrouded.

2.2.4 Mean meteorology instrumentation

The *Polarfront* was equipped with a wide range of meteorological instruments operated by DNMI. These sensors made wind direction, wind speed, air temperature, humidity, atmospheric pressure and sea surface temperature (SST) measurements. Additional NOCS meteorology instrumentation was installed at the same time as AutoFlux. Only the instrumentation relevant to this thesis will be described here, and a summary is given in Table 2.2. This instrumentation will be referred to as mean meteorological instrumentation to distinguish it from the fast response flux measurement instruments (Section 2.2.2). The additional NOCS instrumentation included a NOCS psychrometer and a Vaisala humidity and temperature sensor mounted on the bridge roof. In addition to these instruments humidity and air temperature measurements were made by a DNMI operated Vaisala installed within a Stephenson screen on the bridge roof. Depending on the status of the individual instruments, one of these instruments was designated the preferred instrument. The preferred instrument was either the NOCS psychrometer or the NOCS Vaisala for approximately 92% of the HiWASE measurements.

Both the DNMI and NOCS meteorology instrumentation was logged by the AutoFlux UNIX workstation. The NOCS instrumentation was sampled at 1 Hz. All DNMI meteorological system output 1-minute mean and maximum/minimum values which were logged by the UNIX system. In addition, ship navigation data was sampled and logged on the UNIX system at 1 Hz.

2.2.5 Seastate instrumentation

Two digital cameras were mounted on the bridge of *Polarfront*, one facing fore and one to port. Processing of the images allows whitecapping in the vicinity of the vessel to be quantified (e.g.: Callaghan and White, 2008). The cameras recorded an image with a time interval of between 10 minutes and 1 minute, at a resolution of either 2 or 3 megapixels. The camera resolution enables the whitecap fraction to be determined with a resolution of 0.0001% (pers. comm. Dr Ben I. Moat, NOCS). The images were stored internally on the cameras and NOCS personnel recovered the image data during port visits.

A "WAVEX" directional wave radar system was installed by NOCS personnel in September 2006. The system consists of an X-band dedicated marine radar and measures two-dimensional wave spectra. Wave height is inferred from the measured spectra using a commercially confidential algorithm. A Shipborne Wave Recorder (SBWR;) was installed on *Polarfront* in 1978 by DNMI. Last upgraded in 2006, the SBWR comprises two accelerometers and two pressure sensors installed in pairs on the port and starboard sides of the ship, approximately on the pitch axis of the ship and 1.5 m below the waterline. The signals from the instrument pairs are combined to remove the effects of ship roll and obtain an estimate of in situ wave height. The SBWR has been in routine use worldwide for many years. A 30-minute sample period of raw data from the SBWR is saved every 45 minutes. A comparison of the WAVEX wave heights and the SBWR wave heights showed that the WAVEX was overestimating wave height in the presence of swell (Yelland et al., 2009). By utilizing the wave spectra from the WAVEX, wave height from the SBWR and the whitecap images, a complete picture of the seastate in the locality of the *Polarfront* can be obtained. This will enable the influence of seastate on the turbulent fluxes to be examined.

The WAVEX system included a dedicated PC located aft of the bridge. Summary parameters were output to the AutoFlux workstation and included in the iridium message. NOCS personnel collected raw WAVEX data during ship visits. Raw data from the WAVEX is saved to its computer system twice per hour and spectra and related parameters are saved every five minutes. The SBWR was set to record for 30 minutes out of every 45. The pressure and acceleration measurements are automatically converted to wave height and period parameters and logged by the UNIX workstation.

2.2.6 Air-sea ΔpCO_2 instrumentation

The Polarfront was equipped with a continuous underway IR based air-sea CO_2 concentration system (Pierrot et al., 2009). Installed in 2005, the system is operated by Bjerknes Centre for Climate Research (BCCR) and operates under principles similar to those described by Wanninkhof and Thoning (1993) and Feely (1998). The system is autonomous and outputs surface ocean CO_2 mole fraction (parts per million: ppm) every five minutes and atmospheric mole fraction (ppm) once per hour. The mole fractions are converted to partial pressure (atm) and then fugacity (approximately equivalent to partial pressure) using measurements of air pressure and water vapor pressure made by the ΔpCO_2 system (Appendix A). Both air and water-side measurements are calibrated every 3 hours using standards from the National Ocean and Atmospheric Administration (NOAA).

Measurements obtained from the ΔpCO_2 system are processed, quality controlled and converted to fugacity measurements by BCCR. The accuracy of the measurements is dependent on the temperature difference between the inlet to the system and the equilibrator. When the temperature difference is less than 1°C, the uncertainty in the ΔpCO_2 is estimated to be ± 1 µatm. When the temperature difference is between 1°C and 2°C, the uncertainty is ± 2 µatm. When temperature differences are larger than 2°C the measurements are rejected. Quality control procedures used in HiWASE (Chapter 4) reject air-sea concentration differences smaller than 40 µatm. The estimated maximum uncertainty of the ΔpCO_2 measurement is therefore 5%.

2.2.7 Other instrumentation

Other instrumentation onboard *Polarfront* includes two PRT100 hull contact SST sensors and a Seabird micro thermosalinograph (TSG) supplied by NOCS (Table 2.2). The TSG makes conductivity measurements that are used to determine surface

salinity. The salinity measurements are used to calculate CO_2 solubility. The TSG salinity measurements are calibrated with salinity measurements obtained from a conductivity, temperature and depth (CTD) instrument's surface measurements, Nansen bottle samples and underway bottle samples (Moat, 2010). CTD measurements were made from the *Polarfront* five times per week using a Seabird microCAT CTD. Finally, the crew record hourly observations of present and past weather conditions at Station Mike, which provide a means of indentifying periods of precipitation (Chapter 4).

Table 2.2. Summary of non-fast response instrumentation onboard *Polarfront* used for the results presented in this thesis. Only the measurements used in the processing relevant to this thesis are listed. Further detail, including calibration information, is provided in Moat et al. (2010).

Instrument	Model	Manufacturer	Location	Measures
Mean Meteorology and ΔpCO_2 Sensors				
NOCS Psychrometer	-	NOCS, U.K.	Bridge top, 10.5 m above sea level.	Wet bulb air temperature Dry bulb air temperature
NOCS Vaisala	HMP45a	Vaisala, Finland.	Bridge top, 10.0 m above sea level.	Air temperature Relative humidity
Ship's humidity/temp	PRT100 HMP45D	- Vaisala, Finland.	Stevenson screen on bridge top.	Air temperature Relative humidity
Hull contact SST	PRT100	-	Approximately 1.4 m below waterline.	Sea surface temperature
Thermosalinograph	Seabird SBE45	Sea-bird Electronics Inc. USA	Forward hold, intake at depth of 3m.	Conductivity (salinity)
Infrared CO_2 concentration	-	BCCR, Norway	Forward hold (water intake as for TSG).	CO_2 mole fraction
Atmospheric pressure sensor	PTB220ACA243	Vaisala, Finland.	Meteorological lab (5 m above sea level).	Air pressure
Seastate Sensors				
SBWR	2 * Pressure 2 * Accelerometer	-	Below waterline (-1.4m), fore and aft	Wave height and period
Wave radar	WAVEX	Miros, Norway	Main mast	Directional wave spectra
Digital cameras	2 * CoolPix 8800	Nikon, UK.	Bridge port side	Whitecap fraction

2.2.8 *Motion correction processing*

2.2.8.a. *Introduction*

The air-sea momentum flux (wind stress) can be directly measured using EC. The wind stress, τ (kg.m^{-1}.s^{-2})), is defined as:

$$\tau = \rho\left(\left(\overline{u'w'}\right)^2 + \left(\overline{v'w'}\right)^2\right)^{1/2} \quad (2.1)$$

where ρ is the air density, u, v and w are the along wind, cross wind and vertical wind vector components respectively, primes indicate a fluctuation from the mean and an overbar a time average. Similarly, the air-sea flux of a scalar quantity, for example latent heat flux, F_r (W.m^{-2}), is:

$$F_r = \rho L_{vap}\overline{r'w'} \quad (2.2)$$

where L_{vap} (J.kg^{-1}) is the latent heat of evaporation of water and r is the mixing ratio of water in the air. Accurate determination of the vertical component of the wind vector is thus essential to measurement of all the turbulent fluxes. When measurements are made from a moving platform such as a research ship, the vertical platform motion signal in the vertical component of the wind vector can often be significantly larger than the real vertical wind fluctuations. Hence, this motion contamination must be removed prior to calculation of the fluxes.

Platform motion contaminates the measurements of wind velocity in three ways: 1) instantaneous tilt of the anemometer due to the pitch, roll and heading variations of the platform; 2) angular velocities at the anemometer due to the rotation of the platform about its local coordinate system axis; and 3) translational velocities of the platform with respect to the reference (Earth) frame of reference. On *Polarfront,* the wind velocity measurements are corrected for platform motion using a three-axis accelerometer and angular rate gyro instrument (MotionPak) fixed to the foremast (sometimes referred to as a "strapped down" system to distinguish it from a system with gimbaled sensors). The MotionPak measures acceleration through its three axis, and rotational rates also in three axis. Measurements are output at 100 Hz to the Sonic's analogue channel. The square wave synchronization signal is also input to the Sonic. The Sonic samples at 100 Hz, and then averages all signals to 20 Hz output.

2.2.8.b. Correction method

The following is a description of the procedure used during HiWASE to correct for the effects of platform motion. We make use of software written by Jeff Hare at NOAA, based on the method described in detail in Edson et al. (1998).

The true wind vector in the reference (Earth) frame of reference, $\mathbf{U}_{true}$, can be written as (e.g.: Edson et al., 1998; Fujitani, 1981)

$$\mathbf{U}_{true} = \mathbf{T}\mathbf{U}_{obs} + \boldsymbol{\Omega} \times \mathbf{T}(\mathbf{M} - \mathbf{S}) + \mathbf{V}_{mot} \tag{2.3}$$

where $\mathbf{U}_{obs}$ is the measured wind velocity in the platform frame of reference, **T** is a coordinate transformation matrix that rotates the platform frame coordinates into the reference coordinates, **Ω** is the angular velocity vector of the platform coordinate system, **M** is the position vector of the wind sensor with respect to the platform centre of gravity, **S** is the vector distance from the MotionPak to the platform centre of gravity and $\mathbf{V}_{mot}$ is the translation velocity vector. The position vectors **M** and **S** are difficult to determine, but **M-S** is simply the vector distance between the MotionPak and the anemometer and is easily measured.

In the description that follows, the subscript *obs* will refer to variables in the platform's frame of reference (the measurement frame) and the subscript *true* refers to variables in the Earth's frame of reference (the reference frame). The coordinate system used in Edson et al. (1998) and in the HiWASE correction is the same: the angular coordinates and their respective symbols are roll, ϕ, pitch, θ, and yaw, ψ. The sign convention is right-handed (x,y,z) with x positive forward (to bow), y positive to port, z positive upwards, ψ positive for the ship's bow yawed clockwise from north, ϕ positive for the port side rolled up, and θ positive for the bow pitched down. Note that to conform to the normal convention for heading (and hence make use of the shipboard heading measurements without further correction) we have used a left-handed definition for ψ and therefore introduce a negative sign into the following equations.

The coordinate transformation matrix is thus given by (e.g.: Edson et al., 1998):

$$\mathbf{T}(\phi,\theta,\psi) = \begin{pmatrix} \cos(\psi)\cos(\theta) & \sin(\psi)\cos(\phi) + \cos(\psi)\sin(\theta)\sin(\phi) & -\sin(\psi)\sin(\phi) + \cos(\psi)\sin(\theta)\cos(\phi) \\ -\sin(\psi)\cos(\theta) & \cos(\psi)\cos(\phi) - \sin(\psi)\sin(\theta)\sin(\phi) & -\sin(\theta)\cos(\phi)\sin(\psi) - \sin(\phi)\cos(\psi) \\ -\sin(\theta) & \cos(\theta)\sin(\phi) & \cos(\theta)\cos(\phi) \end{pmatrix} \tag{2.4}$$

This is a 321 rotation (i.e.: the coordinates are first rotated about the z axis (ψ), then about the y axis (θ), then the x axis (ϕ)). For the relatively small angles of rotation experienced by large vessels in the ocean (±10º) the error due to the order of rotation is negligible.

The MotionPak measures 3-axis angular rates of rotation in the platform's frame of reference. The observed angular rate vector, $\mathbf{\Omega}_{obs}$ is thus

$$\mathbf{\Omega}_{obs} = \begin{pmatrix} \dot{\phi}_{obs} \\ \dot{\theta}_{obs} \\ -\dot{\psi}_{obs} \end{pmatrix} \tag{2.5}$$

where the overdot indicates a time derivative. We can therefore rewrite Eqn. (2.3) as

$$\mathbf{U}_{true} = \mathbf{T}(\mathbf{U}_{obs} + \mathbf{\Omega}_{obs} \times \mathbf{R}) + \mathbf{V}_{mot} \tag{2.6}$$

where **R** is the position vector of the anemometer with respect to the MotionPak.

The main challenge to correcting the wind vector in this method is to approximate the angles used in Eqn. (2.4) from the MotionPak measurements of angular rate and acceleration. Several approaches are possible. The method used in HiWASE is the "complimentary filtering method" described in Edson et al. (1998).

The method is applied as follows. The MotionPak accelerometers measure both acceleration due to gravity (which for each axis is dependent on the degree of pitch and roll) and the acceleration due to platform motion:

$$\begin{pmatrix} \ddot{x}_{obs} \\ \ddot{y}_{obs} \\ \ddot{z}_{obs} \end{pmatrix} = \begin{pmatrix} \ddot{x} \\ \ddot{y} \\ \ddot{z} \end{pmatrix} + \begin{pmatrix} -g\sin(\theta) \\ g\sin(\phi)\cos(\theta) \\ g\cos(\phi)\cos(\theta) \end{pmatrix} \tag{2.7}$$

where a double overdot indicates a second derivative with respect to time and g is the gravitational acceleration. The second term on the right hand side of Eqn. (2.7) represents the tilt-induced accelerations. The tilt-induced acceleration will vary much more slowly than the instantaneous motion induced acceleration. The "slow" tilt signal can thus be separated from the accelerometer signal using an appropriate filter. The

"slow" yaw was obtained in a similar way to the pitch and roll: the same filter was applied to the gyroscopic compass signal to acquire a "slow" yaw signal.

The angles can be obtained from time integration of the angular rate gyros. However, the angular rate gyros are subject to small biases, which, when integrated, can lead to significant errors. Filtering the integrated angular rates to separate the high frequency gyro variation from the low frequency variation prevents this.

The platform angles can be approximated using the slowly varying component of the tilts derived from the accelerometer, added to the quickly varying component of the integrated angular rates. Use of the same filter to determine the high and low frequency components ensures that this process functions as an all-pass filter and does not introduce any time delays. The filtering process removes the unwanted drift from the angular rate gyros and maintains the low frequency tilt reference.

2.2.8.c. Complimentary filter design

A Butterworth filter was chosen for the complimentary filter for its flat response in the pass band. The filter, provided by Jeff Hare from the National Oceanic and Atmospheric Administration (NOAA), was designed as a high pass filter (with the filtered component subtracted to obtain a low pass signal) with a pass band of 0.0025 Hz, and a stop band of 0.0015 Hz (losing no more than 10 dB in the pass band and attenuating at least 25 dB in the stop band).

These parameters resulted in a fourth order Butterworth filter with a Butterworth natural frequency (3 dB pass frequency) of 0.0031 Hz. The resulting filter coefficients, used in the difference equation:

$$\begin{aligned} y(n) = b(1)*x(n) + b(2)*x(n-1) + \ldots + b(nb+1)*x(n-nb) \\ - a(2)*y(n-1) - \ldots - a(na+1)*y(n-na) \end{aligned} \tag{2.8}$$

are shown in Table 2.3. The filter is run in both directions to ensure zero phase distortion. Attempts were made to improve the motion correction by tuning the filter coefficients (as well as the filter used for the translational velocities) using for example, the filter suggested by Miller et al. (2008). However, no significant improvement was obtained.

Table 2.3. Filter coefficients for the complimentary filtering used in the filter difference equation, Eqn. (2.8).

	b	**a**
1	0.9874	1.0000
2	-3.9498	-3.9747
3	5.9246	5.9245
4	-3.9498	-3.9248
5	0.9874	0.9750

2.2.8.d. Translational velocities

Translational velocities are calculated by removing the tilt signal from the accelerometer signal (Eqn. (2.7)) and integrating the remaining platform motion acceleration signal. In practice this is done by first rotating the accelerometer signal using the transform matrix (Eqn. (2.4)), subtracting the gravity vector, then integrating the resulting signal with respect to time to determine the velocity. Integration of the accelerometer signal is problematic due to low frequency signals, which result in drift when integrated. To remove this error, the velocities are high pass filtered following integration.

The high pass filter, again provided by Jeff Hare of NOAA, is a Butterworth filter with a pass band of 0.0004166 Hz, and a stop band of 0.0008333 Hz (losing no more than 1 dB in the pass band and attenuating at least 14 dB in the stop band). These parameters resulted in a fourth order filter with a Butterworth natural frequency (3 dB pass frequency) of 0.00055979 Hz and filter coefficients for use in the difference equation (Eqn. (2.8)) as shown in Table 2.4.

Table 2.4.Filter coefficients for the translational velocities used in the filter difference equation, Eqn. (2.8).

	b	**a**
1	0.9977	1.0000
2	-3.9908	-3.9954
3	5.9862	5.9862
4	-3.9908	-3.9862
5	0.9977	0.99542

2.2.9 *Flux instrument changes*

During the three years of the HiWASE project, instruments were periodically exchanged to allow for routine servicing and calibration, or for replacement when faulty. A summary of the changes to the AutoFlux fast response sensors is provided in Table 2.5. A complete description of the sensor changes is in the HiWASE metadata report (Moat et al., 2010). In addition to straightforward swaps of nominally identical instruments, the relative positions of the flux sensors were also changed on two occasions. The initial configuration of the flux instruments is shown in Figure 2.4 and Figure 2.5. Initially, the Sonic was aligned facing to fore. In the early September 2007 refit, the Sonic was rotated approximately 60° to starboard from fore. In January 2008 a new Sonic and MotionPak that were mounted together on a metal plate were installed (Figure 2.6). The new mounting changed the heights of both instruments. Attaching both instruments to a metal plate allowed the alignments between the two instruments to be determined more accurately (Prytherch et al., 2010c) and thus improved the platform motion correction. The Sonic and MotionPak remained in this alignment for the remainder of the project.

2.2.10 *Instrument failures and dropouts*

Except for the initial mobilization cruise (Yelland and Pascal, 2010), the *Polarfront* operated without dedicated scientific personnel onboard for the duration of the HiWASE project. Instrument failures and other problems were thus unlikely to be corrected before the ship returned to port. Monitoring of the flux systems via the Iridium satellite link allowed for any problems with the AutoFlux system to be identified and corrected promptly. There was redundancy in all the data streams required for flux calculation, except for the wind velocity measurements obtained from the sonic anemometer, and platform motion measurements obtained from the MotionPak. These are both reliable instruments, but failures of these instruments did lead to periods where flux measurement was not possible. Most such problems led to a period of data loss of less than a cruise period (28 days) in length. Nevertheless, and perhaps unsurprisingly given the high number of instruments required for flux measurement and the environment in which the instrumentation was operating, there were several longer periods of data loss. These are described here and highlighted in Table 2.5.

On August 16th, 2007 (DOY 228), a junction box on the *Polarfront's* foremast, containing some of the electronic components of AutoFlux, was flooded. This resulted in a loss of all flux data until the junction box was repaired during the next port visit on September 7th 2007 (DOY 250). On April 17th, 2008 (DOY 108), a failure in the Sonic Interface Unit (SIU) led to a loss of the MotionPak measurements and a resulting loss of all the EC flux measurements. The MotionPak output was not monitored using the Iridium data link, and this problem was not identified until analysis of data was carried out on land. The SIU was replaced during the refit in September 2008, and the fault led to a loss of approximately 5 months of flux measurements.

On April 24th, 2009 (DOY 114), the transducer in the Sonic failed, leading to a loss of wind velocity measurements and a resulting loss of all the flux measurements. The Sonic was replaced on May 19th, 2009 (DOY 139). Following the replacement of the Sonic it was noted that the temperature measurement made by the instrument (calculated from speed of sound/time of flight) was high. Following discussion with the instrument manufacturers, it was not thought that this problem would affect the wind velocity measurements. However, the wind velocity measurements became very noisy, with frequent occurrence of unrealistic extreme values (spikes) from the beginning of October 2009 through to demobilization at the end of November 2009. The wind velocity spikes could be removed in post processing. However, when the EC flux measurements obtained throughout 2009 were analysed post cruise, it was discovered that many of the flux measurements were much noisier than previous periods. Because of these data quality issues, the 2009 periods will be examined in future work but will not form part of the analysis presented in this thesis.

There were several periods in 2008 and 2009 during which various problems prevented the measurement of the air-sea CO_2 concentration by the BCCR system. During these periods it is not possible to determine the gas transfer velocity. For 20 days in 2008 between June 19th (DOY 171) and July 9th (DOY 191), and 34 days in 2009 between May 13th (DOY 133) and June 16th (DOY 167), the AutoFlux UNIX workstation failed, resulting in the loss of flux measurements for these periods. The period in 2008 coincided with the period when no MotionPak measurements where made due to the failure of the SIU.

Over the 39 months of the HiWASE deployment period, there are approximately 22 months of usable flux data. 11 months are lost due to the omission of 2009 data. 5 months were lost due to the failure of the SIU and 1 month was lost due to the junction

box flooding. Of the 22 months with usable flux data, there are approximately 10 months that have a large enough ΔfCO_2 ($\Delta fCO_2 > 40$ ppm) for the calculation of EC CO_2 fluxes.

Table 2.5. Summary of key events affecting the AutoFlux fast response instruments during the HiWASE project, and the dates of *Polarfront's* port calls. Numbers preceded by "sn" are serial numbers indicating when a particular instrument (Sonic – S, MotionPak – MP) was installed. Other numbers indicate the day of year (DOY) on which an event occurred. Shading of the IRGA cruise periods indicates when the sensor was shrouded. For other columns, shading indicates the period of the particular event. "Chem' change" indicates a routine replacement of the IRGA internal scrubber chemicals. A ✓ indicates that ΔfCO_2 data is available for the period in question. Other events are as described in the text. A complete description of the HiWASE experiment is given in Moat et al., (2010).

Port call DOY	Sonic & MotionPak	Fore IRGA	S'board IRGA	ΔfCO_2	Other
2006	MOBILISED				
250	S sn391 MP sn791	sn1114	sn1113	✓	
277				✓	
305				✓	
333				✓	
361				✓	
2007				✓	
24				✓	
52				✓	
80				✓	
108				✓	
136				✓	
164				✓	
192				✓	
220				✓	
				✓	228 - 250 JB flooded, no fluxes
246-250	Sonic rotated 60° s'board	sn1264	Chem' change	✓	
276				✓	
304				✓	
332	Noisy sonic temp'			✓	
361				✓	
2008				✓	
24	S sn227 MP sn682. Both raised			✓	
		sn1264 lost		✓	
52		sn1114 installed		✓	
79	Sonic temp' fixed			✓	
107	S and MP lowered			✓	
	108 – 249 SIU failed, no motion data			✓	
135				✓	
		138-151 no data	138-151 no data	✓	
163		Chem' change		✓	

				✓	171 - 191 UNIX box dead
191				✓	
219				✓	
245-249			sn0825 installed	✓	
247				✓	
248				✓	
249				249 - 277 no data	
274-277					
		293/4 shroud removed		✓	
				✓	
303				✓	
333			300 - 333 no data	✓	
364				✓	
2009				✓	
27				✓	
55				✓	
83		sn0614	Chem' change	83 - 111 no data	
111			sn1113		
	114 - transducer failed			✓	
				✓	133 - 167 UNIX box failed
139	S sn391. MP sn682. Sonic temp' high			✓	
167				167 - 195 no data	
195					
223				✓	
			244-249 shrouded	✓	
250-259		sn1114	Chem' change	✓	
				260-269 suspect	
272				✓	
279				✓	
	282 - 334 Sonic wind noisy			287 - 306 broken pump	
307				✓	
		308/9 shroud swapped		✓	
334	DEMOB				

2.3. Location conditions

The North Atlantic in the region of Station Mike experiences high air-sea CO_2 concentration differences and frequent storms, making it an ideal location for measuring CO_2 fluxes in high wind conditions. Mean meteorological and ocean conditions at Station Mike during HiWASE are shown in Figure 2.7. Sea surface temperature (SST), measured with a hull contact PRT100 sensor (Section 2.2.7), had a mean value of 8.9°C (± 2.1°C) during the HiWASE experiment, and varied between a minimum of 5.2°C and a maximum of 15.2°C. The uncertainty ranges given in brackets are plus or minus one standard deviation. Sea surface salinity (SSS) was measured with a thermosalinograph (Section 2.2.7) and calibrated using regular Conductivity Temperature Depth (CTD) profiles and underway bottle samples (Section 2.2.7). The SSS had a mean value of 35.1 psu (± 0.2 psu) during the HiWASE experiment, and varied between 32.7 psu and 35.4 psu. The largest variation in SSS occurred during the summer months (Figure 2.7). Measurements during this period had a higher calibration uncertainty and must be treated with caution (Moat, 2010). Relative humidity (RH) was measured with several different instruments (; Section 2.2.4). RH had a mean value of 81% (± 11%) during the HiWASE experiment and varied between approximately 39% and 106%. The infrequent measurements of RH above 100% were likely due to instrument error.

The true wind speed was calculated from relative wind speed measured with the Sonic (Section 2.2.2) and adjusted to neutral atmospheric stability and 10 m measurement height using ID momentum flux and latent heat flux measurements and bulk sensible heat flux estimates (following Yelland and Taylor, 1996; Appendix B). Fluxes were calculated in 20-minute periods. Hence, the wind speeds and other meteorological and oceanic variables are given here as 20-minute averages. Wind speeds were highest during winter months (Figure 2.7). The average 20-minute wind speed during the HiWASE project of 10.7 $m.s^{-1}$ ± 4.3 $m.s^{-1}$ (Figure 2.8) was significantly higher than the global average of approximately 7 $m.s^{-1}$. The maximum 20-minute wind speed measured at Station Mike during HiWASE was 24.8 $m.s^{-1}$ (Figure 2.8). If periods are restricted to those for which the air-sea CO_2 concentration was large (> 40 μatm), then the maximum 20-minute wind speed measured was 22.7 $m.s^{-1}$ and the mean was 9.3 $m.s^{-1}$ (± 3.9 $m.s^{-1}$; Figure 2.8). This reduction in mean wind speed is due

to the occurrence of strong air-sea CO_2 difference during the summer months when storms are less frequent.

Air-sea CO_2 concentrations at Station Mike (Figure 2.9) were measured using an underway system onboard *Polarfront* operated by colleagues at the Bjerknes Centre for Climate Research (BCCR; Section 2.2.6). The system measured mole fraction using infrared absorption. Mole fractions are converted to fugacities (Appendix A). The atmospheric concentration of CO_2 had a mean value of 375.1 ± 7.6 µatm. The variability of the atmospheric CO_2 concentration during the three years of HiWASE masked any long-term trend. 30 years of atmospheric gas sampling (using flasks) has been performed at Station Mike (Figure 2.10). The air samples clearly show a year on year increase in atmospheric CO_2 concentration as found at other monitoring sites and as expected due to anthropogenic emissions.

The water-side CO_2 concentration, measured in the underway equilibrator, shows a strong seasonal variation, presumably due to variations in temperature, salinity and biological processes (Figure 2.9). The strongest air-sea CO_2 concentration difference occurs in the summer months with air-sea $\Delta fCO_2 > 40 \mu atm$ from May through to October. The air-sea difference at Station Mike during HiWASE varied from approximately 0 to 100 µatm (Figure 2.11). The location remains a sink for atmospheric CO_2 year round. Measurements made in the autumn (September and October) experience the best conditions, i.e. high winds and large air-sea CO_2 concentration difference.

A time series of CO_2 fluxes obtained in 2006 from the BCCR ΔpCO_2 system and two commonly used published wind speed dependent parameterisations of the gas transfer velocity is shown in the upper panel of Figure 2.12. The time series of the difference between the fluxes calculated with the two parameterisations is shown in the lower panel. The mean flux resulting from the cubic parameterisation of *k* reported by McGillis et al. (2001a) is -5.0 mols.m^{-2}.yr^{-1} whilst the mean flux from the quadratic *k* parameterisation of Sweeney et al. (2007) is -3.6 mols.m^{-2}.yr^{-1}. The mean flux difference of 1.4 mols.m^{-2}.yr^{-1} is a significant fraction of the estimated flux, demonstrating the importance in improving the parameterisation of *k*.

Station Mike experiences both high winds and large waves. Significant wave height measured onboard *Polarfront* over the 30-year period from 1980 to 2010 are shown in Figure 2.13. The annual mean significant wave height was typically greater than 2 m, and the annual maximum was typically greater than 10 m.

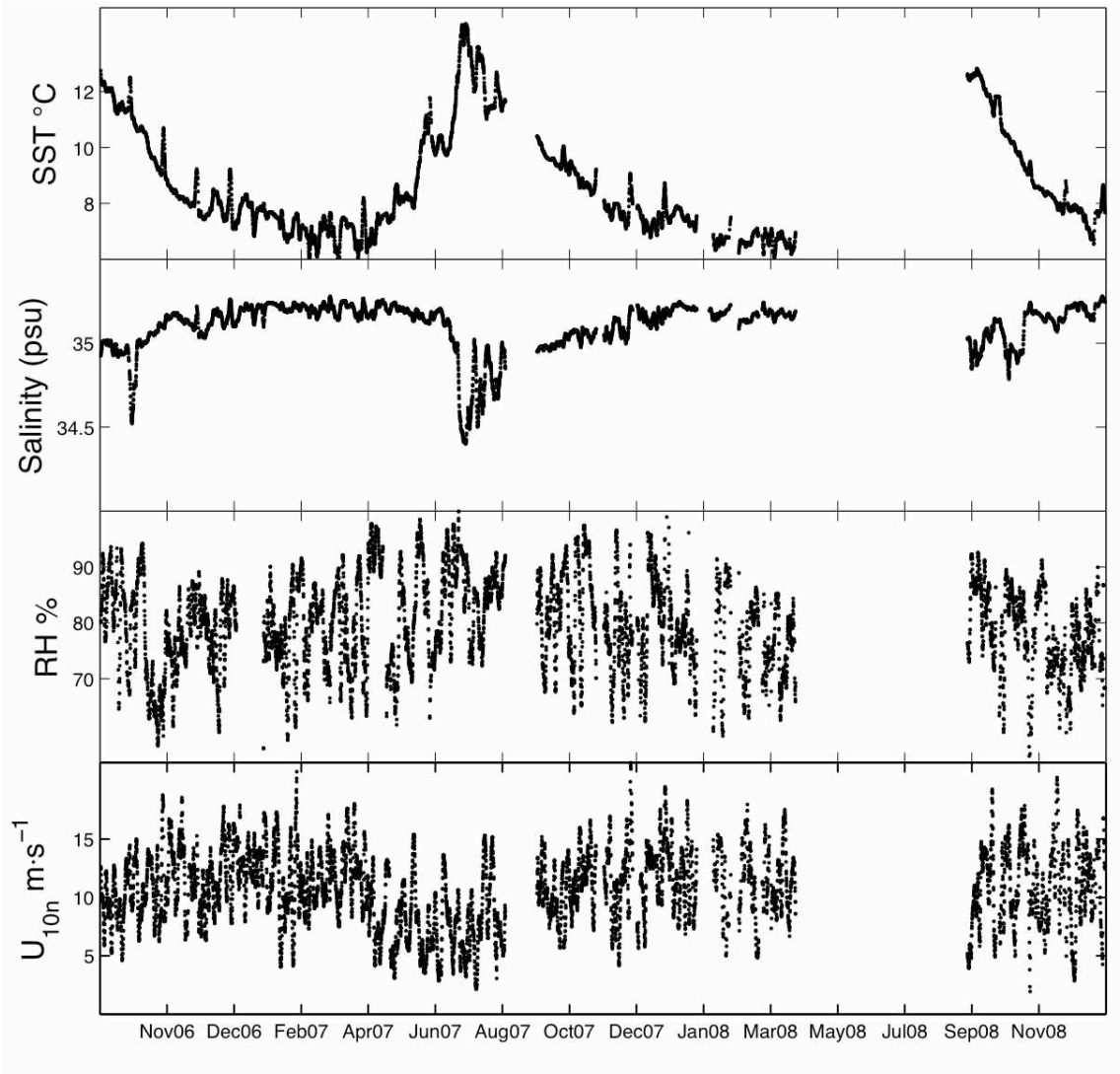

Figure 2.7. Mean conditions at Station Mike (66ºN, 2ºE), measured onboard *Polarfront* during the HiWASE experiment. Top panel: sea surface temperature from hull contact sensor. Second panel: salinity from thermosalinograph. Third panel: relative humidity measured by one of three instruments: NOCS psychrometer, Vaisala, ship's sensor. Bottom panel: true wind speed measured by sonic anemometer on the ship's foremast, adjusted for ship speed over ground, neutral atmospheric stability and 10 m measurement height. Periods for which no flux measurements were made have been omitted.

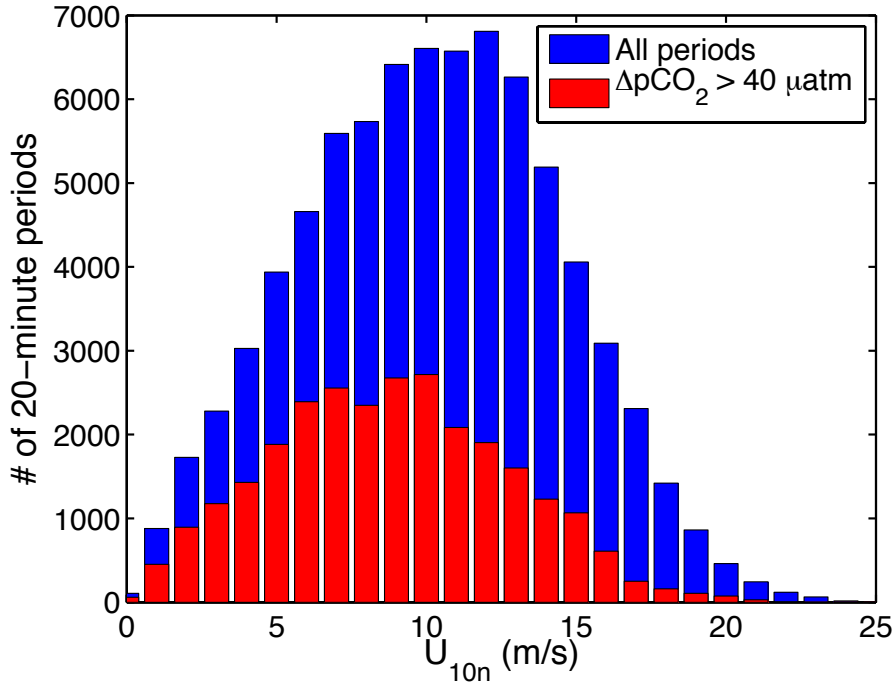

Figure 2.8. 20-minute average true wind speeds measured onboard *Polarfront* at Station Mike during the HiWASE project.

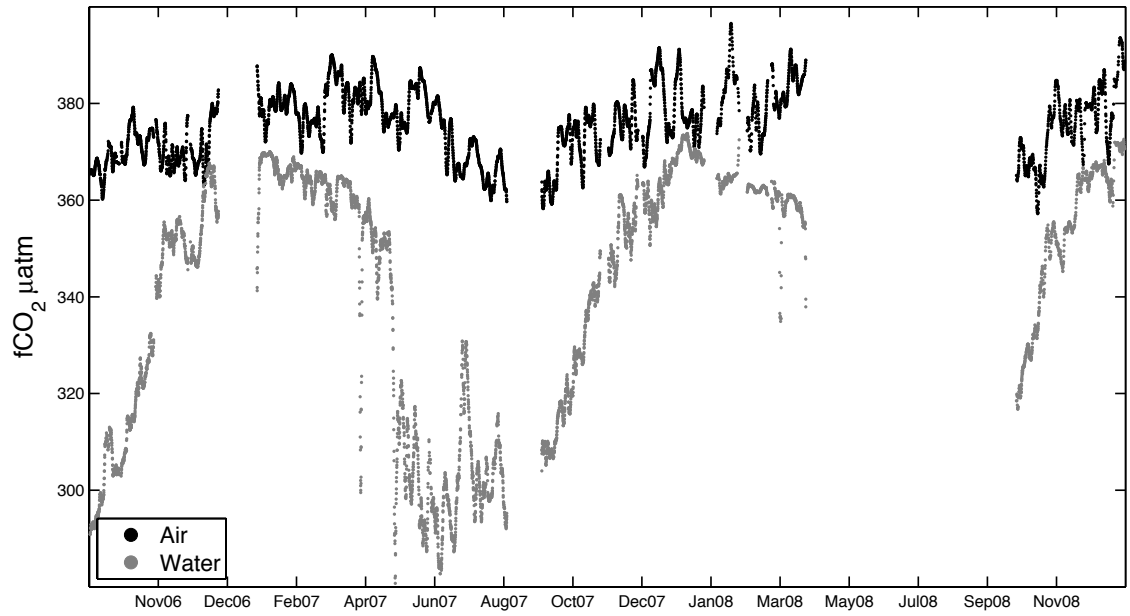

Figure 2.9. Sea and air CO_2 fugacity measured onboard *Polarfront* during HiWASE using the infrared system operated by BCCR (Section 2.2.6). Periods for which no flux measurements were made have been omitted.

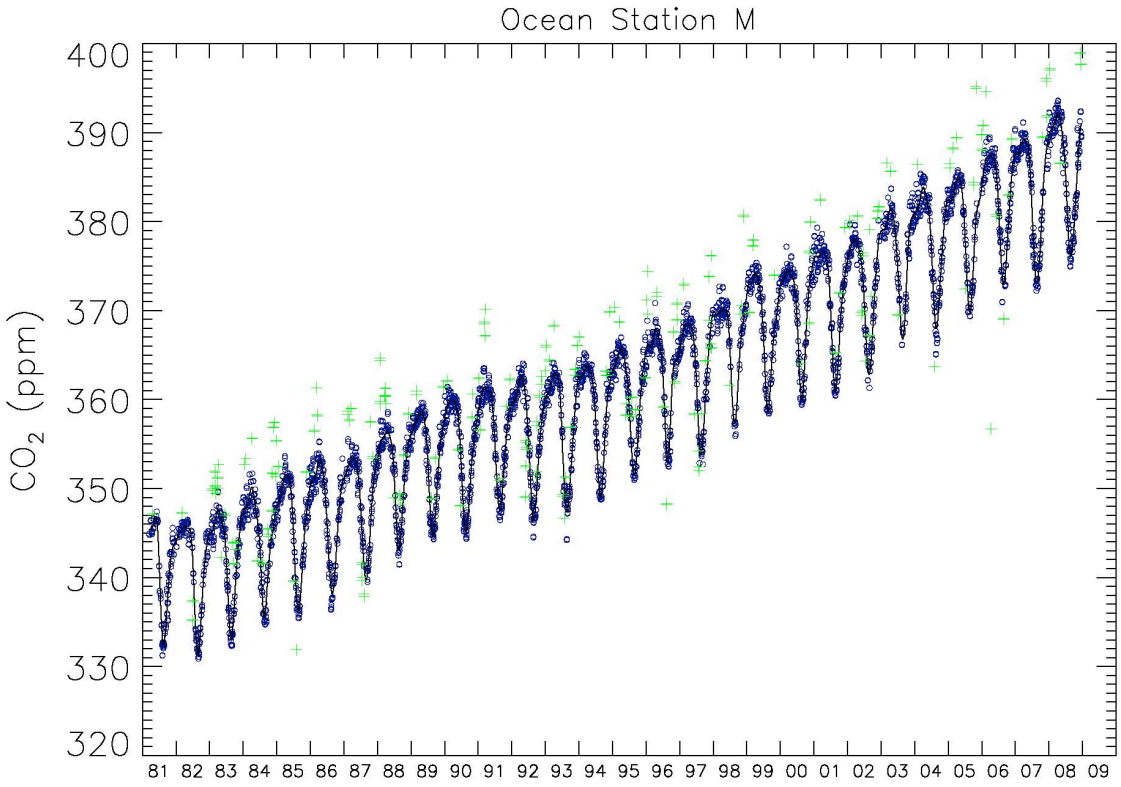

Figure 2.10. Atmospheric CO_2 measurements at Station Mike for the period 1981-2010. Sample flasks were obtained at weekly intervals and sent to the National Oceanographic and Atmospheric Administration (NOAA), USA, for analysis. Green points indicate data flagged as suspicious (for example if the wind was coming off the land).

Graph courtesy of Thomas J. Conway, Global Monitoring Division, NOAA.

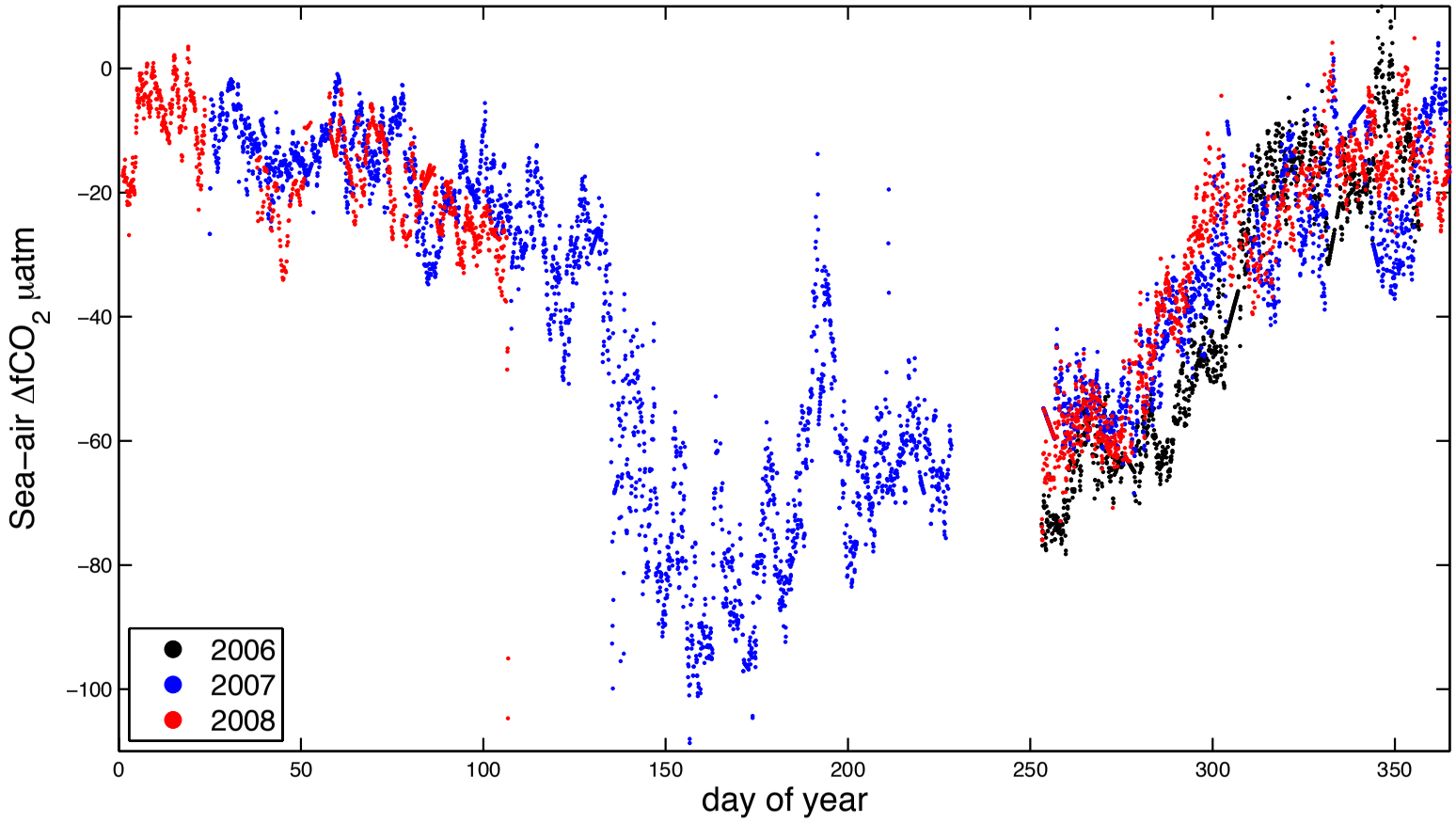

Figure 2.11. Sea – air CO_2 fugacity difference measured onboard *Polarfront* during HiWASE using the infrared system operated by BCCR (Section 2.2.6). Periods for which no flux measurements were made have been omitted.

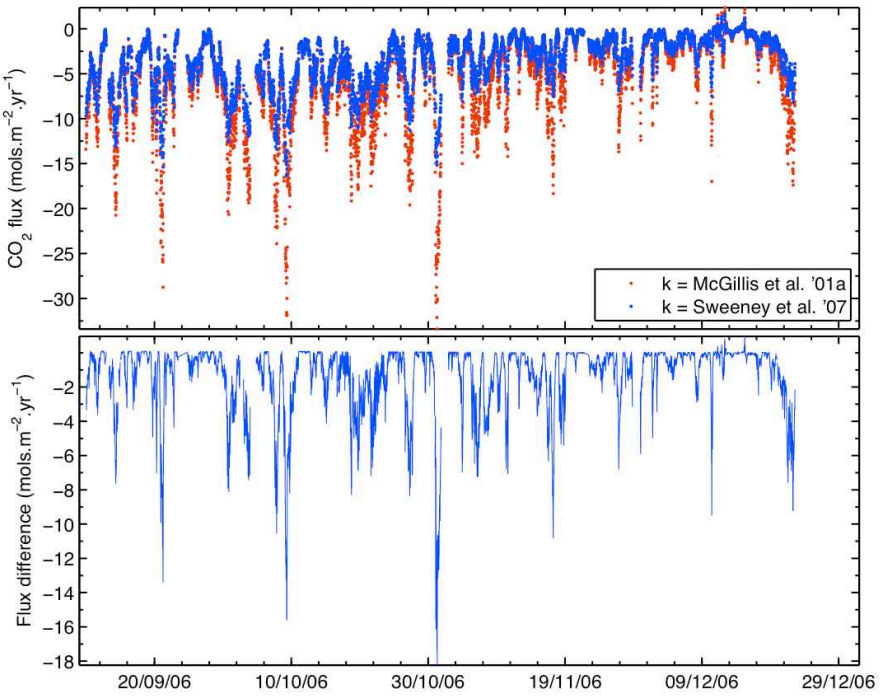

Figure 2.12. Upper panel: Time series of sea-air CO_2 fluxes calculated from the HiWASE BCCR ΔpCO_2 measurements, measured solubility and two published parameterisations of gas transfer velocity (McGillis et al., 2001a; Sweeney et al., 2007). Measurements shown were obtained in 2006 at Station Mike. Lower panel: Difference between the CO_2 fluxes obtained from the two transfer velocity parameterisations.

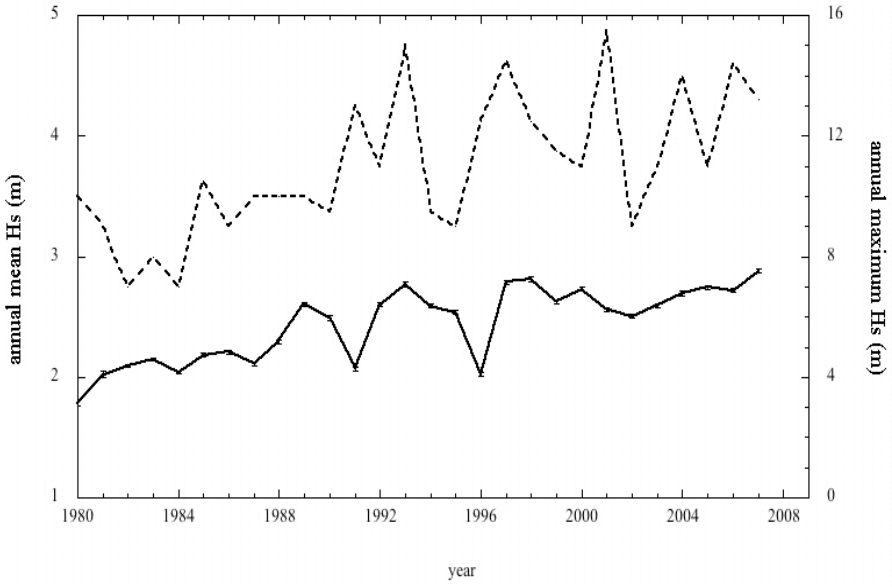

Figure 2.13. Wave height time series at Station Mike for the period 1980-2009. The wave time series shows the mean (solid line) and maximum (dashed line) annual significant wave height for each year. Graph courtesy of DNMI.

3. Humidity cross-sensitivity

3.1. Introduction

This chapter describes the development and testing of a novel method to correct humidity cross-sensitivity in EC CO_2 flux measurements made using open path IRGAs. The majority of the research presented in this chapter has been previously published (Prytherch et al., 2010a). Additional relevant discussion has been added, and the results have been updated to reflect analysis carried out since the date of publication.

The background to this long-standing problem is reviewed in Section 3.2. Section 3.3 and 3.4 briefly review the HiWASE experimental setup and the initial CO_2 flux results that motivated the development of the cross-sensitivity correction. The theoretical basis of the correction is described in Section 3.5 and the method of application used in HiWASE is detailed in Section 3.6. An independent test of the method: determination of the sensible heat flux from sonic temperature measurements, is described in Section 3.7. A discussion of the influence of the Webb et al. (1980) density correction on the cross-sensitivity correction is given in Section 3.8. Further factors affecting humidity cross-sensitivity and the novel correction method are discussed in Section 3.9.

Note that whilst preliminary CO_2 flux results are presented in this chapter, a complete analysis of the HiWASE CO_2 flux results, and the resulting gas transfer relationship, is given in Chapter 4.

3.2. Background

The air-sea flux of CO_2 can be obtained by applying the eddy correlation (EC) method to CO_2 measurements made from either closed-path sensors that precondition the air before measurement (e.g.: McGillis et al., 2001a), or open-path sensors that measure the air in situ. Over land, open-path infrared CO_2/H_2O sensors have generally been considered the standard against which closed-path sensors are evaluated, for example to determine the effects of lag due to the sampling tube required by the closed-path system (e.g.: Leuning and King, 1992). Over the ocean, open-path sensors have a number of advantages: the measurement may be made close to the wind sensor; it avoids the excessively long sampling tubes needed on some ships; and the lower power requirements allows use on buoys. Thus, the successful deployment of open-path

sensors on buoys and ships has the potential to greatly increase understanding of air-sea CO_2 fluxes.

However, since the first oceanic deployments, open-path sensors have given significantly higher flux values than were obtained by other sensors or techniques and this disparity has persisted. Early EC measurements of the air-sea CO_2 flux using open-path instruments (e.g.: Smith and Jones 1985; Wesely, 1982) obtained gas transfer velocity values significantly higher (by approximately an order of magnitude) than those estimated by indirect isotopic methods. The EC estimates were significantly higher than the upper estimates of three independent global estimates. Proposed explanations such as bubble entrainment (Smith & Jones, 1986) and coastal effects (Wesely, 1986) were found to be unable to explain the discrepancy and hence EC measurements of CO_2 flux were in doubt (Broecker et al., 1986).

The disagreement between EC and indirect measurements of the air-sea CO_2 flux has re-surfaced in more recent studies. During the 1996 ASGAMAGE experiment two types of open-path CO_2 sensor were deployed on a fixed platform near the Dutch coast (Jacobs et al., 1999). A detailed analysis of the data (Jacobs et al., 2002a) found gas transfer velocities that were a factor of 2 to 2.5 greater than those from differential tracer experiments (DTEs). Jacobs et al. (2002b) were only able to ascribe part of this difference to vertical concentration gradients and horizontal inhomogeneity. Kohsiek (2000) noted cross-sensitivity to relative humidity in laboratory tests, but application of his deduced correction to the ASGAMAGE data led to “unrealistic results”. The first successful attempt to obtain EC measurements of the air-sea CO_2 flux that were in reasonable agreement with published values were obtained using a closed-path sensor only (McGillis et al., 2001a). An open-path sensor was deployed during this experiment (GasEx-98) but the only transfer velocity results presented were derived from a closed-path sensor. More recent experiments using open-path sensors have again suggested fluxes an order of magnitude greater than would be expected (Tsukamoto et al., 2004; Kondo & Tsukamoto, 2007). Similarly, significantly higher estimates of the air-sea CO_2 flux from open-path sensors have been reported by various other groups in a number of conferences and workshops.

A recent field program in the Baltic Sea has obtained realistic EC CO_2 fluxes using a long-term (~1.5 years) deployment of open-path sensors from a fixed platform at a measurement height of 7.1 m above sea level (Weiss et al., 2007). However, the measurement area featured a water depth of approximately 45 m, a limited fetch of

approximately 100 km, and a maximum mean salinity of 9 psu, resulting in relatively fresh spray and probably less spray generation (Monahan, 1971; Wu 2000). Hence, the measurements reported by Weiss et al. are much less likely to have suffered salt contamination. Some recent attempts at measuring the air-sea CO_2 flux have utilized new sensors combining features of both open and closed path sensors (an open-path sensor with a closed cell around the measurement volume; Miller et al., 2010; Miller et al., 2009). Measurements were reported for only moderate wind speeds (up to 11 $m.s^{-1}$), and stringent quality control was applied, rejecting 90% of the measurements. Similar commercial models are now available and are being deployed by several research groups. Caution must also be applied to the measurements as many of the same limitations that apply to closed path sensors affect these sensors too.

This chapter will demonstrate that the long-standing difficulty with open-path sensors is due to a cross-sensitivity to water vapor fluctuations, similar to that described by Kohsiek (2000), and probably caused by hygroscopic particles (salt) on the sensor lens.

3.3. Experimental setup

The measurements described here were all obtained as part of the UK-SOLAS project "HiWASE" (Brooks et al., 2009) onboard the Norwegian weather ship *Polarfront*. The data used here were obtained between September 2006 and September 2007. Details of the experiment are given in Chapter 2, but pertinent information is summarized here.

The *Polarfront* was equipped with a suite of flux instrumentation (Table 2.1). Ship motion was measured using a Systron Donner MotionPak and corrections were applied to the 20 Hz wind speed measurements used to calculate the EC fluxes (Chapter 6; Edson et al., 1998). The IRGA data were corrected for head deformation effects due to ship motion by relating the results from a shrouded sensor to the MotionPak data and deducing a correction for that sensor when not shrouded (Chapter 5; Yelland et al., 2009). A system for measuring the surface water and atmospheric CO_2 partial pressure was installed on *Polarfront* by the Bjerknes Center for Climate Research (BCCR; Section 2.2.6). The *Polarfront* operated year-round at Station M (66˚N, 2˚E).

3.4. Preliminary CO_2 flux results

Whereas the HiWASE EC flux results for momentum and sensible and latent heat were similar to those calculated from bulk formulae (Chapter 7; Brooks et al., 2009; Yelland et al., 2009), the calculated CO_2 fluxes were typically about 10 times higher than would be expected using accepted values for the transfer velocity (e.g.: Liss & Merlivat, 1986; McGillis et al., 2001a). These initial flux results were calculated using data that had first been corrected on a point-by-point basis for the density dilution effect (Webb et al., 1980; Fairall et al., 2000; Chapter 4).

It was noticed that there was a strong, time-dependent relationship between the IRGA CO_2 concentration and humidity. As an example, Figure 3.1 shows the difference in hourly mean CO_2 concentration from the IRGA and the BCCR system, for a 6 day period in September 2006, plotted against relative humidity. On two occasions the humidity increased over a period of several hours and the IRGA mean CO_2 concentration became biased low. The effect was similar in form and magnitude to that reported by Kohsiek (2000), who suggested that it might be caused by a thin film of water on the sensor optics. However, Figure 3.1 shows that the effect was not consistent, varying from one occasion to another. Thus, an attempt to correct these data using a single laboratory-derived calibration would fail, which may explain Kohsiek's lack of success in correcting the ASGAMAGE data. The variation from case to case suggests that the effect is caused by hygroscopic particles (salt) on the optics, which accumulate before being washed off by rain. In laboratory tests we have observed similarly persistent (> 3 hrs) effects on the IRGA's signal following spraying of the optics with seawater. When fresh water was used the effect was much shorter-lived (< 1 hr). Further discussion of the sensor lens contamination, and methods of reducing it, are given in Section 3.9.2.

The IRGAs used in HiWASE (LICOR 7500) use one detector to measure the infrared absorption of both H_2O and CO_2, and cross-sensitivity will result from imperfections in the sensor's frequency response. The cross-sensitivity response is estimated during factory calibration procedures, and a correction is applied in the IRGA's automated software (LI-COR Biosciences, 2004). Again, the inconsistency of the cross-sensitivity observed during HiWASE, thought to be due to the presence of hygroscopic particles, shows why this correction did not adequately remove the effect from the CO_2 measurements.

The 20 Hz data from the IRGA also showed a marked negative correlation between H_2O and CO_2 (Figure 3.2), similar to the mean behavior shown in Figure 3.1. As expected from similarity theory, the non-dimensional cospectra for the scalars (Figure 3.3) were similar to the universal curves presented, for example, by Kaimal et al. (1972). The normalised temperature and humidity cospectra were similar to each other but the CO_2 and humidity cospectra were almost identical. This suggests that the CO_2 cospectra were almost completely dominated by the dependence of the measured CO_2 signal on humidity across the entire frequency range.

For the 20-minute example shown in Figure 3.2 the sensible and latent heat fluxes were respectively 6.5 $W.m^{-2}$ and 63.6 $W.m^{-2}$ upwards and the calculated CO_2 flux was 89.4 $mol.m^{-2}.yr^{-1}$ downwards: this CO_2 flux is nearly an order of magnitude larger than would be expected for the measured conditions (a 13 $m.s^{-1}$ wind speed and an air-sea pCO_2 of 75 μatm). Given these flux directions, rising parcels of air would be both moister and have lower CO_2 content than sinking parcels, i.e. the sign of the correlation in Figure 3.2 is as expected. However, it will be shown in Section 3.5 below that the magnitude of the correlation is unrealistic. Note that when both the latent heat and CO_2 fluxes are in the same direction (not observed in the data reported here), we would expect the cross-sensitivity to lead to underestimation, and potentially change the direction, of the measured CO_2 flux.

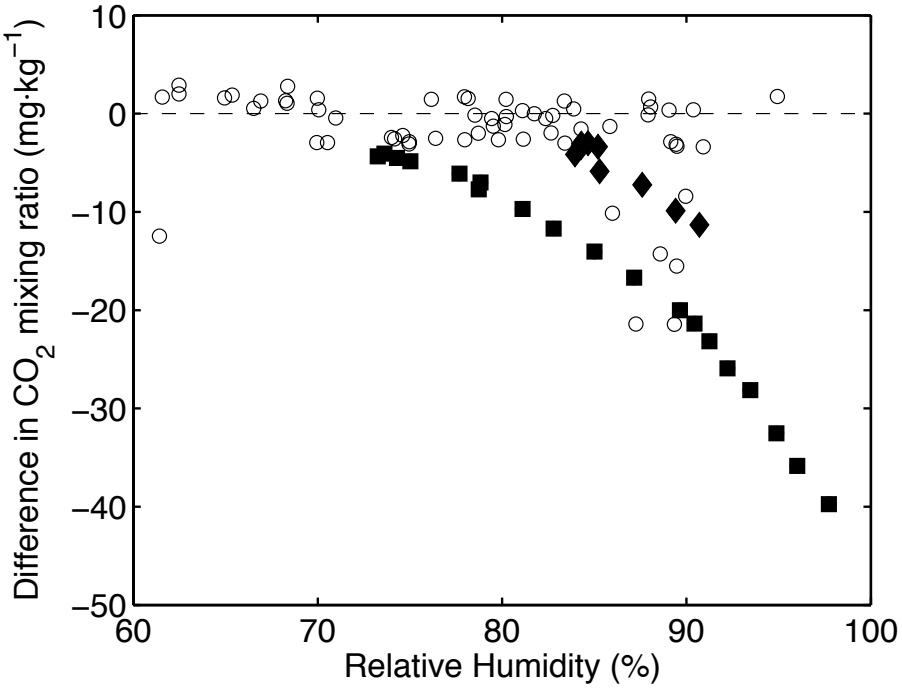

Figure 3.1. Difference (IRGA - BCCR) in CO_2 concentration with respect to relative humidity for hourly mean values from 2006. Two periods of consecutive measurements are highlighted with ■ and ◆ (from Prytherch et al., 2010a).

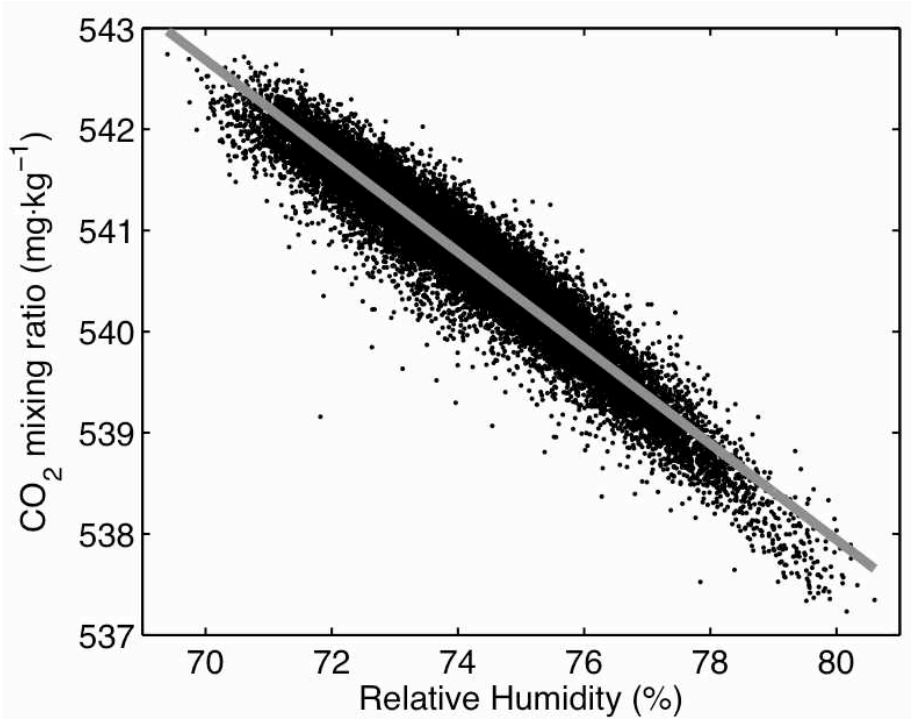

Figure 3.2. Individual 20 Hz CO_2 concentration and relative humidity values from the IRGA for a 20-minute period from 2006: the first order fit is shown (from Prytherch et al., 2010a).

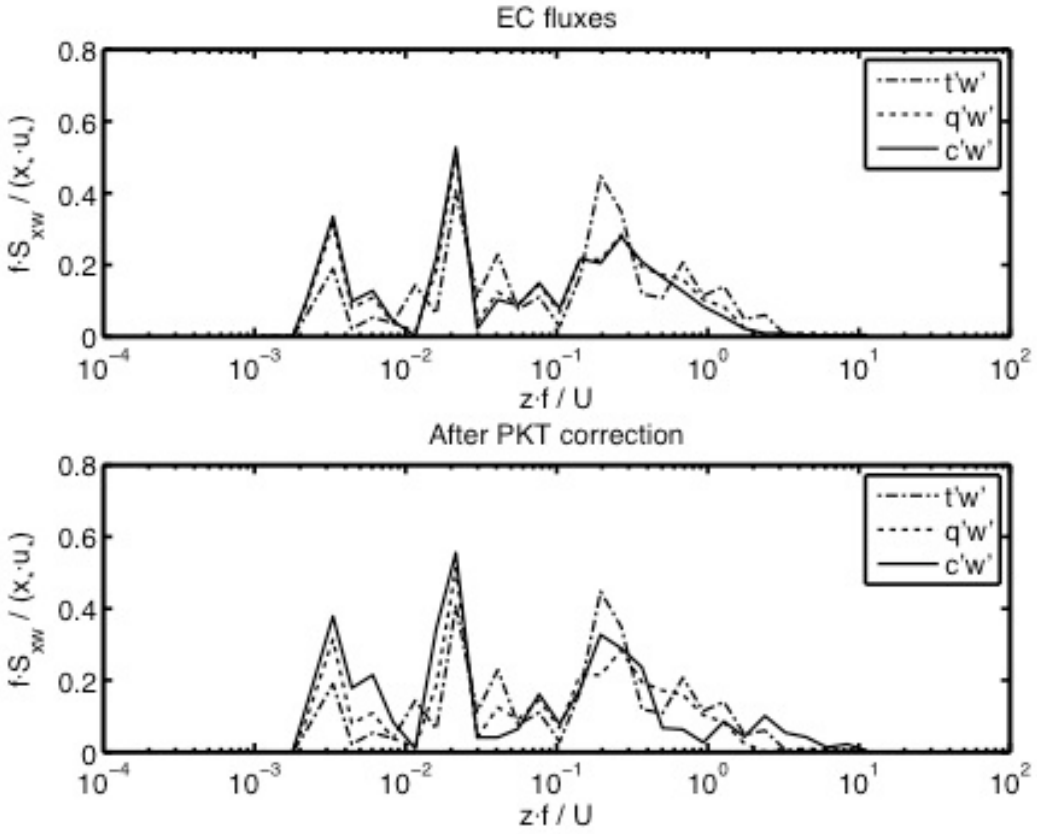

Figure 3.3. Cospectra of the vertical wind and the scalar variables, t, q, and c (normalized by $t*u*$, $q*u*$ and $c*u*$ respectively e.g.: Kaimal et al., 1972) shown with respect to non-dimensional frequency. The CO_2 spectrum has been inverted for ease of comparison. Top panel: Preliminary result. Note near-identical shape of $c'w'$ and $q'w'$ spectra. Bottom panel: Spectra following application of PKT correction to CO_2 data (from Prytherch et al., 2010a).

3.5. Theory

Consider a parcel of air that has moved through a vertical distance Δz to reach the measurement point. The amount by which the humidity of the air is different from its surroundings will depend on the vertical gradient of humidity, and the difference in CO_2 content will similarly depend on the vertical gradient of CO_2. The vertical gradient of a scalar quantity x is (e.g.: Geernaert, 1990):

$$\frac{\kappa_v z}{x_*}\frac{\partial \bar{x}}{\partial z} = \phi_s \qquad (3.1)$$

where κ_v is the von Karman constant and z the height. The scale variable x_* is defined with reference to the flux such that $x_* u_* = \overline{x'w'}$ where u_* is the friction velocity, an overbar indicates a time average, w is the vertical component of the wind speed and an accent indicates a fluctuation from the mean. Assuming that the dimensionless profile ϕ_x for CO_2 mixing ratio c, and water vapor mixing ratio r, are equal (McGillis et al., 2001b show some evidence for this), i.e.:

$$\frac{\kappa_v z}{r_*}\frac{\partial \bar{r}}{\partial z} = \phi_r = \phi_c = \frac{\kappa_v z}{c_*}\frac{\partial \bar{c}}{\partial z} \tag{3.2}$$

then applying Eqn. (3.1) shows that the expected ratio of the variations in the two quantities at the measurement point is given by:

$$\frac{\partial \bar{c}}{\partial \bar{r}} = \frac{c_*}{r_*} \tag{3.3}$$

In Figure 3.2, c is plotted against relative humidity (*RH*): the property on which the error depends. We can calculate the relationship between *RH* and r (due to the small temperature fluctuations over the ocean it is effectively linear) and hence we can determine $\partial \bar{c} / \partial \overline{RH}$ for use in the correction process:

$$\frac{\partial \bar{c}}{\partial \overline{RH}} = \frac{\partial \bar{c}}{\partial \bar{r}} \Big/ \frac{\partial \overline{RH}}{\partial \bar{r}} \tag{3.4}$$

For widely accepted values of the CO_2 transfer velocity the expected value of $\partial \bar{c} / \partial \overline{RH}$ for the sample shown in Figure 3.2 is of order 10^{-8} whereas the gradient obtained from a linear fit to Figure 3.2 is an order of magnitude greater. The small expected value of $\partial \bar{c} / \partial \overline{RH}$ directly follows from the CO_2 flux over the ocean being typically much smaller than the water vapor flux.

3.6. Correction procedure

A method of correcting the *c* estimates for this cross-sensitivity was suggested by Peter K. Taylor (pers. comm.) and is described here. Prior to the cross-sensitivity correction, the density dilution effect is removed on a sample-by-sample basis by converting the measured CO_2 concentration to a mixing ratio using the fast response measurements of temperature and humidity (see discussion in Chapter 4).

For each 20 minute sample period, a first order polynomial, λ, is fitted to the *RH* and *c* data (e.g.: Figure 3.2) and used to remove the dependence of CO_2 on *RH* so that $\partial\bar{c}/\partial\overline{RH} = 0$, i.e.:

$$c_{\mathrm{det}} = c - (\lambda - \bar{c}) \tag{3.5}$$

where c_{det} is the detrended CO_2 mixing ratio. The method thus makes no initial assumption with regard to the "correct" values for the flux or the gradient (with the exception of the assumption of equivalence of the dimensionless profiles). Testing showed that use of second to fifth order fits made no significant difference to the results: the mean of PKT corrected transfer velocities, binned by wind speed, varied from choice of polynomial order by less than 5% and the standard error of the binned values varied by less than 1%.

Despite the detrending adjustment, the CO_2 data still have a $w'c'$ correlation, which enables calculation of an initial estimate for c_*. This value for c_* and the observed r_* value are used in Eqn. (3.3) to recalculate an estimate for the expected gradient $\partial\bar{c}/\partial\overline{RH}$. The CO_2 mixing ratio data are readjusted to have this gradient, i.e.:

$$c = c_{\mathrm{det}} + (RH - \overline{RH})\frac{\partial\bar{c}}{\partial\overline{RH}} \tag{3.6}$$

and the procedure is iterated until a stable CO_2 flux value is obtained. In the example shown in Figure 3.2 the value of the detrended flux estimate (based on $\partial\bar{c}/\partial\overline{RH} = 0$) was 6 mol.m^{-2}.yr^{-1} and the solution converged after 3 iterations to 8.5 mol.m^{-2}.yr^{-1} (c.f. the uncorrected estimate of 89.4 mol.m^{-2}.yr^{-1}). The code (MATLAB) for applying this correction is given in Appendix C.

Approximately 90% of the iterated CO_2 fluxes converge to within 1 mol.m^{-2}.yr^{-1} in less than 10 iterations. Of the fluxes that take 10 or more iterations, 43% do not

converge within 20 iterations. A limit of 9 iterations to converge within 1 $mol.m^{-2}.yr^{-1}$ was applied to the CO_2 iteration. For the fluxes that do converge within this limit, the mean number of iterations was 3.7 ± 1.8 (Figure 3.4a).

It is possible to use *r* instead of *RH* in the PKT correction process by substituting it in Eqn. (3.10) and omitting the linear conversion (Eqn. (3.4)). A set of fluxes was calculated from measurements made in 2006 (n = 1464) using *r* and compared to fluxes from the same measurements calculated using *RH*. The mean bias between the two sets was small, 0.4 $mol.m^{-2}.yr^{-1}$, but there was considerable variation: the RMS difference was 28.2 $mol.m^{-2}.yr^{-1}$ and r^2 was 0.71. Whilst it is thus apparent that the PKT correction introduces considerable scatter into the flux measurements, the close mean agreement between the results iterated using two different variables demonstrates the robustness of the correction. The error corrected for by the PKT method is dependent on *RH*, and as such this was the variable used in the process for the results presented in the remainder of this thesis.

The sections below, 3.7 and 3.8, describe a variety of tests of this detrend-and-iterate correction method, termed the "PKT method" hereafter.

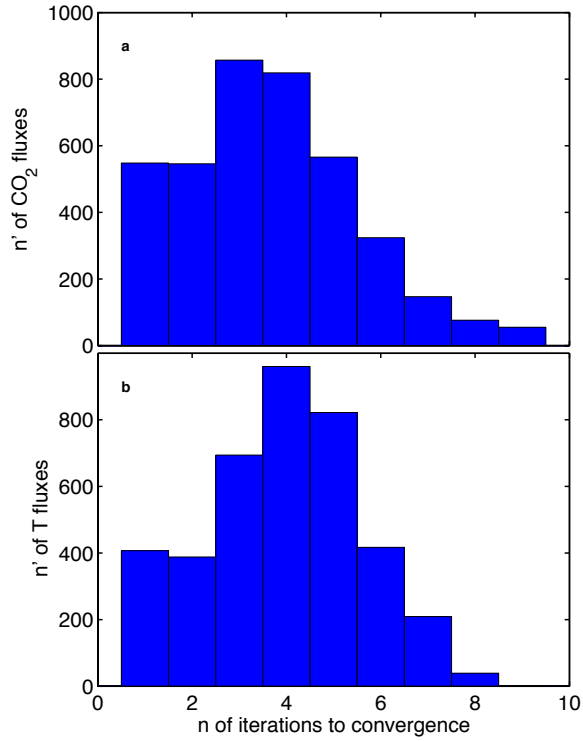

Figure 3.4. Number of iterations till convergence for the PKT corrected (a) CO_2 and (b) temperature fluxes. The maximum number of allowed iterations for both CO_2 and temperature is 10, and the convergence limits are 1 $mol.m^{-2}.yr^{-1}$ (for CO_2) and 0.5 $W.m^{-2}$ (for temperature). 3938 quality controlled measurements are shown.

3.7. Validation of the PKT correction procedure

To independently test the PKT method, it was used to derive the sensible heat flux (rather than the CO_2 flux) without first converting sonic temperature to air temperature as is done in the standard EC method. The standard method is described first, followed by the test.

A sonic anemometer measures the time of flight on 3 axes and calculates the "sonic temperature", T_s, via;

$$T_s = \frac{v_s^2}{403} \tag{3.7}$$

where v_s is the speed of sound (e.g.: Kaimal and Gaynor, 1991). Sonic temperature closely approximates the virtual temperature of air, allowing the air temperature, T, to be calculated from:

$$T = \frac{T_s}{1 + (0.51 \times q)} \tag{3.8}$$

where q is the specific humidity. The air-sea flux of sensible heat is then determined from the cross correlation of T and w using the EC method in the standard fashion (Chapter 4).

To test the PKT method, we use T_s instead of T to calculate the "sonic heat flux". This flux has a small but consistent positive bias when averaged against the EC sensible heat flux results calculated in the standard fashion (Figure 3.5). This bias is dependent on specific humidity. To remove this humidity contribution we apply the PKT method as follows. The dependence of T_s on q is removed using a first-order polynomial fit. This significantly over-corrects the temperature data and the "detrended heat flux" results show a large low bias compared to the standard EC sensible heat fluxes. Analogously to the CO_2 case we make use of the similarity-based relationship:

$$\frac{\partial \overline{T}}{\partial \overline{q}} = \frac{T_*}{q_*} \tag{3.9}$$

with q_* determined from the EC measurements. Eqn. (3.9) is then applied iteratively to repeatedly adjust the gradient of the temperature/humidity relationship until it

converges to a stable value. More than 99% of the iterated temperature fluxes converge to within 0.5 $W.m^{-2}$ in less than 10 iterations. A limit of 9 or fewer iterations to converge within 0.5 $W.m^{-2}$ was applied to the PKT temperature iteration. For the fluxes that do converge within this limit, the mean number of iterations was 3.9 ± 1.7 (Figure 3.4b).

The reliance of Eqn. (3.9) on the accuracy of the q_* values introduces additional noise into the corrected flux measurements (as shown by the larger error bars on the "PKT corrected flux" in Figure 3.5). However, for upward (positive) fluxes the sensible heat fluxes obtained from the PKT method compare extremely well in the mean with those obtained from the standard EC method (top panel, Figure 3.5), showing that the iterative procedure successfully removes the large low bias seen in the detrended flux. For downward (negative) fluxes, the PKT corrected fluxes are larger than the EC fluxes.

If RH and RH_* are used in place of q and q_* in the PKT correction for temperaure (Eqn. (3.9)); note that RH is used in the PKT CO_2 correction), then the PKT results are biased high by approximately 30% relative to the EC sensible heat flux measurements. This is unsurprising as the humidity bias in the sonic temperature measurements is dependent on q, not RH (Eqn. (3.8)).

Measurements made from winds onto the *Polarfront's* bows (relative wind directions 120°-240°, bow-on = 180°) are subject to greater platform motion contamination (see analysis in Chapter 6.4). Removing these 794 data from the original 3938 data shown in the top panel of Figure 3.5 results in the negative (downwards) PKT corrected flux measurements also agreeing extremely well with those obtained from the standard EC method (bottom panel, Figure 3.5). This independent test demonstrates that the PKT method of detrending and iterating removes the humidity dependence of the sonic temperature, and successfully recovers the sensible heat flux regardless of the sign of the flux.

Similarly, Figure 3.6 shows the HiWASE transfer velocities calculated from the original CO_2 flux measurements, the measurements detrended with respect to humidity, and the measurements after iteration. The bottom panel of Figure 3.6 shows the results with bow-on measurements (relative wind directions 120°-240°) removed. The PKT corrected transfer velocities are similar to those obtained in other air-sea interaction experiments using closed path sensors (McGillis et al., 2001a). A more detailed analysis of the HiWASE CO_2 flux measurements, including least squares fits to the results is given in Chapter 4 of this thesis.

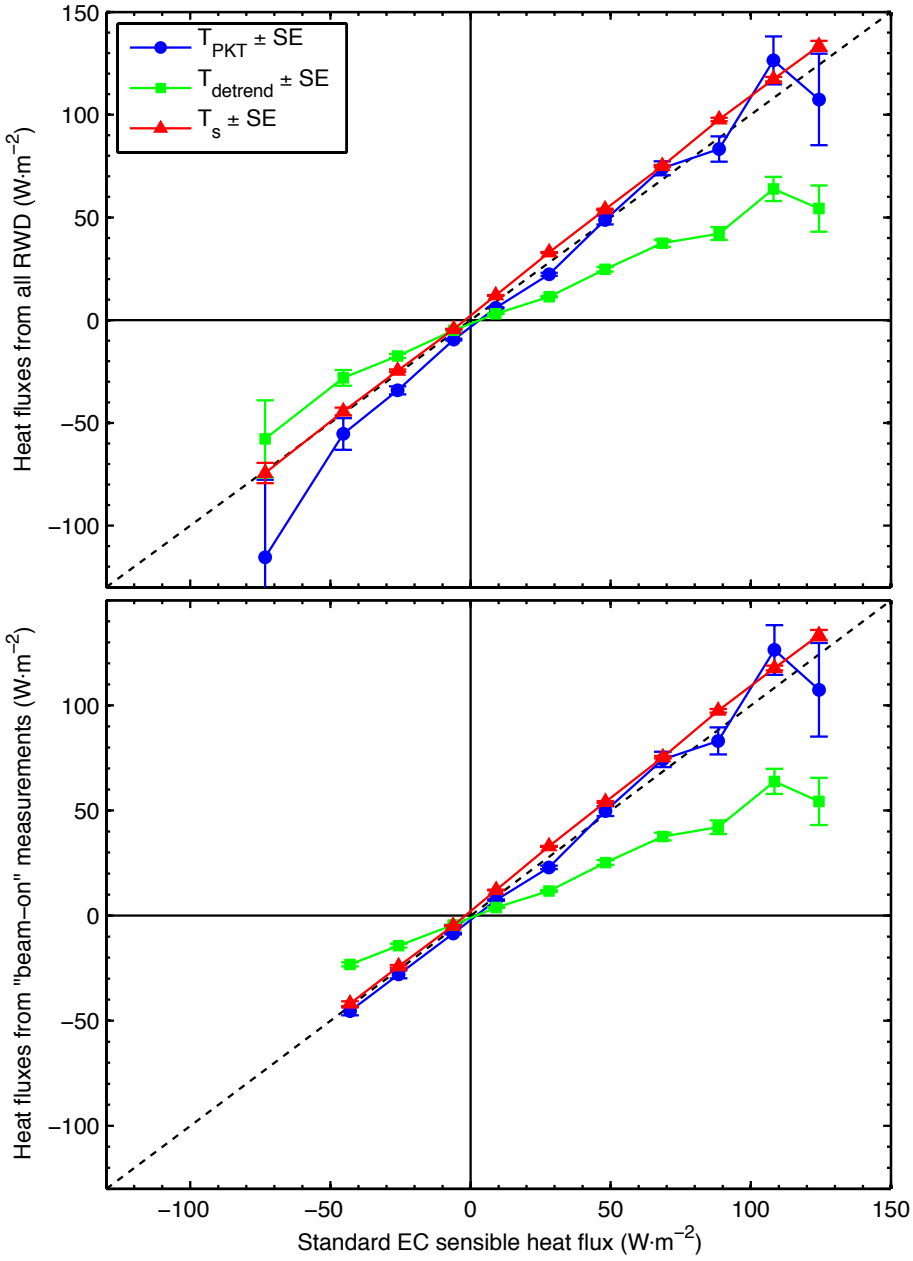

Figure 3.5. Heat fluxes averaged against the standard EC sensible heat flux results: "sonic flux" calculated using T_s (red line); flux after detrending against specific humidity (green line); flux after iteration (blue line), i.e. "PKT corrected flux". The top panel shows measurements from all relative wind directions (60°-340°, bow-on = 180°). The bottom panel has bow-on fluxes (120°-240°) omitted. Error bars show standard error of the mean. The dashed line shows 1:1 agreement.

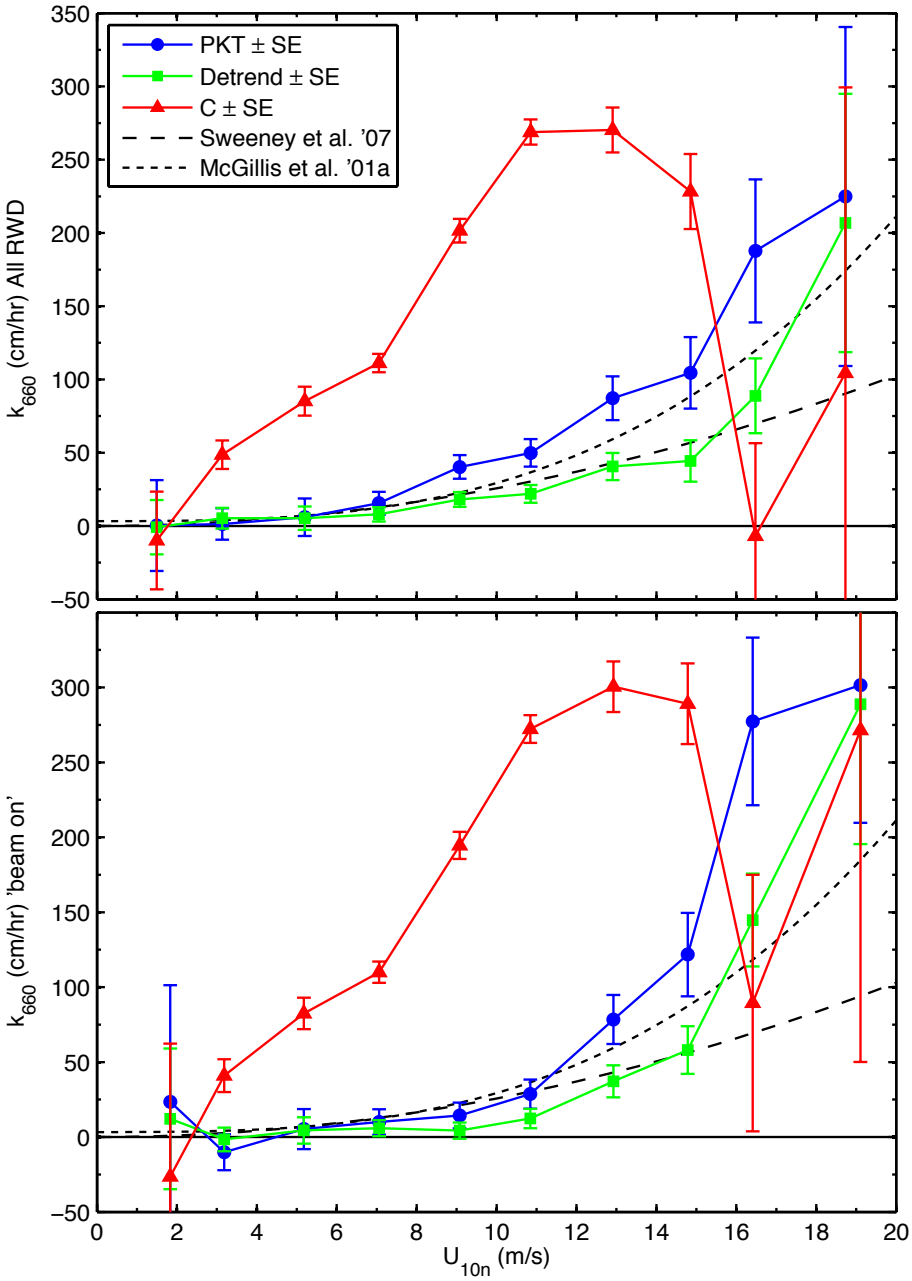

Figure 3.6. Transfer velocities (k_{660}) averaged against the 10 m neutral wind speed (U_{10n}) in 2 ms^{-1} wide bins (centred on the mean wind speed in each 0-2, 2-4, 4-6 etc bin); error bars show the standard error of the mean, n = 3938. Results show transfer velocities calculated from: the initial EC CO_2 fluxes (red); the CO_2 fluxes after detrending against humidity (green); and the fluxes after iteration (blue line), i.e.: the "PKT corrected flux". The top panel shows measurements from all relative wind directions (60°-340°, bow-on = 180°). The bottom panel has bow-on fluxes (120°-240°) omitted. Two previously published gas transfer relationships that encompass most of the range of existing parameterisations are also shown.

3.8. Webb et al., (1980) density correction

Figure 3.7 shows the transfer velocities calculated from CO_2 data that were corrected for the effects of density dilution on a sample-by-sample basis prior to applying the PKT correction. The Webb et al. (1980) density correction removes the effects of water vapor and temperature variations on CO_2 (and on other minor atmospheric constituents, including water vapor) concentration measurements. The PKT method, whilst correcting for a physically different effect, also removes a dependence of CO_2 on humidity prior to iteration. Since both the Webb et al. (1980) density correction and the PKT method remove humidity effects from the measured CO_2, it was thought that applying both might result in an over-correction (pers. comm. O'Dowd; McVeigh, 2009). To test this the data were re-analysed by applying only the temperature part of the Webb et al. (1980) density correction. To reduce processing load, only a subset of the HiWASE measurements (n = 1500) were analysed in this way. Figure 3.7 shows that application of this "half Webb" correction changed the results by an amount typically less than one standard error. The results were similarly unaffected if the PKT correction was applied first, and the half Webb correction applied subsequently. Initial application of the Webb et al. (1980) density correction has a sound physical basis, and removes spurious noise from the data prior to further analysis; hence the full Webb et al. (1980) density correction should be applied prior to the PKT correction.

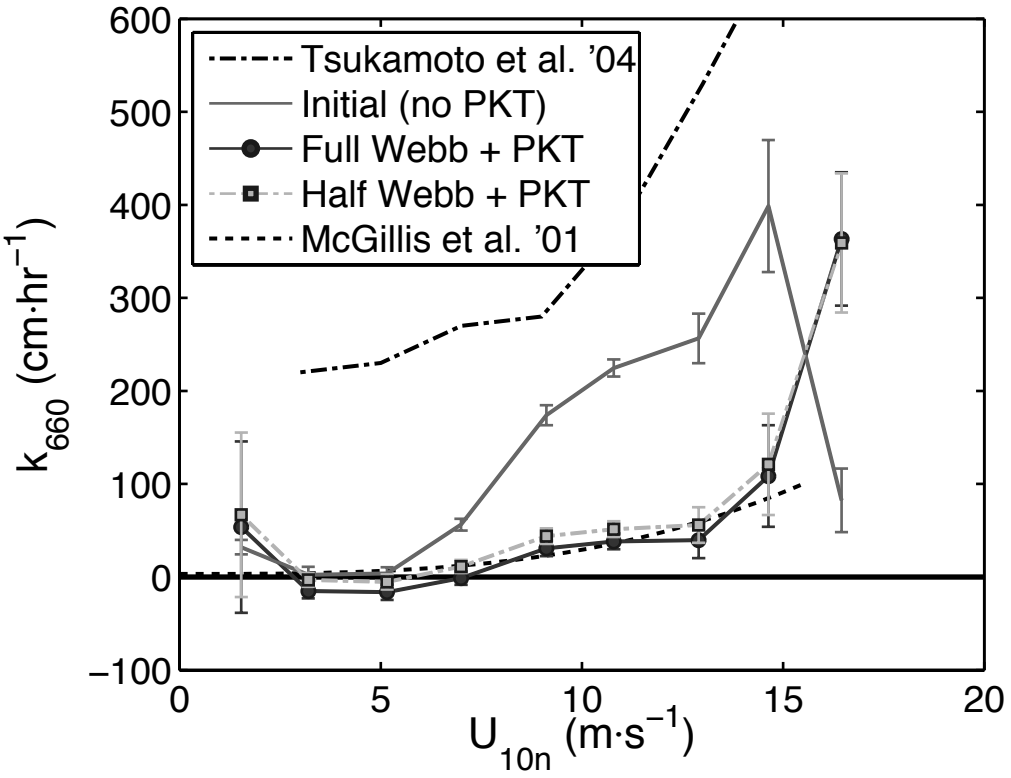

Figure 3.7. Transfer velocities (k_{660}) averaged against the 10 m neutral wind speed (U_{10n}) in 2 m.s^{-1} wide bins (centred on the mean wind speed in each 0-2, 2-4, 4-6 etc bin); n = 1500, error bars show the standard error of the mean. Results are as indicated in the key (from Prytherch et al., 2010a).

3.9. Discussion

3.9.1 PKT correction dependence on latent heat flux

The IRGAs used in HiWASE measure both fast response humidity and CO_2. The latent heat fluxes used in the PKT correction (Eqn. (3.3)) are derived using EC from the IRGA fast response humidity measurements. The EC derived latent heat fluxes may be affected by several of the same sources of error that can impact the EC CO_2 fluxes (e.g.: flow distortion, Chapter 7; platform motion, Chapter 6). Hence, use of the EC latent heat flux, may introduce additional noise into the PKT corrected CO_2 fluxes.

To investigate this uncertainty, r_* in the PKT correction can instead be obtained from bulk estimates (e.g.: Smith, 1988) or ID latent heat flux measurements made onboard *Polarfront*. Both the bulk and ID measurements are much less variable than the EC measurements. The ID measurements are not thought to be as affected as the EC measurements by platform motion (Chapter 6), but are a less direct measurement and are dependent on several assumptions. A brief description of ID measurement is given

in Chapter 1.3 and a selection of bulk latent heat flux relationships are described in Chapter 7.5.1.

A comparison of PKT corrected CO_2 fluxes, where the latent heat flux used in the correction (Eqn. (3.3)) is either an EC measurement ("PKT-EC"), an ID measurement ("PKT-ID") or a bulk estimate (Smith, 1988; "PKT-Smith '88") is shown in Figure 3.8. The variance of the binned PKT-ID measurements is approximately 7% less than the PKT-EC measurements for the wind speed range $6 \le U_{10n} \le 16$ m.s^{-1}, whilst using the bulk estimate of latent heat flux reduces the bin variability by approximately 12% relative to the PKT-EC measurements over the same wind speed range. All three methods agree reasonably well with one another over most of the wind speed range, though the PKT-EC measurements are biased high relative to the PKT-ID and PKT-Smith '88 measurements.

The "correct" value of the bulk latent heat flux is not yet determined (see discussion in Chapter 7.5.1) and the PKT-Smith '88 estimate includes uncertainty resulting from the uncertainty in the bulk flux value. The ID and bulk estimates of the latent heat flux depend on bulk heat and humidity measurements, and may incorrectly estimate the sign of the flux when the latent heat is small (pers. comm. Dr Margaret J. Yelland, NOCS). Hence, despite the resulting increase in variability, the inherent uncertainty in, and less direct nature of, the ID and bulk flux estimates means that the PKT-EC correction method is preferred. This method of applying the PKT correction is used for the remainder of this thesis. The use of the bulk or ID latent heat fluxes to reduce the variability in the measurements will be investigated in future work (Chapter 8).

3.9.2 Cleaning of IRGA sensor

During development of the PKT correction, laboratory based experiments were conducted applying salt and freshwater spray to the IRGA lenses (Section 3.4). The tests showed some prolonged effects on the sensor's measurements from salt water, but did not provide a reliable method of detecting contaminated data. Similarly, attempts to make use of the *Polarfront* crew's meteorology reports to identify rain events and hence estimate which periods of data were "clean" or "dirty" also proved inconclusive. In September 2008, an automated washing system was fitted to the IRGAs on *Polarfront*. The system was designed to apply a jet of freshwater to the top and bottom lens of the unshrouded IRGA at a regular interval (approximately every 12 hours). A relatively

small amount of measurements were obtained whilst the washing system was in place due to unrelated technical difficulties (Chapter 2). Hence, an analysis of the impact of sensor cleansing on the cross-sensitivity was not possible.

The IRGA manufacturer suggests that use of a "water resistant windscreen type coating" (e.g.: Rain-X®) may help to repel water droplets from the sensor window (LI-COR Biosciences, 2004). For HiWASE, it was decided that the use of these wax based products would not be appropriate on ship based deployments due to possible contamination of the coating by the ship's exhaust fumes. An investigation is ongoing into the use of other chemicals (e.g.: Sigmacote®; Sigma-Aldrich) to repel water and contaminants (e.g.: salt) held in solution from the IRGA sensor lens (see future work, Chapter 8).

3.9.3 Spectral PKT correction

The PKT correction has very recently been applied by an independent research group to ship-based air-sea EC CO_2 fluxes measured during an experiment in the Southern Ocean (SO-GasEx: Edson et al., 2011). The gas transfer velocity results obtained were similar to those found in HiWASE (Prytherch et al., 2010b; Chapter 4).

Edson et al. (2011) also describe a modification to the PKT cross-sensitivity correction. This modification makes use of the CO_2 and humidity cospectra to determine the cross-sensitivity, and hence will be referred to here as the spectral PKT correction. Note that details of the HiWASE spectra are not given here but are described in detail in Chapter 6.

The cospectra of a fluctuating constituent, x', is symbolized here as $S_{w'x'}(f)$. The spectral PKT correction calculates a cross-sensitivity coefficient, $\mu(f)$ which quantifies the difference due to the mixing ratio fluctuations of humidity r', between the measured CO_2 mixing ratio fluctuations c'_{meas}, and the "true" value, c':

$$S_{w'c'}(f) = S_{w'c'_{meas}}(f) - \mu(f) S_{w'r'}(f) \tag{3.10}$$

Determination of the cross-sensitivity coefficient requires determination of the actual cross correlation between CO_2 and water vapor. This is estimated by tuning the cospectral measurements to the results of the standard PKT correction. Despite the tuning requirement, the spectral PKT correction is preferred by Edson et al. (2011) due to a reduction of standard error compared with the standard PKT correction. The

analysis presented in the rest of this thesis will only feature measurements corrected with the standard PKT correction.

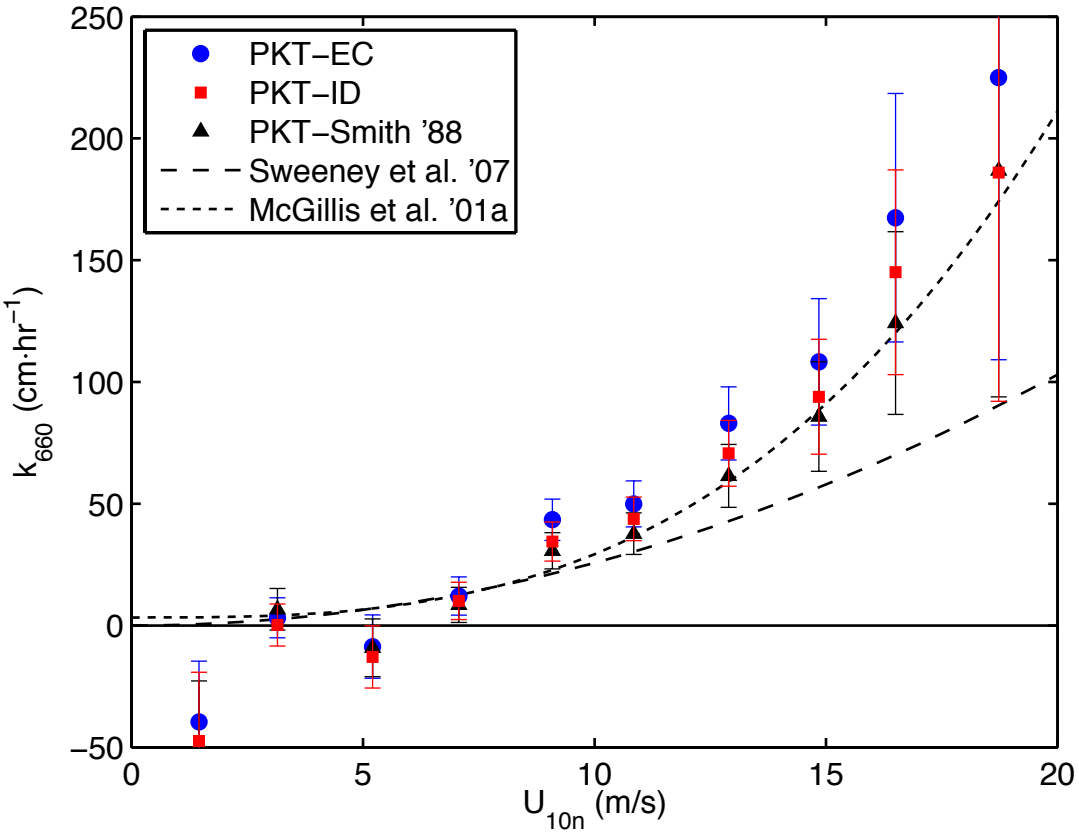

Figure 3.8. Transfer velocities (k_{660}) averaged against the 10 m neutral wind speed (U_{10n}) in 2 ms^{-1} wide bins (centred on the mean wind speed in each 0-2, 2-4, 4-6 etc bin); error bars show the standard error of the mean, n = 3350. The PKT correction has been applied using a latent heat flux determined from either EC measurements (blue circles), ID measurements (red squares) or a bulk relationship (Smith, 1988, black triangles).

3.10. Summary

This chapter has described a cross-sensitivity to water vapor observed in CO_2 measurements from open-path sensors (Section 3.4). The cross-sensitivity is likely caused by contamination of the sensor lens by hygroscopic particles, and is in addition to the effects automatically corrected for by the instrument's internal processing. A novel correction for the cross-sensitivity error, termed the PKT correction, has been described (Sections 3.5 and 3.6). To validate the correction it is used to obtain the sensible heat flux from sonic temperature measurements (Section 3.7). The PKT

method of determining the sensible heat flux is independent of the usual calculation of sensible heat flux from air temperature measurements, and gives very similar results. Application of the correction to HiWASE CO_2 flux measurements obtains results that are similar to those obtained from previous open-ocean experiments (Section 3.8). Further discussion of the correction is given in Section 3.9, and the HiWASE PKT corrected CO_2 fluxes are described in detail in Chapter 4. This novel correction technique could allow correction of the large amount of air-sea CO_2 flux data obtained from open path sensors during previous experiments performed by a number of groups world wide, hence the amount of CO_2 flux data available for analysis should greatly increase.

4. CO_2 flux results

4.1. Introduction

This chapter describes a gas transfer to wind speed relationship derived from the HiWASE CO_2 flux measurements. The majority of the results and analysis presented in this chapter have been previously published (Prytherch et al., 2010b). Additional details of the methodology used have been added (Sections 4.2.1, 4.2.2 and 4.2.3), and the results updated to represent analysis carried out since the date of the original publication (Section 4.6).

The measurement procedure is described in Section 4.2, including an analysis of the flux loss that results from the averaging period used, and the uncertainty resulting from application of density dilution correction. The quality control procedures applied are detailed in Section 4.3. The gas transfer velocity measurements are described in Section 4.4 and the wind speed dependence of the measurements is analysed in Section 4.5. A brief examination of the effect on the flux measurements from periods when the *Polarfront* is steaming, and the robustness of the transfer velocity fits is given in Section 4.6. The results and the implications are discussed in Section 4.7. This chapter takes the same ("classical") approach to determining the gas transfer velocity dependence on wind speed as used in most other experiments, i.e.: flow distortion, platform motion and relative wind direction errors are not considered. These are examined elsewhere in this thesis, in Chapters 6 and 7.

4.2. Flux measurement

4.2.1 Averaging period length

During HiWASE, fast response measurements were made at 20 Hz, and EC fluxes of momentum, sensible and latent heat and CO_2 were calculated from 20-minute sample periods. Measurements were initially obtained in 58.33-minute periods, corrections for platform motion applied, and the measurements then divided into three 20-minute sections. Further details of this process are given in Chapter 2.

Some flux measurements were also calculated from the longer, 58.33-minute periods, allowing the amount of signal contained in turbulent fluctuations with periods longer than 20-minutes to be determined. Due to the amount of processing resources available, only a limited number of flux measurements were made with the longer periods. Of the measurements available, those with low sensible and latent heat fluxes

(< 5 $W.m^{-2}$, n = 14), or small CO_2 fluxes (smaller than 5 $mols.m^{-2}.yr^{-1}$, n = 20) were found to have noisy scalar signals and were removed from this analysis. Averaged flux ogives of the remaining 31 periods are shown in Figure 4.1 and Figure 4.2. The measurements shown were made at wind speeds in the range 9-13 $m.s^{-1}$. Note that a signal is apparent in the momentum and scalar ogives at frequencies associated with platform motion, ~ 0.1 Hz. A discussion of the causes of this signal, and a more detailed spectral analysis of the HiWASE fluxes, is presented in Chapter 6.

From the calculated ogives, it is possible to determine the proportion of the flux signal contained at frequencies below some period. Two representative periods were chosen, 20-minutes and 10-minutes. The proportions of the averaged flux signals at frequencies lower than these periods are shown in Table 4.1. For all of the HiWASE turbulent fluxes except the crosswind flux, the proportion of flux signal contained in fluctuations at periods longer than 20-minutes is between 1 and 4%. There are increasingly few samples made as the measurement frequency decreases. Thus, the signal at periods longer than 20-minutes may be due to low frequency noise and may not represent a real flux signal. As expected from the ogives shown in Figure 4.1 and Figure 4.2, the proportion of the flux signal contained in fluctuations with periods of 10-minutes or longer is larger, approximately 8% for the humidity and CO_2 scalar fluxes.

The choice of sampling period in EC experiments is always a compromise between factors which argue for a longer averaging period (i.e.: obtaining the entire flux signal; and obtaining robust flux estimates, Chapter 5.4), and factors which argue for a shorter period (i.e.: ensuring stationarity, Chapter 5.6; minimizing data loss from events such as ship maneuvers; and maximizing the number of high wind speed measurements). For each flux (momentum, latent heat, sensible heat and CO_2) measured during HiWASE, the estimated proportion of the flux signal at periods longer than 20-minutes period is insignificant relative to the various measurement uncertainties (e.g.: Chapters 5, 6 and 7). It is also notable that application of the PKT correction does not significantly increase the low frequency noise in the temperature and CO_2 fluxes, in contrast to the "spectral PKT" method described by Edson (2011; Section 3.9.3).

Table 4.1. Percentage of flux contained in variation at periods longer than indicated. Fluxes calculated from 58.33-minute averages. Percentage loss calculated as an average of 31 measurements obtained in 2006 with sensible and latent heat fluxes > $|5|$ $W.m^{-2}$ and PKT corrected CO_2 fluxes larger than 5 $mols.m^{-2}.yr^{-1}$. Measurements have been corrected for platform motion.

Flux	**Signal > 20-minutes (%)**	**Signal > 10-minutes (%)**
Along wind momentum (*u'w'*)	1.4	3.7
Cross wind momentum (*v'w'*)	6.3	1.3
Latent heat (*r'w'*)	3.8	8.1
Sensible heat (*T'w'*)	1.8	3.6
PKT sensible heat (*PKTT'w'*)	0.9	1.5
CO_2 (*c'w'*)	3.4	8.0
PKT CO_2 (*PKTc'w'*)	4.1	7.6

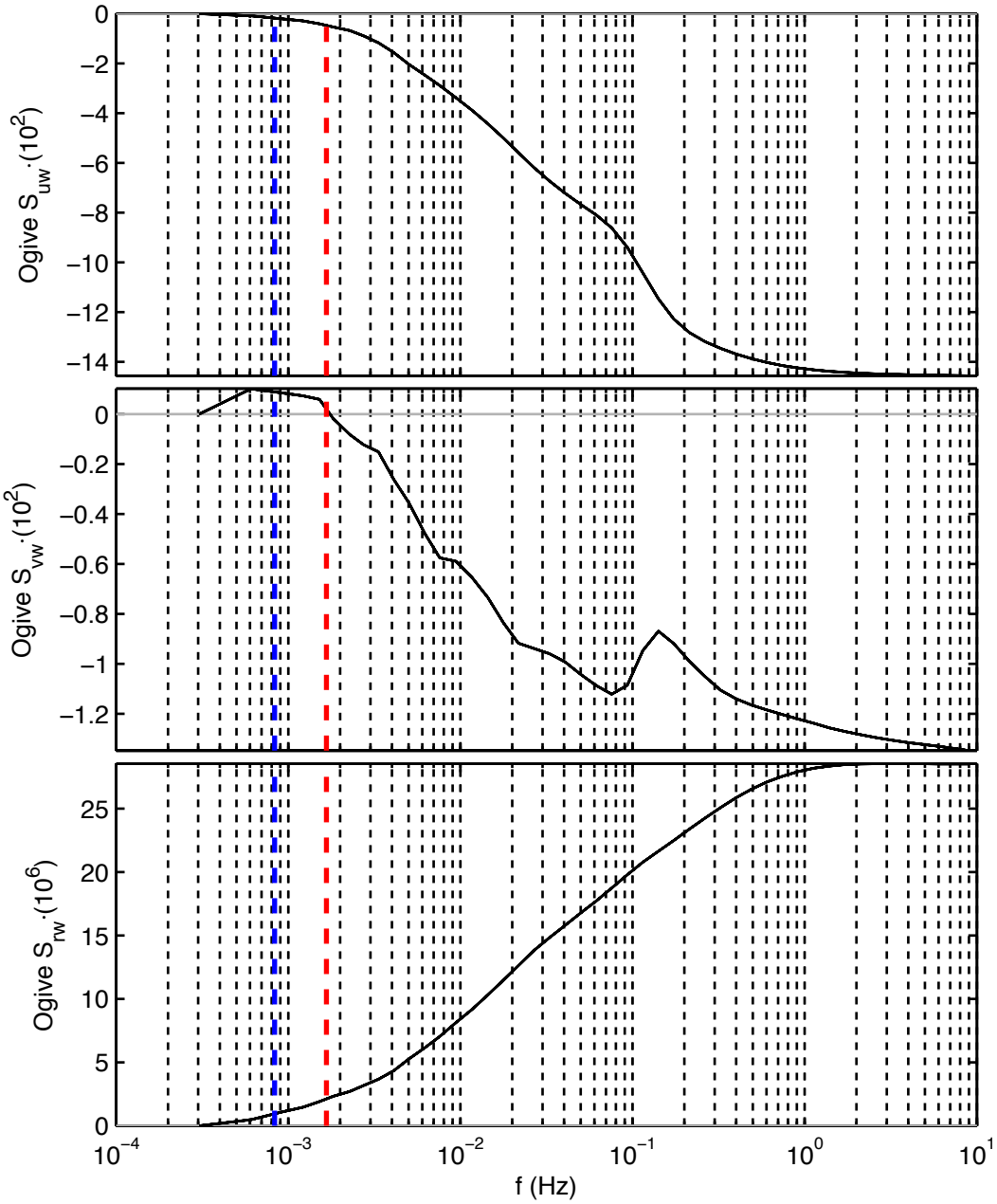

Figure 4.1. Ogive cospectral function of 58.33-minute flux periods. Averages are of 31 measurements obtained during 2006 with sensible and latent heat fluxes > |5| $W.m^{-2}$ and PKT corrected CO_2 fluxes larger than 5 $mols.m^{-2}.yr^{-1}$. Measurements have been corrected for platform motion. The frequencies corresponding to 20-minute (blue line) and 10-minute (red line) periods are highlighted.

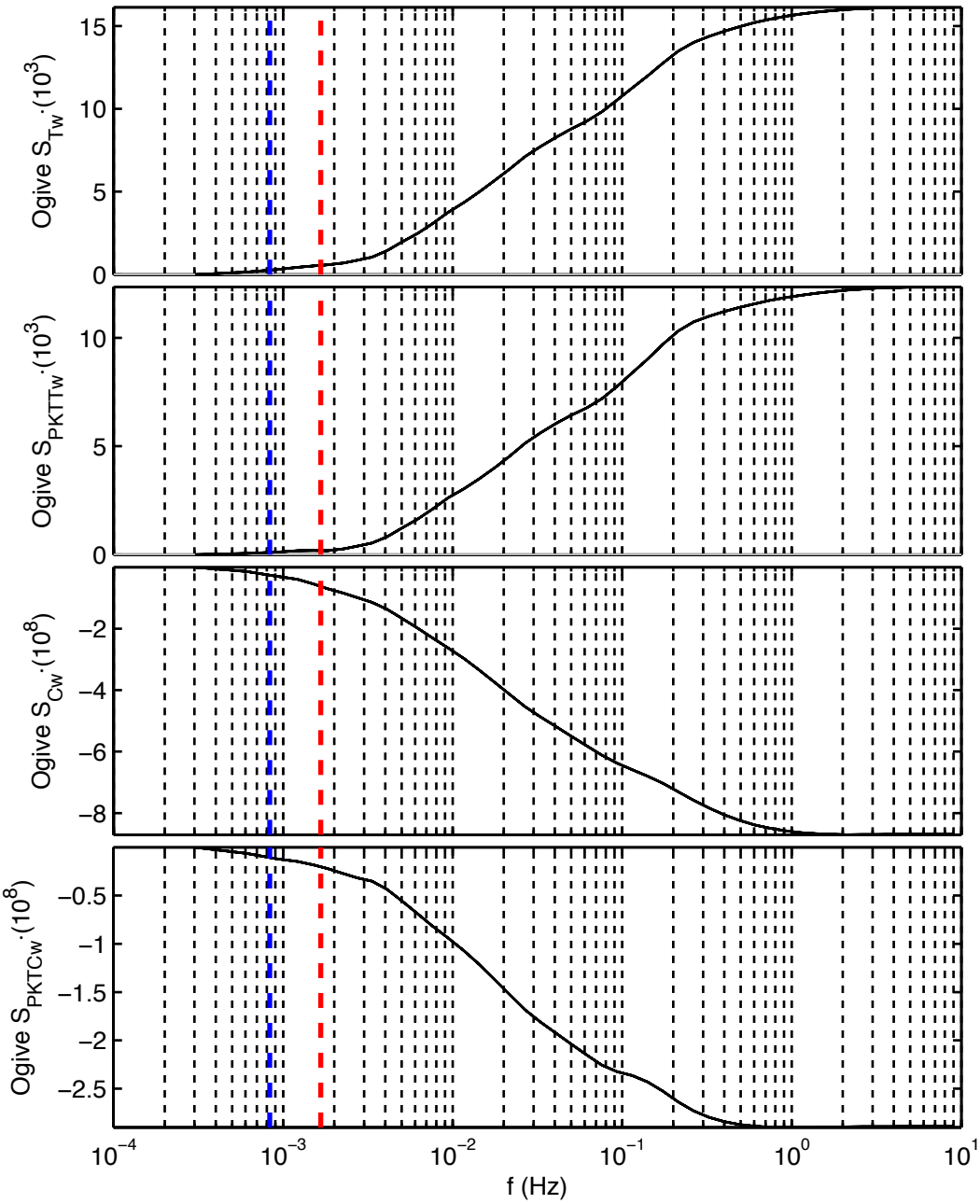

Figure 4.2. Ogive cospectral function of 58.33-minute flux periods. Averages are of 31 measurements obtained during 2006 with sensible and latent heat fluxes > |5| $W.m^{-2}$ and PKT corrected CO_2 fluxes larger than 5 $mols.m^{-2}.yr^{-1}$. Measurements have been corrected for platform motion. The frequencies corresponding to 20-minute (blue line) and 10-minute (red line) periods are highlighted.

4.2.2 *Webb et al. (1980) density correction*

The fast response IRGAs used for CO_2 and H_2O flux measurement in HIWASE measure mass density. These measurements must be converted to mixing ratios to enable the fluxes to be calculated. In the presence of sensible or latent heat fluxes, the air density, and hence the mass density measurements made by the IRGAs will be modified (Webb et al., 1980). This effect can be corrected for, but for CO_2, the magnitude of the correction can be similar or larger than the magnitude of the true flux, and can change its direction (e.g.: Fairall et al., 2000).

A correction for the density effect can be determined from the sensible and latent heat fluxes and applied to a mass flux calculated from mass density measurements (Webb et al., 1980). For example, applying the correction to measurements of CO_2 mass density, C_{CO2}, enables the true CO_2 flux, F_c, to be calculated as:

$$F_c = \overline{w'C'_{CO_2}} + \left(\frac{m_a \overline{C_{CO_2}}}{m_v \overline{\rho}_a} \right) \overline{w'\rho'_v} + \left(1 + \frac{m_a \overline{\rho}_v}{m_v \overline{\rho}_a} \right) \left(\frac{\overline{C_{CO_2}}}{\overline{T}} \right) \overline{w'T'} \qquad (4.1)$$

where m_a and m_v are the molecular masses of dry air and water vapor respectively, $\overline{\rho_a}$ is the mean dry air density, $\overline{\rho_v}$ is the mean moist air density (see Glossary). The Webb et al. (1980) density correction can also be applied to the CO_2 mass density measurements on a point-by-point basis to obtain the CO_2 mixing ratio c (e.g.: Fairall et al., 2000):

$$\rho_a c' = C'_{CO_2} + \left[\frac{m_a \rho'_v}{m_v \overline{\rho}_a} + \left(1 + \frac{m_a \overline{\rho}_v}{m_v \overline{\rho}_a} \right) \frac{T'}{\overline{T}} \right] \overline{C_{CO_2}} \qquad (4.2)$$

The point-by-point version of the Webb et al. (1980) density correction has the advantage that cospectra of the CO_2 mixing ratio can be calculated and compared with ideal spectral curves (e.g.: Kaimal et al., 1972). When applied to a subset of HiWASE measurements (n = 570) the two forms of the Webb et al. (1980) density correction agree extremely closely (mean difference = 0.04 % ± 0.49 %, $r^2 > 0.99$).

A different method for removing the effect of density variations on the mass flux measurements is to directly obtain the mixing ratios of the constituents. These can be calculated by determining the dry air density from fast response (20 Hz) measurements

of pressure, temperature and humidity and the ideal gas law. The fast response moist air density, ρ_v, is first calculated from the ideal gas law:

$$\rho_v = \frac{n}{V} = \frac{P}{RT_v} \tag{4.3}$$

where n is the air mass, V is the volume, P is the air pressure (mb, with 1 mb $\approx$ 100 $N.m^{-2}$), T_v is the virtual temperature (K) and R is the ideal gas constant (287.04 $J.K^{-1}.kg^{-1}$). The moist air density is then used with the H_2O mass concentration, C_{H_2O}, to determine the dry air density ρ_a:

$$\rho_a = \rho_v - C_{H_2O} \tag{4.4}$$

which is used to derive the mass mixing ratios of H_2O, r, and CO_2, c, defined as:

$$r = \frac{C_{H_2O}}{\rho_a}, \; c = \frac{C_{CO_2}}{\rho_a} \tag{4.5}$$

This correction method will be referred to here as the direct method.

Both the Webb et al. (1980) and direct methods of correcting the density dilution effect have been used in experiments making air-sea EC CO_2 flux measurements (e.g.: McGillis et al., 2001a: Webb et al. method; Miller et al., 2010: direct method). In order to determine the most appropriate dilution correction method to use in HiWASE, a subset (n = 436) of CO_2 fluxes calculated with either the Webb et al. (1980, Eqn. (4.2)) or direct (Eqns. (4.3), (4.4) and (4.5)) density dilution corrections were compared (Figure 4.3). Small fluxes (< 5 $mols.m^{-2}.yr^{-1}$, n = 141) and outlier differences (percentage differences > 100 %, n = 32) were excluded. The bias between the two sets of measurements was less than 2% and the correlation was high, r^2 = 0.96. However, there was significant variability in the difference between the two sets of fluxes, the standard deviation of the percentage differences was ~ 26% (Figure 4.3). This is not unexpected and is analogous to the additional noise that is introduced by the PKT correction (Chapter 3). Use of the direct dilution correction instead of the Webb et al. (1980) density correction led to a small reduction (~ 4%) in the standard error of the binned transfer velocities for the subset of measurements analysed. Hence, the direct

method of removing the density dilution effect was applied to the HiWASE CO_2 flux measurements reported here.

The Webb et al. (1980) density correction is known to be a significant source of uncertainty in EC CO_2 flux measurements. For instance, McGillis et al. (2001a) reported measurements from a closed path system that thermally equilibrated the air samples prior to measurement, removing the temperature fluctuation portion of the density dilution effect. McGillis et al. (2001a) estimated that the uncertainty in the CO_2 flux measurements they reported resulting from the humidity component of the Webb et al. (1980) density correction was ~ 45%.

The direct density dilution correction makes use of fast response measurements of dry air density, whilst the Webb et al. (1980) density correction uses only the mean dry air density. Dry air density is calculated from air pressure measurements; with air pressure measured using a sensor in the (unsealed) IRGA electronics box on the *Polarfront's* foremast. The low resolution of this pressure sensor (1 mb) and possible damping of high frequency fluctuations by the box (see the discussion of these effects, and the pressure measurements made during HiWASE, in Chapter 5), may contribute to the differences between the two versions of the dilution correction.

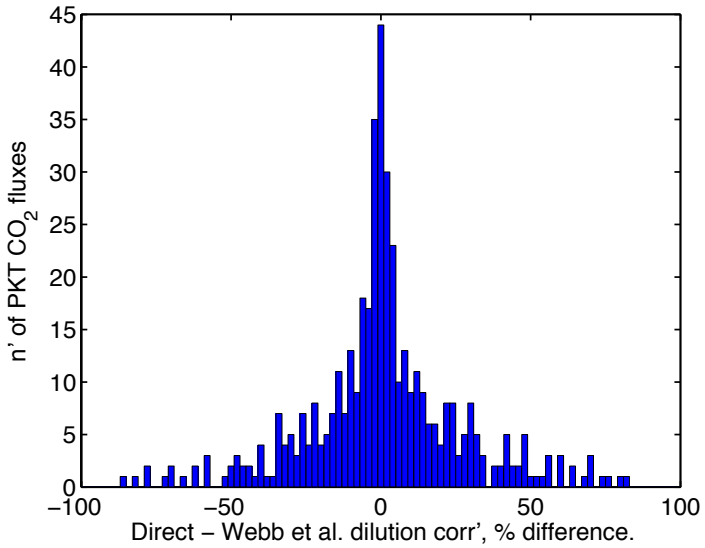

Figure 4.3. Histogram of the percentage difference between PKT corrected CO_2 fluxes obtained from mixing ratios calculated with either the Webb et al. (1980) density correction (Eqn. (4.2)) or with the direct method (Eqns. (4.3), (4.4) and (4.5)). The histogram shows 436 flux measurements obtained in 2006. Fluxes smaller than 5 mols.m^{-2}.yr^{-1} (n = 141) or with percentage differences larger than 100 % (n = 32) have been removed from the analysis.

4.2.3 *Covariance calculation*

EC fluxes were calculated in HiWASE from 20-Hz measurements in 20-minute averages. Standard data conditioning procedures (e.g.: Stull, 1988) were applied to the measurements prior to flux calculation, and are described here. The measurements were windowed using a cosine-tapered (Tukey) window with the ratio of taper to constant sections set at 0.5. A correction factor was applied to the spectral density to compensate for the windowing.

The windowed measurements were linearly detrended, and outlier values (> ± 8 σ) were removed and the data linearly interpolated. The flux, F_x, was then calculated as the sum over frequency, f, of the conditioned cospectra, i.e.:

$$F_x = \sum_f S_{w'x'}(f) \tag{4.6}$$

where the cospectra, $S_{w'x'}(f)$, is defined as the real component of the cross spectrum $G_{w'x'}(f)$, which is in turn defined as:

$$G_{w'x'}(f) = FT^*_{w'}(f) \bullet FT_{x'} \tag{4.7}$$

where $FT_{x'}$ is the Fourier transform of *x'* and $FT^*_{x'}$ is the complex conjugate of $FT_{x'}$.

Calculation of EC fluxes using this spectral calculation is equivalent to calculating the fluxes by determining the covariance, and has the advantage of also obtaining the cospectra of the measurements.

To remove humidity cross-sensitivity, the PKT correction (Chapter 3; Prytherch et al., 2010a) was applied to all HiWASE CO_2 flux measurements.

4.3. Quality control procedures

In the available dataset there were 28,717 20-minute sampling periods with corresponding flux measurements, ΔpCO_2 values and auxiliary data (i.e. mean meteorological, salinity and navigation data). Of these, 15,479 were omitted due to the relatively small size (< 40 μatm) of the air-sea ΔpCO_2, which occurred during winter months. Several on-station periods obtained exceptionally scattered flux measurements, possibly due to problems with instrument setup or data transfer, and measurements from these on-station periods (2733 measurements) were removed. Quality control criteria were applied automatically to the remaining 10,505 sampling periods.

To remove extreme outliers, periods were rejected if the calculated transfer velocity was outside a cutoff value of ± 900 cm.hr^{-1} (1163 periods). This removed about 10% of the data: the remaining data all lay within ± 3 standard deviations of the mean (calculated using all 10,505 measurements). Increasing the cutoff value made no significant change to the mean transfer velocity to wind speed relationship (a cutoff of ± 1100 cm.hr^{-1} caused a 2 % decrease in k at a wind speed of 7 m.s^{-1} and an increase in k of 2% at 15 m.s^{-1}). Decreasing the cutoff value caused a larger change in the mean relationship (a cutoff of ± 700 cm.hr^{-1} caused an 18% decrease in k at a wind speed of 7 m.s^{-1} and a 13% decrease at 15 m.s^{-1}).

Periods were rejected by the automated quality control if the crosswind momentum flux was larger than the along wind flux (710 periods) or if the relative wind direction was outside 60-340 (for the fore IRGA, 90-340 for the starboard IRGA, bow-on = 180; 853 periods). These periods are thought to be strongly affected by flow distortion, which is examined in detail in Chapter 7. Periods were also rejected when the PKT correction did not converge (653 periods). These automated quality control procedures rejected a total of 6567 periods. The results discussed in the remainder of this paper are based on the remaining 3938 measurements. Discounting winter months when the ΔpCO_2 was small, the accepted measurements represent approximately 30% of the total. For comparison, quality control procedures on a recent long term EC CO_2 flux experiment on a fixed platform in the Baltic Sea passed approximately 34% of the available periods (7820 30 minute periods passed from a 16 month long experiment; Weiss et al., 2007), and a recent open ocean EC experiment onboard a research vessel passed approximately 10% (Miller et al., 2009).

4.4. Gas transfer velocities

The HiWASE gas transfer velocities, averaged by 10-metre neutral wind speed, U_{10n} in 1 m.s^{-1} bins and normalised to a Schmidt number of 660 via:

$$k_{660} = k\left(\frac{660}{Sc}\right)^{-n} \tag{4.8}$$

where Sc was determined from sea surface temperature and n was assumed to equal 0.5, (appropriate for wavy conditions; Jähne et al., 1987b), are shown in Figure 4.4 and summarized in Table 4.2 (Prytherch et al., 2010b). Due to the small number of measurements in the bins centred on 18 m.s^{-1} (# = 6), 19 m.s^{-1} (# = 5) and 20 m.s^{-1} (# = 1), these bins have been combined. Also shown in Figure 4.4 is the mean relationship and wind-averaged EC transfer velocities of McGillis et al. (2001a), and the mean relationship of Sweeney et al. (2007). Error bars show standard error: for the measurements of McGillis et al., standard error has been estimated from the published standard deviations, experiment length and assumption of a Rayleigh distribution of wind speeds (e.g. Wanninkhof et al., 2002).

For a smooth sea surface, laboratory results suggest that a Schmidt number exponent of 2/3 is appropriate (Jähne et al., 1987b). If n = 2/3 is used to calculate transfer velocities from measurements made at wind speeds less than or equal to 3 m.s^{-1}, the binned transfer velocities centred on 1 m.s^{-1}, 2m.s^{-1} and 3 m.s^{-1} are 10.0 cm.hr^{-1}, 5.5 cm.hr^{-1} and 6.0 cm.hr^{-1} respectively. This removes the negative binned transfer velocity value at approximately 3 m.s^{-1} (Table 4.2), suggesting that this choice of exponent is more appropriate in low wind conditions. The use of a varying Schmidt number exponent will be investigated in further work. However, for consistency and to aid comparison with previously published results, an exponent of 0.5 is used to calculate all HiWASE transfer velocities presented in this thesis.

The flux measurements from the HiWASE experiment are more scattered than those of McGillis et al. (2001a). This is unsurprising: measurements were made using open-path sensors and in an opportunistic manner on a weathership rather than during a dedicated research cruise. Following the method of Fairall et al. (2000), individual flux measurement uncertainty for a 20-minute sampling period is estimated at about 43% at wind speeds of 10 m.s^{-1} (Chapter 5.4). Quality control procedures were applied in automated fashion and there was no manual examination of each spectrum (as done in other studies), Additionally, the PKT correction, whilst removing a large source of bias,

could introduce significant additional variability through its dependence on the accuracy of the temperature and humidity fluxes. Application of the PKT correction procedure to sonic temperature measurements, in a manner analogous to the CO_2 flux correction (Chapter 3; Prytherch et al., 2010a) increased the temperature flux variability by a factor of 5, although the mean flux results agreed to within 7%. However, application of the PKT correction led to an increase of only 3% in the variability of k for the majority of the wind speed bins, suggesting that the correction is removing both variability and bias resulting from hygroscopic particle contamination from the CO_2 flux measurements.

A possible source of error in EC flux measurements is flow distortion by platform superstructure affecting both the turbulent components of the flow and the mean speed and height of the flow (Yelland et al., 1998). The effect of flow distortion on the turbulent flow at exposed sensor positions and minimally disturbed wind directions is expected to be smaller for scalar fluxes than for momentum fluxes as they are dependent on only the vertical component of the wind vector (Pedreros et al., 2003). To investigate the impact of flow distortion effects on the HiWASE flux results, latent heat fluxes measured on *Polarfront* using both the EC and ID methods were compared with bulk estimates (Chapter 7). Bias in the EC flux measurements as a result of flow distortion was found to be small compared to the existing uncertainty in k in the results presented here.

Table 4.2. Gas transfer velocities calculated from measured CO_2 fluxes, and averaged by wind speed (ΔU_{10n} = 1 m.s^{-1}, centred on integer wind speed values). $U_{10n}av$ is the mean of the wind speed measurements within each bin, and # is the number of elements in each wind speed bin (from Prytherch et al., 2010b).

$U_{10n}av$ (m.s^{-1})	$k_{660}av$ (cm.hr^{-1})	#	Standard error
1.2	8.62	10	35.5
2.2	6.05	26	30.9
3.0	-3.45	88	14.6
4.0	7.36	112	19.7
5.0	8.14	163	20.3
6.0	4.71	302	13
7.0	37.5	402	10.7
8.0	9.87	407	11.3
9.0	29.47	428	12.2
10.0	45.24	588	11
10.9	54.83	455	12.5
12.0	67.12	295	17.9
13.0	101.59	281	20
14.0	84.21	160	30
15.0	140.48	122	33.1
16.0	73.05	68	47.7
16.7	190.14	19	73.7
18.5	233.89	12	96.9

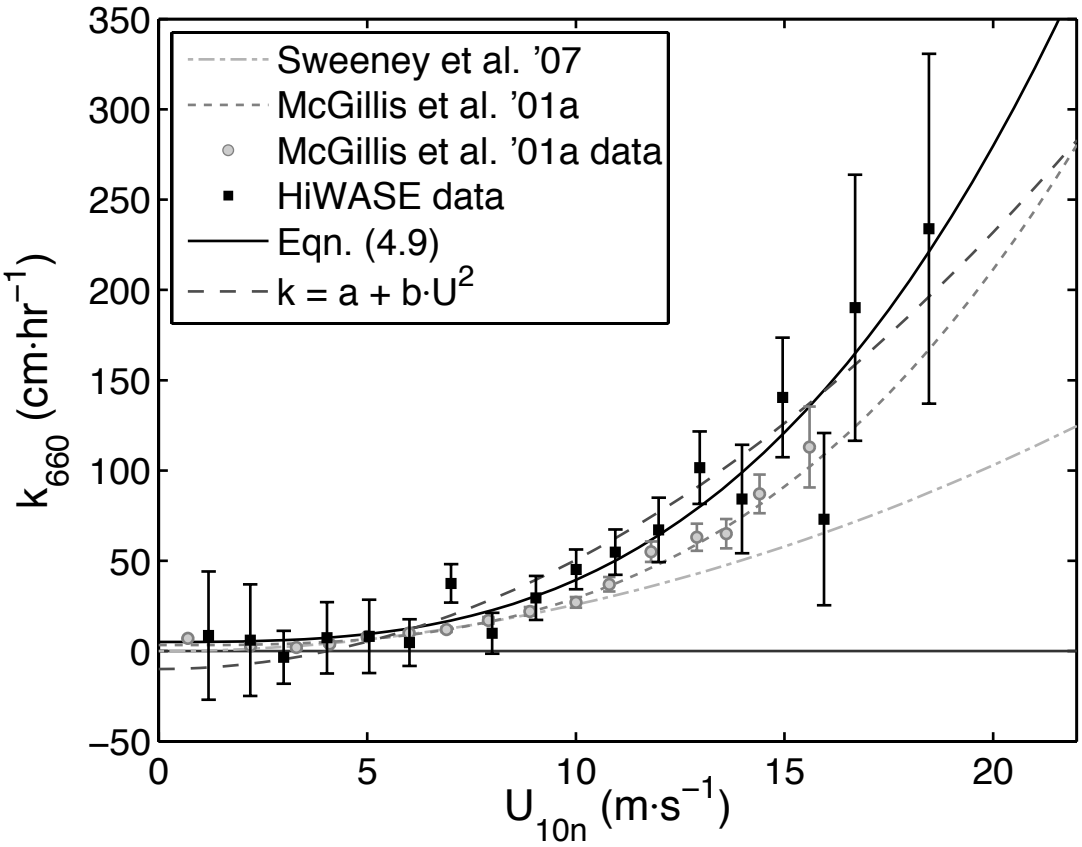

Figure 4.4. Transfer velocities (k_{660}) averaged against the 10 m neutral wind speed (U_{10n}) in 1 ms^{-1} bins, error bars show the standard error of the mean. Results are as indicated in the key. Standard error for the McGillis et al. (2001a) data set has been estimated from published standard deviations, assuming a Rayleigh distribution of wind speed during the period of the experiment (Prytherch et al., 2010b).

4.5. The wind speed dependence of *k*

The HiWASE transfer velocity results include measurements at higher wind speeds than previously published for the open ocean. The highest wind speed measurement was at U_{10n} = 19.6 m.s^{-1}. The highest bin averaged wind speed, centred on 18.5 m.s^{-1}, is based on 12 points. The very high variability (standard error) of this average means it must be treated with caution. However, we have no particular reason to distrust these measurements. The previously reported highest wind speed result for open ocean EC measurements (made in the North Atlantic using a closed-path IRGA) was obtained at 15.5 m.s^{-1}: this was based on only 4 points (McGillis et al., 2001a).

Assuming the same functional form as chosen by McGillis et al. (2001a), ($k_{660} = a + bU_{10n}^{n}$), a cubic least squares fit to the binned measurements was found to best describe the HiWASE transfer velocities (Table 4.3). A quadratic least squares fit

obtained nearly as high correlation with the measurements, but resulted in a negative intercept and systematically overestimated *k* in the well-sampled moderate wind speed range (7 to 12 m.s^{-1}). Both the quadratic and cubic fits are shown in Figure 1.2. The cubic fit to the results obtained by the "classical approach" described in this chapter is:

$$k_{660} = 5.3 + 0.034U_{10n}^3 \qquad (4.9)$$

A fit to the individual data gives a similar cubic relationship: $k_{660} = 7.62 + 0.034U_{10n}^3$. Due to the high variability of the data, the correlation of this fit is very low. A variable-exponent fit to the binned data ($k_{660} = a + bU_{10n}^n$) determined an exponent of 3.1. Using a different functional form, $k_{660} = bU_{10n}^n$, and a variable exponent determined an exponent of 2.8 (Table 4.3). These results give confidence that a cubic fit is the best representation of the wind speed dependence in the HiWASE CO_2 flux measurements. Eqn. (4.9) is similar to, but higher than the fit determined from the data of McGillis et al. (2001a; $k_{660} = 3.3 + 0.026\,U_{10n}^3$).

Uncertainty in the choice between a quadratic and cubic gas transfer dependence on wind speed leads to an uncertainty in the global CO_2 flux of the order 70% (Takahashi et al., 2002). Both quadratic and cubic wind speed relationships are capable of satisfying the global radiocarbon budget constraint (McGillis et al., 2001a). However, the results reported here are higher than those of McGillis et al. (2001a; 37% higher at a U_{10n} of 7 m.s^{-1}, 32% higher at 15 m.s^{-1}). Conditions at the measurement site, the influence of factors other than wind speed, such as seastate and bubbles, or measurement error, may explain this discrepancy.

Some proportion of the variability in *k* is due to the dependence of gas transfer on kinetic factors other than wind speed. Bubbles, primarily the result of wave breaking, have been shown to exert an influence on gas transfer by both providing an additional medium through which transfer can occur, and by disrupting the interfacial layer at the sea surface (e.g. Woolf, 1997). The concentration of bubbles near the surface, commonly described in terms of fractional coverage of whitecaps, *W*, is often found to scale as the cube of the wind speed (e.g., Monahan and Spillane, 1984).

As previously discussed in Chapter 1.4.3, a gas transfer model including a dependence on both wind speed and *W* was applied to a relatively small sample of open ocean whitecap measurements for which coincident, EC measurements of *k* were also available (Asher et al., 2002). The *W*-incorporating model agreed well with cubic wind

speed dependence of the measurements. However, the bubble-mediated exchange component of the model accounted for less than 25% of the total *k* at the wind speeds encountered (up to 16 m.s^{-1}), and is too small to explain the disparity between published quadratic and cubic wind speed based parameterisations of *k*. A different *k* model, incorporating wave-breaking effects via a fetch dependence, was tuned to encompass the spread of published parameterisations (Woolf, 2005), but this requires validation from simultaneous seastate and flux measurements. A preliminary examination of the seastate dependence of the HIWASE CO_2 flux measurements is presented in Appendix D.

Bubble-mediated gas exchange implies an inverse dependence of trace gas transfer on gas solubility (Woolf, 1997). EC field measurements of Dimethyl Sulfide (DMS) have shown a lower transfer velocity than is usually obtained from EC CO_2 flux measurements, as might be expected since DMS solubility is about an order of magnitude larger than for CO_2 (Huebert et al., 2010). Simultaneous flux measurements of trace gases with differing solubilities would improve understanding of bubble-mediated exchange.

Table 4.3. Coefficients of least squares fit to wind speed averaged transfer velocities. Coefficients calculated for the relationship $k_{660}av = a + bU_{10n}av^n$ in a least squares fashion, where $k_{660}av$ is the wind speed averaged (ΔU_{10n} = 1 m.s^{-1}) gas transfer velocity, normalised to $Sc = 660$ and $U_{10n}av$ is the mean wind speed in each bin. Parameter uncertainties are the standard error. The *r*-squared correlation has been calculated between the least squares fit and $k_{660}av$ (from Prytherch et al., 2010b). The two lines below the divider are fits to the HiWASE measurements without periods when the ship's Speed Over Ground (SOG) was greater than 2 m.s^{-1} and the lowest line is the fit to the functional form $k_{660}av = bU_{10n}av^n$ (Figure 4.5).

n	*a*	*b*	r^2	#
1	-45.3 ± 16.74	11.16 ± 1.54	0.77	3938
2	-9.66 ± 8.93	0.6 ± 0.057	0.87	3938
3	**5.29 ± 7.02**	**0.034 ± 0.003**	**0.90**	**3938**
4	14.49 ± 6.91	0.002 ± 0.0002	0.89	3938
Variable, n = 3.07 ± 0.6	*6.03 ± 9.7*	*0.028 ± 0.048*	*0.90*	*3938*
SOG < 2 m.s^{-1}, n = 3	**1.12 ± 11.54**	**0.033 ± 0.005**	**0.74**	**3393**
SOG < 2 m.s^{-1}, n = 3.79 ± 1.22	*7.63 ± 14.09*	*0.0034 ± 0.0119*	*0.76*	*3393*
$k_{660} = bU_{10n}^n$, ***n =2.82 ± 0.38***		***0.058 ± 0.061***	***0.90***	***3393***

4.6. Effect of ship steaming

The *Polarfront* spends the majority of its time on-station drifting with its main engines off. The ship steams back onto station when it has drifted away beyond a prescribed distance from Station Mike. Vibrations caused by the ship's engines and more violent ship motion when the ship is steaming at higher speeds may affect flux measurement and hence the effect on the HiWASE results due to removal of steaming periods was investigated. Periods were removed if the ship Speed Over Ground (SOG) was greater than 2 m.s^{-1} (n = 545, leaving 3393 measurements remaining in the analysis). The maximum wind speed of this reduced "HiWASE–SOG" dataset was 19.3 m.s^{-1}, and there were a total of 133 flux measurements at wind speeds over 15 m.s^{-1}.

The "HiWASE-SOG" measurements, binned by U_{10n} in 1 m.s^{-1} wide bins, are shown below in Figure 4.5. The least squares, cubic and variable exponent least squares fits (of the forms $k_{660} = a + bU_{10n}^{n}$ and $k_{660} = bU_{10n}^{n}$) to the two sets are shown in Figure 4.5, and the coefficients of the fits given in Table 4.3. Measurements with and without the SOG > 2 m.s^{-1} periods, binned in 2 m.s^{-1} wide bins, are shown in Figure 4.6, and the coefficients of the fits given in Table 4.4.

Removal of the periods when the *Polarfront* was steaming reduces the binned transfer velocities by approximately 18% at a wind speed of 7 m.s^{-1} and by 8% at a wind speed of 15 m.s^{-1} (2 m.s^{-1} wide bins, Figure 4.6). As for the full HiWASE dataset, the least squares fit to the HiWASE–SOG measurements suggests that a cubic dependence of transfer velocity on wind speed is more appropriate than a quadratic, and the relationship obtained from the measurements is again slightly higher than the cubic relationship obtained by McGillis et al., (2001a).

There is a small mean difference (approximately 3% for wind speeds $6 \le U_{10n} \le 20$ m.s^{-1}) between the least squares fits to the full HIWASE data set binned by either 1 m.s^{-1} or 2 m.s^{-1} wide bins. This difference can be ascribed to the variability in the HiWASE flux measurements. However, regardless of what bin width is selected, and whether or not ship-steaming periods are included, the HiWASE measurements show that an approximately cubic dependence of gas transfer on wind speed is more appropriate than a quadratic dependence.

Table 4.4. Coefficients of least squares fit to wind speed averaged transfer velocities. Coefficients calculated for the relationship $k_{660}av = a + bU_{10n}av^n$ in a least squares fashion, where $k_{660}av$ is the wind speed averaged ($\Delta U_{10n} = 2$ m.s^{-1}) gas transfer velocity, normalised to $Sc = 660$ and $U_{10n}av$ is the mean wind speed in each bin. Parameter uncertainties are the standard error. The *r*-squared correlation has been calculated between the least squares fit and $k_{660}av$. The two lines below the first divider are fits to the HiWASE measurements without periods when the ship's Speed Over Ground (SOG) was greater than 2 m.s^{-1} and the lowest line is the fit to the functional form $k_{660}av = bU_{10n}av^n$ (Figure 4.6).

n	*a*	*b*	r^2	#
n = 3	**4.42 ± 5.23**	**0.035 ± 0.002**	**0.98**	**3938**
n = 2.66 ± 0.33	*-0.51 ± 7.57*	*0.095 ± 0.092*	*0.98*	*3938*
SOG < 2 m.s^{-1}, n = 3	**0.99 ± 5.22**	**0.031 ± 0.002**	**0.97**	**3393**
SOG < 2 m.s^{-1}, n = 2.81 ± 0.42	*-1.32 ± 7.70*	*0.055 ± 0.067*	*0.97*	*3393*
$k_{660} = bU_{10n}^n$, ***n =2.68 ± 0.22***		***0.090 ± 0.057***	***0.98***	***3938***

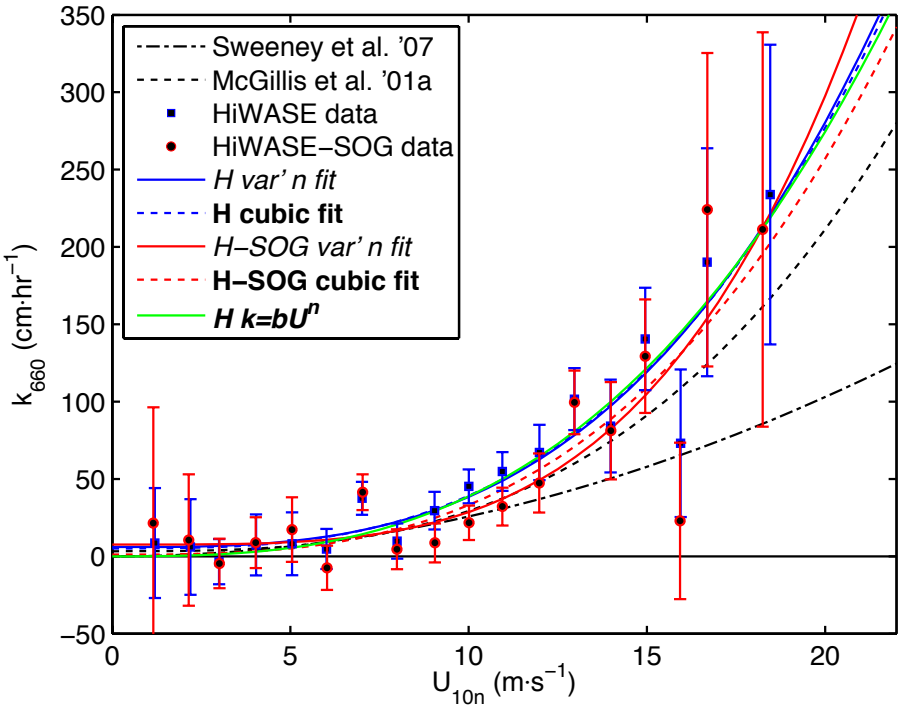

Figure 4.5. Transfer velocities (k_{660}) averaged against the 10 m neutral wind speed (U_{10n}) in 1 m.s^{-1} wide bins, error bars show the standard error of the mean. HiWASE data with (blue, *n* = 3938) and without (red, *n* = 3393) ship steaming periods (speed over ground (SOG) > 2 m.s^{-1}) are shown. Least squares fits to both sets of data, with either cubic (dotted line) or variable (solid line) exponents, are also shown. Also shown is the fit of the HiWASE data to the functional form $k_{660}av = bU_{10n}av^n$ (green line).

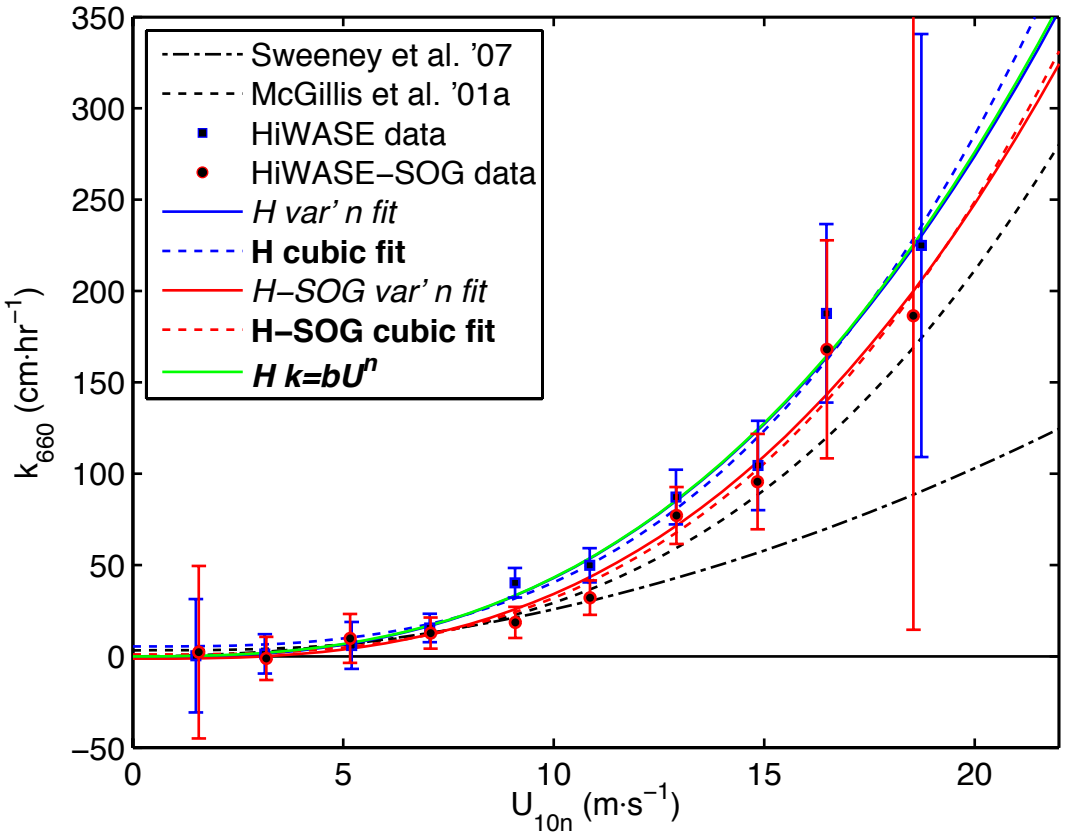

Figure 4.6. Transfer velocities (k_{660}) averaged against the 10 m neutral wind speed (U_{10n}) in 2 m.s^{-1} wide bins, error bars show the standard error of the mean. HiWASE data with (blue, n = 3938) and without (red, n = 3393) ship steaming periods (speed over ground (SOG) > 2 m.s^{-1}) are shown. Least squares fits to both sets of data, with either cubic (dotted line) or variable (solid line) exponents, are also shown. Also shown is the fit of the HiWASE data to the functional form $k_{660}av = bU_{10n}av^n$ (green line).

4.7. Summary, conclusions and implications

This chapter has described the HIWASE EC CO_2 flux and gas transfer velocity measurements. Details of the EC calculation used to obtain the measurements, including an analysis of the choice of averaging period and the uncertainty resulting from the density dilution correction is given in Section 4.2. The quality control procedures applied to the measurements are described in Section 4.3.

The measurements here form the largest reported set of directly measured air-sea CO_2 flux data obtained over the open ocean (Section 4.4, Figure 1.2). The data include measurements at higher open ocean wind speeds than have previously been obtained: 159 flux measurements were made at winds of over 15 m.s^{-1} (Table 4.2). A new parameterisation of the gas transfer velocity as a cubic function of neutral wind speed at

10 m has been determined (Section 4.5, Eqn. (4.9)). The measurements have a high degree of variability, and two of the 1m.s^{-1}-bin averages (at 7 and 16 m.s^{-1}) are not well represented by the cubic relationship. There are several significant sources of uncertainty in air-sea EC CO_2 flux measurements that may contribute to this variability. Humidity cross-sensitivity has been examined in the preceding Chapter 3. Other significant sources of uncertainty include the low signal to noise ratio, platform motion and flow distortion. These are examined in detail in this thesis in Chapters 5, 6 and 7 respectively.

5. Error analysis

5.1. Introduction

Air-sea EC flux measurements from moving platforms are subject to numerous sources of error. This thesis has addressed the three most significant sources in detail. Humidity cross-sensitivity of open path IRGAs was examined in Chapter 3, and a novel correction method was determined. The impact of platform motion on the wind vector, and the residual error following motion correction is examined in Chapter 6. Chapter 7 addresses the error resulting from airflow distortion caused by the *Polarfront's* superstructure. Other sources of error are addressed in this chapter. The accuracy of the various flux instruments used in HiWASE is examined in Section 5.2. The MotionPak measurements are not discussed here but the motion correction is examined in detail in Chapter 2 and Chapter 6. The sensitivity of the EC flux measurements to errors in the mean atmospheric measurements is examined in Section 5.3. A method for estimating the uncertainty of an individual flux measurement is described in Section 5.4.1. An estimate of the uncertainty in the latent heat and CO_2 fluxes using simultaneous flux measurements is described in Section 5.4.2.

Open path IRGAs are subject to an error due to deformation of the sensor head caused by motion of the instrument (Section 5.5). A method to quantify and correct for the effect of deformation is described in Section 5.5.2, and the results of applying the correction to the HiWASE measurements are shown in Section 5.5.3.

Further sources of error affecting air-sea EC flux measurements are discussed in Section 5.6, and their magnitude relative to the other errors considered in this thesis is discussed. Finally, the various sources of error discussed in this chapter are summarized in Section 5.7.

5.2. Instrument accuracy

For the Sonic and IRGA used for flux measurement during HiWASE, the instrument manufacturer's stated accuracies and resolutions are shown in Table 5.1. The high accuracy of the wind velocity measurements suggest that any measurement uncertainty will be substantially less than error resulting from platform motion (Chapter 6) or flow distortion (Chapter 7) effects. The resolution of the pressure sensor is similar in magnitude to the signal that might be expected from vertical movement of the sensors

due to wave induced ship motion (vertical motion of up to approximately 10m, Chapter 6). The low resolution means that the pressure sensor may not resolve the turbulent pressure variations due to profiling. The likely impact of this is discussed in Section 5.3.

The eddy covariance technique relies on a cross-correlation average. For HiWASE, this was a 20-minute average of 20 Hz measurements. The cross-correlation significantly reduces the impact of the random uncertainty of any individual measurement. However, over the ocean, the flux of CO_2 can be very small, and the turbulent fluctuations in CO_2 concentration can be of similar size to the measurement accuracy, leading to a poor signal to noise ratio. The ratio of the IRGA measurement accuracy to the mean standard deviation of CO_2 and H_2O concentration measured during HiWASE is shown in Table 5.2. The inherent measurement error of the IRGA is approximately 30% of the typical standard deviation of the CO_2 concentration. This signal to noise problem is especially apparent at low wind speeds, where the measurement error is more than 60% of the typical CO_2 variation. The variation in the CO_2 concentration becomes larger with wind speed and ΔpCO_2 and hence the flux measurement becomes more robust. The focus of HiWASE was on higher wind speeds, and no attempt was made to quantify factors that may influence low wind speed fluxes such as convection and surfactants. Hence, the low wind speed (less than approximately 5 $m.s^{-1}$) CO_2 flux measurements should be treated with caution.

For H_2O, the typical concentration variability relative to instrument accuracy is much larger than for CO_2. Even at low wind speeds, measurement accuracy is only a few percent of the concentration variability, and thus, the instrument's accuracy is not expected to significantly affect the latent heat flux measurement.

Without significant improvements in sensor technology, the poor signal to noise ratio of air-sea EC CO_2 flux measurements will remain a significant obstacle in determining appropriate parameterisations. Lengthy experiments making numerous measurements to reduce the uncertainty, as was the approach of HiWASE, are not always practical and involve significant cost.

The accuracy of an individual flux measurement is dependent on the length of the averaging period of the measurement as well as on the instrument accuracy. Estimates of the accuracy of HiWASE EC CO_2 flux measurements are discussed in Section 5.4.1.

Table 5.1. Principal components of the HiWASE turbulent flux instrumentation and, where given, the manufacturer's stated accuracies and resolutions for the measured parameters.

Instrument	Measurement	Accuracy (RMS)	Resolution
Sonic	Wind speed	< 1%	0.01 $m.s^{-1}$
	Direction	< ± 1°	1°
	Speed of sound	< ± 0.5%	0.01 $m.s^{-1}$
IRGA	CO_2 density	0.0061 $mmol.m^{-3}$	-
	H_2O density	0.0047 $g.m^{-3}$	-
	Air pressure	± 1.5%	1 mb

Table 5.2. Mean ratio (%) of the IRGA's specified accuracy to the standard deviation of the 20-Hz measurements in each 20-minute HiWASE flux average. Analysis performed on quality-controlled measurements obtained in 2006 at the stated wind speed ranges.

Measured parameter	IRGA noise ratio (%) for given wind speed (U_{10n}) range				
	ALL	0-5 $m.s^{-1}$	5-10 $m.s^{-1}$	10-15 $m.s^{-1}$	15-20 $m.s^{-1}$
n	492	26	208	256	2
H_2O	2.7	3.8	3.3	2.4	2.1
CO_2	29.5	63.0	31.7	26.8	16.2

5.3. Sensitivity analysis

5.3.1 Error in mean temperature and humidity

The determination of EC latent heat, sensible heat and CO_2 fluxes requires measurement of the fluctuations of air temperature and the mixing ratios of humidity and CO_2 respectively. These quantities were not measured directly in the HiWASE experiment but were instead each derived from measurements of sonic temperature, H_2O and CO_2 concentration and air pressure made by the fast response instrumentation. The "direct" method employed in HiWASE is described in Section 4.2.2, Eqns. (4.3), (4.4) and (4.5). As the air temperature and mixing ratio calculations are affected by mean changes in the measured humidity, pressure, and temperature, the scalar fluxes are also dependent on the mean of these measurements. In order to estimate the magnitude of the flux uncertainty resulting from errors in the mean of the fast response inputs, it is necessary to estimate the size of the possible mean error. This is accomplished by comparing the mean of the fast response scalar measurements to those obtained from the mean meteorology instrumentation (described in Section 2.2.4) on *Polarfront*.

For air temperature, the mean bias between the fast response mean air temperature and the minute-mean meteorology air temperature measurement was 1.2 ± 1.5 K and the RMS difference was 1.7 ± 0.9 K. For specific humidity, the mean bias between the fast response measurement and the mean meteorology measurement was -0.04 ± 1.06 $g.kg^{-1}$ and the RMS difference was 0.6 ± 0.8 $g.kg^{-1}$.The mean sensors are positioned approximately 4 m below the height of the instruments on the foremast. A small portion of the difference in measured values between the mean and foremast instruments (up to approximately 0.1 K and up to approximately 0.05 $g.kg^{-1}$) may be due to the profiles of the atmospheric quantities (see discussion of profiling effects in Appendix E).

Results of a sensitivity analysis of the scalar flux measurements are shown in Table 5.3. Here the fast response input values were changed by either a multiplying factor determined by the ratio of the biases given above to the mean value (e.g.: mean temperature bias of 1.2 K, mean air temperature of 283.5 K, multiplying factor of 0.5%), or by a constant representing the likely maximum mean offset. The values used are stated in the table. The calculated fluxes were then compared with fluxes obtained without changes to the inputs. The quality control procedures applied to the flux measurements use some fixed limits, and hence the number of measurements available in each analysis varies.

To avoid iteration in the calculation, the temperature input change was applied to the sonic temperature measurement rather than the air temperature measurement. The changes to the input temperature resulted in changes to the sensible heat fluxes (calculated with and without the PKT correction) of approximately one percent, and changes to the latent heat and CO_2 fluxes of less than one percent (Table 5.3).

Similarly, to avoid introducing iterations the humidity input change was applied to the input H_2O concentration instead of to the specific humidity. The mean moist air density during HiWASE was approximately 1.2 $kg.m^{-3}$. Hence, a specific humidity of 1 $g.kg^{-1}$ will be approximately equivalent to an H_2O concentration of 1.2 $g.m^{-3}$. The input H_2O concentration was modified with an offset of ± 0.6 $g.kg^{-1}$. This offset is a significant fraction of the mean H_2O concentration measured during HiWASE, which was typically less than 10 $g.kg^{-1}$. The change in mean H_2O concentration caused only minor variation in the latent heat, sensible heat and CO_2 fluxes. It caused larger changes in the PKT corrected fluxes, particularly the CO_2 flux, where the increase in H_2O concentration resulted in an increase in the flux of 3.8 ± 15.9 % (Table 5.3). The change

in humidity used in the sensitivity analysis was deliberately at the high end of what is plausible for an error in the mean fast response humidity measurement. There does not appear to be an overall directional bias between the fast response and mean meteorology humidity measurement: overall, during HiWASE, the fast response – mean meteorology mean humidity difference was -0.04 ± 1.06 $g.kg^{-1}$. If this value is applied as an offset, it results in a change in the PKT CO_2 flux of -0.2 ± 1.6 %.

5.3.2 Pressure measurement

The 20 Hz air pressure is measured using a pressure sensor supplied with the IRGAs positioned inside the IRGA electronics boxes. The electronic boxes are not airtight and are positioned on the *Polarfront's* foremast. Fast response air pressure is used to determine moist and dry air densities, and hence the mixing ratios of H_2O and CO_2 using the direct method (Eqns. (4.1) to (4.3)).

The fast response pressure sensor has a low resolution (1 mb; Table 5.1). In addition, high frequency pressure fluctuations may be damped by the location of the sensor inside a box. Turbulent pressure fluctuations over the ocean are routinely assumed to be insignificant in EC flux calculations. However, recent results reported by Miller et al. (2010) suggest that pressure fluctuations due to height changes resulting from ship motion can be significant. If the ship motion-induced pressure variations are uncorrelated with vertical wind, then they will not lead to a flux as the cross-correlation of the CO_2 measurements with w in the EC calculation acts to filter out random noise. However pressure fluctuations induced by ship motion may be partially correlated with the vertical wind due to flow distortion effects, incomplete motion correction, or real wind-wave correlations (e.g.: Hristov et al., 2003). Miller et al. show that for extreme vertical motion of 10 m, the approximately 1 mb change in pressure can induce changes in CO_2 mixing ratio of approximately 0.4 ppm (assuming a background concentration of 380 ppm), similar in size to the true atmospheric fluctuations of CO_2.

During HiWASE, the vertical motion experienced at the *Polarfront's* foremast with beam-on winds was typically of the order 1 m (Chapter 6), implying a typical heave induced pressure variation of 0.1 mb. For typical conditions during HiWASE (U_{10n} = 10 $m.s^{-1}$, mean C_{H2O} = 6.5 $g.m^{-3}$, mean C_{CO2} = 15.5 $mmol.m^{-3}$, mean T = 285 K, mean P = 1019 mb,) the change in CO_2 mixing ratio caused by a 0.1 mb change in pressure is approximately 0.05 ppm, an order of magnitude smaller than the standard deviation of CO_2 mixing ratio in a 20-minute sample (typically 0.5 ppm).

The sensitivity of the HiWASE scalar fluxes to pressure variation was examined by subtracting the mean pressure from the pressure measurements, and increasing the residual fluctuations by a factor of two. The low resolution of the sensor means that the resulting fluctuations are large, 2 mb or more. The resulting change in the heat fluxes was minor, though the effect on the CO_2 (9.7 ± 25.4%) and the PKT corrected CO_2 (8.5 ± 71.7 %) fluxes was larger (Table 5.3), demonstrating some sensitivity to pressure variations of the EC CO_2 fluxes as first observed by Miller et al. (2010).

A low EC CO_2 flux sensitivity to pressure variation was found in an earlier experiment. The previous experiment was carried out on *RRS Discovery* and observed only a slight (order of 1 %) sensitivity of the fluxes to an increase in the pressure variations by a factor of five (pers. comm. Dr M. J. Yelland, NOCS). The pressure sensor used in this test measured at approximately 1 Hz, and had a resolution of greater precision than 0.1 mb. This result suggests that the pressure fluctuations are not strongly correlated with the fluctuations in the vertical wind speed component.

If the ship motion-induced pressure signal caused significant variation in the CO_2 mixing ratio, then there would be a strong signal in the CO_2 spectra at the frequencies associated with platform motion. Whilst some variation is observed in the HiWASE CO_2 spectra at these frequencies, it is not large, and the cospectra at these frequencies are dominated by the signal resulting from either incomplete platform motion correction or wave induced wind fluctuations (see the detailed spectral analysis of the HiWASE measurements in Chapter 6). The motion frequency signal in the CO_2 spectra may result from sensor head deformation, and is reduced by the correction procedure described in Section 5.5.

Pressure was also measured using an instrument inside the *Polarfront's* laboratory (not sealed). This instrument measured pressure as a one-minute mean value. The sensor was located approximately 5 m below the height of the foremast, and hence a 0.5 mb offset might be expected between the two sensors. The RMS difference between the foremast and laboratory pressure sensors was 2.5 ± 0.3 mb. The sensitivity of the scalar fluxes to a mean offset in the pressure of ± 3 mb was found to be very small, less than 0.5 % for all fluxes (Table 5.3).

5.3.3 *Summary*

Overall, the sensitivity of the HiWASE EC flux measurements to errors in the mean temperature and humidity measurements is small. The sensitivity of the PKT corrected fluxes is larger, but, for realistic estimates of the mean errors, the sensitivity error is substantially less than that from other sources such as platform motion (Chapter 6).

Recent results by Miller et al. (2010) suggest that heave induced pressure fluctuations could have a significant impact on EC CO_2 fluxes, and have not been accounted for in previous EC experiments. However, this assumes that the profiling pressure fluctuations are correlated with the vertical wind fluctuations, which may not be the case. The low resolution of the fast response pressure sensor used in HiWASE may mean that heave induced variations in pressure are not accurately determined. There is good agreement between HiWASE fluxes calculated using either the direct determination of mixing ratio or the Webb et al. (1980) density correction (Chapter 4). However, the Webb et al. (1980) density correction as applied to the HiWASE fluxes (and in all previous studies) does not include a term to account for the density dilution effect resulting from pressure fluctuations. Calculation of this pressure term would require a more accurate determination of the turbulent covariance of the pressure and vertical wind than is possible with the sensors used during HiWASE.

It is not possible to accurately quantify the flux error resulting from ship motion induced pressure changes using the instrumentation available in HiWASE. However, the likely effect on the CO_2 measurements, based on the typical vertical motion experienced at the *Polarfront's* foremast, is small. Additionally, a strong platform motion frequency signal is not observed in the HiWASE CO_2 spectra (Chapter 6), suggesting that heave induced pressure fluctuations are not a significant source of error in the HiWASE CO_2 flux measurements.

Table 5.3. Sensitivity of HiWASE EC fluxes to a mean change in the input measurements. The mean ratio (%) of the difference between the modified and unmodified fluxes to the unmodified flux is shown for each flux, uncertainties are standard deviation. Analysis performed on measurements obtained in 2006 at wind speeds $6 \le U_{10n} \le 16$ m.s^{-1}. Small fluxes (heat fluxes smaller than 5 W.m^{-2} or CO_2 fluxes smaller than 5 mol.m^{-2}.yr^{-1}) have been removed from the analysis.

Input and change	***n***	**Resulting fractional (%) change to EC flux**				
		F_r	F_T	$F_{T\ PKT}$	F_C	$F_{C\ PKT}$
$T_s \times 100.5\%$	202	-0.1 ± 0.0	-0.1 ± 0.1	0.0 ± 0.0	-0.1 ± 0.2	-0.3 ± 1.8
$T_s \times 99.5\%$	193	0.1 ± 0.0	0.1 ± 0.1	0.0 ± 0.1	0.1 ± 0.2	0.4 ± 1.6
$T_s + 2$ K	198	-0.2 ± 0.0	-1.0 ± 0.3	-0.7 ± 0.2	0.1 ± 0.7	-0.2 ± 1.6
$T_s - 2$ K	190	0.2 ± 0.0	1.0 ± 0.3	0.7 ± 0.1	-0.1 ± 0.7	0.4 ± 2.4
$C_{H_2O} \times 100.7\%$	201	0.7 ± 0.0	-0.1 ± 0.2	0.0 ± 0.1	-0.1 ± 0.3	0.0 ± 0.6
$C_{H_2O} \times 99.3\%$		-0.7 ± 0.0	0.1 ± 0.2	0.0 ± 0.1	0.1 ± 0.3	0.0 ± 0.3
C_{H_2O} + 0.6 g.m^{-3}	190	0.1 ± 0.2	-0.1 ± 0.0	-0.3 ± 0.6	0.0 ± 0.1	3.8 ± 15.9
C_{H_2O} – 0.6 g.m^{-3}	197	-0.1 ± 0.2	0.1 ± 0.0	0.3 ± 0.5	0.0 ± 0.1	-1.3 ± 12.5
$dP \times 2$	184	-0.4 ± 0.6	0.0 ± 0.2	0.4 ± 1.0	9.7 ± 25.4	8.5 ± 71.7
$P + 3$ mb	203	0.0 ± 0.0	0.4 ± 0.1	0.3 ± 0.1	0.0 ± 0.2	0.0 ± 0.2
$P - 3$ mb	203	0.0 ± 0.0	-0.4 ± 0.1	-0.3 ± 0.2	0.0 ± 0.2	0.1 ± 0.8

5.4. Flux measurement uncertainty

5.4.1 Flux measurement statistical uncertainty

The random sampling uncertainty in an individual EC flux measurement is primarily dependent on the length of the averaging period used to determine the flux. This section uses the simple method described by Fairall et al. (2000) to estimate the sampling uncertainty in the HiWASE CO_2 flux measurements. Various other different methods for estimating the sampling uncertainty in land based EC measurements are described in the review by Billesbach (2011).

The sampling uncertainty in an EC flux of quantity x, ΔF_x (described in detail in Fairall et al., 2000, and summarised here), can be expressed as:

$$\Delta F_x = \Delta\left(\overline{w'x'}\right) \approx \frac{\sigma_w \sigma_x}{\left(T_{per} / \tau_i\right)^{1/2}} \qquad (5.10)$$

where σ_w and σ_x are the standard deviations of the vertical wind velocity and the variable x in question, T_{per} is the length (s) of the averaging period and τ_i is the integral time scale for velocity fluctuations, defined by Fairall et al. (2000) as:

$$\tau_i \approx 12z/U \tag{5.11}$$

where U is wind speed. Note that the true value of the integral time scale is uncertain.

For infrared measurement of atmospheric components such as CO_2, the analysis by Fairall et al. (2000) assumes that σ_x is primarily dependent on: surface flux variability; atmospheric processes uncorrelated with surface exchange; and random internal sensor noise at the integral time scale. If the last two factors are considered negligible, then the fractional uncertainty can be estimated as:

$$\frac{\Delta F_x}{F_x} \approx \frac{3\sigma_w/u_*}{\left(UT_{per}/12z\right)^{1/2}} \tag{5.12}$$

In near neutral conditions, the quantity σ_w/u_* will be approximately equal to 1.2 (e.g.: Stull, 1988). Again, this derivation relies on numerous assumptions (and when first derived by Wyngaard, 1973, was described as "reckless") and is highly uncertain.

During HiWASE the averaging period was 20 minutes and the measurement height was approximately 14.5 m. Therefore, for a wind speed of 10 $m.s^{-1}$, the sampling uncertainty in each EC flux measurement can be estimated from Eqn. (5.6) as approximately 43%. For a wind speed of 15 $m.s^{-1}$, the uncertainty is approximately 35% and at 20 $m.s^{-1}$ the uncertainty is 31%. The high sampling uncertainty in each measurement demonstrates the requirement for long-term experiments with high numbers of observations when making air-sea EC CO_2 flux measurements.

In practice, numerous experimental factors affect the choice of averaging period. For example: the period must be short enough to ensure stationarity is a reasonable approximation (Section 5.6); the period must be short enough to minimize the number of bad measurements lost due to ship maneuvering; and the period must be long enough to minimize the amount of flux loss. The choice of a 20-minute period is a compromise between these competing factors and is discussed further in Chapter 4.

5.4.2 *Comparison of scalar fluxes from two IRGAs*

For the majority of the HiWASE experiment, one of the two foremast IRGAs operated with a shroud in place. The shroud sealed the instrument from the environment in order to determine corrections for the effect of sensor head deformation (Section 5.5). The shrouds were usually alternated between the two IRGAs during port visits. For relatively brief periods during HiWASE, both IRGAs were operated unshrouded. There were approximately 51 days during HiWASE in which the *Polarfront* was at Station Mike, both IRGAs were unshrouded and all instrumentation required for flux measurement were operational.

Comparison of the simultaneous flux measurements from the two, independent IRGAs provides a means of estimating the measurement uncertainty in the latent heat and CO_2 fluxes. The variability of the ratio of the simultaneous flux measurements from the two instruments is a measure of the inherent measurement uncertainty in the fluxes. The spatial separation of the two IRGA sensors is about 1 m. The separation may cause the two sensors to measure different turbulence (e.g.: Nilsson et al., 2010; Section 5.6), though this effect will reduce with increasing wind speed. The same Sonic unit measures the wind vector used with each of the IRGA's output for flux measurement.

Following quality control, 22 CO_2 flux measurements made simultaneously by the two IRGAs were available (a, Figure 5.1). The measurements were made in conditions of low to moderate wind speed ($3 \le U_{10n} \le 14$ m.s^{-1}) and strong air-sea ΔpCO_2 (> 50 µatm). The CO_2 fluxes are reasonably correlated, $r^2 = 0.78$, and the correlation is significant at the 99% level. Following the application of the PKT correction, the correlation between the measurements from the two sensors is reduced: $r^2 = 0.25$. The correlation is significant at the 95% level (two sided $p = 0.018$). The increased variability from use of the PKT correction is unsurprising since the correction introduces additional noise to the flux measurements, and is dependent on both the fast response humidity measurements and the humidity flux, also measured by the IRGAs (Chapter 3). The mean difference between the two sets of PKT flux measurements is not statistically significant at the 95 % level (paired Student's t-test, $p = 0.21$). Note that the results of the correlation and paired confidence tests must be treated with caution due to the small sample size.

Despite the small sample size, the results shown in a, Figure 5.1 suggest that there is some correlation in the humidity cross sensitivity error exhibited by the two sensors. A linear regression of the PKT flux measurements has a similar slope to a

regression of the non-PKT measurements (a, Figure 5.1), suggesting that the PKT corrections has not significantly altered the mean relationship between the measurements from the two sensors, but has reduced the large transfer velocities believed to be due to humidity cross-sensitivity.

The same comparison was made for latent heat fluxes. Latent heat fluxes were calculated during HiWASE using both the EC and ID techniques. Less stringent quality control procedures are required for latent heat fluxes (i.e.: no requirement for strong air-sea CO_2 concentration difference) and there were 32 latent heat fluxes measured simultaneously with the two IRGAs (b, Figure 5.1). The correlation of both the EC and ID latent heat fluxes was higher than for the CO_2 fluxes: EC $r^2 = 0.98$, ID $r^2 = 0.94$. Both correlations are significant at the 99% level. Both the significantly stronger air-sea humidity signal and the greater number of measurements in the analysis can explain the better agreement of the latent heat fluxes, relative to the CO_2 fluxes.

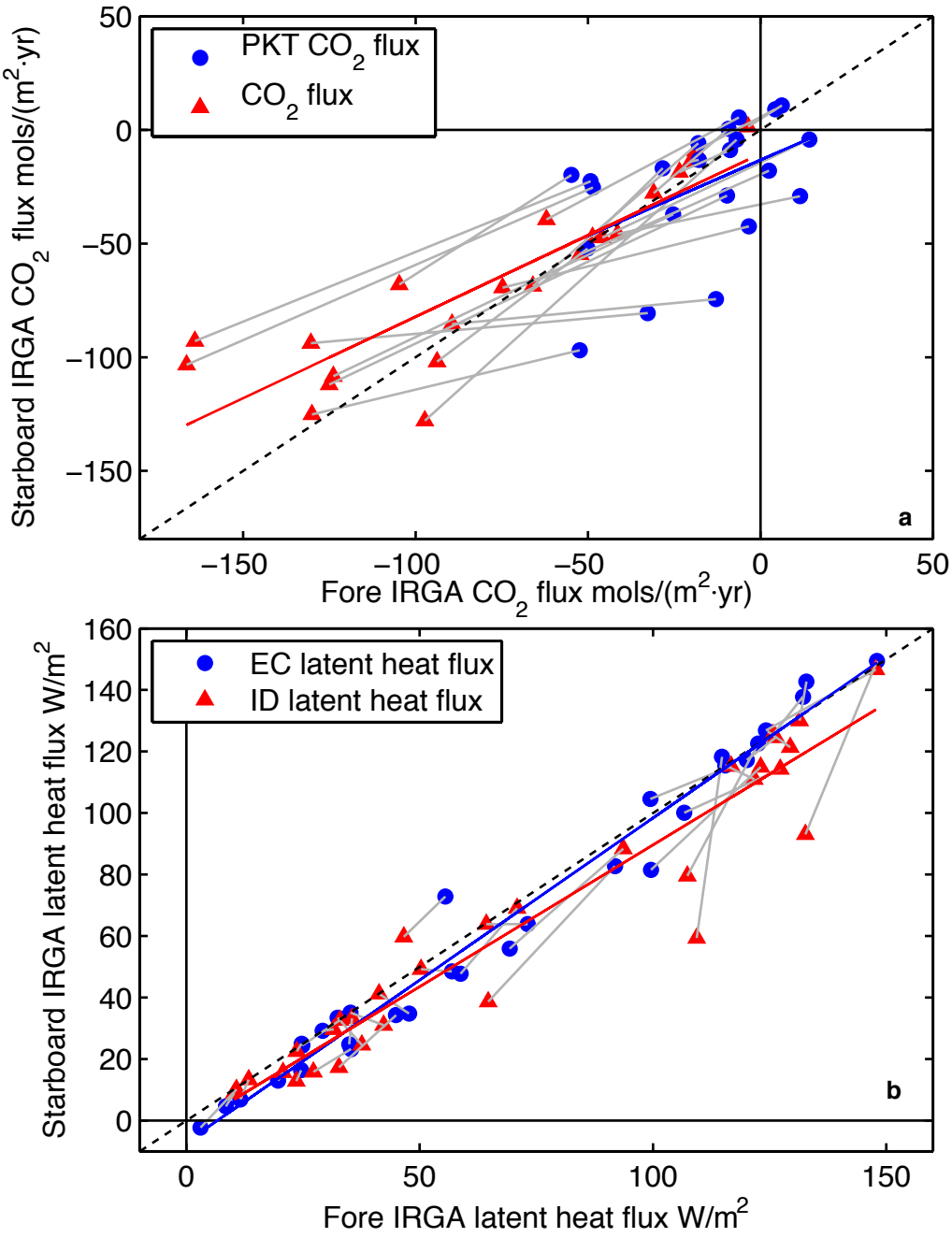

Figure 5.1. Scalar fluxes measured simultaneously with the fore and starboard IRGAs onboard *Polarfront*. a) EC CO_2 flux measurements (n = 22) with (blue circles) and without (red triangles) the PKT correction. b) Latent heat flux measurements (n = 32) made using the EC (blue circles) and ID (red triangles) techniques. The grey lines indicate simultaneous measurements with the different techniques, blue and red lines are linear regressions of the respective data.

5.5. IRGA head deformation

5.5.1 Introduction

Experiments conducted at the beginning of HiWASE found that the LICOR 7500 IRGAs, used for fast response measurement of CO_2 and H_2O are sensitive to both motion of the instrument and to the angle that the instrument is oriented with respect to the vertical. The sensor head is attached to the body of the instrument by three aluminium rods. These rods deform slightly in response to a force across them, which leads to an erroneous signal.

The head deformation error, and a simple method to reduce it, has been described in an earlier publication (Yelland et al., 2009). This section will review the correction method, and present the results of applying the correction to the HiWASE measurements.

5.5.2 Correction method

To determine the head deformation correction, the IRGAs were operated with a shroud in place in order to seal the instrument from the environment. The shroud enabled a "null" measurement to be obtained from the instrument that was used to derive the coefficients of a correction to be applied to the instrument's measurements when unshrouded. During HiWASE, one of the two IRGAs on the *Polarfront's* foremast was typically operating shrouded, though there were also a few limited periods where both instruments were operated unshrouded (Section 5.4.2). The shroud was usually swapped between the two IRGAs during port visits. The regular swapping of the shroud allowed a time varying correction to be determined for each sensor. The shrouds were intended to be installed such that they did not touch the sensor head itself and affect the measurement. However, the shrouds were often fitted in non-ideal circumstances and the quality of the fitting is uncertain.

The concentration measurements output by the IRGAs, $C_{CO2}meas$ and $C_{H2O}meas$, are assumed to be a combination of a "true" constituent concentration C_{CO2} and C_{H2O}, and platform motion in the x and y planes:

$$C_{CO_2}meas = C_{CO_2} + a_1 \times \ddot{x}_{obs} + a_2 \times \ddot{y}_{obs} \tag{5.13}$$

and

$$C_{H_2O}meas = C_{H_2O} + b_1 \times \ddot{x}_{obs} + b_2 \times \ddot{y}_{obs} \quad (5.14)$$

where $\ddot{x}_{obs}$ and $\ddot{y}_{obs}$ are the platform accelerations measured by the MotionPak accelerometers in the bow-stern and port-starboard directions respectively. With the IRGA shrouded, for each 20-minute flux measurement period, the coefficients a_1, a_2, b_1 and b_2 can be determined by multiple linear regressions between the "null" output of the shrouded sensor and the MotionPak accelerometer output.

Example coefficient values determined for the fore IRGA during a 20 day shrouded period are shown in Figure 5.2. Values for the starboard IRGA during a different shrouded period are shown in Figure 5.3. The mean of the coefficient values from each shrouded period was used to determine a correction that could be applied to the sensor when unshrouded. The coefficients determined during HiWASE for both IRGAs are shown in Table 5.4 and Table 5.5. The unshrouded IRGA measurements were corrected with the coefficients determined during the shrouded period that was closest in time.

The head deformation effect for a particular sensor may vary with time due to weakening of the IRGA struts. The variation of the coefficients from period to period was typically small relative to the uncertainty in the coefficients.

Replacement of the IRGA unit in use led to the largest changes in coefficients. Details of instrument installation and changes during the HiWASE experiment are given in Chapter 2 and the metadata report (Moat et al., 2010). The fore IRGA was initially the unit with serial number 1114. In September 2007 (DOY 249) this unit was replaced with the IRGA with serial number 1264. This unit was lost in February 2008 and unit 1114 was reinstalled. The coefficients obtained when the 1264 sensor was installed (Table 5.4) are markedly different to those from the 1114 sensor. The coefficients obtained late in 2008 from the 1114 sensor are similar to the values obtained from the sensor earlier in the experiment.

The unit that was initially installed as the starboard IRGA was serial number 1113. In September 2008 (DOY 246) this unit was replaced with serial number 825. As was the case for the fore IRGA, the measured coefficients (Table 5.5) vary only slightly between the periods when 1113 was installed but change more significantly after unit 825 is installed. The internal chemicals of both IRGAs were changed during HiWASE. The chemicals in the fore IRGA were changed in mid 2008 (DOY 163) and the chemicals in the starboard IRGA were changed in September 2007 (DOY 249). The changing of the internal chemicals did not lead to significant changes in the measured

coefficients. The variation in the mean head deformation correction coefficients thus appears to be primarily dependent on which IRGA unit is used. Variation in the mean coefficients from a single unit with time is typically within one standard deviation of the mean, thus there was no significant variation in the coefficients over time.

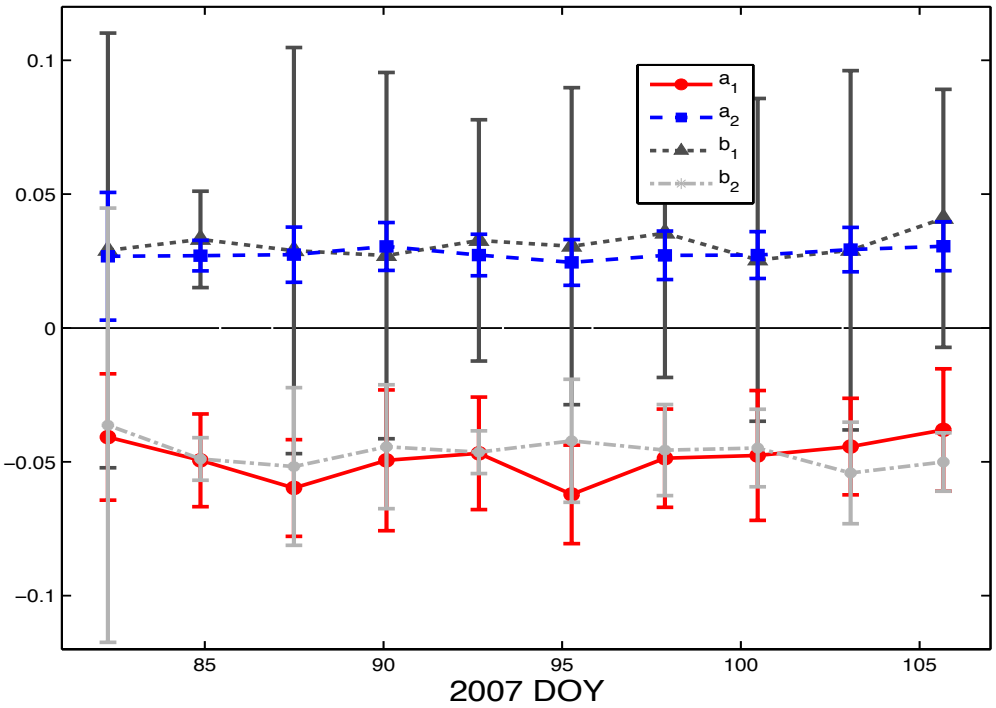

Figure 5.2. IRGA head deformation coefficients (Eqns. (5.13) and (5.14)). Coefficients are obtained from the fore IRGA (serial number 1114) during a shrouded period in 2007. Outliers (values more than 3 standard deviations from the coefficient mean) have been removed. Uncertainties shown are ± 1 standard deviation.

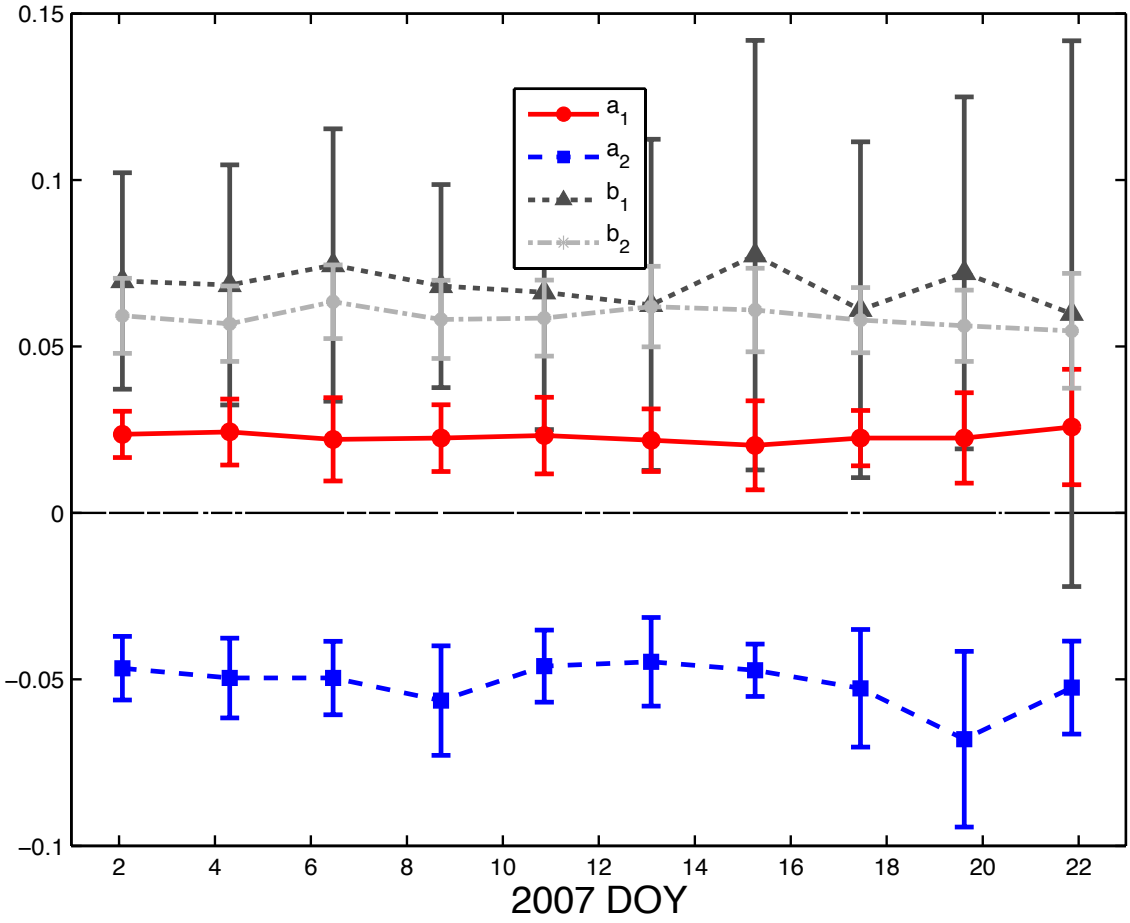

Figure 5.3. IRGA head deformation coefficients (Eqns. (5.13) and (5.14)). Measurements obtained from the starboard IRGA (serial number 1113) during a shrouded period in 2007. Outliers (values more than 3 standard deviations from the coefficient mean) have been removed. Uncertainties shown are ± 1 standard deviation.

Table 5.4. Head deformation correction coefficients (used in Eqns. (5.13) and (5.14)) determined for the fore IRGA. Coefficients were obtained from a regression of platform accelerations and concentration measurements from the fore IRGA during periods in which the instrument was shrouded. Uncertainties are standard deviation. Periods for which the coefficients are obtained from, and applied to, are given as day of year. Bold indicates when a different IRGA unit was used (serial number 1264, in place of serial number 1114).

Obtained from	a_1	a_2	b_1	b_2	**Applied to**
2006 278:304	-0.049 ± 0.012	0.004 ± 0.006	0.051 ± 0.025	-0.051 ± 0.006	251:319
334:359	-0.047 ± 0.026	0.005 ± 0.008	0.048 ± 0.040	-0.032 ± 0.009	320:09
2007 25:50	-0.046 ± 0.009	0.011 ± 0.008	0.037 ± 0.045	-0.056 ± 0.009	10:65
81:106	-0.049 ± 0.022	0.028 ± 0.011	0.031 ± 0.060	-0.047 ± 0.03	66:121
142:153	-0.054 ± 0.033	0.019 ± 0.011	0.048 ± 0.145	-0.075 ± 0.034	122:177
192:218	-0.058 ± 0.068	0.011 ± 0.018	0.020 ± 0.138	-0.055 ± 0.024	178:228
280:301	**0.006 ± 0.018**	**-0.018 ± 0.014**	**0.102 ± 0.039**	**0.016 ± 0.011**	**254:317**
339:354	**0.000 ± 0.000**	**0.000 ± 0.000**	**0.000 ± 0.003**	**0.000 ± 0.002**	**318:365**
2008 278:293	-0.044 ± 0.010	0.020 ± 0.010	0.032 ± 0.034	-0.073 ± 0.010	251:297

Table 5.5. Head deformation correction coefficients (used in Eqns. (5.13) and (5.14)) determined for the starboard IRGA. Coefficients were obtained from a regression of platform accelerations and concentration measurements from the starboard IRGA during periods in which the instrument was shrouded. Uncertainties are standard deviation. Periods for which the coefficients are obtained from, and applied to, are given as day of year. Bold indicates when a different IRGA unit was used (serial number 825, in place of serial number 1113).

Obtained from	a_1	a_2	b_1	b_2	**Applied to**
2007 1:22	0.023 ± 0.012	-0.051 ± 0.016	0.068 ± 0.050	0.059 ± 0.012	251:99
113:123	0.026 ± 0.026	-0.048 ± 0.019	0.054 ± 0.095	0.088 ± 0.015	100:149
177:186	0.024 ± 0.091	-0.047 ± 0.039	0.065 ± 0.372	0.089 ± 0.058	150:228
306:321	0.028 ± 0.016	-0.041 ± 0.029	0.056 ± 0.067	0.065 ± 0.039	253:365
2008 250:273	**-0.082 ± 0.031**	**-0.029 ± 0.019**	**0.242 ± 0.106**	**0.053 ± 0.025**	**250:365**

5.5.3 Results of applying the head deformation correction

The head deformation correction was shown to reduce the variability in an initial data set of "null" fluxes measured by the shrouded IRGAs (Yelland et al., 2009). The correction also reduces the variability of the complete set of null HiWASE fluxes (Figure 5.4). Applying the head deformation correction reduces the mean of the null latent heat fluxes from 2.2 $W.m^{-2}$ to 1.68 $W.m^{-2}$, and reduces the variability by 10%. The head deformation correction reduces the variability of the null CO_2 fluxes by 3%, though increases the mean from 53.6 $mols.m^{-2}.yr^{-1}$ to 55.8 $mols.m^{-2}.yr^{-1}$. The remaining variability in the shrouded flux measurements may result from instrument noise or air leaks in the shrouds. The PKT correction (Chapter 3) is dependent on the latent heat flux, and hence has not been applied to the shrouded CO_2 flux measurements. The IRGA sensor lenses are not always cleaned before shrouding and as such, the shrouded measurements are also subject to a possible humidity cross-sensitivity error from salt contamination.

When applied to unshrouded measurements, the head deformation correction results in a slight reduction in the humidity and CO_2 variance spectra (Figure 5.5). As would be expected for an error relating to instrument motion, the reduction is apparent

at frequencies associated with wave and ship motion, approximately 0.08 Hz to 0.25 Hz (Chapter 6).

The air-sea latent heat flux is large relative to the CO_2 flux, and the head deformation correction has only a small effect on the humidity cospectra (Figure 5.5) and the latent heat flux. HiWASE EC latent heat flux measurements with and without the head deformation correction applied are very similar (r^2 = 0.99: Figure 5.6). The head deformation correction slightly reduces the mean difference between, and the variability of the ratio of the HiWASE EC latent heat fluxes to a bulk estimate (Smith, 1988) from 0.86 ± 0.39 to 0.87 ± 0.37.

The air-sea CO_2 signal is typically much smaller than the humidity signal, and the effect of the head deformation correction on the CO_2 cospectra is larger. There is significant variation in the cospectra at the frequencies affected (Figure 5.5). The PKT corrected CO_2 cospectra shows increased variation following head deformation correction due to the iterative nature of the correction and the dependence on latent heat flux measurements.

Gas transfer velocities calculated from PKT corrected CO_2 flux measurements, with and without the head deformation correction applied are shown in Figure 5.7. The measurements are binned by wind speed, and the bins are averages of the 3775 measurements from both the head deformation corrected and non-head deformation corrected data sets that were passed by the quality control procedures. Gas transfer measurements without the head deformation correction applied are smaller than those that are corrected, and at high wind speeds, when the effect of head deformation is greater, have an unrealistic, negative dependence on wind speed. The variability of the measurements without the head deformation correction applied is approximately 7% higher than the variability of the corrected gas transfer velocities.

5.5.4 Head deformation discussion

The head deformation corrections make a large difference to the CO_2 flux measurements. If the corrections are not applied then the HiWASE gas transfer measurements are physically unrealistic at high wind speeds (> 12 $m.s^{-1}$; Figure 5.7). The high sensitivity to head deformation in the high wind speed measurements reduces the confidence that can be placed in these measurements. The uncertainty in the head deformation correction coefficients (Table 5.4 and Table 5.5) will contribute to the uncertainty in the transfer velocity measurements. The coefficients determined for a particular sensor do not vary significantly with time. Hence, a more sophisticated

correction could be determined in a laboratory test, instead of the in situ method used in HiWASE. This will be investigated in future work (Chapter 8).

The HiWASE IRGAs are oriented differently with respect to the *Polarfront*. The starboard IRGA is rotated 90° to starboard about its vertical axis, with respect to the fore IRGA. This orientation difference may in part explain the difference in the correction coefficients determined from two instruments. This was suggested by the initial testing used to determine the correction (Yelland et al., 2009) but requires confirmation. If IRGA measurements from moving platforms have a dependence on the orientation of the IRGAs with respect to the direction of motion, there are important implications. In addition to challenges when comparing results from two or more instruments that may be oriented differently to one another, issues arise when attempting to determine the influence of factors with relative wind direction dependence. For example a sensor may measure a difference between a "fore" effect and a "beam" effect that may be the result of sensor head deformation.

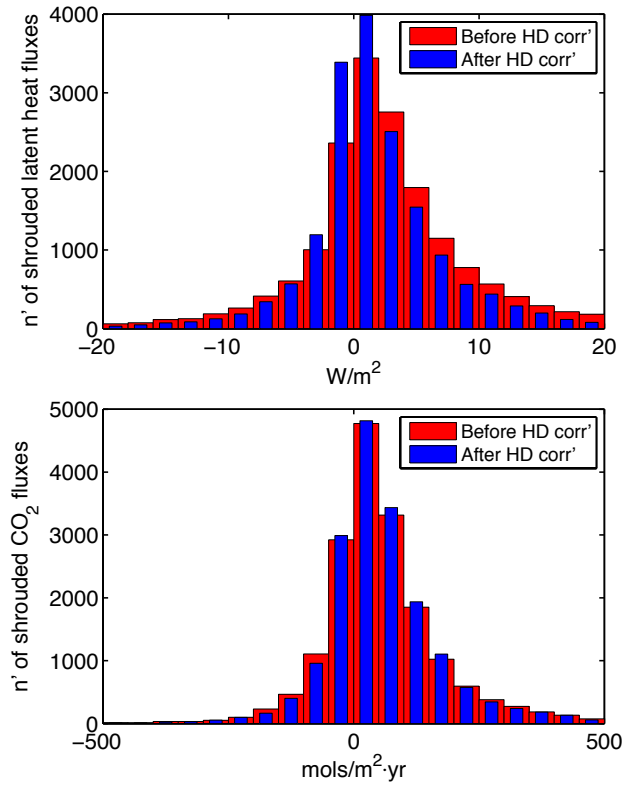

Figure 5.4. Histograms of HiWASE EC latent heat (top panel, n = 17,489) and CO_2 (bottom panel, n = 18,272) fluxes, measured using shrouded IRGAs. Measurements with (blue) and without (red) application of the head deformation correction are shown. Outliers (latent heat fluxes outside ± 20 $W.m^{-2}$ and CO_2 fluxes outside ± 500 $mols.m^{-2}.yr^{-1}$) have been removed.

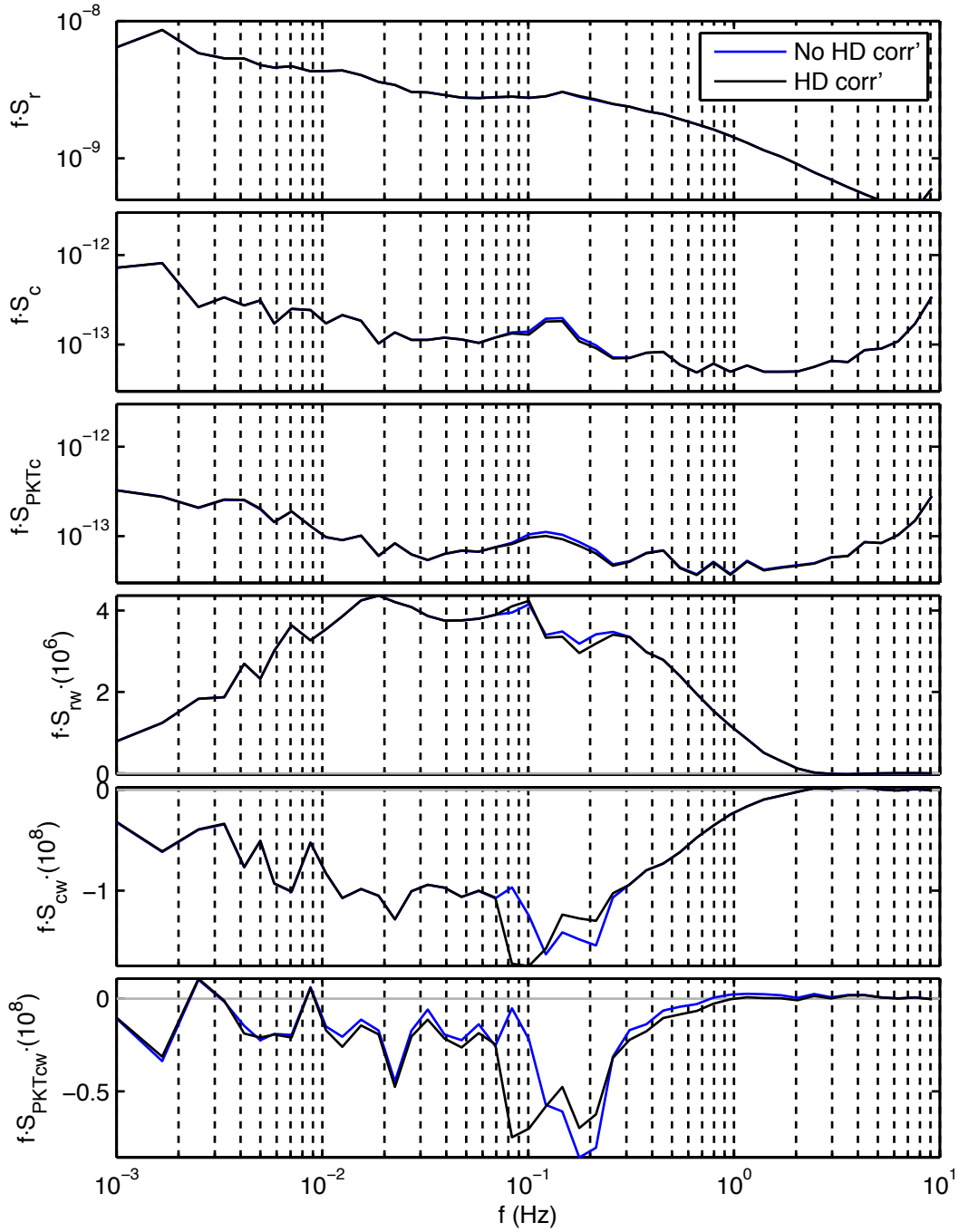

Figure 5.5. Averaged, absolute 20-minute spectra and cospectra with (black line) and without (blue line) head deformation correction. Spectra are an average of 309 measurements made with the fore IRGA at wind speeds of $10 \leq U_{10n} \leq 12$ m.s^{-1}. Measurements have been corrected for platform motion.

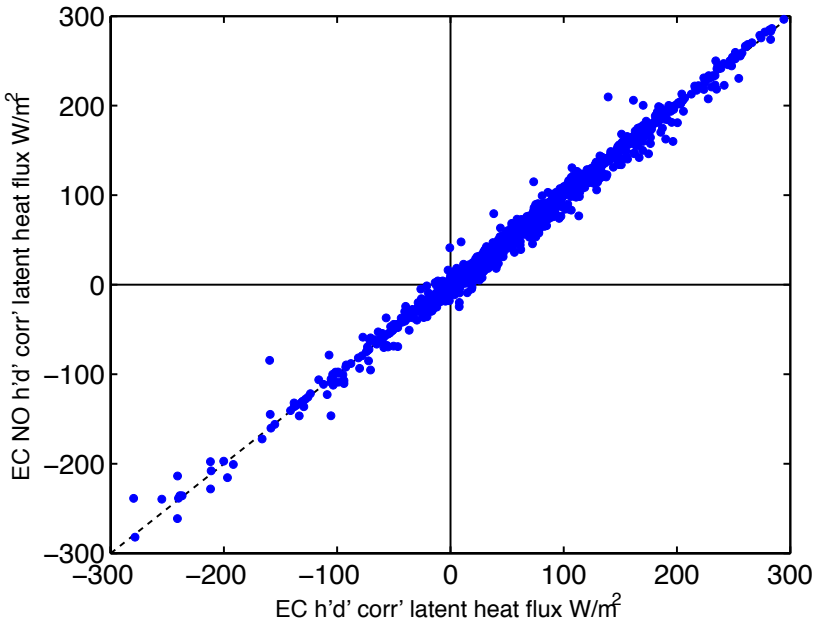

Figure 5.6. HiWASE EC latent heat fluxes, with (x-axis) and without (y-axis) head deformation correction applied. 11,375 quality controlled measurements are shown, r^2 = 0.99.

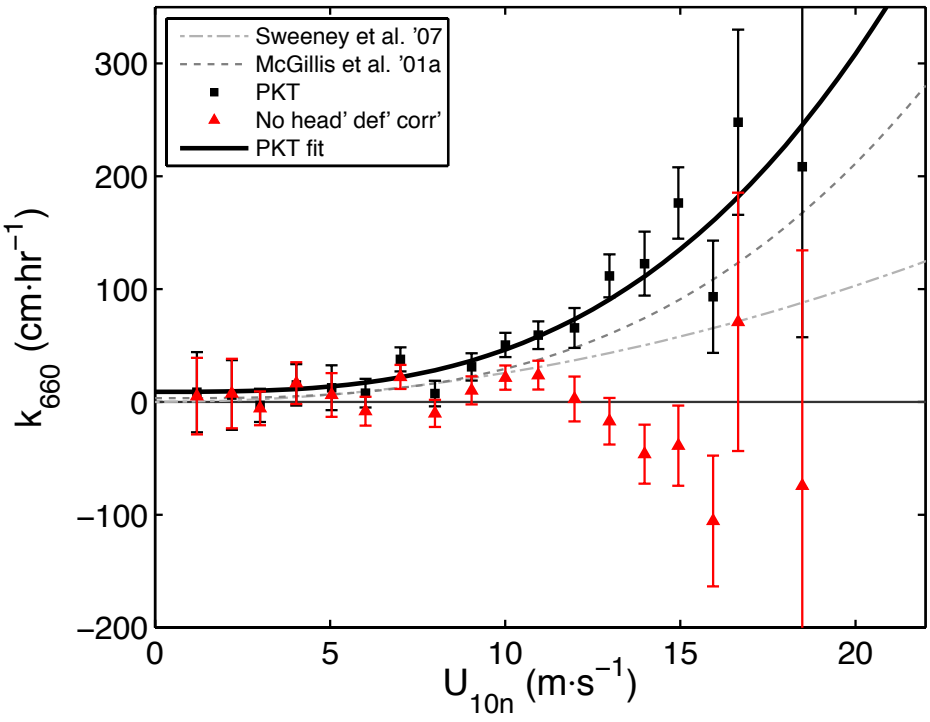

Figure 5.7. Transfer velocities (k_{660}) averaged against the 10 m neutral wind speed (U_{10n}) in 1 ms^{-1} bins, error bars show the standard error of the mean. Gas transfer to wind speed relationships shown are as indicated in the key. The 3775 periods that passed quality control of both the PKT and non-head deformation corrected data sets are included.

5.6. Other sources of error

There are numerous sources of error that must be considered when making air-sea EC trace gas flux measurements. The reviews of Businger (1986) and Fairall et al., (2000) list many of these sources. This thesis examines the most significant sources in detail: humidity cross-sensitivity in Chapter 3; platform motion in Chapter 6; and flow distortion in Chapter 7. The uncertainty relating to density variation from heat and moisture fluxes (Webb et al., 1980), and errors from time delay between sensors and sensor time response are discussed in Chapter 4. Possible errors from vertical profiling of the sensors caused by platform motion are discussed briefly in Appendix E.

This chapter has addressed the flux uncertainty due to instrument noise, sampling error, as well as an additional source of measurement error caused by head deformation under acceleration of the IRGA sensor. There are several other potential sources of error, which will be discussed here.

During HiWASE, fast response H_2O and CO_2 concentration was determined from infrared absorption. Band broadening effects can cause absorption measurement errors. This effect is automatically corrected for by the internal processing of the IRGAs (LI-COR, 2004). Similarly, the error caused by crosswinds on the determination of temperature from speed of sound measurement is automatically corrected for by the Sonic's internal processing (Gill Instruments Ltd, 2004).

Uncertainty in the alignment between wind instrument and the motion-measuring instrument introduces errors into air-sea flux measurement (Brooks, 2008). A 1° error in the roll alignment has been shown to result in a 3.7% error in momentum flux measurement. Errors from pitch and yaw offsets were found to be smaller. The effect on scalar fluxes would presumably be smaller due to the dependence of the flux on only one component of the wind vector. The HIWASE instrument alignments are detailed in Prytherch et al., (2010c). The alignments were generally determined to accuracies better than 1°, and thus any resulting error can be considered small. Uncertainty in the position offset between the anemometer and motion instrument will also introduce a flux error. To reduce the uncertainty in the momentum flux resulting from position offsets to within the accuracy of the Sonic's wind speed measurements (0.01 $m.s^{-1}$), it is necessary to determine instrument offsets to an accuracy of approximately 6 cm (Brooks, 2008). This is readily achieved in HiWASE due to the close proximity of the flux sensors.

Solar insolation and heat from the sensor's internal electronics can cause an artificial sensible heat flux within the measurement volume of open path IRGAs (e.g.: Burba et al., 2008). This sensible heat flux leads to dilution of the air density (i.e.: Webb et al., 1980) that is not accounted for by a correction derived from temperature measurements from a separate instrument (i.e.: the Sonic). The temperature gradient across the instrument is expected to be highest in daytime, but will also be present in nighttime due to the increased cooling of the upper sensor head, which does not contain significant amounts of electronics relative to the instrument body. Direct measurement of this effect requires careful temperature measurement within the averaging path of the IRGA and was not performed during HiWASE. Experiments over land have found that this effect can lead to underestimation of CO_2 fluxes by ~ 19%. This effect would presumably decrease with higher wind speeds when the air parcels spend less time within the IRGA measurement volume. Overall, HiWASE gas transfer velocities measured in daytime (defined as 07:12-16:48 GMT) were 7% lower than nighttime (defined as 19:12-04:48 GMT) values measured at wind speeds in the range $6 \le U_{10n} \le 16$ m.s^{-1}. Daytime latent heat fluxes were on average 5% lower and sensible heat fluxes were 2% lower than nighttime values. Future work will examine the effects of the diurnal cycle on the flux measurements in more detail using shortwave radiation measurements made onboard *Polarfront*.

The presence of surfactants has been observed in laboratory experiments to lead to reductions in measured gas transfer velocity of up to 60% (Bock et al., 1999). Measurements in the open ocean have found surfactants resulting from, for example, biological processes, suppressing the formation of microscale waves and hence reducing friction velocity and gas transfer (Frew et al., 2004). The effect of surfactants is expected to be most important in low wind conditions. Low wind flux measurements will also be affected by diurnal warming of the ocean, leading to significant convection and buoyancy fluxes. McGillis et al. (2004) observed an increase of 40% in nighttime CO_2 flux measurements over daytime fluxes due to the loss of upper ocean stratification and deeper convective mixing with nighttime cooling. The measurements reported by McGillis et al. (2004) were at a mean wind speed of 6.0 m.s^{-1} with a standard deviation of 1.3 m.s^{-1}. At higher winds, diurnal warming effects are minor, but may contribute to the small difference between HiWASE daytime and nighttime fluxes discussed above. HiWASE was focused on moderate and high winds and did not attempt to measure surfactants or convective processes. This, and the low signal to noise ratio at low winds

(Section 5.2) means that the low wind speed measurements in HiWASE are treated with caution.

Over the ocean, stationarity is commonly assumed to hold for periods of up to around one hour. A recent EC experiment in light (1-11 $m.s^{-1}$) winds (Miller et al., 2009) found that 75% of its flux measurements, calculated from 13.7 minute averages, failed criteria for stationarity (Foken and Wichura, 1996). Jacobs et al. (2002b) examined the effect of non-stationarity of CO_2 concentration using a one –dimensional model and a varying water side CO_2 concentration. The results suggested that the primary effect of non-stationarity in the CO_2 field was to increase the flux variability (explaining approximately 50% of the scatter observed in the model results), but that there might also be a bias. The bias was found to decrease with wind speed, causing measured transfer velocities to be overestimated by ~ 13% at U_{10n} = 6 $m.s^{-1}$ and 2% at U_{10n} = 14 $m.s^{-1}$. Note that this modeling experiment used EC fluxes calculated from 55-minute averages. The high number of flux measurements obtained in HIWASE and the focus on higher wind speeds has enabled the selection of a relatively short averaging period, which will reduce the effect on the fluxes of non-stationarity of the wind and CO_2 fields. Wind field non-stationarity would also affect the momentum fluxes. The ID momentum fluxes are in very good agreement with bulk estimates, whilst the variation observed in the EC momentum fluxes is shown to be mainly due to signal at the frequencies associated with platform motion (Chapter 6 and 7).

The spatial separation of scalar flux instrumentation (i.e.: the Sonic and IRGAs) causes an attenuation of the measured flux due to the loss of correlation between the sensors at small eddy scales. The effect of sensor separation on air-sea scalar flux measurements is estimated to lead to flux loss of order 3% for a sensor seperation of 0.3 m, dependant on the relative positions of the sensors and the relative wind direction (Nilsson et al., 2010).

Overall, frequency response errors (i.e.: digital sampling, time response, filtering, sensor separation and scalar path averaging in the measurement volume of the IRGAs) are estimated to cause uncertainties of 5-30% in EC flux measurements (e.g.: Burba and Anderson, 2007). The impact of these errors will typically be higher for low wind speeds. The reasonable agreement between the HiWASE cospectra and idealized cospectral curves (Chapter 6; Kaimal et al., 1972) suggests that the effect of frequency response errors on the HiWASE fluxes is small.

The errors discussed in this section are small relative to the size of the other errors examined in more detail, and to the sampling uncertainty. Biases resulting from the errors discussed here cannot be ruled out, but are assumed to be negligible.

5.7. Error analysis summary

This chapter has examined the errors affecting air-sea EC flux measurements not covered in the Chapters on humidity cross-sensitivity (Chapter 3), platform motion (Chapter 6) and flow distortion (Chapter 7).

The accuracy of the flux instrumentation used during HiWASE was examined in Section 5.2. The accuracy of the CO_2 measurement by the IRGAs, and the low CO_2 concentration over the ocean, leads to a very low signal to noise ratio. At winds less than 5 $m.s^{-1}$ the measurement uncertainty of the IRGA is larger than half the mean standard deviation of the CO_2 measurements made during HiWASE. The ratio improves with increasing wind speed, but sensor noise is significant (> 10% standard deviation) at all wind speeds. Noise in the scalar measurements will not contribute to the flux unless it is correlated with the vertical wind speed fluctuations.

The HiWASE scalar fluxes are dependent on calculations of mixing ratios and air density. Hence, they are dependent on the mean of the atmospheric quantities measured, as well as the fluctuations. A comparison was made of the differences between the humidity, temperature and pressure measurements used in the flux calculations and those from other instruments onboard *Polarfront* in order to determine an estimate of the mean uncertainty in these measurements. The determined uncertainty was used in a sensitivity analysis to examine possible biases in the flux measurements from errors in the mean measurements (Section 5.3). Overall, the humidity, CO_2 and temperature fluxes were found to be insensitive to mean changes, with resulting flux changes of order 1% or less. Use of the PKT correction increased the sensitivity of the flux changes to mean changes in humidity, particularly for CO_2. However, for realistic mean temperature errors, the resulting change in the PKT CO_2 flux was small (< 1 %).

Recent experimental results (Miller et al., 2010) have demonstrated that there may be a heave induced pressure variation error in EC CO_2 flux measurements that has not been previously accounted for. The pressure component of the Webb et al. (1980) density correction had not been applied in any previous EC experiments. Miller et al. directly determine CO_2 mixing ratio from a closed path system and a high-resolution pressure sensor, and hence do not quantify the error that may result from omission of

vertical ship motion-induced pressure fluctuations. The resolution of the pressure sensor used to correct measurements of CO_2 and H_2O concentration is low relative to the likely size of pressure fluctuations (Section 5.3.2) and it is not possible to directly quantify any error in the HiWASE measurements that may result. However, an analysis of the HiWASE spectra and cospectra (Chapter 6), and estimates of the change in CO_2 mixing ratio due to the typical vertical motion experienced on *Polarfront*, suggests that any motion-induced pressure effect is small. In addition, pressure effects may not be correlated with fluctuations in the vertical wind speed component and therefore may not contribute to the flux.

A method for estimating the statistical uncertainty in a flux measurement is described in Section 5.4.1. The estimate of uncertainty is a function of the averaging time of the measurement and is dependant on several assumptions. The uncertainty in a 20-minute flux measurement can be estimated as ~ 43%. An examination of simultaneous flux measurements made by the two IRGAs used in HiWASE was also made (Section 5.4.2). For flux measurements of both CO_2 and humidity, a statistically significant correlation was observed between the measurements from the two sensors.

The humidity and CO_2 fluxes measured by the IRGAs are subject to an error caused by deformation of the sensor head (Section 5.5). A simple correction, determined by alternately operating one of the IRGA with a shroud (Yelland et al., 2009), was applied to the HiWASE measurements. The correction was found to slightly reduce the variability of both the shrouded "null" fluxes and the measured H_2O and CO_2 fluxes. The majority of this reduction occurs in the range of frequencies associated with platform motion. The correction coefficients were found to be dependent on the sensor used and the orientation of the sensor with respect to the vessel. Not applying the correction to the CO_2 fluxes results in physically unrealistic transfer velocities at wind speeds above approximately 12 $m.s^{-1}$. The head deformation effect has important implications for all ship based experiments using the LICOR-7500 IRGA. The head deformation for a particular sensor was found not to change significantly with time, suggesting that improved corrections could be determined from laboratory tests (see future work, Chapter 8).

Other sources of error affecting EC flux measurements were discussed in Section 5.6, including instrument alignment, sensor heating and stationarity. These errors were shown to be small relative to the errors examined elsewhere in this thesis (i.e.: humidity cross-sensitivity, platform motion and flow distortion).

6. Platform motion

6.1. Introduction

Measurement of air-sea fluxes via the EC technique relies on accurate determination of the vertical fluctuations in wind velocity. If measurements are made at sea from moving platforms such as buoys or research ships, measurements of all three components of the wind velocity will include a signal caused by the motion of the measurement platform. This motion may be due to wave effects, wind buffeting of the platform, or deliberate maneuvering of the platform.

For the majority of its time at Station Mike, *Polarfront* operated with its main engines off. Data when the vessel was steaming at more than 2 $m.s^{-1}$ are removed during quality control procedures. The largest source of platform motion is thus expected to be from wave-induced movement of the vessel. The wave-induced signal in air-sea flux measurements from moving platforms can be significant, dwarfing the true signal (e.g.: Edson et al., 1998; Miller et al., 2008).

This chapter describes the effects of platform motion on the HiWASE air-sea EC fluxes. Measurements of the wave field at Station Mike, obtained with the *Polarfront's* Ship Borne Wave Recorder (SBWR), will be described, and are shown to have the same frequency range as a large signal apparent in the (uncorrected for motion) wind spectra and cospectra (Section 6.2). This signal is thus ascribed to be due to platform motion.

The measured wind speed data are corrected for the effects of platform motion in post-processing using a method based on a widely-used technique (Section 6.3; described in more detail in Chapter 2: Edson et al., 1998). The correction results in a significant reduction in the wave induced signal but some signal does remain. The cause of this residual signal may be either incomplete removal of the platform motion signal by the correction procedure, or it may be a real signal resulting from wind-wave interactions (Section 6.4.1). The residual signal is also apparent in cospectra reported in other EC experiments on moving platforms (e.g.: Miller et al., 2008; McGillis et al., 2001a).

The magnitude of the residual platform motion signal is shown to be dependent on relative wind direction (Section 6.4.2). Note that standard quality control procedures as applied to all of the HiWASE air-sea fluxes shown in the chapter (described in Chapter 4) remove measurements with mean relative wind directions less than 60° or

greater than 340° (bow-on = 180°; these limits are for the fore IRGA. For the starboard IRGA, the limits are 90° and 340°). Winds and waves onto the *Polarfront's* bow result in a greater range of motion at the foremast than do winds onto the ship's beam due to the wave induced motion of the ship about its centre of gravity. A simple correction to remove the residual wave scale signal through modification of the cospectra is described and applied to the PKT corrected CO_2 fluxes (Section 6.4.4).

Here and throughout this thesis, spectral and cospectral energy densities are commonly shown multiplied by frequency. For a graph of spectral energy density, multiplied by frequency and plotted against logarithmic frequency ($f \cdot S_x$ vs. $\log f$), the area under the curve between any pair of frequencies is proportional to the variance (for spectra) or the flux (for cospectra) contained in that range of frequencies. The spectra and cospectra are often shown here as averages of several observational periods, with the spectral densities binned by frequency.

6.2. Wave measurement

Wave induced platform motion for a vessel such as the *Polarfront* would be expected to occur at the frequency of the dominant waves. Non-directional wave field measurements were obtained onboard *Polarfront* from a Ship Borne Wave Recorder (SBWR; Section 2.2). The wave spectra measured with the *Polarfront* SBWR have spectral peaks at approximately 0.09 Hz and a range of wave motion from approximately 0.05 to 0.3 Hz (Figure 6.1). For clarity, this frequency range will be referred to here as the wave scale.

The SBWR utilizes two sets of water pressure and vertical acceleration measurements. The acceleration measurements are used to estimate ship heave. The ship heave is determined at the ship's centre of gravity. Hence, the heave measured by the SBWR may be smaller than that experienced at the bow (the location of the flux instrumentation and the MotionPak), particularly when bow-on to the waves. The ship is approximately 50 m long and will have limited motion response to waves shorter than this when the direction of wave motion is bow-on (although the pressure sensors do obtain higher frequency information). The ship is about 10 m wide. The SBWR pressure sensors remove the effects of roll.

For a fully developed wind-sea, the expected peak frequency of the wave spectra, f_p, can be estimated using the semi-empirical Pierson-Moskowitz (PM)

spectrum (Pierson and Moskowitz, 1964). Minor development of the original PM spectral equation allows f_p to be estimated directly from U_{10} (Tucker and Pitt, 2001: page 100):

$$f_p = {}^{0.47g}\!/\!_{\pi U_{10}} \tag{6.1}$$

The PM spectrum predicts a wave spectra peak at approximately 0.2 Hz for U_{10} = 6.5 m.s^{-1} and at approximately 0.1 Hz for U_{10} = 13 m.s^{-1}. The PM spectrum variation with wind speed is shown in Figure 6.1.

The spectral peak in SBWR data is seen at lower frequencies than predicted by Eqn. (6.1), suggesting that the SBWR measurements are of mixed sea conditions and the lower frequency waves may include components of swell (Figure 6.1). Additionally, the wave field at Station Mike (and in general in the open ocean; Tucker and Pitt, 2001) is unlikely to be fully developed. Greater variation of the SBWR spectral level with wind speed occurs at high frequencies, suggesting a stronger influence of wind-sea at these frequencies. The SBWR does not correct for the ship speed through the water, and so the measured frequency may be modified relative to the wave frequency. Periods when the ship speed over ground was greater than 2 m.s^{-1} have been removed from the analysis.

Except at the lowest wind speeds, there is substantially more wave energy in the SBWR measurements when the mean wind direction is onto the *Polarfront's* bow than when it is 10° aft of the starboard beam (the most frequently occurring relative wind direction, Section 2.3). This can be explained at least in part by the *Polarfront's* standard operating procedure when on-station. When on-station the ship drifts beam-on to the mean wind. The ship orientates bow-on only when the combination of wind and wave induced ship motion becomes too uncomfortable for the crew. There is therefore an artificial selection of stronger wave motion for a given wind speed in periods when the *Polarfront* is bow-on to the wind.

The SBWR measurements described here do not include a correction to account for the ship's response to wave motion. Initial analysis of the SBWR measurements showed that application of the ship response correction to the *Polarfront* measurements led to estimates of significant wave height, *Hs*, which were too large by 10-20% (Clayson, 1997). In other experiments in which an SBWR was used and the ship response correction was applied, such as on *RRS Discovery*, the most significant effect

of the correction on the SBWR spectra was to increase the spectral shoulder at about 0.2 Hz by up to a factor of 2. A similar correction would not explain the difference between the bow-on and beam-on wave spectra measured onboard *Polarfront*.

Platform motion spectra derived from MotionPak measurements are shown in Figure 6.2. All three components of motion show a large signal with a peak between 0.1 and 0.2 Hz. The vertical component of platform motion shows a signal between 0.06 and 0.3 Hz, corresponding closely to the wave scale observed in the independent SBWR measurements. The peak of the fore-aft and vertical platform motion spectra is at a higher frequency than the spectral peak of the SBWR measurements (Figure 6.1). This may be a result of the bow located MotionPak having greater response to the higher frequency wind sea. Unlike the MotionPak, the SBWR's accelerometers are located approximately at the ship's centre of gravity, and are not affected by pitch.

The MotionPak platform motion spectra are substantially higher for bow-on winds than for other relative wind directions. The placement of the MotionPak on the foremast of the *Polarfront*, far forward of the ship's centre of gravity, means it is subject to a greater range motion for waves onto the ship's bows than for waves onto the beams. The effect of relative wind direction on the motion correction procedure of the EC fluxes is discussed in Section 6.4.2.

Directional wave spectra were measured onboard *Polarfront* by a WAVEX wave radar system (Chapter 2.2). It was not possible to fully analyse the WAVEX measurements in time to include them in this thesis, but an initial analysis suggests that the local wave field almost always consists of more than one wave system. There is typically a combination of swell, old wind sea (generated locally but no longer wind driven due to a change in wind direction and/or a decrease in wind speed) and wind driven sea (pers. comm. T. Palmer, NOCS, 2011).

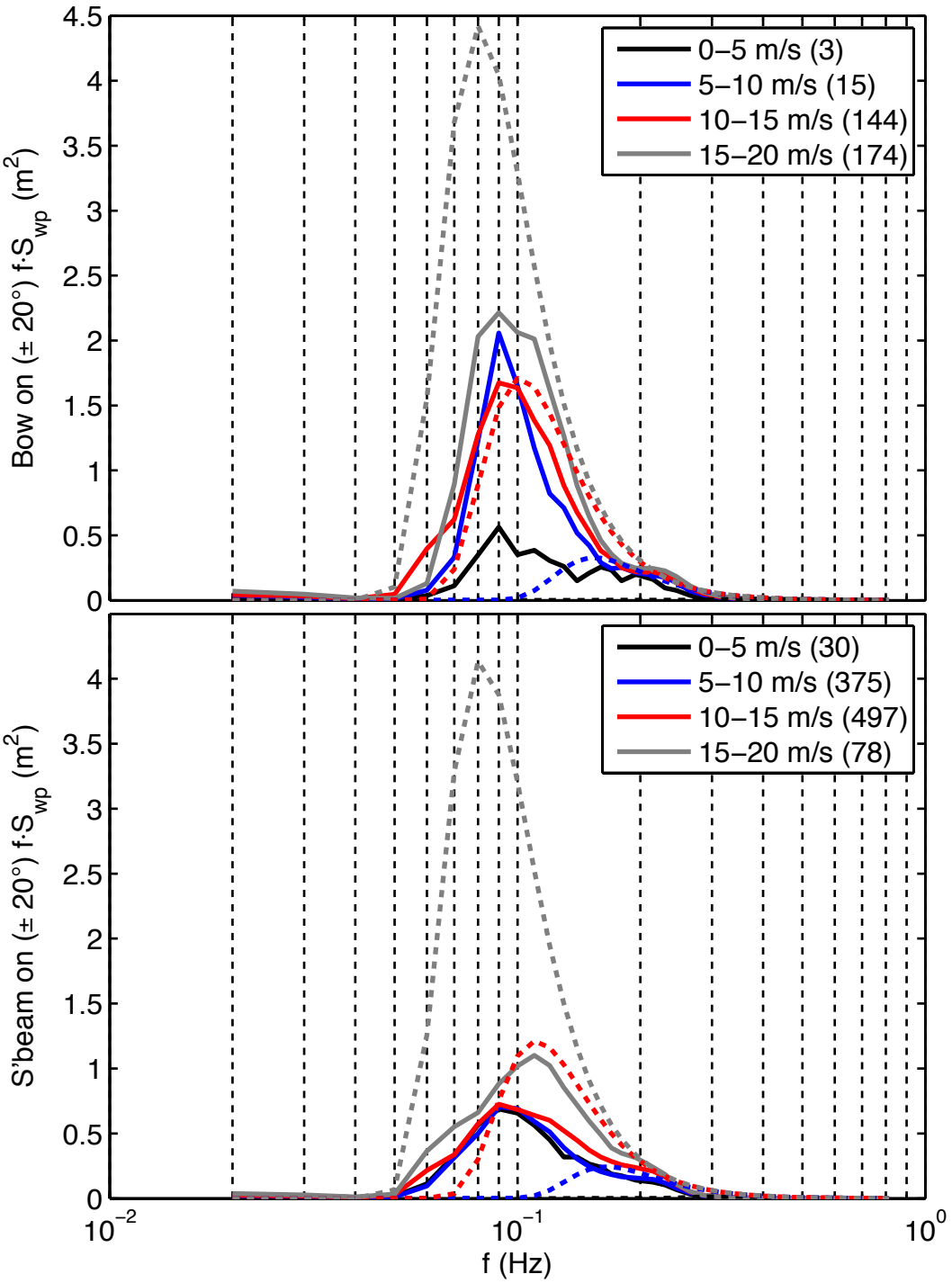

Figure 6.1. Wave spectra measured by the SBWR in 2006. Measurements (solid lines) are from periods when the ship was not steaming (speed over ground < 2 $m.s^{-1}$). Observational periods are divided into bow-on (± 20°) and 10° aft of starboard beam-on (± 20°) winds and separated by wind speed. The number in brackets indicates the number of measurements in each average. Also shown are the semi-empirical Pierson-Moskowitz wave spectra for fully developed seas (dashed lines), at the mean wind speed of the measurement periods.

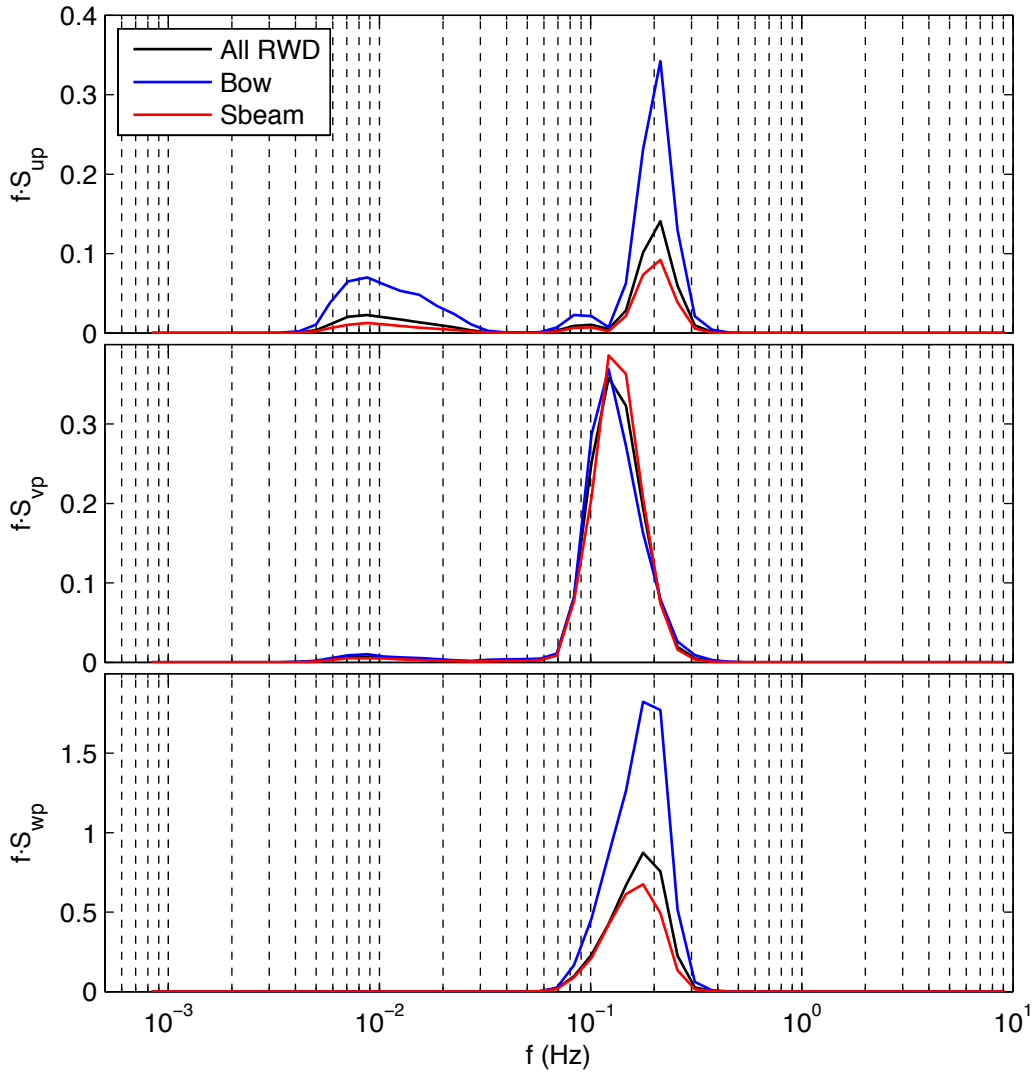

Figure 6.2. Averaged platform velocity spectra in the fore-aft (u_p), port-starboard (v_p) and vertical (w_p) directions. Spectra are averages of 1558 observational periods with mean wind speed in the range $10 < U_{10n} < 15$ m.s^{-1} and are separated by relative wind direction into bow-on (± 20°. n = 148) and 10° aft of starboard beam-on (± 20°. n = 765) sets.

6.3. Motion signal correction

6.3.1 Correction procedure

The air-sea flux results presented in this thesis are calculated from 20-minute averages. Prior to the calculation of EC fluxes, a correction for the effect of platform motion was applied to the measured wind speed. The correction procedure is closely based on that described in Edson et al., (1998) and is described in more detail in Chapter 2.2.8.

The AutoFlux system onboard *Polarfront* recorded measurements in 58.33-minute long sections. Each 58.33-minute section was sub-divided into three, slightly overlapping sections, each approximately 23.4 minutes in length (28,096 measurements at 20 Hz). Prior to flux calculation, 2048 measurements were removed from the beginning and end of each section in order to remove transient signals that may result from the 2-way filtering used in the motion correction procedure. Fluxes were then calculated from the remaining 20-minute periods.

To investigate the possible transient signal, the motion correction routine (Section 2.2.8) was run with the wind vector and platform motion inputs set to constant values (i.e.: constant wind speed of 10 $m.s^{-1}$, constant vertical acceleration of 1 *g*). A transient signal was apparent in the resulting "motion-corrected" wind vector. After removing the 2048 measurements from the beginning and end of the period, the remaining transient signal was small, of the order 0.01 $m.s^{-1}$. This is less than the precision of the Sonic. Examination of the transient signal prior to shortening of the measurement section suggested that the signal was most evident in the start of the first and the end of the last 23.4-minute section of each longer 58.33-minute section, due to the filtering being applied to the longer section. Following the transient removal process, no significant bias was found between wind spectra of the three 20-minute subsections. It is therefore reasonable to conclude that the transient signal has been successfully removed.

To reduce processing load, the motion correction procedure was applied to each 58.33-minute section prior to division into 23.4-minute subsections. To ensure that the order of processing did not introduce additional error, a set of fluxes were calculated with the motion correction applied separately to each of the shorter, 23.4-minute sections. The two different processing orders gave almost identical results: the mean u_* difference between the two methods was less than 0.1%, the mean CO_2 flux difference less than 1%.

6.3.2 Results

The effectiveness of the motion correction procedure was examined through a comparison of measurements with and without the motion correction applied. The comparison was made to a set of flux periods obtained on *Polarfront* in 2006. Representative variance spectra (Figure 6.3) and cospectra (Figure 6.4) are shown from an average of 127 measurements with mean wind speed $10 \le U_{10n} \le 12$. Without motion

correction, the three components of the wind spectra exhibit a strong signal between approximately 0.05 and 0.3 Hz (Figure 6.3). This corresponds closely to the range of frequencies of wave motion observed in the SBWR measurements (Figure 6.1). The signal at these frequencies can be assumed to be strongly influenced by wave induced movement of the measurement platform. The large wave scale signal in the non-motion corrected vertical wind spectra leads to large signals in the cospectra (Figure 6.4). The wave scale cospectral signal is often in the opposite direction to the flux at other frequencies and the momentum flux (Figure 6.4) shows a wave scale signal in both directions, suggesting that platform motion may change the phase of the vertical perturbations. This change of flux direction at the wave scale is also observed in other experiments (e.g.: McGillis et al., 2001a; Miller et al., 2008; Schulz et al., 2005; Song et al., 1996).

Application of the motion correction procedure removes most of the higher frequency portion of the wave scale signal from the wind variance spectra. Some wave scale signal, with a peak at approximately 0.1 Hz, remains in all three components (Figure 6.3). The variance of the three components of the wind vector is substantially reduced by the motion correction, with the vertical component reduced by 46% (Table 6.1). The uncorrected temperature covariance, T_w, has such a large wave scale signal that the uncorrected flux is commonly either very small or has the wrong sign. Corrected, the flux has the right sign and the correction causes a large percentage change in the magnitude.

Note that the PKT correction is dependent on the magnitude of the latent heat flux, and thus, unlike the non-PKT spectra, the PKT temperature and CO_2 spectra differ depending on whether or not the motion correction has been applied (Figure 6.3). As the correction is dependent on the mean value of the flux, the effect of the platform motion error can affect the PKT fluxes at frequencies outside the wave scale. For example, non-motion corrected PKT temperature cospectra are on average negative (into the ocean) at all frequencies in the example shown in Figure 6.4.

6.3.3 Platform motion and wind-wave interaction

Following motion correction, the averaged HiWASE wind spectra are similar in appearance to motion corrected spectra obtained in other air-sea EC experiments (e.g.: McGillis et al., 2001a; Miller et al., 2008; Song et al., 1996). In particular, the wave scale signal apparent in the HiWASE wind spectra and cospectra is also apparent in the

results of other air-sea interaction experiments. The residual wave scale signal in the motion corrected winds causes the reported spectra and cospectra to differ from the idealized shapes (Section 6.4.1). The presence of the wave scale signal may simply show that the motion correction procedure does not fully correct the platform motion. However, the physical cause of the residual wave scale signal is uncertain and will be discussed further here.

The EC CO_2 cospectra measured by McGillis et al, (2001a) are reproduced in Figure 6.5. The cospectra show a clear wave scale signal acting to increase the flux into the ocean. The wave scale signal is of a similar or larger relative size than the wave scale signal in the HiWASE CO_2 measurements (Figure 6.4). The signal is also comparable with the signal apparent in the HiWASE cospectra split by wind speed (see later discussion in Section 6.4.3 and Figure 6.18. Note that the PKT corrected CO_2 cospectra shown in Figure 6.18 are averages of both positive and negative fluxes).

A wave scale signal is apparent in the wind vector and momentum flux cospectra presented by Miller et al, (2008). The spectra and cospectra reported by Miller et al. (2008) at a range of heights above the ocean are reproduced here in Figure 6.6. For comparison HiWASE fluxes were measured at a height of ~ 14 m. Whilst the EC measurements of McGillis et al. (2001a) and Song et al. (1996) were obtained onboard research ships (and had similar motion correction procedures applied as on HiWASE), the measurements of Miller et al. (2008) were obtained onboard *RP FLIP*, a specially designed stable measurement platform with a 100m draft. Flux measurements on *FLIP* are made from a mast mounted on a 20 m long boom protruding from the vessels superstructure. *FLIP* is especially insensitive to wave-induced vertical motion (typical vertical motion ~ 1cm.s^{-1}, compared to typical ship vertical motion of 1 m.s^{-1}). The vertical wind variance spectra measured onboard *FLIP* exhibit a wave scale signal of similar relative magnitude to that seen in the HiWASE *w* spectra (Figure 6.3). The wave scale peak in the 13.8 m *FLIP* measurements is at ~ 0.05 m^2.s^{-2}, compared to the higher peak in the HiWASE *w* spectra at ~ 0.2 m^2.s^{-2}. However, the HiWASE spectra shown in Figure 6.3 are measured at 10 m wind speeds of 10-12 m.s^{-1}, whereas the *FLIP* measurements (Figure 6.6) are at a 10 m wind speed of 7.3 m.s^{-1}. The averaged HiWASE *w* spectra measured at wind speeds of 6-8 m.s^{-1} discussed later (Figure 6.16, Section 6.4.3) have wave scale signal of similar size to that reported by Miller et al., with a peak at ~0.08 m^2.s^{-2}.

The *FLIP* cospectra also have a large wave scale signal (Figure 6.6). The cospectral signal is substantially reduced by the application of standard motion correction procedures, but some signal, of similar size (peak at ~0.02) to the signal in the 6-8 $m.s^{-1}$ HiWASE momentum flux cospectra (Figure 6.17), remains. The decrease in the size of the *FLIP* wave scale signal with height leads Miller et al. (2008) to ascribe the signal to real wind correlations with wave motion, associated with wind-wave interactions (e.g.: Hristov et al., 2003).

The *FLIP* flux measurements were made on a well-exposed boom. However, distortion of the airflow by the boom or mast may still influence the flux measurements. In addition, large structures such as the hull of *FLIP* can modify upstream airflow some distance away from the structure (e.g.: Yelland et al., 2002). Distinguishing errors related to motion and flow distortion is challenging as both depend on relative wind direction. The impact of flow distortion on the HiWASE flux measurements is examined in detail in Chapter 7.

The HiWASE spectra and cospectra are also similar to those obtained from fixed platform air-sea EC experiments (e.g.: DeLeonibus, 1971). The residual wave scale signal that is present in the HiWASE spectra and cospectra after motion correction is also apparent in the spectra and cospectra reported in these experiments, which observe wave scale peaks in the measurements of *w* variance spectra at 0.25-0.3 $m^2.s^{-2}$ for 7.5 m wind speeds of approximately 10 $m.s^{-1}$. The wind stress measurements reported by DeLeonibus (1971) were obtained from a fixed platform (in water depth ~ 60m) near Bermuda. The EC instrumentation was at a height of 7.5 m. The vertical wind spectra from this experiment clearly show a large signal at the frequency of dominant wave motion. As the measurements are not subject to platform motion the wave scale signal is ascribed by the author to wind-wave interaction, though the large measurement platform used may have resulted in unknown flow distortion effects.

Smith (1980) observed a wave scale signal in momentum flux cospectra obtained from a tied down (but not fixed) tower in high winds. The wave scale signal observed in the tied down tower (typically small but occasionally up to 15% of the total flux) was described by Smith (1980) as larger than the signal observed in other experiments over smaller waves or from a tower placed on a beach. However, Smith (1980) was unable to determine what proportion of the signal was due to wind wave interaction.

The influence of wind-wave interaction on turbulence and surface stress remains an area of debate (e.g.: Jansen, 1999, Taylor and Yelland, 2001b) and several

experiments suggest that any wind wave interaction influence on air-sea fluxes will be small at the wind speeds typically found at Station Mike. For example, air-sea EC wind stress measurements from a fixed tower found that a wave signal was only apparent in the wind velocity spectra in conditions of fast, strong swell ($U_{10n} / \upsilon_p \leq 0.5$, $Hs_{swell} \gg Hs_{wind}$ where υ_p is the wave phase speed and Hs_{swell} and Hs_{wind} are the significant wave heights of the swell and wind components of the wave field respectively (Drennan et al., 1999), conditions that are rarely encountered at Station Mike.

It is therefore uncertain what proportion, if any, of the wave scale signal in the HiWASE wind spectra measurements is due to imperfect motion correction and what proportion is a real signal resulting from wind-wave interactions.

6.3.4 55-minute flux measurements

Initially for the HiWASE experiment air-sea fluxes were computed as 55-minute averages (58.33 minute measurement, with removal of data from the beginning and end of the section to reduce transients). Averaged turbulent variance spectra from 21 55-minute measurements obtained in 2006 at wind speeds between $10 \leq U_{10n} \leq 12$ are shown in Figure 6.7. A relatively small subset of measurements is used due to the amount of computing time required for processing. Cospectra from the same periods are shown in Figure 6.8. The longer periods include a small signal at frequencies below those included within a 20-minute averaging period. At the moderate to high wind speeds of interest, any signal at these frequencies is likely due to slow variation of the ship's heading or other maneuvering. An examination of the flux reduction resulting from a reduction in the averaging period from 55 to 20 minutes found the flux reduction to be minor (Chapter 4).

During the course of the HiWASE experiment, the original motion correction procedure was updated in order to improve the rotation of the motion-corrected winds into the ship frame of reference (i.e.: correction for small yaw offsets in the orientation of the MotionPak with the ship) and to correct for the ship speed obtained from the ship's navigation data. A comparison of the "new" motion correction method with the previous "old" method, as applied to 55-minute spectra and cospectra is also shown in Figure 6.7 and Figure 6.8. The "new" processing made only a small difference to the resulting fluxes, with a small reduction in the low frequency signal. The change was most apparent in the crosswind spectrum where the low frequency signal is significantly

reduced by the "new" method. The new motion correction reduced the mean u_* from the periods shown by approximately 4%. The scalar fluxes were changed by this factor or less. However, the PKT corrected CO_2 flux was more strongly affected: the new motion correction increased the mean flux value of the samples shown by 11%. The PKT corrected fluxes are more sensitive to noise, which is compounded here by the small sample size. For the remainder of this thesis the "new" motion correction procedure is used. Unless otherwise stated, all further flux measurements presented in this thesis are 20-minute averages that were obtained by subdividing a 58.33-minute section, with the motion correction applied to the longer section prior to division into subsections.

Table 6.1. Change (%) to the average variance / covariance found by comparing motion corrected and non-motion corrected measurements. Spectra are turbulent variables measured using the EC technique during HiWASE. The analysis was performed on 127 measurements obtained during 2006.

Spectra / Cospectra	**S_x Symbol**	**% Change after motion correction.**
Alongwind spectra	***u***	-34
Crosswind spectra	***v***	-10
Vertical wind spectra	***w***	-46
Alongwind momentum cospectra	***u'w'***	8
Crosswind momentum cospectra	***v'w'***	-79
Latent heat cospectra	***r'w'***	0
Sensible heat cospectra	***T'w'***	1025
PKT sensible heat cospectra	***PKT T'w'***	-159
CO_2 cospectra	***c'w'***	-17
PKT CO_2 cospectra	***PKT c'w'***	-28

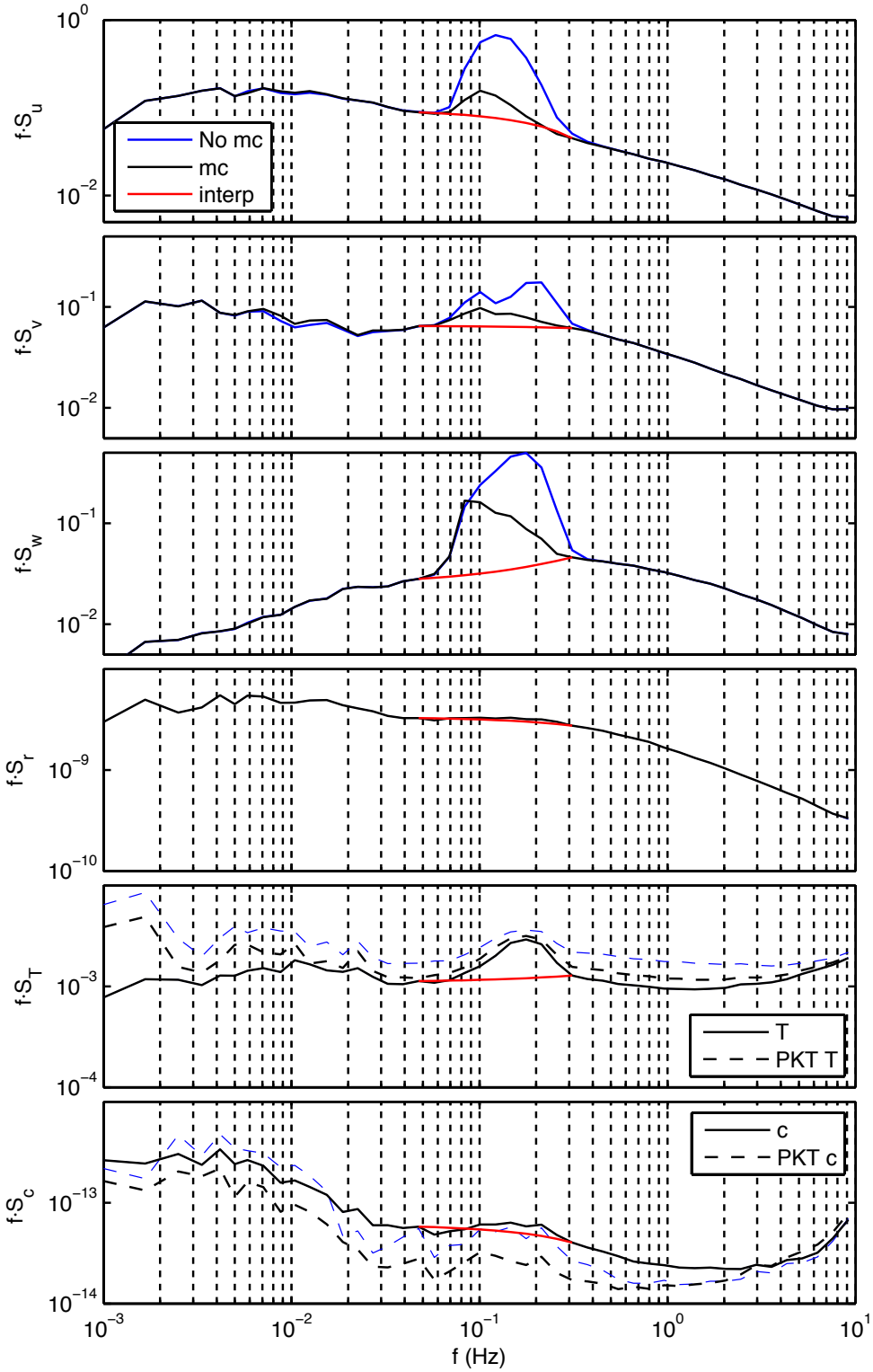

Figure 6.3. Averaged variance spectra, with (black line) and without (blue line) correction for platform motion. Averages are of 127 measurements obtained during 2006 at wind speeds $10 \le U_{10n} \le 12$. The red line is a linear interpolation between the spectral values at 0.05 Hz and 0.3 Hz.

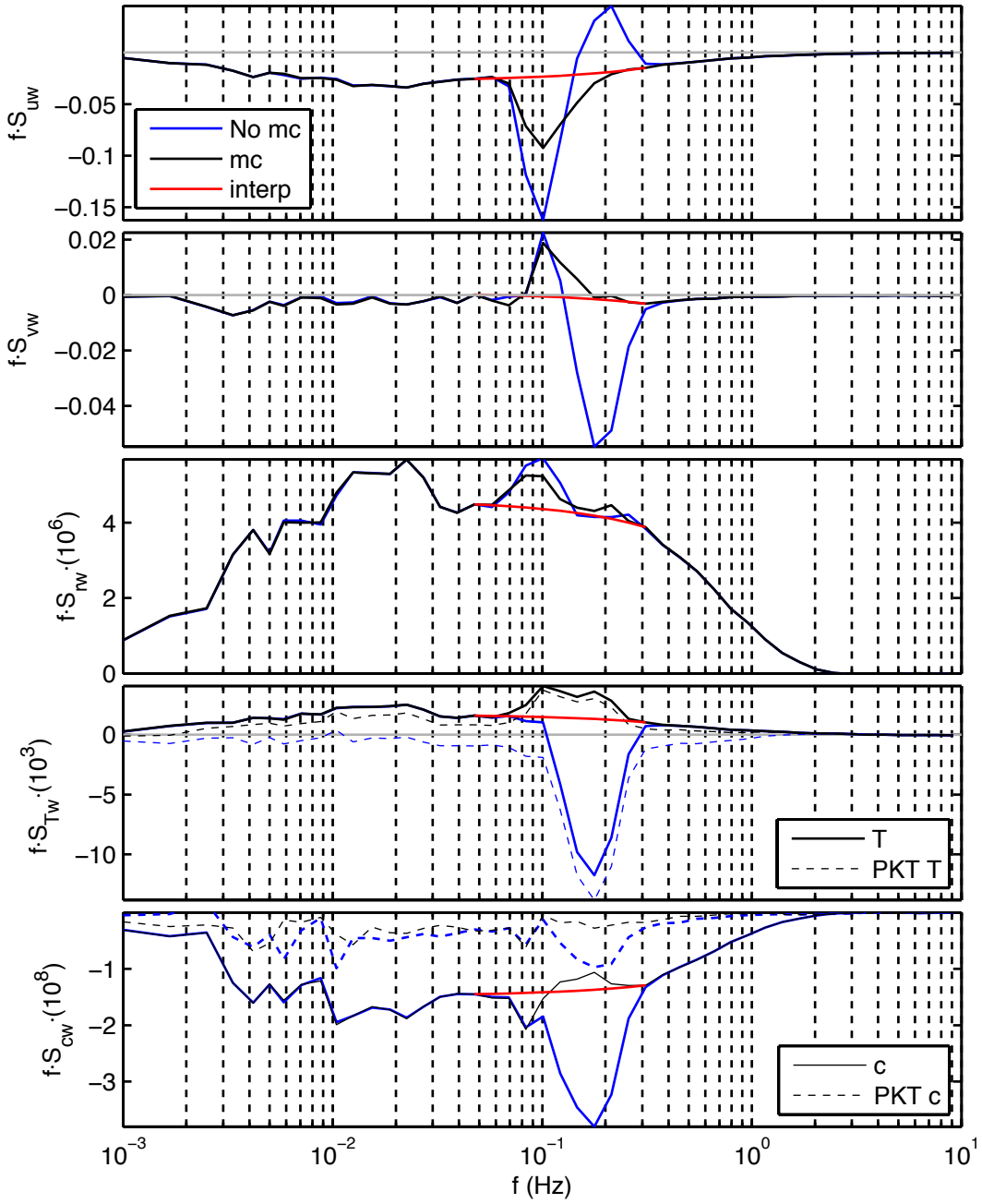

Figure 6.4. Averaged cospectra, with (black line) and without (blue line) correction for platform motion. Averages are of 127 measurements obtained during 2006 at wind speeds $10 \le U_{10n} \le 12$. The red line is a linear interpolation between the cospectral values at 0.05 Hz and 0.3 Hz.

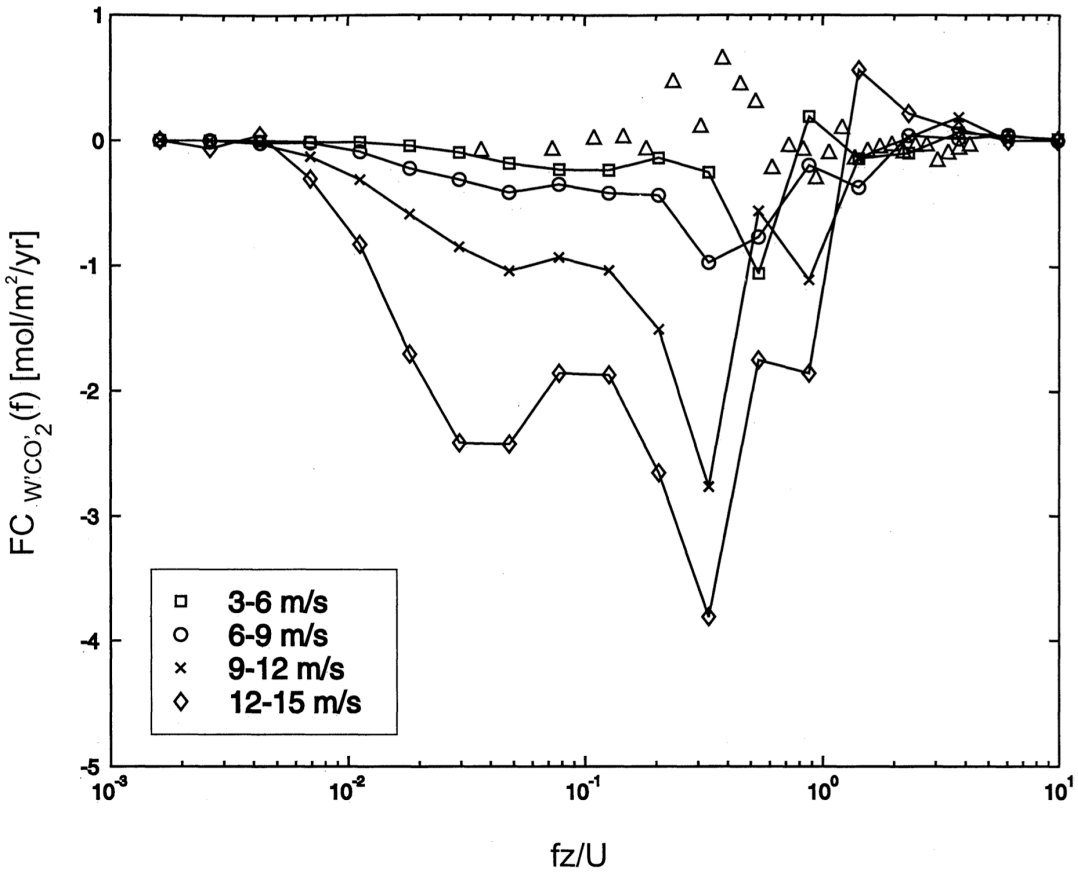

Figure 6.5. Copy of Figure 5 from McGillis et al., (2001a). Original caption: [Cospectra of vertical wind fluctuations and atmospheric CO_2 fluctuations measured during GasEx-98 with the direct covariance CO_2 flux system. Ensemble spectral densities for the wind speed range 3-6 m.s^{-1} (squares), 6-9 m.s^{-1} (circles), 9-12 m.s^{-1} (crosses) and 12-15 m.s^{-1} (diamonds). Cospectra of vertical wind fluctuations and zero reference gas measured during calibration intervals (triangles) are shown for comparison. The NDIR [closed path IRGA] chopper wheel is affected by rotational accelerations, and the predominant noise occurs at the frequency of ship motion caused by waves.]

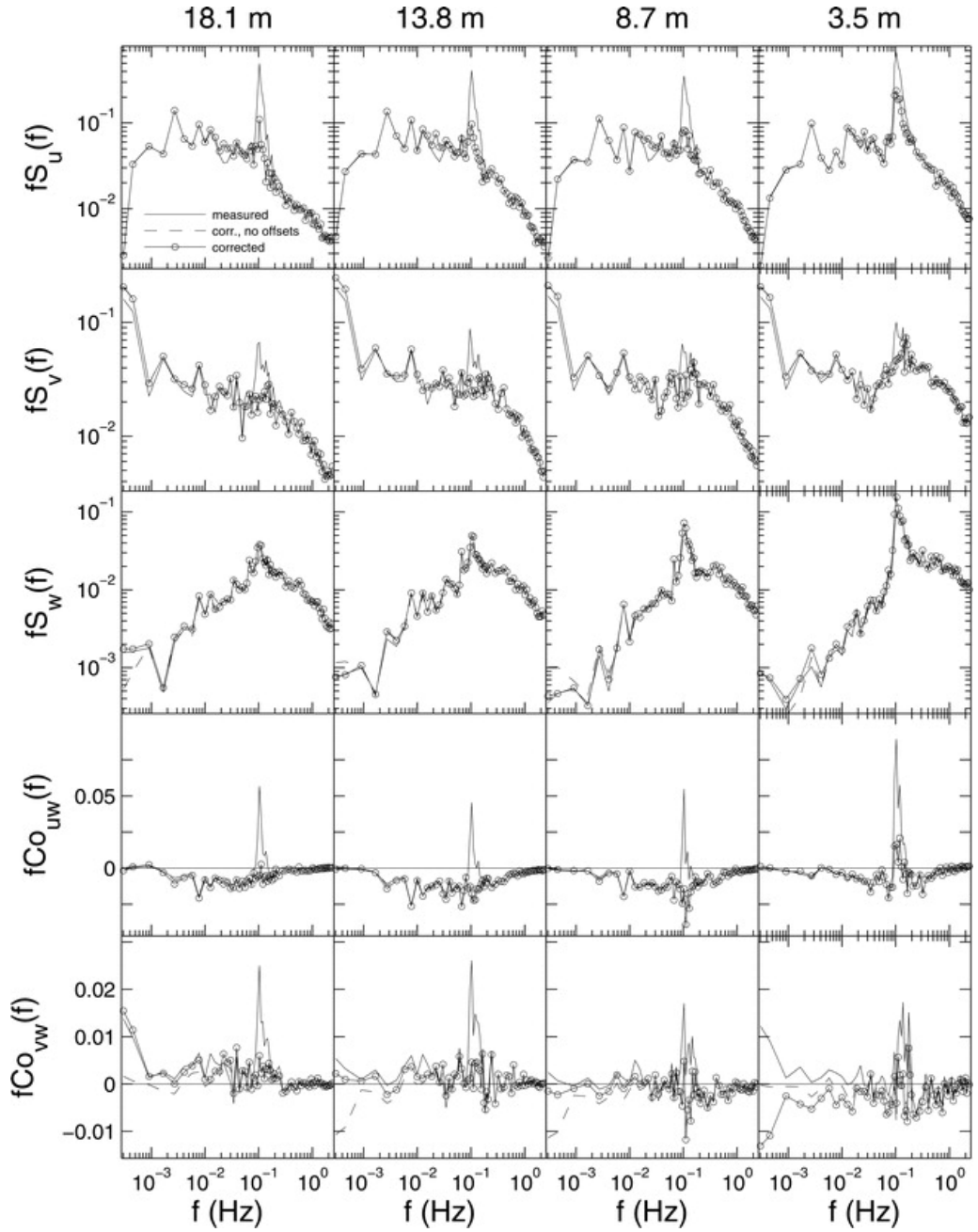

Figure 6.6. Copy of Figure 4 from Miller et al., (2008). Original caption: [Measured and motion-corrected velocity spectra and cospectra at four heights above the mean ocean surface measured from R/P *FLIP*. The mean 10-m wind speed was 7.3 m s^{-1}. Spectra and cospectra are frequency weighted and shown in natural coordinates: measured (solid curve), motion corrected without accounting for anemometer-mounting offset angles (dashed curve), and motion corrected including the anemometer-mounting offsets (solid curve with open circles). (row 1) Alongwind velocity component, *u*; (row 2) crosswind velocity component, *v*; (row 3) vertical velocity component, *w*; (row 4) alongwind stress cospectrum, *uw*; and (row 5) crosswind stress cospectrum, *vw*. Each column represents one of the four measurement levels: (column 1) 18.1 m; (column 2) 13.8 m; (column 3) 8.7 m; and (column 4) 3.5 m.]

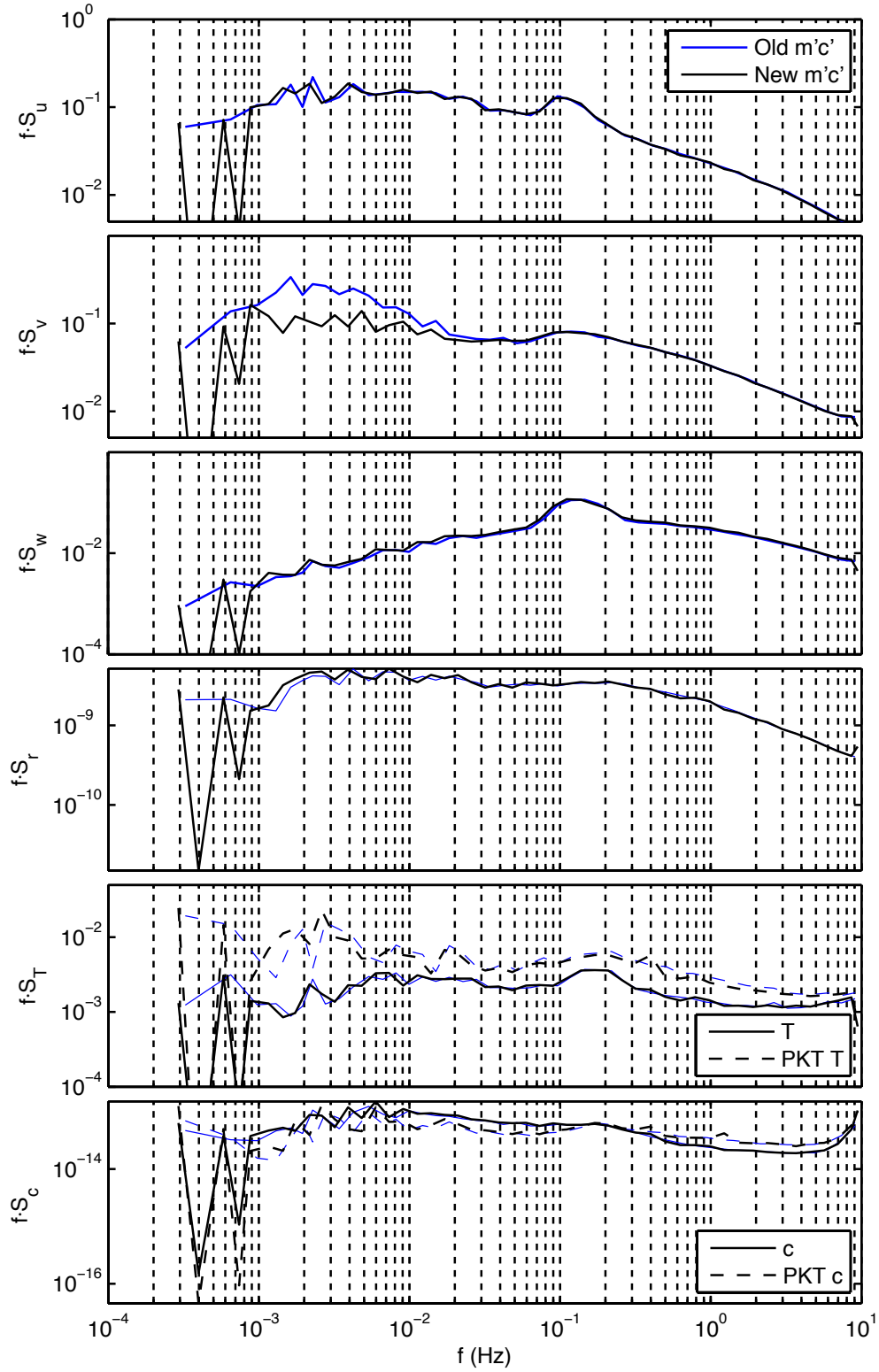

Figure 6.7. Averaged variance spectra of variances obtained from 58.33-minute periods. Averages are of 21 measurements obtained during 2006 at wind speeds $10 \le U_{10n} \le 12$. Spectra have been corrected for platform motion using either an older ("old", blue line) or more recent ("new", black line) version of the motion correction procedure.

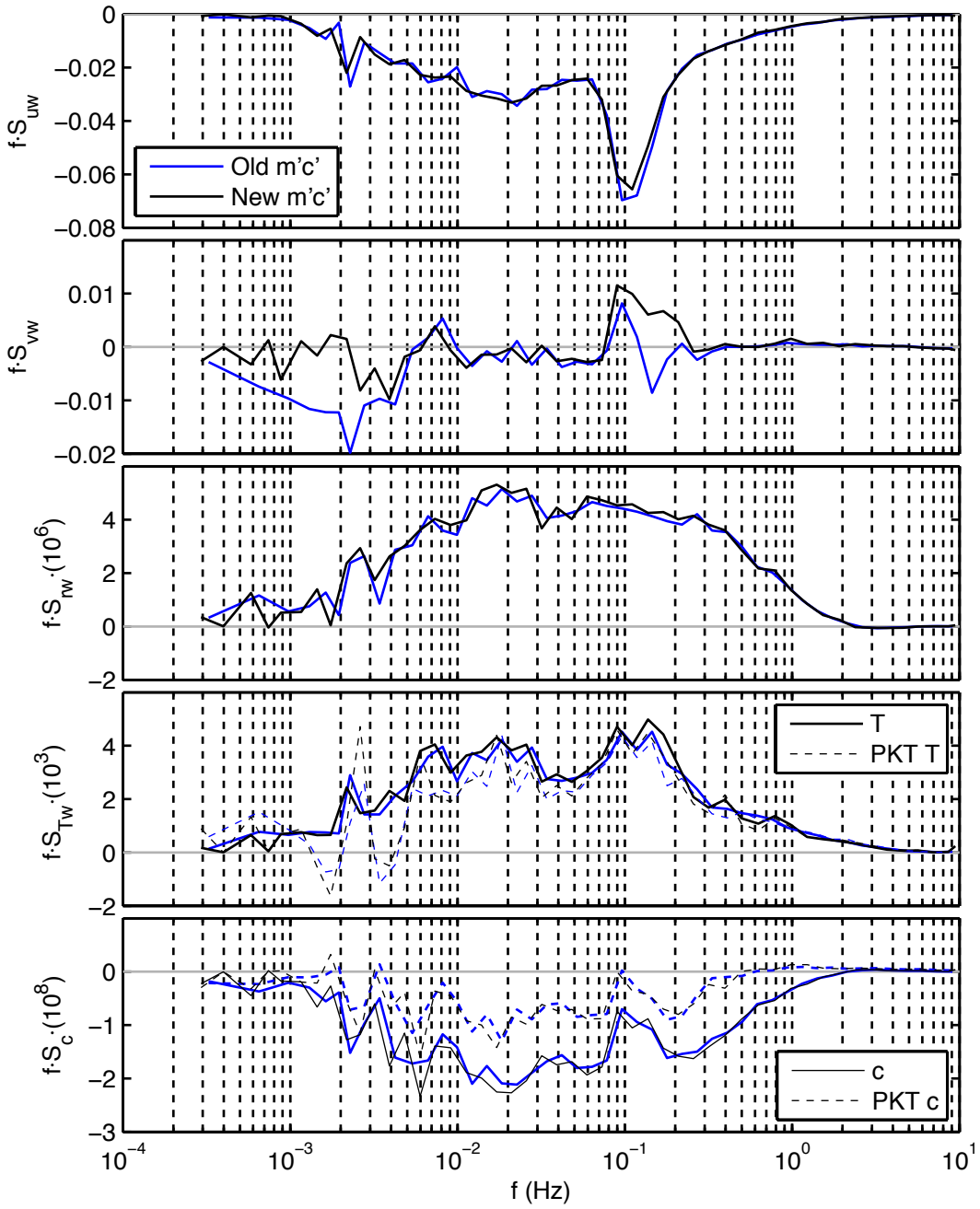

Figure 6.8. Averaged cospectra of fluxes obtained from 58.33-minute periods. Averages are of 21 measurements obtained during 2006 at wind speeds $10 \le U_{10n} \le 12$. Cospectra have been corrected for platform motion using either an older ("old", blue line) or more recent ("new", black line) version of the motion correction procedure.

6.4. Measurements corrected for platform motion

6.4.1 Residual wave scale signal

Averaged variance spectra of 20-minute motion corrected measurements obtained onboard HiWASE are shown in Figure 6.9. For comparison with other spectra shown in this section, the 70 measurement periods included in the averages were obtained at mean wind speeds of $10 \le U_{10n} \le 12$. Spectra and cospectra of fluxes obtained over a wider range of wind speeds are shown in Section 6.4.3. The wind spectra all exhibit a signal at approximately 0.1 Hz. This corresponds to the wave scale and can be ascribed to be either uncorrected platform motion or wave induced fluctuations (Section 6.3).

Scalar variance spectra are also shown in Figure 6.9. The humidity (*r*) spectra have some low frequency noise, but do not show any wave scale signal. Both the air temperature (*T*) and the PKT temperature (*PKT T*) spectra show a strong signal at the wave scale, as well as both low and high frequency noise. The adiabatic lapse rate is approximately $0.01°C.m^{-1}$. An estimate of the effect on the temperature spectra from this level of variation and the typical vertical motion experienced at the *Polarfront's* foremast suggest that adiabatic changes could explain the temperature spectra wave scale signal. The signal could also be caused by movement of the sensor through the vertical profile of temperature. This is examined in Appendix E. The method used to estimate the spectral signal resulting from either adiabatic changes or profiling is the same, and is detailed in Appendix E. There is a small wave scale signal present in the CO_2 and PKT CO_2 (*PKT c*) spectra, as well as low and high frequency noise. Both the *PKT T* and *PKT c* spectra differ from the non-PKT versions.

The averaged cospectra of these measurements are shown in Figure 6.10. The momentum fluxes show a strong wave scale signal with a peak at approximately 0.1 Hz. The crosswind cospectra also show a relatively large 0.1 Hz peak wave scale signal. The humidity cospectra shown here do not exhibit as strong a wave scale signal relative to the cospectral levels at other frequencies, although there is a small peak at 0.1 Hz. The air temperature (and *PKT T*) cospectra show a large 0.1 Hz spike and a substantial reduction in the cospectral level at about 0.2 Hz. A wave scale signal in the CO_2 cospectra is harder to distinguish, though there are peaks at about 0.07 and 0.15 Hz. The PKT CO_2 cospectra has significant signal between 0.07 and 0.2 Hz. The PKT corrections introduces additional noise into both the *T* and *c* cospectra, but the cospectra show that the low and high frequency noise in the temperature and CO_2 spectra do not

correlate with wind fluctuations and hence have not resulted in a significant cospectral signal.

Cospectral ogive functions are shown in Figure 6.11. In general, the ogives show that the cospectra are well behaved, converging to approximately constant values at 0.001 Hz and 2 Hz. The exception is the crosswind cospectra, with noise at a wide range of frequencies (not unexpected since the crosswind stress is approximately zero), and a large wave scale signal. A wave scale signal is also apparent in the momentum flux and temperature ogives. The PKT CO_2 ogive converges to a substantially smaller value than the CO_2 ogive, demonstrating the significant reduction in flux resulting from the correction.

Scaling of individual spectra by the appropriate flux magnitude allows the spectral shape of different fluxes to be compared with "ideal" spectral shapes. The "ideal" spectra and cospectra shown here were developed from a series of experiments in Kansas (Kaimal et al., 1972). Note that the "ideal" curves were developed over land and may differ from air-sea spectra by, for example, not showing any wind-wave interaction. Variance spectra scaled in this manner are shown in Figure 6.12, with the spectra either scaled by friction velocity (u_*) or the appropriate flux scale. The normalised spectra are shown with respect to a dimensionless frequency ($f_{nd} = f \times z / U_{rel}$). The ideal curves shown here are valid for neutral atmospheric conditions, whereas the majority of measurements made during HiWASE are in slightly unstable conditions. The mean dimensionless stability (z/L) for the 70 measurements shown was -0.09. The normalised HiWASE wind spectra agree well with the ideal spectra at higher frequencies ($f_{nd} > 0.4$), though the along wind spectra is slightly low. The wave scale signal is especially apparent in the w spectra and results in the measured spectra being higher than the ideal curve at the wave scale frequencies. At lower frequencies ($f_{nd} < 0.06$), the HiWASE wind spectra are larger than the ideal shape. This may be due to atmospheric instability, changes in ship heading or non-stationarity in the airflow.

The humidity variance spectra are higher than the ideal curve, and show substantial low frequency noise (Figure 6.12). The temperature spectra exhibit both low and high frequency noise at levels above the ideal curve. The CO_2 spectra are significantly higher than the ideal curve. The ideal curve shown here was obtained over land from temperature measurements. The relatively small size of air-sea gradients compared with those over land may explain the discrepancy between the HiWASE

scalars and the ideal curves. For CO_2, the small air-sea gradient may mean that it does not scale well with temperature, and the ideal curve shown here is not appropriate.

Normalised HiWASE cospectra and ideal cospectral curves from the Kansas experiments (Kaimal et al., 1972) are shown in Figure 6.13. Note that Kaimal et al. (1972) do not state an ideal curve for crosswind cospectra, and hence the HiWASE crosswind cospectra are not shown here. The averaged fluxes all agree reasonably well with the ideal spectral shapes. The largest differences between the measured spectra and the ideal shapes are at the wave scale frequencies. The cospectra are also low relative to the ideal curves at $0.03 < f_{nd} < 0.1$ Hz. This disparity may be reduced by removal of the wave scale signal and the subsequent reduction in the cospectral normalization. The measured CO_2 cospectra are highly variable at all frequencies. At high frequencies, the CO_2 cospectra are lower than the ideal curves. This may be due to the low sensor accuracy relative to the small size of the CO_2 fluctuations over the ocean (see sensitivity analysis, Chapter 5.2). At high frequency, where the spectral densities are low, the IRGA used in HiWASE may not capture all of the variation. However, the spectral shape of both the PKT corrected and non-PKT corrected fluxes are in broad agreement with the ideal spectra, indicating that application of the PKT correction does not significantly alter the spectra shape in the mean. This is in contrast to the results of applying the PKT correction reported by Edson et al. (2011), who found that the PKT correction over-corrects at low frequency and under corrects at high frequency, and does not result in cospectra with the expected spectral shape. This behavior is not observed in the HiWASE results (in fact, Figure 6.13 show the opposite effect on the high and low frequency portions of the *PKT c* cospectra). The causes of this difference are uncertain.

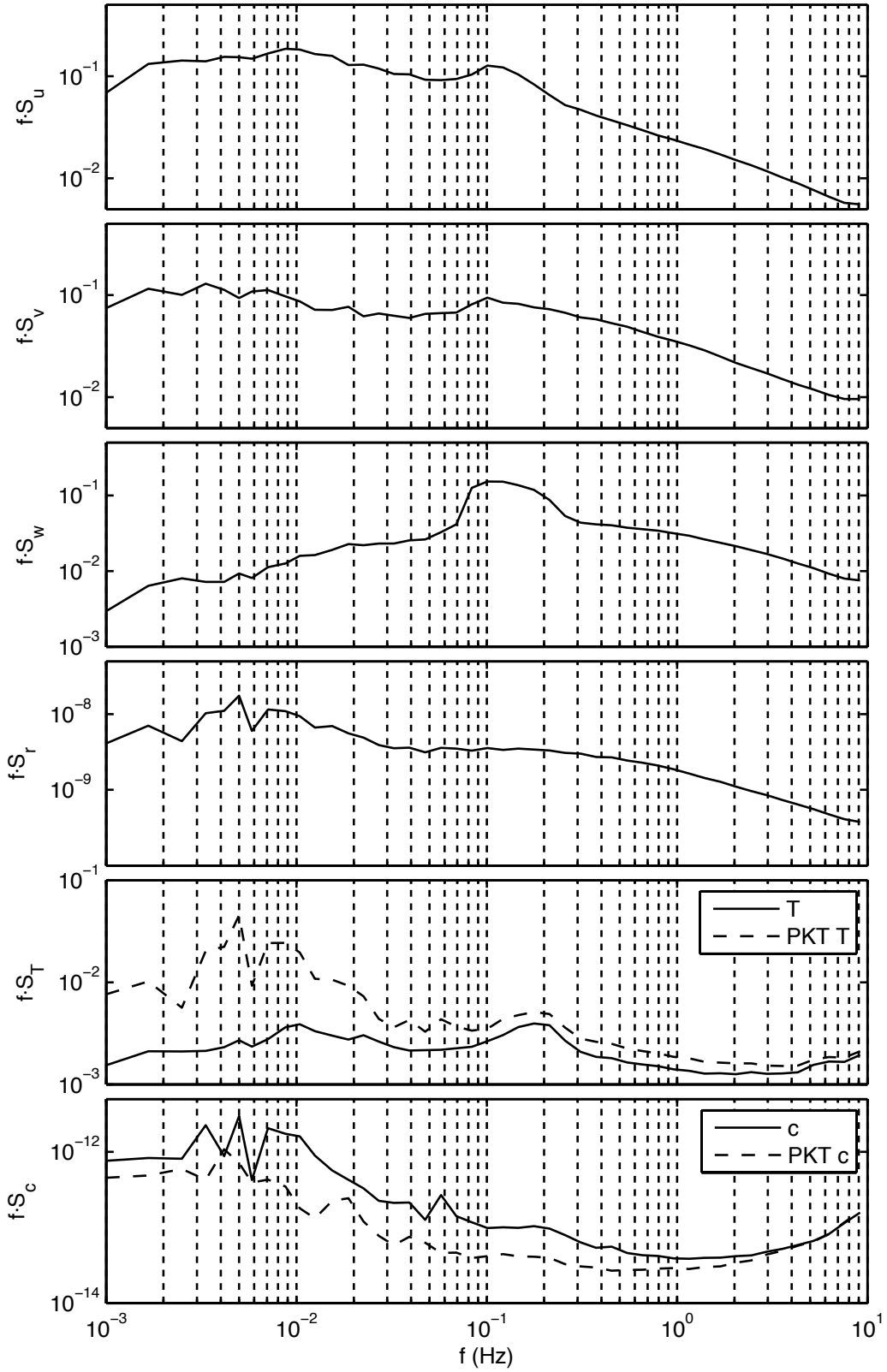

Figure 6.9. Averaged spectra of variances obtained from 20-minute periods. Averages are of 70 measurements obtained during 2006 at wind speeds $10 \le U_{10n} \le 12$. Measurements have been corrected for platform motion.

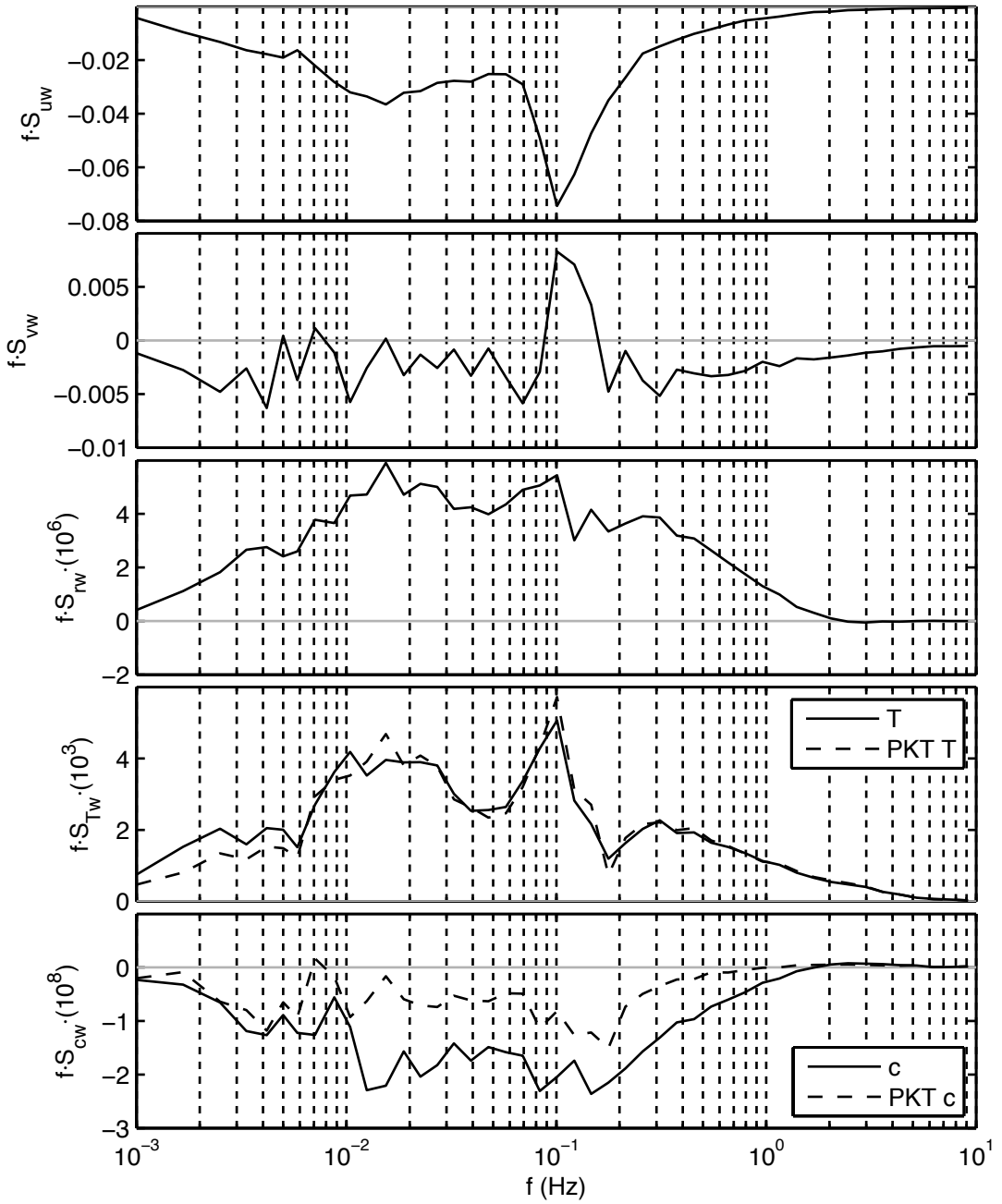

Figure 6.10. Averaged cospectra of fluxes obtained from 20-minute periods. Averages are of 70 measurements obtained during 2006 at wind speeds $10 \le U_{10n} \le 12$. Measurements have been corrected for platform motion.

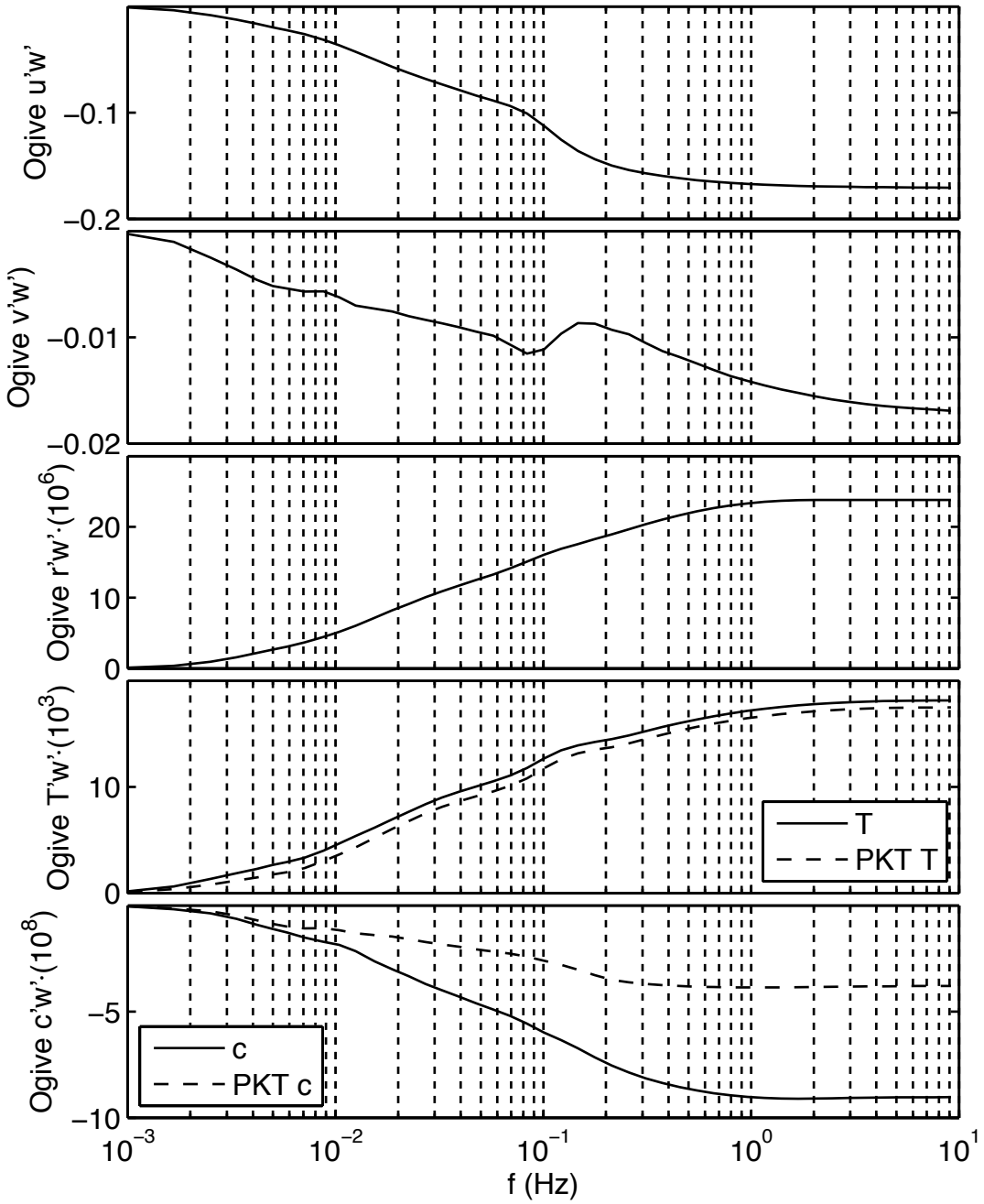

Figure 6.11. Ogive cospectral function of 20-minute flux periods. Averages are of 70 measurements obtained during 2006 at wind speeds $10 \le U_{10n} \le 12$. Measurements have been corrected for platform motion.

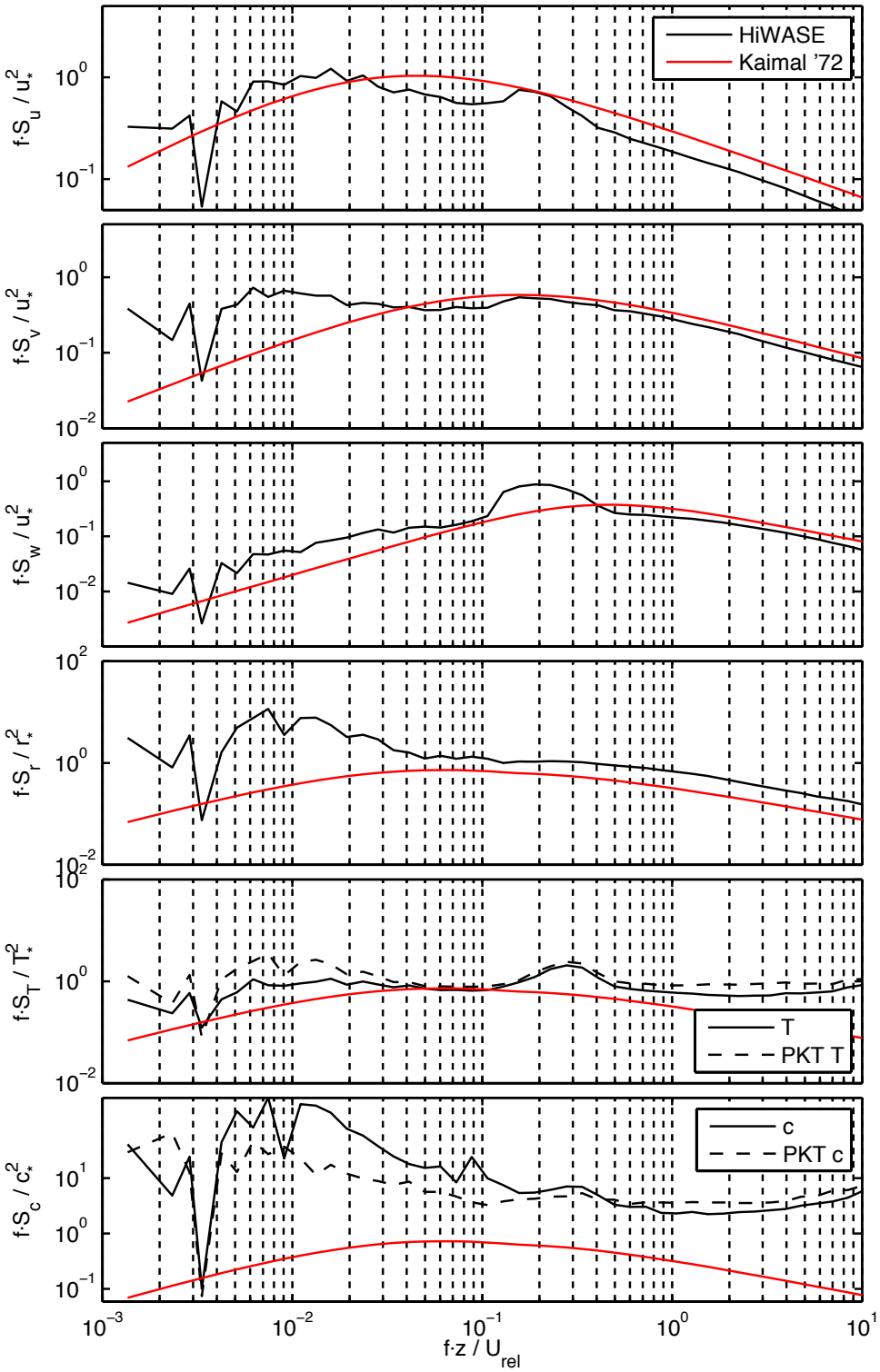

Figure 6.12. Normalised variance spectra. Averages are of 70 measurements obtained during 2006 at wind speeds $10 \le U_{10n} \le 12$. Measurements have been corrected for platform motion. Also shown are the ideal, neutral atmospheric stability spectral curves from the "Kansas" series of EC experiments over land (Kaimal et al., 1972). Note that the x-axis is non-dimensional frequency.

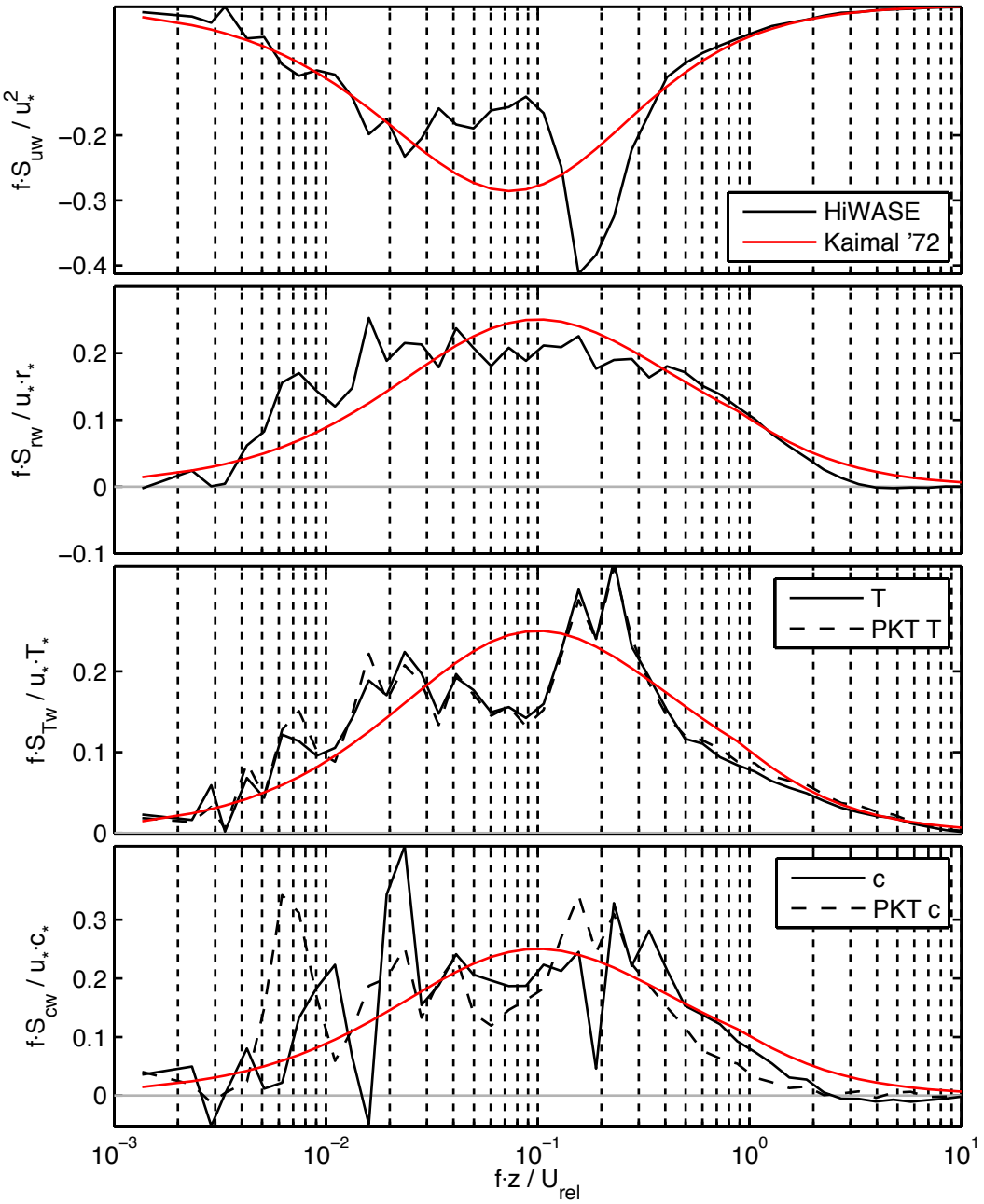

Figure 6.13. Normalised cospectra of 20-minute fluxes. Averages are of 70 measurements obtained during 2006 at wind speeds $10 \le U_{10n} \le 12$. Measurements have been corrected for platform motion. Also shown are the ideal, neutral atmospheric stability spectral curves from the "Kansas" series of EC experiments over land (Kaimal et al., 1972). Note that the x-axis is f_{nd}, non-dimensional frequency.

6.4.2 *Variation with wind direction*

The SBWR spectra demonstrate that the *Polarfront* experiences greater wave motion when winds (and in most cases waves) are onto the ship's bow (Figure 6.1). As discussed in Section 6.2, this is at least partly due to an operational selection for rougher conditions with bow-on winds. At the ship's bow, where the flux instruments are located, the motion with bow-on winds will be greater than that measured at the ship's centre of gravity by the SBWR. This is evident in the platform motion measured by the MotionPak (Figure 6.2). The wave scale signal in the measured atmospheric spectra is also significantly larger for bow-on wind directions than for beam-on winds (Figure 6.14). This is particularly evident for the vertical component of wind speed. The mean wind speed of the three sets shown differs by less than 0.1 $m.s^{-1}$, and thus the increased *u* and *v* spectral levels for bow-on winds are not due to higher mean wind but indicate increased variability. Whilst the increased variability in the bow-on wind spectra can in part be ascribed to the smaller number of measurements in the average (80, as compared to 473 for starboard beam-on wind directions), the bow-on vertical wind spectra consistently shows increased variance at a frequency of about 0.2 Hz. The peak of the motion signal in the bow-on vertical wind spectra and the resulting cospectra is at higher frequency than for other wind directions, suggesting that the higher frequency platform motion associated with bow-on winds (vessel pitching as opposed to rolling) is contaminating the signal.

The variance spectra for bow-on CO_2 are lower than the spectra from other wind directions (Figure 6.14). This is due to a lower mean ΔpCO_2 (58.2 µatm) for the bow-on measurements than for the beam-on (62.7 µatm) or all wind direction measurements (63.3 µatm). The variance of the PKT corrected temperature spectra is significantly increased compared to the air temperature spectra for beam-on winds, though the additional variance is not correlated with wind speed fluctuations and the cospectra (Figure 6.15) are in good agreement. A 0.2 Hz spike is also evident in the scalar variance spectra, and is largest in the bow-on measurements (Figure 6.14). The presence of this signal in the scalars suggests that it may be due to vertical motion of the sensor through the atmospheric profile. The vertical motion experienced at the *Polarfront's* foremast is largest when winds are onto the ships' bow (e.g.: Figure 6.2). The effect of sensor movement through the air column is discussed in more detail in Appendix E. A spike is also visible in the bow-on air temperature spectra at approximately 5 Hz. This high frequency signal may be a resonance signal resulting from vibration of the sensor.

The cospectra of measurements obtained when winds were onto the bow consistently show a large signal at the wave scale (Figure 6.15). Whilst the wave scale signal in the momentum flux is no larger for bow-on wind directions than it is for beam-on directions, it covers a wider range of frequencies, from about 0.05 to 0.3 Hz. The bow-on scalar cospectra all display a large, downward (into the sea) signal at frequencies of about 0.08 to 0.3 Hz. This bow-on wave scale signal is significantly larger than for other relative wind directions. The bow-on wind wave scale signal appears to be downwards regardless of the flux direction at other frequencies, or the atmospheric stability. The mean dimensionless atmospheric stability (z/L) for the bow-on wind direction periods in Figure 6.15 is -0.04, equal to the mean stability for the measurements at all relative wind directions. For starboard beam ("Sbeam" in the figure) relative wind directions, the scalar cospectra have a different wave scale shape, with an upwards peak at about 0.15 Hz and a downwards peak at about 0.08 Hz.

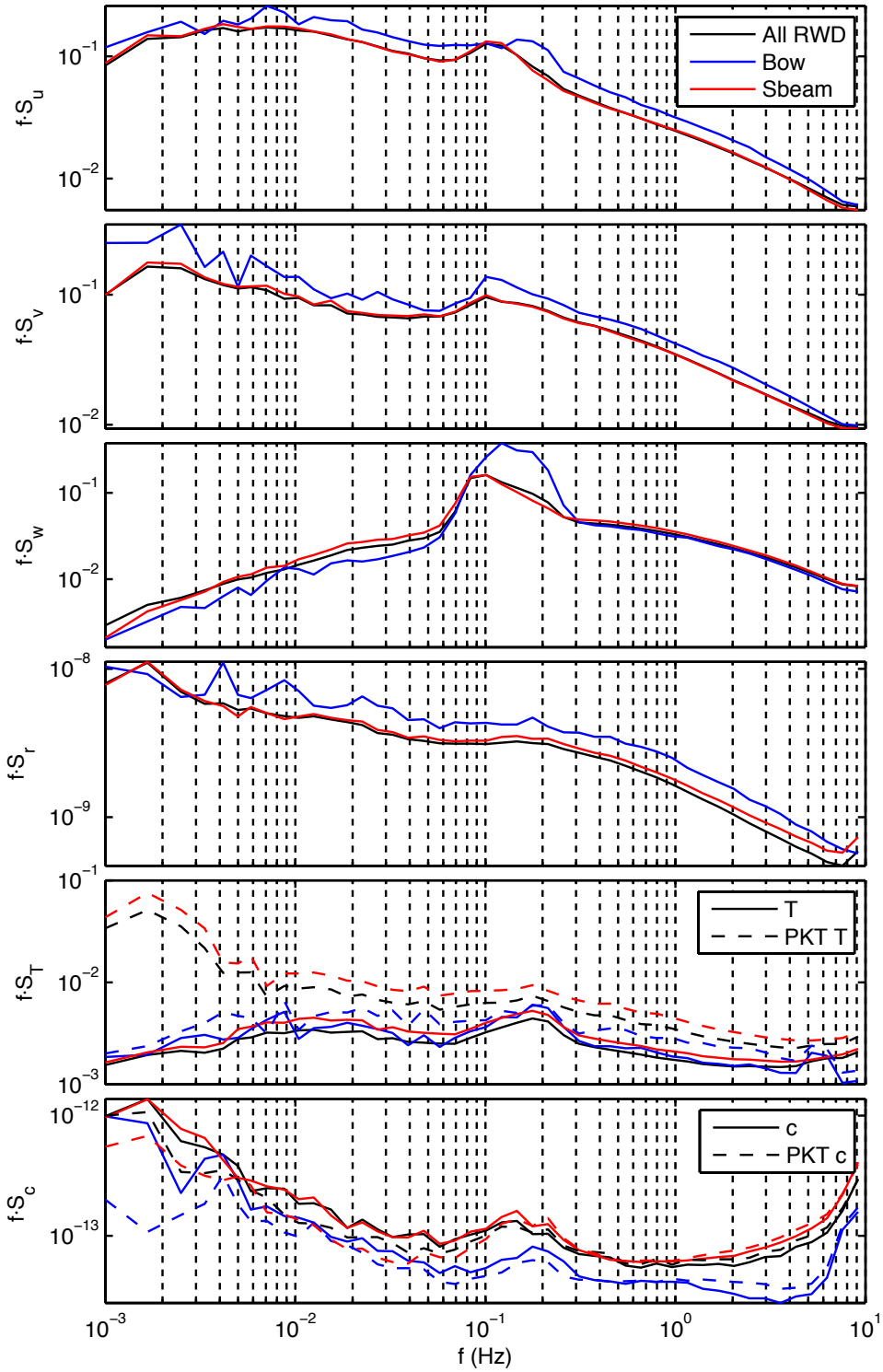

Figure 6.14. Averaged variance spectra obtained from 20-minute periods and separated by relative wind direction into bow-on (± 20°, n = 32) and 10° aft of starboard beam-on ("Sbeam"; ± 20°, n= 470). The number of measurements at all relative wind directions is 815. Averages are of measurements obtained at wind speeds $10 \le U_{10n} \le 12$. Spectra have been corrected for platform motion.

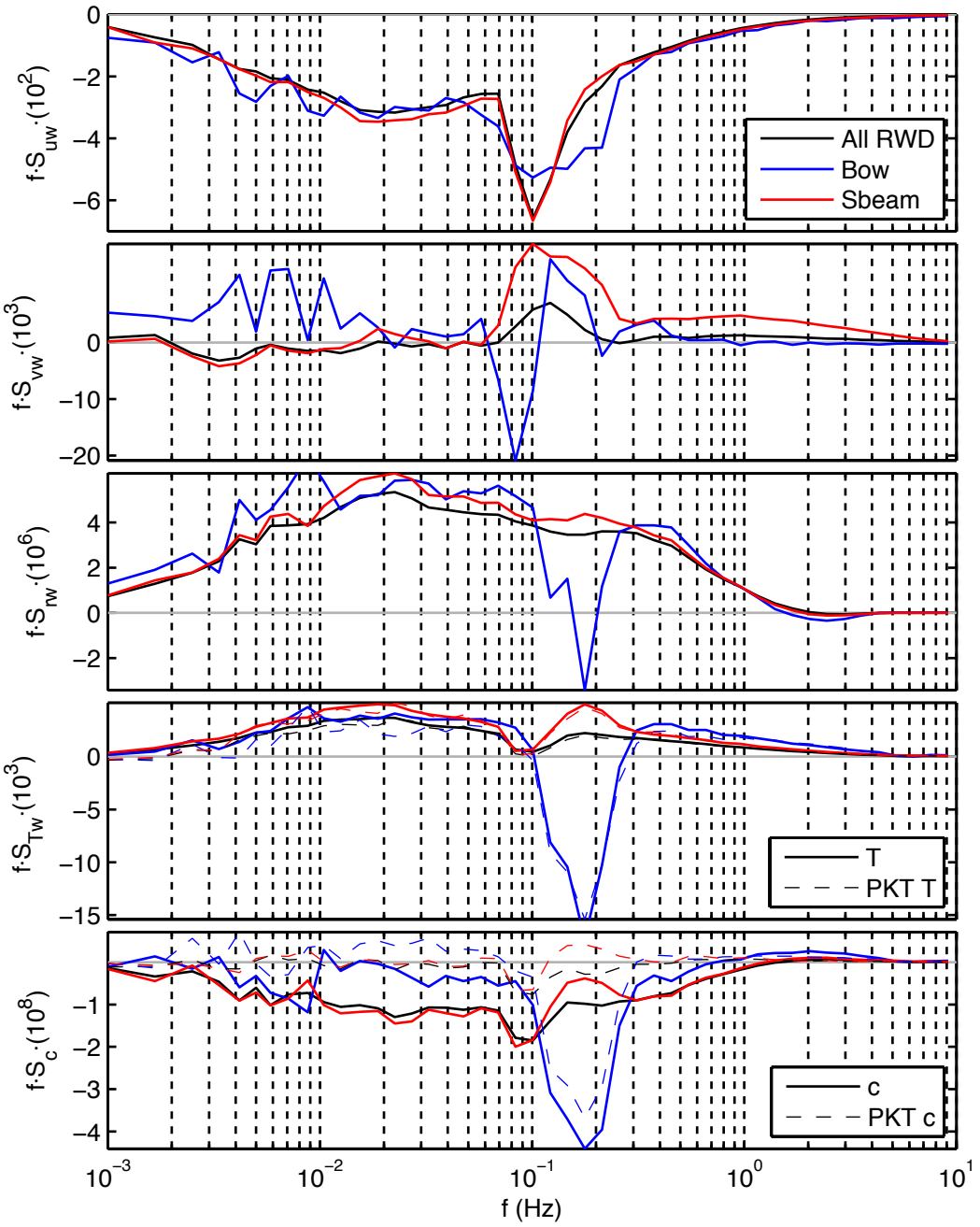

Figure 6.15. Averaged cospectra of fluxes obtained from 20-minute periods and separated by relative wind direction into bow-on (± 20°, n = 32) and 10° aft of starboard beam-on (± 20°, n= 470). The number of measurements at all relative wind directions is 815. Averages are of measurements obtained at wind speeds $10 \le U_{10n} \le 12$. Cospectra have been corrected for platform motion.

6.4.3 *Variation with wind speed*

The analysis in previous sections of this chapter has focused on a narrow range of wind speeds in order to compare spectra (and cospectra) without normalization. In this section the variation of the motion signal with wind speed will be examined, and spectra and cospectra at a wider range of wind speeds will be compared.

Averaged HiWASE variance spectra at a range of wind speeds are shown in Figure 6.16. Only periods when winds were away from the ship's bows are shown (outside 120°-240°, bow-on = 180°. Relative wind direction limits are discussed in Section 6.4.4). As expected, the wind spectral levels increase with wind speed. A 0.1 Hz peak is apparent at all wind speeds in the *u* and *w* spectra. In the *w* spectra for winds of 6-8 $m.s^{-1}$, there is a large low frequency spike at about 0.06 Hz. The spike is present in about 10% of the measurements. The low frequency signal may be due to ship maneuvers not removed by quality control procedures, but at such low frequency (an approximately 17 minute period) relative to the averaging period length, any signal will be poorly resolved and should be treated with caution. The signal does not result in any noticeable signal in the cospectra (Figure 6.17 and Figure 6.18).

A wave scale signal is also apparent in the scalar variance spectra at all wind speeds (Figure 6.16). For humidity, the signal is small and appears to slightly decrease with wind speed. The signal is slightly reduced by the head deformation correction (Chapter 5.5), suggesting that it is caused by deformation of the IRGA. At all wind speeds ranges except the highest, wave scale signal in the air temperature and PKT temperature spectra are similar. At the lowest wind speed range, the *PKT T* wave scale signal becomes very large, presumably due to a relatively large cospectral wave scale compared with the small temperature flux at these wind speeds. As previously discussed (Section 6.4.2), the PKT temperature has increased variance relative to the air temperature spectra, but the additional variance does not appear to correlate with the wind speed fluctuations. The CO_2 and PKT CO_2 variance spectra is dependent on both ΔpCO_2 and wind speed and hence does not display a simple increase in variance with increasing wind speed.

Average cospectra of the same measurement periods also demonstrate increasing variance with increasing wind speed (Figure 6.17). The momentum flux cospectra shows a wave scale signal, with a peak at about 0.1 Hz, which increases with wind speed. There is also a wave scale signal in the crosswind cospectra, and the variability

of the cospectra increases with wind speed. The humidity cospectra increase with wind speed, but a wave scale signal is not readily apparent.

The HiWASE air temperature cospectra (Figure 6.18) show a strong wave scale signal with an upward spike at about 0.2 Hz and a downwards spike at about 0.1 Hz. Both signals increase with wind speed, with the downward signal significantly increasing in size for winds above 12 $m.s^{-1}$. The frequencies at which these spikes occur suggests that the upwards signal may be a result of the spike in the temperature spectra, and the downwards signal may be a result of the wave scale signal in the *w* spectra. The *PKT T* cospectra have a similar shape and wind speed dependence to the air temperature cospectra. The CO_2 cospectra (Figure 6.18) also have a large downwards wave scale signal with a peak at 0.1 Hz. The signal is only apparent for wind speeds greater than 10 $m.s^{-1}$. At lower wind speeds, any wave-induced signal may be the same size or smaller than the normal CO_2 cospectral variability. The *PKT c* cospectra are similar, though with lower cospectral levels at all frequencies. Again, a significant wave scale signal is not apparent at winds below 12 $m.s^{-1}$.

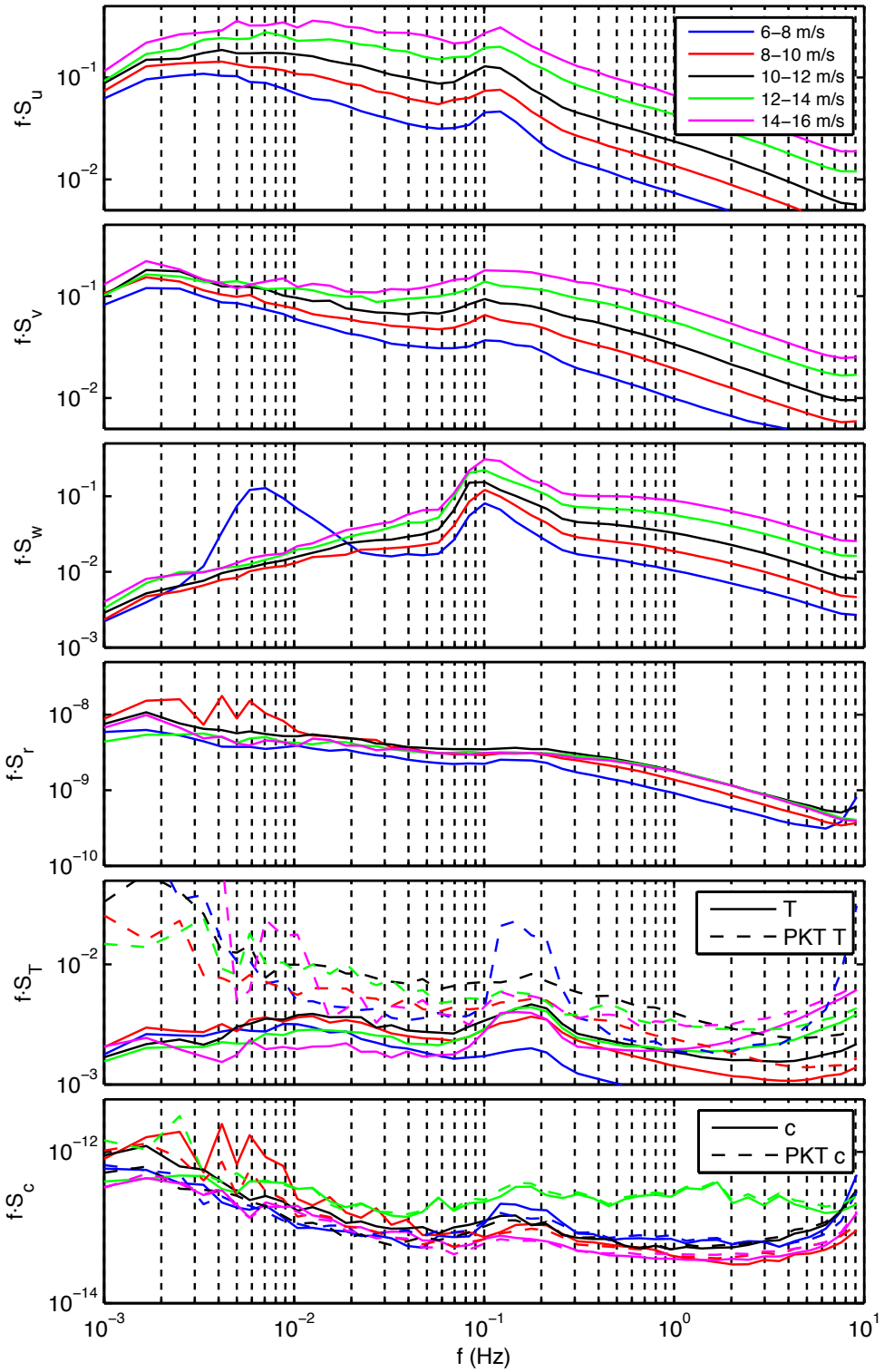

Figure 6.16. Averaged variance spectra of HiWASE 20-minute periods separated into U_{10n} ranges: 6-8 m.s^{-1} (n = 528), 8-10 m.s^{-1} (n = 577), 10-12 m.s^{-1} (n = 616), 12-14 m.s^{-1} (n = 336) and 14-16 m.s^{-1} (n = 136). Measurements have been corrected for platform motion. Periods with relative wind direction onto the bows (120°-240°), speed over the ground > 2 m.s^{-1}, or stable atmospheric (z/L > 0) have been removed.

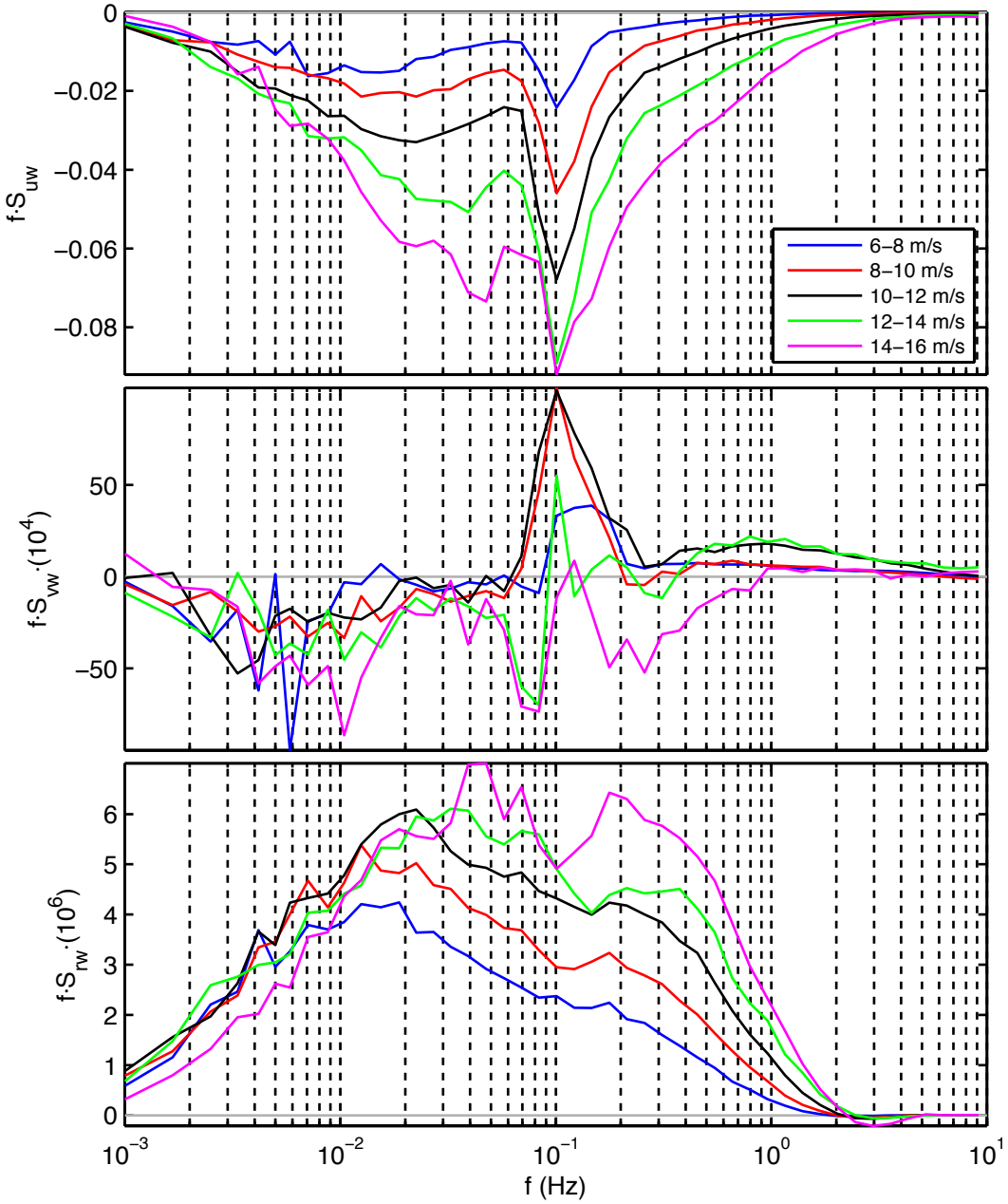

Figure 6.17. Along wind, crosswind and latent heat cospectra of the periods in Figure 6.16.

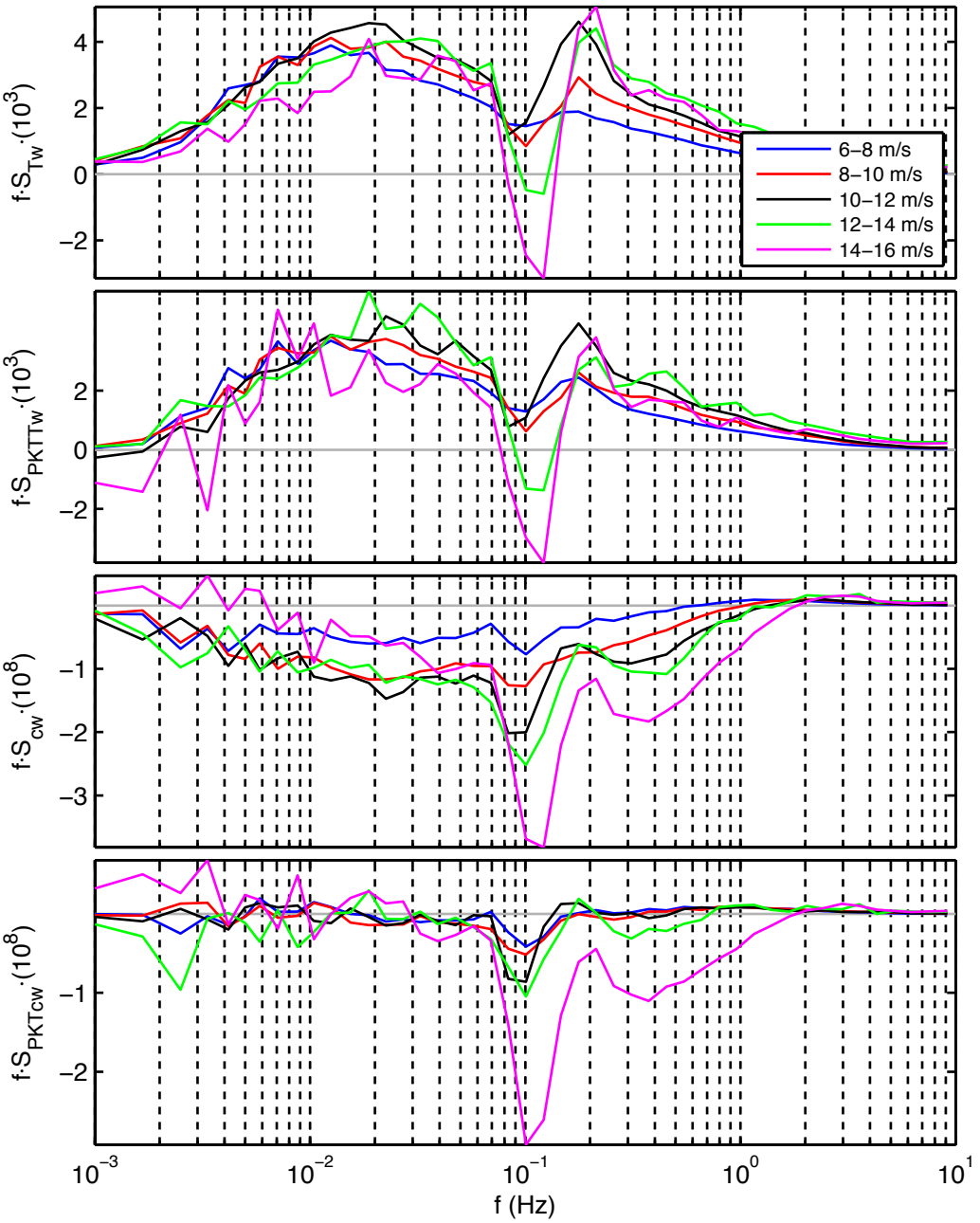

Figure 6.18. Temperature and CO_2 (with and without the PKT correction) cospectra of the periods in Figure 6.16.

6.4.4 Cospectral Motion Correction

6.4.4.a. Method

As discussed in Section 6.3.3, some unknown proportion of the flux resulting from the wave scale signal may be an error caused by platform motion, with the remaining proportion being real signal caused by wind-wave interaction. Removal of all of the wave scale signal flux from the PKT corrected CO_2 fluxes would allow the calculation of an upper bound on the possible influence of platform motion error on the HiWASE gas transfer velocity to wind speed relationship. The same is true for the other EC fluxes, as detailed in Chapter 7.

To remove the wave scale signal, the frequency range of the signal first needs to be defined. The SBWR wave spectra (Figure 6.1), platform motion (Figure 6.2) and wind vector measurements (Figure 6.3) suggest that a reasonable choice for frequencies corresponding to wave induced platform motion is 0.05 to 0.3 Hz. PKT corrected CO_2 cospectra, $S_{PKT\_C'w'}$ can thus be modified with an additional "motion correction" by replacing the cospectral values at the wave scale with a linear interpolation between the cospectral values at 0.05 Hz and 0.3 Hz (examples of this interpolation are shown in Figure 6.4).

The ratio of the new interpolated cospectra, $S_{PKT\_c'w'\_mc}$, to that of the original cospectra enables a fractional correction to be applied to the gas transfer velocity k obtained from the CO_2 flux in question:

$$k_{corr} = k \times (1 + ((S_{PKT\_c'w'\_mc} - S_{PKT\_c'w'}) / S_{PKT\_c'w'})) \qquad (6.2)$$

where k_{corr} is a gas transfer velocity with the wave scale signal removed. This additional, interpolation based motion correction, applied in this way, will be referred to henceforth as the Cospectral Motion Correction (CMC).

Individual PKT corrected CO_2 cospectra are very variable. Application of the CMC to individual 20-minute spectra resulted in some extreme transfer velocity values. The variability of individual spectra may lead to errors in applying the CMC. To investigate the significance of spectral variability on the CMC, the correction was also applied to averaged spectra. The wave scale signal is significantly larger for bow-on relative wind direction (RWD; Section 6.4.2). The sign of the signal can also be independent of the direction (into or out of the ocean) of the flux outside of the wave scale. The CO_2 cospectra were thus binned by wind speed (bin width of 2 $m.s^{-1}$),

relative wind direction (bow-on and beam-on as defined below) and direction of the flux at frequencies outside the 0.05 Hz to 0.3 Hz wave scale. The CMC was then determined for the binned fluxes and applied to each measurement within the bin. The CMC applied in this way is termed the "binned" CMC. Prior to applying the cospectral correction, 3938 CO_2 flux measurements were passed by quality control procedures. The CMC and binned CMC adjustments led to a further 135 measurements being removed by the transfer velocity cutoff limit of ± 900 cm.hr^{-1} (see Section 4.3 for details of quality control procedures). Note that whilst the binning in the CMC might be expected to reduce the uncertainty in the correction, the wind and wave conditions are likely to vary between samples, and hence the standard CMC is likely more appropriate than the binned CMC.

This section will describe the results of applying the CMC and binned CMC to the HiWASE PKT CO_2 fluxes. The results of applying the CMC to the other HiWASE EC fluxes are shown in Chapter 7.

6.4.4.b. Results

The HiWASE PKT corrected transfer velocities wind directions (n = 3803), are compared with the CMC and binned CMC results in the top panel of Figure 6.19. Note that the PKT results shown here differ slightly from those shown previously (Figure 4.6) and subsequently in this thesis (Figure 8.1) due to the requirement here of a one-to-one comparison of PKT with CMC results. The quality control applied to the CMC results reduces the overall number of measurements, resulting in changes to the PKT averages. The PKT transfer velocities binned by wind speed, and the percentage difference resulting from the PKT correction, are shown in Table 6.2. For wind speeds of up to 16 m.s^{-1}, the CMC and binned CMC are in very close agreement and reduce the gas transfer dependence on wind speed by a similar amount. Above 16 m.s^{-1}, the CMC and binned CMC do not agree quite as closely but there are only 43 measurements in the two highest bins (Table 6.2). The lowest wind speed bin, with a mean U_{10n} of 1.5 m.s^{-1} and containing 18 measurements, is significantly increased by both the CMC and binned CMC. There is very little flux at this wind speed and the signal to noise ratio may be too low for the CMC to give reasonable results.

To determine the wind speed dependence of the beam-on transfer velocities, least squares regression and the functional form used in McGillis et al., (2001a) is again used ($k_{660} = a + bU_{10n}^{n}$). The lowest wind speed bin was excluded from the curve fitting process. The least squares fit to the standard CMC measurements in the wind speed range 2-20 m.s^{-1} is $k_{660} = -0.09 + 0.02U_{10n}^{3.1}$ (r^2 = 0.99). The least squares regression to the binned CMC measurements in the wind speed range 2-20 m.s^{-1} is $k_{660} = 7.79 + 0.0008U_{10n}^{4.3}$ (r^2 = 0.92; top panel, Figure 6.19). The difference between the two fits is mostly due to the two highest wind speed bins.

The wave scale signal varies with relative wind directions (Section 6.4.2). The wave scale signal, and hence the CMC, is much larger for bow-on wind directions compared to other wind directions (Section 6.4.2). The bow-on wave scale signal is also larger for the other EC fluxes such as latent heat (Chapter 7). The strong wave scale signal with bow-on winds might explain the observed difference in the CMC and binned CMC at higher winds. To determine acceptable RWD limits for the CMC, the variation with RWD of the ratio of the wave scale signal to the total flux ($\left|S_{X'w'} - S_{X'w'\_mc}\right| / S_{X'w'}$) was determined (Figure 6.20). The ratio in the vertical wind spectra and scalar flux measurement was highest for relative wind directions of 120° – 240° and hence, this range was used as the definition of bow-on winds for the purposes of applying the CMC. Of the 3803 quality controlled PKT and CMC measurements available, 713 are defined as bow-on using this definition.

For most wind speeds ($2 \le U_{10n} \le 18$ m.s^{-1}), the bow-on PKT transfer velocities are higher than found in previous experiments, and the CMC and binned CMC reduce the binned transfer velocities, though by different amounts (middle panel, Figure 6.19). The CMC gas transfer velocities decrease with wind speed. The CMC results for bow-on winds suggest that for these measurements the wave scale signal is dominating the cospectra.

For relative wind directions away from the bow, the scatter in the PKT and CMC results is much smaller. Except for at the lowest wind speeds (< 2 m.s^{-1}), for beam-on relative wind directions (< 120° and > 240°, n = 3090), both the CMC and binned CMC reduce the PKT gas transfer velocities by a similar amount (bottom panel, Figure 6.19) and are in close agreement with each other even at the highest wind speed bin centred at 19 m.s^{-1}. The beam-on binned PKT transfer velocities, and the percentage difference resulting from the CMC and binned CMC, are shown in Table 6.3. The close agreement

between the two methods suggests that for these relative wind directions, the wave scale signal is being correctly removed at all wind speeds. However, the possibility that both methods are incorrectly modifying the fluxes (and that the wave scale signal may be a real component of the turbulent flux) cannot be ruled out.

The least squares fit to the standard CMC beam-on measurements in the wind speed range 2-20 m.s^{-1} is $k_{660} = -8.6 + 0.00735U_{10n}^{3.6}$ (r^2 = 0.98). The binned CMC gave very similar results to the standard CMC, with a least squares regression to the beam-on measurements in the wind speed range 2-20 m.s^{-1} resulting in $k_{660} = -8.6 + 0.0061U_{10n}^{3.7}$ (r^2 = 0.99; Figure 6.19). The highest correlation fit to the PKT beam-on measurements in the 0-20 m.s^{-1} wind speed range is: $k_{660} = -4.9 + 0.0663U_{10n}^{2.9}$ (r^2 = 0.94), i.e.: an approximately cubic relationship. In contrast the CMC results have a slightly stronger dependence on wind speed than that found in other experiments, when the functional form is usually quadratic or cubic.

6.4.4.c. Discussion

The HiWASE CO_2 transfer velocity results shown in Figure 6.19 provide an estimate of the possible range of platform motion error and/or real wave signal in the EC gas transfer measurements. If the standard motion correction procedures applied during HiWASE have successfully removed the platform motion signal from the measured wind, i.e. all the "wave scale" signal is due to a real influence of the waves on the fluxes, then the PKT transfer velocities are appropriate. In contrast, if the entire wave scale signal that remains after applying the standard motion correction is caused by platform motion, or some other measurement-related cause such as flow distortion (Chapter 7) then the CMC transfer velocities are the best estimate. The percentage difference for each wind speed bin following application of the CMC and binned CMC is shown in Table 6.2 (all relative wind directions) and Table 6.3 (beam-on winds). At low wind speeds (below about 8 m.s^{-1}) the CMC transfer velocities are very small and the percentage changes are thus very high. The wave scale signal in the low wind speed CO_2 flux is a significant portion of the integrated CO_2 cospectra (e.g.: Figure 6.18). There is also little CO_2 signal relative to noise at low winds (Chapter 5) and hence, the CMC may only be adding noise at these wind speeds.

For moderate to high wind speeds ($7 \le U_{10n} \le 20$ m.s^{-1}), the possible error due to platform motion effects may explain approximately 20-50% of the signal in the CO_2 fluxes (Table 6.2 and Table 6.3). Although the wave scale signal increases in size with

increasing wind speed (Section 6.4.3), the size of the signal relative to the integrated CO_2 cospectra decreases with wind speed.

The dependence on relative wind direction of the wave scale signal in the cospectra (Figure 6.15) suggests that at least some of the wave scale signal is due to platform motion. However, the artificial selection of rougher seas with bow-on winds, and the resulting larger bow-on wave signal (e.g.: Figure 6.1 and Figure 6.2), means that a wind-wave interaction signal could be higher for bow-on winds.

The standard error of the measurements is large and the PKT and CMC results are usually less than two standard errors apart. At lower winds speeds (< 12 $m.s^{-1}$) most previously published relationships are within 2 standard errors of the mean of the HiWASE measurements. With or without the CMC, the HiWASE transfer velocity results (top and bottom panel, Figure 6.19) have a cubic or higher dependence on wind speed. At wind speeds over 15 $m.s^{-1}$, the beam-on CMC results are higher than those reported in previous air-sea gas transfer experiments. Note however, that the relationships from previous experiments are extrapolated for winds over 15 $m.s^{-1}$. For all relative wind directions (top panel, Figure 6.19), if the two highest wind speed bins are excluded from the least squares fits to the HiWASE measurements, then again the approximately cubic dependence of the HiWASE results is independent of the wave scale signal. Therefore, despite the large scatter in the results, they demonstrate that the observed cubic relationship of gas transfer with wind speed is not dependent on the wave scale signal.

Table 6.2. HiWASE transfer velocities as shown in the top panel of Figure 6.19. The percentage differences of the CMC or binned CMC binned transfer velocities relative to the PKT values are shown in brackets. The number of measurements in each bin is also shown.

U_{10n} bin ($m.s^{-1}$)	***n***	**PKT k_{660} ($cm.hr^{-1}$)**	**CMC k_{660} ($cm.hr^{-1}$)**	**Binned CMC ($cm.hr^{-1}$)**
0-2	18	0.3	-	-
2-4	154	1.3	1.5 (9)	0.1 (-93)
4-6	365	13.8	7.2 (-48)	3.8 (-72)
6-8	752	18.7	2.9 (-84)	3.3 (-82)
8-10	906	42.3	19.8 (-53)	26.2 (-38)
10-12	890	57.0	25.8 (-55)	30.7 (-46)
12-14	469	109.0	49.9 (-54)	74.2 (-32)
14-16	206	168.6	87.5 (-48)	101.9 (-40)
16-18	38	259.4	107.8 (-58)	82.9 (-68)
18-20	5	203.2	164.3 (-19)	236.8 (17)

Table 6.3. Beam-on (relative wind direction less than 120° and greater than 240°, bow-on = 180°) HiWASE transfer velocities as shown in the bottom panel of Figure 6.19. The percentage differences of the CMC or binned CMC binned transfer velocities relative to the PKT values are shown in brackets. The number of measurements in each bin is also shown.

U_{10n} bin ($m.s^{-1}$)	n	PKT k_{660} ($cm.hr^{-1}$)	CMC k_{660} ($cm.hr^{-1}$)	Binned CMC ($cm.hr^{-1}$)
0-2	7	23.5	101.3 (331)	97.7 (316)
2-4	122	-10.2	-10.0 (-2)	-11.1 (8)
4-6	293	11.6	7.5 (-35)	3.6 (-69)
6-8	627	11.3	2.5 (-78)	-0.2 (-102)
8-10	751	17.1	6.9 (-60)	10.6 (-38)
10-12	737	28.5	14.4 (-49)	15.2 (-47)
12-14	367	85.7	46.3 (-46)	62.1 (-28)
14-16	162	162.6	101.1 (-38)	105.5 (-35)
16-18	21	277.3	176.8 (-36)	169.3 (-38)
18-20	3	301.6	257.1 (-15)	281.0 (-7)

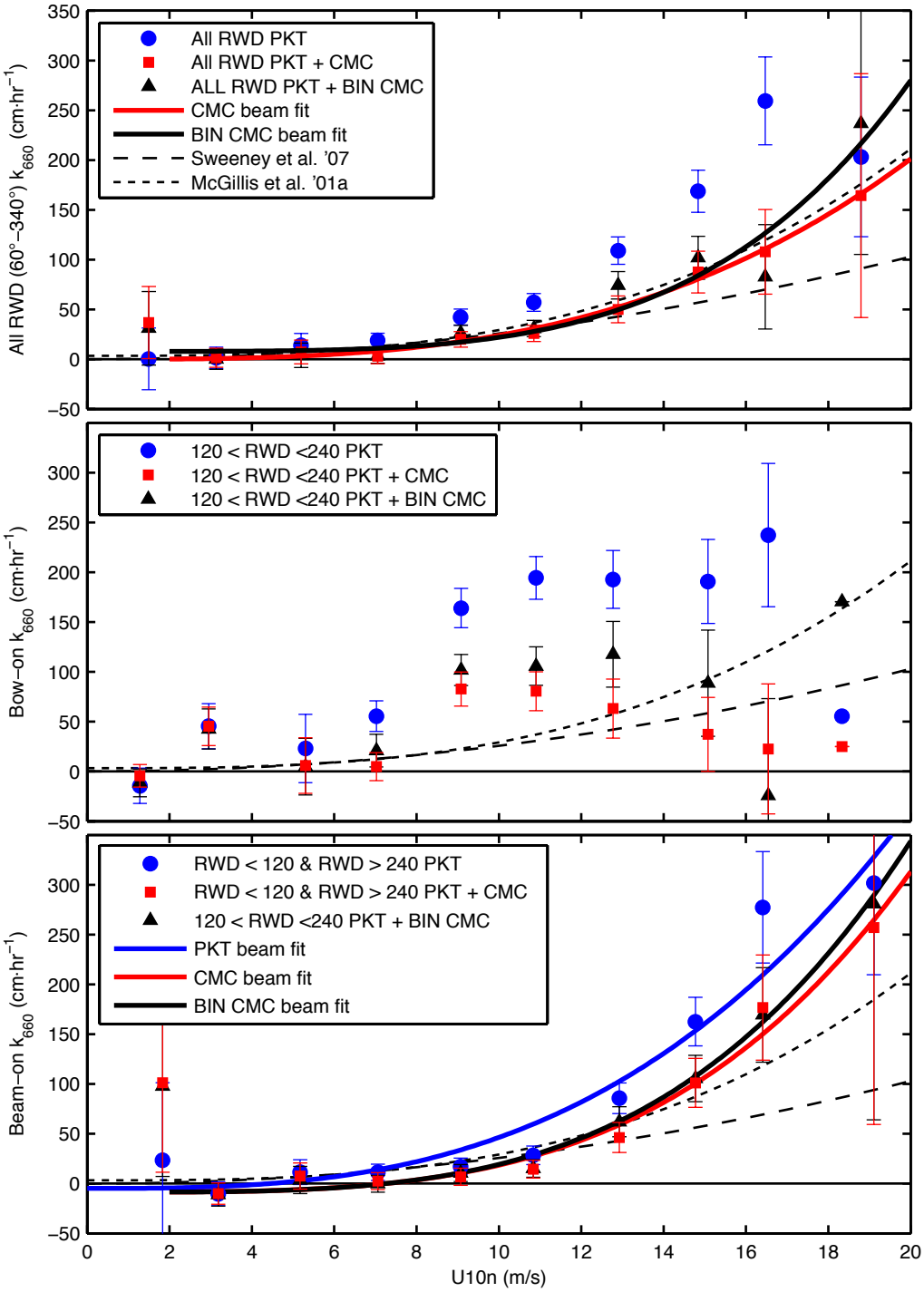

Figure 6.19. HiWASE transfer velocities. Results as indicated in the key are described in the text. Measurements binned by U_{10n} in 2 m.s^{-1} wide bins. Error bars show standard error. Measurements are shown sub-divided by Relative Wind Direction (RWD). Top panel, all acceptable RWD: Fore LICOR: 60°-340°, Starboard LICOR 90°-340°, bow-on = 180° (n = 3803). These measurements are divided into bow-on (middle panel, n = 713) and beam-on (bottom panel, n = 3090). Also shown are least squares fits to the measurements as indicated in the key, with the lowest wind speed bin excluded from the CMC fits.

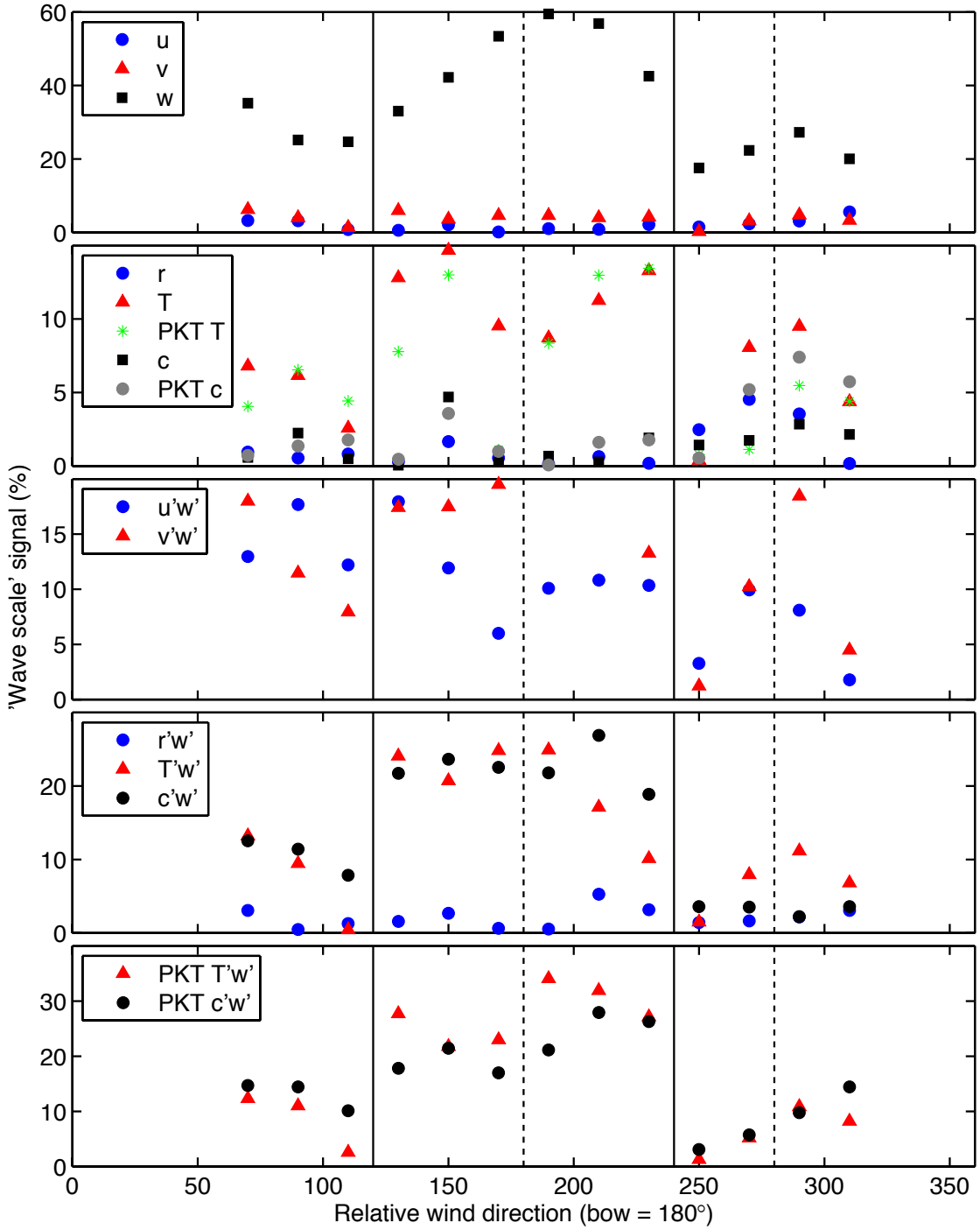

Figure 6.20. Variation of the fractional wave scale signal (%) in the EC spectra and fluxes with relative wind direction. Spectra and cospectra are averaged in relative wind directions bins (bin width = 20°). "Wave scale signal" is defined in the text. Periods included are at measured wind speeds of $10 \le U_{10n} \le 15$ m.s^{-1} (n = 1626). Averages of less than 3 measurements are not shown. Dashed lines indicate bow and starboard beam directions.

6.5. Summary and conclusions

Wind vector measurements that are obtained onboard a moving platform will be contaminated by motion of the platform (Section 6.2). This must be corrected in order to accurately measure the turbulent airflow and obtain measurements of the air-sea fluxes. This chapter has described the results of applying a standard motion correction procedure (Edson et al., 1998) to the wind measurements obtained during HiWASE. The correction removes a substantial proportion of the wave scale signal in the variance spectra, cospectra and fluxes (Section 6.3). However, some residual wave scale signal does remain in the wind and temperature spectra. The residual signal may be caused by real, wave-induced fluctuations, or it may be due to incomplete removal of the platform motion signal (Section 6.4.1). The residual signal is larger for winds (and hence often also waves) onto the ship's bow, which lead to a greater range of motion at the ship's bow compared with rolling of the ship caused by beam-on wind and waves (Section 6.4.2). The *Polarfront* operations artificially select bow-on wind and wave directions during rougher conditions. Hence, the measured platform motion is significantly higher when the winds are bow-on to the ship (Section 6.2).

The motion correction method and resulting spectra and cospectra from HiWASE are similar to results obtained in other air-sea flux experiments performed on moving platforms (e.g.: McGillis et al., 2001a: Figure 6.5; McGillis et al., 2004; Miller et al., 2008: Figure 6.6). In particular, the wave scale signal observed in the HiWASE measurements is of a similar magnitude to that often observed in the other experiments (Section 6.3.3). A residual wave scale signal of similar size to that observed in HiWASE is also reported in some EC experiments conducted from fixed platforms (e.g.: DeLeonibus, 1971). However, since previous studies do not quantify the wave scale signal seen in their results, it remains uncertain what proportion of the wave scale signal in the HiWASE fluxes is due wind-wave interaction and what proportion is due to incomplete platform motion correction.

Motion correction procedures applied in other air-sea flux experiments on moving platforms (e.g.: Edson et al., 1998; McGillis et al., 2001a; McGillis et al., 2004; Miller et al., 2008; Miller et al., 2010) are similar to those used in HiWASE. If a significant portion of the residual wave scale signal is due to platform motion, then other EC gas transfer experiment results may be similarly affected by platform motion contamination.

The residual wave scale signal poses a significant challenge in attempting to determine seastate influences on air-sea fluxes measured with EC (see discussion in Section 6.3.3). Greater understanding of the effect of wind-wave interactions on turbulent transfer is required to improve the parameterisation of air-sea gas transfer.

Removal of the residual wave scale signal from the cospectra using a simple correction method (termed the CMC correction, Section 6.4.4) allows an estimation of the maximum error that could be caused by incomplete platform motion correction. Two different methods for applying the CMC have been tested. With the highly variable bow-on measurements removed, the results of applying both methods agreed very closely for the full range of wind speeds (up to 20 $m.s^{-1}$), suggesting that the wave scale signal is being successfully removed. If, as is likely, the wind and wave conditions are varying between samples, then the standard CMC is more appropriate than the binned CMC. In addition, the standard CMC method results in a smoother, less scattered relationship, and a higher correlation of the least squares fit, than the binned CMC (r^2 = 0.99 versus r^2 = 0.92). Hence, the standard CMC is preferred for the remainder of this thesis.

Removal of the entire wave scale signal reduces the (binned by wind speed) gas transfer velocities by approximately 20-50%. The relative size of the wave scale signal in the CO_2 cospectra, and hence the effect of the CMC, reduces with increasing wind speed. Both the complete set (i.e.: all acceptable relative wind directions) and beam-on HiWASE gas transfer velocity results, with or without the CMC, suggest that a strong (cubic or higher) dependence on wind speed is appropriate. Despite the large scatter in the measurements, the CMC demonstrates that the cubic relationship of gas transfer to wind speed observed in the HiWASE measurements is not dependent on either platform motion correction error or on wind wave interactions.

7. Flow distortion

7.1. Introduction

Large structures such as ships cause distortions to airflow approaching and passing over the structure. This modification of the airflow is referred to here and elsewhere simply as flow distortion. The distortion can affect the speed, height and turbulent characteristics of the airflow (e.g.: Oost et al., 1994). Both EC and ID flux measurements can be affected by flow distortion. EC flux measurements require the determination of airflow turbulence at a wide range of frequencies, and are thus affected by any change to the turbulence caused by flow distortion. ID flux measurement is dependent on a smaller, high frequency range of turbulence: the inertial subrange. The relatively small eddies within this range have been shown not to be significantly affected by flow distortion (Edson et al., 1991; Oost et al., 1994). Unlike EC, ID flux measurements are dependent on the height at which the measurement is made and will be affected by any change in the height of the airflow caused by flow distortion. Additionally, the dependence of measured fluxes on wind speed is often of interest in air-sea interaction experiments. If the measured wind speed is affected by flow distortion then, regardless of the flux measurement technique used, a further error will be introduced into the relationship of the flux to wind speed and to the calculation of the transfer coefficients. Flow distortion effects are strongly dependent on relative wind direction (e.g.: Yelland et al., 1998), and may thus be correlated with errors resulting from incomplete platform motion correction (Chapter 6).

This chapter examines the impact of flow distortion on the HiWASE flux measurements, with the aim of quantifying the flow distortion effect on the EC CO_2 flux measurements. Modeling of the airflow over *Polarfront* has enabled the effects of flow distortion on the airflow height and mean speed to be estimated, and corrections determined (Section 7.2). A comparison of HiWASE ID and EC measurements with bulk estimates allows the impact of flow distortion on the momentum (Section 7.3), latent heat (Section 7.4.1) and sensible heat fluxes (Section 7.4.2) to be estimated.

The momentum flux results demonstrate the successful measurement of this flux with both the EC and ID techniques during HiWASE, and allow the results of the CFD correction on the vector measurements to be examined. The latent heat and sensible heat flux results give insight into the effect of flow distortion on turbulent scalar flux measurements, in particular through the comparison of the CFD corrected (and hence

assumed free of flow distortion effects) ID latent heat flux measurements and the EC latent heat fluxes. By assuming that the effect of flow distortion on the EC CO_2 fluxes is analogous to the effect on the EC latent heat fluxes, the impact of flow distortion on the gas transfer velocity measurements can be estimated (Section 7.5). This is a reasonable assumption since a), both are scalars and should be affected in the same way by any impact of flow distortion on the vertical wind fluctuations, and b), both are measured by the same sensor.

The number of HiWASE flux measurements included in the various analyses in this chapter varies due to the different quality control criteria applied, as described here. Momentum and sensible heat flux measurements are made using the Sonic on the *Polarfront's* foremast. The acceptable relative wind direction limits for these fluxes are 60°-340° (bow-on = 180°). The latent heat and CO_2 fluxes are derived from density measurements made by the IRGAs combined with the Sonic data and have additional quality control criteria applied and so fewer measurements are available for analysis. The same quality control criteria used for CO_2 fluxes are applied here to latent heat and sensible heat fluxes to make the heat flux datasets better proxies for determining flow distortion effects on the CO_2 flux dataset. CO_2 and humidity measurements are made with one of two IRGAs. The relative wind direction limits are dependent on which IRGA is used. If the fore IRGA is used, the acceptable limits are 60°-340°. If the starboard IRGA is used, the acceptable limits are 90°-340°. Further relative wind direction criteria are discussed in the text. More detail on quality control criteria is given in Section 4.3.

7.2. Flow distortion modeling.

Numerical Computational Fluid Dynamic (CFD) modeling has been successfully used to estimate the modification to the mean airflow caused by the structure of several different research ships (Yelland et al., 2002). CFD modeling allows the flow distortion induced changes to mean height and speed of the airflow to be estimated. It is therefore possible to use CFD modeling to correct both ID fluxes and the mean wind speed for the effects of flow distortion. It is not possible to use the CFD technique to determine the modification to the turbulence characteristics resulting from flow distortion (e.g.: Oost et al., 1994). Therefore, EC fluxes cannot be directly corrected using the results of CFD modeling.

The flow distortion caused by a particular ship is strongly dependent on the size and shape of the vessel and the airflow modeling must be carried out for each vessel for which a flow distortion correction is required. Additionally, flow distortion effects are observed to vary significantly with relative wind direction (e.g.: Yelland et al., 1998; Yelland et al., 2002). Hence, the determined corrections are only appropriate for a relatively narrow range of wind directions about that at which they were determined (approximately ± 10 °).

CFD modeling of the airflow over *Polarfront* has been used to obtain estimates of the flow distortion effects on the flow height and mean wind speed for bow-on and 10° aft of starboard beam-on winds (Moat and Yelland, 2009). As the most frequent mean relative wind direction for the *Polarfront* whilst on-station is 10° aft of the starboard beam (using the standard meteorological convection of wind direction TO), this relative wind direction (i.e.: 280°, bow-on = 180°) was used in place of the true starboard beam direction (at 270°). The change to the airflow was determined at the location of the Sonic on the *Polarfront's* foremast and took account of the Sonic's position changes during the course of HiWASE.

The CFD modeling found that flow distortion effects were largely independent of wind speed (Yelland et al., 2002). The CFD modeling determined that for winds onto the *Polarfront's* bow, the mean wind speed at the effective measurement height (i.e. actual height minus vertical displacement) was biased low by less than 0.5% and the flow height was displaced approximately 1.3 m upwards. For winds 10° aft of the starboard beam, the CFD modeling determined that at the anemometer location the wind speeds were biased 8% high and displaced approximately 4.4 m upwards. The flow height adjustment during the beam-on model runs began occurring approximately 7 seconds upstream from the vessel. Due to the relatively long period over which the beam-on flow height changes, the level of turbulence of the flow may adjust in some part prior to reaching the Sonic (Yelland et al., 2002). Due to the uncertainty in the height adjustment of the beam-on wind flow, the beam-on flow distortion corrections were not automatically applied to the HiWASE ID fluxes or to the measured wind speed. To ensure that there was not a step change in the wind speeds and ID fluxes with relative wind direction, all ID fluxes (i.e.: momentum and latent heat fluxes) and neutral 10 m wind speed, U_{10n}, measured onboard *Polarfront,* regardless of relative wind direction, were adjusted with the bow-on flow height correction (i.e.: fluxes and wind speed were adjusted as if the measurement height was 1.3 m lower). As the bow-on

wind speed bias was small, less than 0.5%, only the height adjustment was applied to the bow-on wind speed measurements.

On *Polarfront*, the IRGAs used for fast response measurement of humidity and CO_2 are offset vertically (by approximately 1 m) and horizontally (by approximately 60 cm) from the location of the Sonic. The flow distortion biases at the effective measurement heights of the IRGAs will therefore be different to those determined at the location of the Sonic, but are not currently available from the CFD analysis. This may affect the scalar flux measurement. Flux measurements with spatially separated sensors may also be subject to flux attenuation effects through a loss of correlation between the sensors at small scales (Nilsson et al., 2010). This may affect measurements made with the two IRGAs differently due to their different position offsets from the Sonic.

7.3. Momentum flux

7.3.1 Previous experimental results

Measurements of the momentum flux, F_u, were made during HiWASE using both the EC and ID technique. The neutral 10 m drag coefficients, CD_{10n}, obtained from these techniques are compared with bulk estimates of the drag coefficient in Figure 7.1. The bulk estimates shown were obtained in previous experiments from both EC and ID measurements on various types of platform. The relationship of Smith (1980) was derived from EC measurements at a height of 13.4 m on a well-exposed tower. The tower was in 60 m of water, approximately 10 km off the northwest Canadian coastline. The tower was securely tied down and designed to withstand high winds and seas. However, it was found to be subject to slight motion effects, and a wave scale signal with a magnitude of up to 15% of the flux was present in some of the measurements. The measurements used were obtained in long fetch and near neutral atmospheric conditions.

EC measurements from the same tower, combined with ID measurements from a research vessel, were used to derive the drag coefficient relationship of Large and Pond, (1981). This relationship was based on 1591 measurements (1-hour averages), more than 10 times as many as used by Smith (1980). For wind speeds above 10 $m.s^{-1}$, this relationship agrees closely with that of Smith (1980).

The relationship of Yelland et al. (1998) was derived from ID measurements onboard a large research ship, with a CFD derived correction applied to remove the

effects of flow distortion. The measurements used were obtained from bow-on (± 10°) winds in open ocean conditions. The Yelland et al., (1998) and Smith (1980) bulk estimates are in close agreement with one another for wind speeds from 6-22 $m.s^{-1}$. An increase in drag coefficient with increasing wind speeds (for moderate to high wind speeds) is found in these and most other experimental results.

7.3.2 HiWASE results

A large data set of momentum flux measurements was obtained during HiWASE. For the analysis presented here, measurements were excluded if: the relative wind direction was outside 60°-340° (bow-on = 180°); the crosswind to along wind flux ratio was larger than 1; or if the ship speed over ground was larger than 2 $m.s^{-1}$ (approximately 4 kn). Other quality control criteria applied to all HiWASE measurements are described in detail in Chapter 4.

At low wind speeds there is significant uncertainty in the relationship of the drag coefficient to wind speed, and many parameterisations in the literature do not extend to low winds. Due to the focus of the HiWASE experiment on high wind speeds, factors that may influence low wind speed fluxes such as surfactants or convective flux were not investigated. As such, whilst all wind speeds are included in the analysis, the discussion in this chapter will focus on flux measurements at wind speeds above 6 $m.s^{-1}$, which constitute 92% of the total available measurements.

All ID fluxes and wind speeds are corrected for the modeled rise in flow height determined for bow-on winds (Section 7.2). The bow-on ID drag coefficients are in good agreement with the bulk estimates for wind speeds of 7-23 $m.s^{-1}$, (b, Figure 7.1). For winds onto the *Polarfront's* starboard beam, the ID drag coefficients are biased low by approximately 20% relative to the bulk estimates (c, Figure 7.1), but are brought into much better agreement if the CFD derived wind speed adjustment of -8% is applied (d, Figure 7.1). With the appropriate CFD wind speed adjustments applied, the starboard beam and bow-on ID momentum fluxes agree very closely with one another. This implies that the effects of flow distortion have been successfully corrected for with the CFD modeling.

The CFD modeling suggests that airflow onto the *Polarfront's* starboard beam is raised in height by 4.4 m. This large change in flow height was found to begin some distance away from the vessel. It is not possible to adjust the starboard beam-on measurements for the effect of flow height displacement due to the unknown adjustment

of the flow turbulence to the height change prior to measurement (Section 7.2). As a result, measurements from all directions are adjusted by the flow height change determined for bow-on winds of 1.3 m. If the height change for the starboard beam-on airflow was larger than 1.3 m, then the ID drag coefficient measurements should be biased high. The mean difference between the bow-on and starboard beam-on ID measurements is of the order 4 % (the starboard measurements are ~ 4% higher than the bow-on measurements), suggesting that any error resulting from flow height change is small, and that the starboard beam-on turbulence has adjusted to some degree to the change in flow height.

EC drag coefficient measurements onboard *Polarfront* do not exhibit a physically realistic dependence on wind speed (Figure 7.1). EC measurements for wind directions within ± 10 ° of bow-on (b, Figure 7.1) and starboard beam-on relative wind directions (c, Figure 7.1) show either a negative slope or no dependence on wind speed. The beam-on wind speed adjustment (d, Figure 7.1) does not improve the EC CD_{10n} to wind speed relationship. At wind speeds below about 15 $m.s^{-1}$, the EC measurements overestimate the drag coefficient (relative to bulk estimates and ID measurements) whilst for higher winds the EC measurements underestimate the coefficient. The EC drag coefficients for bow-on winds show an extremely unrealistic (negative) dependence on wind speed. For bow-on wind directions, the CFD modeling suggests that the effect of flow distortion will be small, whilst the residual wave scale signal in the bow-on cospectra was found to be large (Chapter 6). The error in the bow-on EC drag coefficients is thus likely due to platform motion.

Application of the CMC (Chapter 6.4.4) to the EC momentum fluxes results in drag coefficient measurements that have a physically realistic relationship with wind speed (i.e.: increasing). For bow-on measurements, removal of the residual wave scale signal from the EC momentum flux with the CMC somewhat overcorrects the bias in the EC drag coefficients (b, Figure 7.1). For wind speeds less than ~ 14 $m.s^{-1}$, the CMC measurements are low relative to the bulk or ID measurements. For higher wind speeds, the CMC measurements are biased high. For these wind directions, the relative size of the wave scale signal removed by the CMC can be very large. There may be too much uncertainty in the bow-on cospectra for the CMC to work correctly, or the correction may be removing a significant real wave correlated signal.

The beam-on CMC drag coefficients are in reasonable agreement with the bulk estimates for wind speeds of 6-18 $m.s^{-1}$ (c, Figure 7.1). Following application of the -

8% CFD wind speed adjustment, the CMC measurements are in good agreement with bulk and ID measurements for wind speeds of 6-12 $m.s^{-1}$. At higher winds, the CMC measurements are biased high, suggesting that the CMC is overcorrecting, though to a lesser extent than for the bow-on measurements. (d, Figure 7.1).

The effect of the CMC on the HiWASE measurements is to reduce the EC flux at low winds and increase the flux at high winds. This suggests that the wave scale signal removed by the CMC is not caused by wind-wave interaction; however, it is not currently possible to distinguish a wave-correlated signal from platform motion error. The CMC does not reduce the variability of the EC drag coefficients. The variability of the ID measurements is approximately half that of the CMC and EC measurements.

7.3.3 Drag coefficient variation with wind direction

The variation of the HiWASE drag coefficient measurements with relative wind direction is shown in Figure 7.2. The starboard beam-on measurements shown here have been adjusted with the CFD derived -8% wind speed adjustment. The ID and CMC measurements display a similar dependence on relative wind direction. As described in Chapter 6.4.1, this is difficult to interpret: either a) the wave scale signal removed by the CMC is primarily due to platform motion, which does not affect the ID measurements, or b) the majority of the wave scale signal is caused by wind wave interaction, and this interaction is not measured by the ID technique.

The ID and CMC measurements suggest that flow distortion effects increase as winds move away from bow-on. For ID measurements, the results in Figure 7.2 show that much of this error can be corrected for using the CFD derived corrections. The EC measurements show less variation with wind direction, though as shown in Figure 7.1, this may be due to platform motion related errors. A wide wind speed range is used in Figure 7.2 ($6 \leq U_{10n} \leq 20$ $m.s^{-1}$) and hence, the EC underestimates of the drag at low wind speeds, and overestimates of the drag at high wind speeds (Figure 7.1) will cancel out to some degree, resulting in mean values that appear more reasonable. The starboard beam CFD wind speed correction worsens the agreement between the EC measurements and the bulk estimate.

7.3.4 Discussion

The use of the ID technique to measure air-sea fluxes is an area of ongoing debate (e.g.: Yelland et al., 1998; Janssen, 1999; Taylor and Yelland, 2001b; Janssen, 2001). Janssen (1999) suggested that the ID technique may underestimate the surface stress at high winds (> 15 $m.s^{-1}$) due to neglecting wave induced pressure fluctuations in the calculation of the TKE budget. Janssen (1999) suggests that due to the uncertainty regarding the assumptions in the ID technique, the EC technique should be preferred for measurement of air-sea fluxes. In contrast, Taylor and Yelland (2001b) argued that their in situ data at two different measurement heights were in good agreement, with those at 17.5 m being only a few % larger than those at 5.5 m, suggesting that any wave-induced effects were very small. The HiWASE ID drag coefficients are in good agreement at high wind speeds with a bulk estimate obtained from EC measurements from a fixed tower (Smith, 1980). However, the HiWASE EC drag coefficients at high wind speeds are biased low relative to the ID measurements and bulk estimates, suggesting that any increase in drag coefficient due to pressure fluctuations is masked by the apparent platform motion error in the EC measurements. Whilst the CMC beam-on fluxes are similar to the bulk and ID estimates, this does not rule out the significance of pressure fluctuations: any wave induced pressure fluctuation effects on the momentum flux cospectra would presumably be apparent within the frequency range associated with wave motion, and would thus be removed by the CMC. Thus, it may be that either the ID and CMC measurements similarly do not account for a proportion of the air-sea flux, or that the wave induced stress is very small.

It is interesting that other ship based experiments use a wide range of wind directions. Figure 7.1a suggests that this approach may well be masking some problems in other datasets. For example, Yelland (1997, pages 121-122) pointed out that Large and Pond (1982) selected their 135° "appropriate" relative wind direction range for their ship-based data by comparing that data with data from the tower.

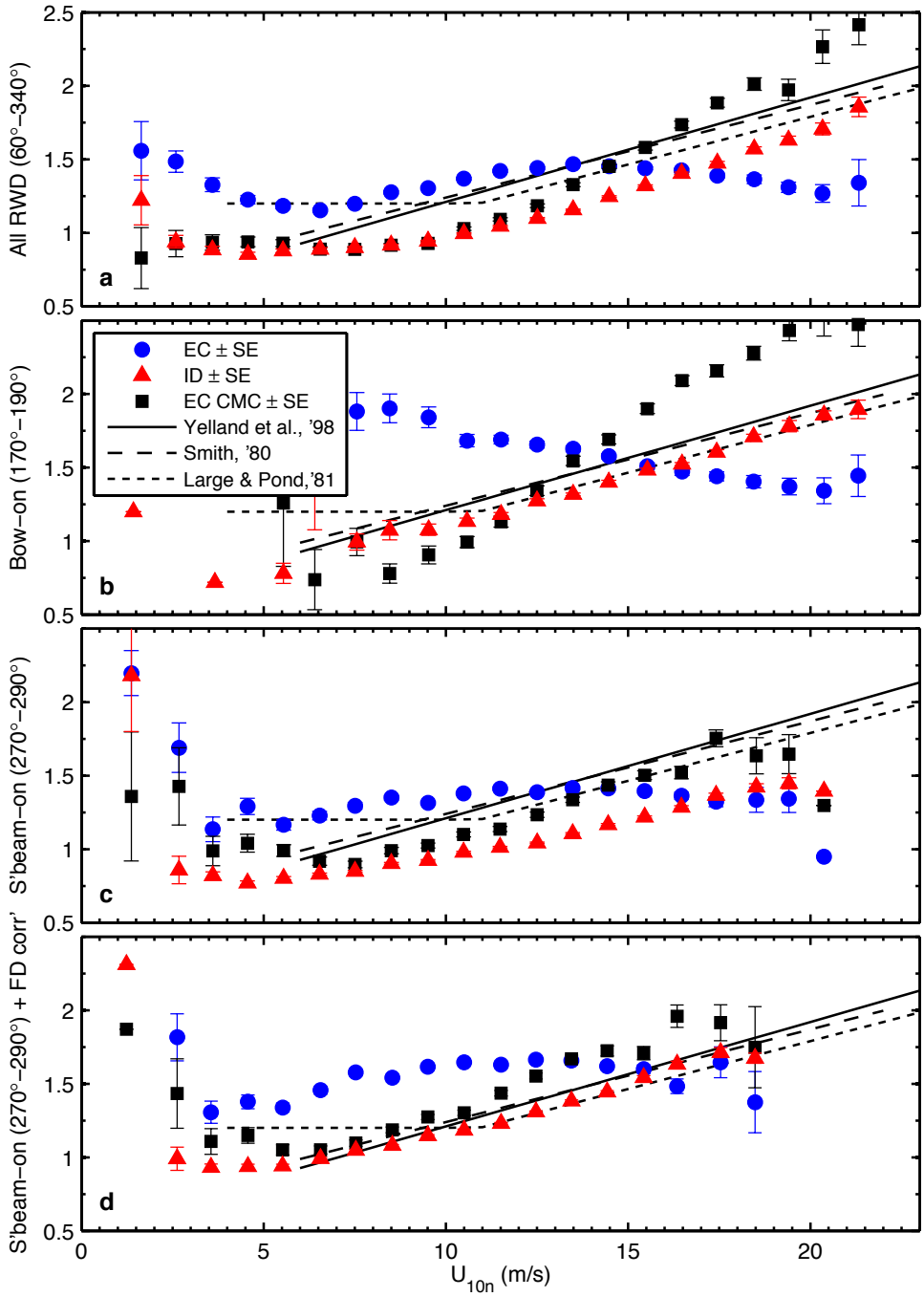

Figure 7.1. Neutral 10 m drag coefficients (1000 CD_{10n}) measured during HiWASE using the ID, EC and CMC techniques as indicated in the key. Measurements are binned by U_{10n} (bin width = 2 m.s^{-1}). The panels show measurements obtained from three relative wind directions, a) 60°–340° (n = 17944), b) 170°-190° (n = 1927), and 270°–290° (n = 6736), without (c) and with (d) the CFD modeling derived -8% wind speed correction (FD corr'). Measurements made when the ship was steaming (speed over ground > 2 m.s^{-1}) and outlier values (1000 CD_{10n} outside the range 0-3, n = 1435) have been removed from the analysis. Also shown are three bulk parameterisations from the literature.

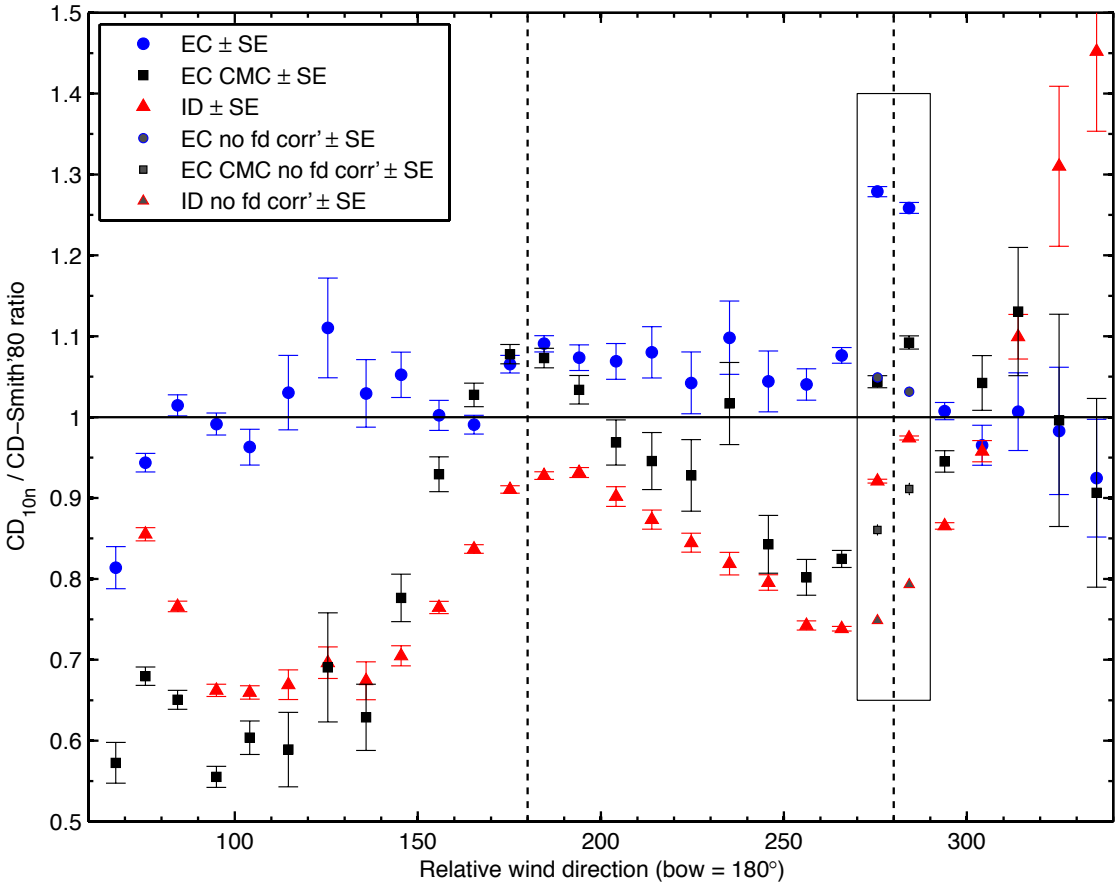

Figure 7.2. Variation of Neutral 10 m drag coefficients (1000 CD_{10n}) measured during HiWASE with relative wind direction. Results (n = 16,163) as indicated in the key are divided by a bulk drag coefficient (Smith, 1980) and binned by relative wind direction (bin width = 10°). Starboard beam-on (280° ± 10°) measurements have been adjusted with the CFD modeling derived -8% wind speed correction. Measurements made at wind speeds outside of the range $6 \leq U_{10n} \leq 20$ m.s^{-1} (n = 2104), when the ship was steaming (speed over ground > 2 m.s^{-1}) and outlier values (1000 CD_{10n} outside the range 0-3, n = 608) have been removed from the analysis. The dashed lines indicate the bow-on and nominal starboard beam-on directions. Box indicates those relative wind directions for which the CFD derived -8% wind speed adjustment was determined, and data are shown with and without ("no fd corr'") the adjustment.

7.4. Flow distortion effects on scalar fluxes

7.4.1 Latent heat flux

Flow distortion is expected to have a lesser effect on the measurement of scalar fluxes than on momentum fluxes as scalar fluxes depend on only one component of the wind vector (e.g.: Pedreros et al., 2003). Air-sea latent heat fluxes (F_r) were measured during HiWASE with the EC and ID techniques. As for the momentum flux, a wave scale signal was visible in the motion corrected EC latent heat flux cospectra. The wave scale signal in the latent heat cospectra was smaller than the signal in the momentum flux and other scalars. The CMC (Chapter 6.4.4) was used to remove the signal, and the ID, EC and CMC latent heat fluxes were compared with a bulk estimate (Figure 7.3; Smith, 1988).

7.4.1.a. Previous experimental results

Analogously to the gas transfer velocity, a dimensionless neutral transfer coefficient is defined for humidity. The humidity transfer coefficient, C_E, is termed the Dalton number and defined as:

$$C_E = {-F_r} \Big/ {U_{10n}\left(\bar{r} - r_s\right)} \tag{7.1}$$

where the subscript *s* denotes that the humidity mixing ratio, *r*, is determined at the sea surface. A selection of humidity transfer coefficient results from previous air-sea interaction results are shown in Table 7.1. Results from several experiments, mostly utilizing EC measurements, were summarized by Smith (1988), who suggested that the best available value for the heat transfer coefficient in near neutral conditions was $C_E = 1.2 \times 10^{-3}$. This estimate does not have any wind speed dependency. The semi-empirical COARE algorithm (Fairall et al., 2003) suggests a weak dependence of C_E on wind speed, with the coefficient increasing from about 1.1×10^{-3} at 3 m.s^{-1} to 1.2×10^{-3} at wind speeds of 20 m.s^{-1}.

The experiment reported by Large and Pond (1982) used ID measurements to estimate a mean $C_E = 1.15 \times 10^{-3}$ in unstable ($z/L < 0$) atmospheric conditions. A more recent experiment using the ID technique to measure open ocean latent heat fluxes onboard a research ship estimated that the near neutral mean $C_E = 1.0 \times 10^{-3}$ (Dupuis et

al., 2003). A slight increase with wind speed (approximately 20% increase for a 10 m.s^{-1} wind speed increase) was observed, though this variation was within the range of uncertainty of the measurements. EC fluxes from the same experiment measured a higher value, $C_E = 1.23 \times 10^{-3}$, that was constant with wind speed (Pedreros et al., 2003). This value was obtained for unstable conditions. In stable ($z/L > 0$) conditions, the coefficient determined for the EC measurements was lower: $C_E = 1.11 \times 10^{-3}$. There thus remains some uncertainty over the most appropriate value and wind speed dependence of C_E. Bulk latent heat fluxes calculated with the C_E of Smith (1988) will be used in the following analysis, though no particular preference is expressed for any bulk relationship.

7.4.1.b. HiWASE results

This thesis is primarily concerned with the measurement of the gas transfer velocity. HiWASE EC latent heat fluxes are measured with the same instrumentation as used to determine the CO_2 flux. In addition, the ability to measure latent heat fluxes using the ID technique, and the smaller (relative to gas transfer velocities) uncertainty of the humidity transfer coefficient, make the latent heat flux a useful proxy for estimating the effects of flow distortion on the EC CO_2 flux. For this reason, the set of HiWASE latent heat fluxes presented here are limited to those from the same 3938 measurement periods used for the CO_2 results (Chapter 4). In addition, the removal of periods when the ship was steaming (speed over ground > 2 m.s^{-1}) has been found to reduce variability at low wind speeds. These periods have also been removed from the analysis of all fluxes presented in this chapter. The acceptable relative wind direction limits in the quality control applied to these measurements is dependent on the IRGA used (Section 7.1).

The ratios of HiWASE latent heat fluxes to a commonly used bulk estimate (Smith, 1988), relative to U_{10n}, are shown in Figure 7.3. As for momentum (Section 7.3), fluxes measured at low wind speed (< 6 m.s^{-1}) are not discussed. For bow-on relative wind directions, (b, Figure 7.3), the ID flux measurements show little variation with wind speed except at the highest winds, where relatively few measurements are available. The ID measurements are biased low by ~ 9% relative to the bulk estimate of Smith, (1988). The ID measurements from winds onto the *Polarfront's* starboard beam (c, Figure 7.3) are similar to those measured with bow-on winds. If the CFD derived wind speed correction is applied to the starboard beam ID fluxes (d, Figure 7.3), the

measured fluxes are increased and become very similar to the bulk estimate of Smith (1988). The difference between the beam-on and bow-on measurements is ~ 9%. This may be due to the unknown flow height change that is appropriate to apply to the data for beam-on winds (Section 7.2).

There is a significant low bias (about 30% relative to Smith) in the bow-on (180° ± 10°) EC latent heat fluxes (b, Figure 7.3) at the moderate wind speeds in which the majority of the measurements were made ($7 \le U_{10n} \le 14$ m.s^{-1}, $n = 67$), and the bias is approximately constant with wind speed. The CMC only removes part of this bias. The bias increases at high wind speeds (> 16 m.s^{-1}). However, there are relatively few measurements in the highest wind speed bins (5 in the bin centred at 16.5 m.s^{-1} and 1 in the bin centred at 18.2 m.s^{-1}). The remaining bias may be due to some combination of platform motion related error and flow distortion effects. The residual wave scale signal in the latent heat fluxes was typically smaller than for other fluxes, but, as for CO_2 (Chapter 6) and momentum flux measurements (Section 7.3), was significant for bow-on measurements. Note that for latent heat, the CMC does not appear to overcorrect, as was the case for the bow-on momentum flux.

The EC and CMC measurements for starboard beam-on winds (280° ± 10°) are in reasonable agreement with the ID measurements (c, Figure 7.3). The CMC makes only a small difference to the starboard beam EC latent heat fluxes. Application of the CFD derived wind speed correction (d, Figure 7.3) brings the EC and CMC measurements into close agreement with the bulk estimate of Smith (1988) for wind speeds of 6-15 m.s^{-1}. The agreement between the ID, bulk and EC measurements suggests that any flow distortion bias in the EC scalar measurements is no larger than that determined for the ID measurements, i.e.: starboard beam-on measurements biased high by approximately 9%. Note that as for the momentum fluxes (Section 7.3), applying the CMC does not reduce the variability of the binned fluxes. This is the case for both beam-on and bow-on measurements.

7.4.1.c. Latent heat flux variation with wind direction

The variation of the HiWASE latent heat fluxes with relative wind direction is shown in Figure 7.4. The starboard beam-on bulk fluxes have been calculated with the CFD derived -8% wind speed adjustment. For starboard beam winds, the ID, EC and CMC fluxes are similar, and in the range of values found in other experiments. The ID bow-on measurements are approximately 9% lower than the starboard beam-on

measurements. The port beam (90° ± 10°) ID and EC measurements, where no flow distortion adjustment has been applied, are ~ 10% lower than the bow-on ID measurements. The EC and CMC fluxes become progressively smaller relative to the ID and bulk estimates as winds move onto the bow. The effect of flow distortion on the starboard beam and the port beam measurements acts to bias the ID and EC measurements high and low respectively. When measurements from all relative wind directions (60°-340°: a, Figure 7.3) are averaged, the binned ID measurements are similar to those onto the ship's bows (b, Figure 7.3), showing that much of the flow distortion effect has been cancelled out by the differing directions of the bias on the beam-on winds.

Wider bow and beam relative wind direction limits have been previously selected when discussing the gas transfer velocity to maximize the number of available measurements (Chapter 6.4). The HIWASE latent heat flux measurements with these wider limits are shown in Figure 7.5. Here, bow-on is defined as 120°-240° and beam-on refers to all fluxes measured with winds away from the ship's bows (outside 120°-240°). Note that the relative wind direction limits from the quality control procedures (Section 7.1) also apply. The beam-on ID measurements, with (d, Figure 7.5) and without (c, Figure 7.5) the CFD wind speed adjustment, are very similar (overall mean difference less than 1% for winds 7-16 $m.s^{-1}$) to the measurements obtained with winds within 10° of the ship's bows (b, Figure 7.3). Whilst the measurements do not agree exactly with the bulk estimate shown (Smith, 1988), they are within the range of estimates found in other experiments (Table 7.1). We can conclude that the effect of flow distortion on the beam-on ID measurements is small (though this is in part due to the cancelling out of biases for winds from different directions).

The EC and CMC measurements for beam-on winds are very similar to the ID measurements. The difference appears to increase slightly in the highest wind speed bin, however this bin consists of only four measurements. The mean difference between the beam-on EC measurements and the bow (± 10°) ID measurements is ~ 2% for wind speeds of 7-16 $m.s^{-1}$. For the CMC measurements, the difference is ~ 1%. If the bow-on ID measurements, with the appropriate CFD derived corrections applied, are assumed to be unaffected by flow distortion, we can conclude that the overall impact of flow distortion on the beam-on set of EC latent heat fluxes is small. The full set of EC and CMC measurements at all acceptable relative wind directions (i.e.: the data shown in a, Figure 7.3) are also similar to the ID measurements. The largest differences are in the

high wind speed bins, which consist of relatively few measurements. The mean difference between the full set of EC measurements and the bow (± 10°) ID measurements is approximately -6% for wind speeds of 2-20 $m.s^{-1}$. For the CMC measurements, the difference is approximately -5%. The apparent effect of flow distortion on the port and starboard beam-on measurements allows the uncertainty of the beam-on scalar fluxes due to flow distortion to be estimated as ± 9%.

7.4.1.d. Sensor separation

The beam-on ID latent heat fluxes (c, Figure 7.3) do not have as close agreement with the bow-on fluxes (b, Figure 7.3) as do the bow-on and beam-on momentum flux measurements (Figure 7.1). This may be due to the difference in the flow distortion biases at the location of the Sonic and the IRGAs (Section 7.2). The two IRGAs used to measure fast response H_2O concentration are located in different positions on the *Polarfront's* foremast and thus may be subject to different flow distortion effects. The fore IRGA is mounted on a pole extending approximately 60 cm forward from the handrail at the fore-starboard corner of the foremast. The starboard IRGA is mounted on a pole extending approximately 60 cm to starboard from the same corner (Chapter 2). The variation of the HIWASE latent heat flux measurements with relative wind direction can be examined separately for the fore IRGA (a, Figure 7.6) and the starboard IRGA (b, Figure 7.6). The starboard beam measurements are high relative to the bow fluxes for each IRGA. The ID latent heat fluxes measured with the fore IRGA and for winds within 10° of the bows or the starboard beam are higher by ~ 5% than the equivalent measurements from the starboard IRGA. The difference is similar in magnitude to the difference between the beam and bow measurements from both IRGAs, suggesting that different flow distortion effects at the instrument positions could explain the disparity. This will be addressed in future CFD experiments.

Differences in EC fluxes measured with the two IRGAs could also be a result of different flux attenuation effects caused by sensor separation (e.g.: Nilsson et al., 2010). Nilsson et al. find that horizontal sensor separation (with respect to the mean relative wind direction) leads to larger flux attenuation than does vertical sensor separation. This effect is not observed in the HiWASE measurements (Figure 7.6), where the measurements with the fore IRGA and starboard beam-on winds are higher than the measurements with the starboard IRGA and starboard beam-on winds.

7.4.1.e. Atmospheric stability

The majority of the HiWASE measurements are made in slightly unstable atmospheric conditions (Figure 7.7). Approximately 12% of the measurements are made in slightly stable conditions. The stable measurements have a mean dimensionless stability, *z/L,* of 0.03. Note that the dimensionless stabilities are calculated from bulk estimates of the heat and momentum fluxes and bulk estimates of the air-sea temperature difference. For the measurements made in stable conditions, the mean air-sea temperature difference at Station Mike was small, less than 0.5 K. Uncertainty in the air-sea temperature difference is expected to be of the order 0.2 K, and there is thus some uncertainty over the correct dimensionless stability value.

The humidity transfer coefficient estimates from the HiWASE EC and ID latent heat flux measurements for both stable and unstable conditions are shown in Table 7.1. Both the EC and ID coefficient estimates are similar to those obtained from previous experiments. Note that this thesis is primarily concerned with determination of the gas transfer velocity, and as such the stated values of C_E should be treated as preliminary. A more detailed examination of the HiWASE heat flux measurements is planned (Chapter 8).

Latent heat flux measurements made in unstable conditions are similar to the overall data set (compare a, Figure 7.8 and d, Figure 7.5). EC measurements in stable conditions are similar to unstable measurements, though are highly scattered due to the relatively small number of measurements (b, Figure 7.8). ID measurements in stable conditions are higher than unstable values by approximately 10%. The difference between the unstable and stable measurements is of the opposite sign to the stability dependence observed by Pedreros et al., (2003). The reason for the difference in the HiWASE ID measurements is uncertain, however in stable conditions, the height of the surface layer may be lower than the height of the instrumentation, and the assumptions of both the EC and ID techniques may not be valid. The stable conditions are only slightly stable, and over the mid to high latitude ocean, the atmospheric conditions will generally be unstable. As the HiWASE EC measurements in stable conditions are similar to the unstable measurements, the stable periods have not been removed from the flux analysis.

Table 7.1 Humidity transfer coefficients determined during HiWASE and in previous open ocean experiments. Uncertainties are standard deviation. Where known, the number of measurements, wind speed range, and atmospheric conditions used to determine the coefficient are given. The HiWASE results (shown in d, Figure 7.5 and Figure 7.8) and the bulk coefficient used in Figure 7.3, Figure 7.4, Figure 7.5, Figure 7.6 and Figure 7.8 are highlighted.

Reference	**Experiment**	$C_E \times 10^{-3}$	**Atmos' stability**	**Wind speed range (m.s^{-1})**	***n***
HiWASE	**Ship based EC**	**1.07 ± 0.34** **1.12 ± 0.35**	**Unstable** **Stable**	**1.4-16.6** **4.9-14.5**	**2418** **313**
HiWASE	**Ship based ID**	**1.05 ± 0.23** **1.24 ± 0.36**	**Unstable** **Stable**	**1.4-16.6** **4.9-14.5**	**2418** **313**
Smith, (1988)	**Summary of EC experiments**	**1.2**	**Neutral**	**-**	**-**
Dupuis et al., (2003)	Ship based ID	1.0 ± 0.31	Neutral	1-19	480
Pedreros et al., (2003)	Ship based EC	1.23 ± 0.24 1.11 ± 0.35	Unstable Stable	1-19 3-17	380 47
Friehe and Schmitt, (1976)	Summary of EC experiments	1.32 ± 0.72	Neutral	-	30
DeCosmo et al., (1996)	North Sea fixed platform EC	1.12 ± 0.24	Neutral	5-18	170
Large and Pond, (1982)	Ship based ID	1.15 ± 0.22	Unstable	4-14 m.s^{-1}	93

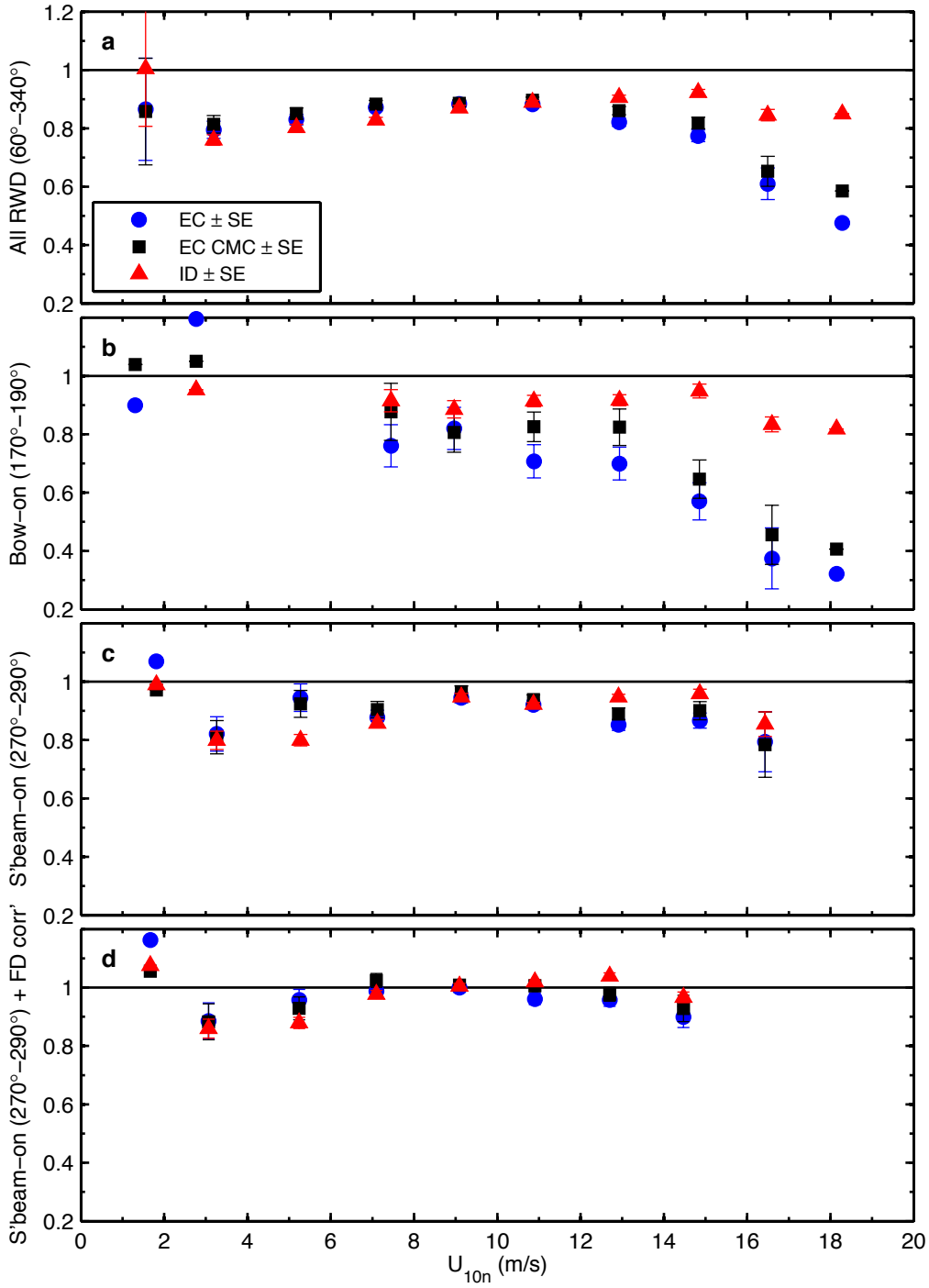

Figure 7.3. Ratios of HiWASE latent heat flux measurements to a bulk estimate (Smith, 1988). Measurement techniques are as indicated in the key. Ratios are binned by U_{10n} (bin width = 2 m.s^{-1}). Measurements are shown for three representative relative wind directions, a) 60°–340° (n = 3028), b) 170°-190° (n = 94) and 270°–290°, without (c, n = 1109) and with (d, n = 1097) the CFD modeling derived wind speed correction. Measurements made when the ship was steaming (speed over ground > 2 m.s^{-1}) and outlier ratios (ratio outside the range 0-2) have been removed from the analysis.

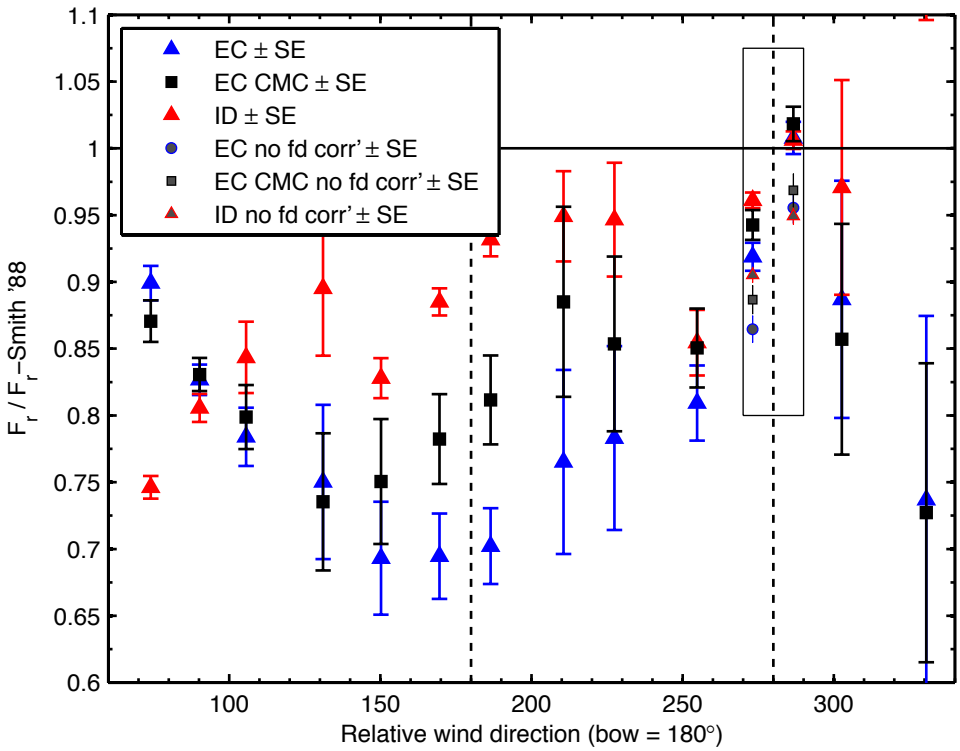

Figure 7.4. Variation of latent heat fluxes measured during HiWASE with relative wind direction. Results (n = 2656) as indicated in the key are divided by a bulk latent heat flux (Smith, 1988) and binned by relative wind direction (bin width = 20°). Measurements made at wind speeds outside the range $6 \leq U_{10n} \leq 16$ m.s^{-1} (n = 455), when the ship was steaming (speed over ground > 2 m.s^{-1}) and outlier values (ratios outside the range 0-2, n = 175) have been removed from the analysis. The dashed lines indicate the bow-on and nominal starboard beam-on directions. Box indicates those relative wind directions for which the CFD derived -8% wind speed adjustment was determined, and data are shown with and without ("no fd corr'") the adjustment.

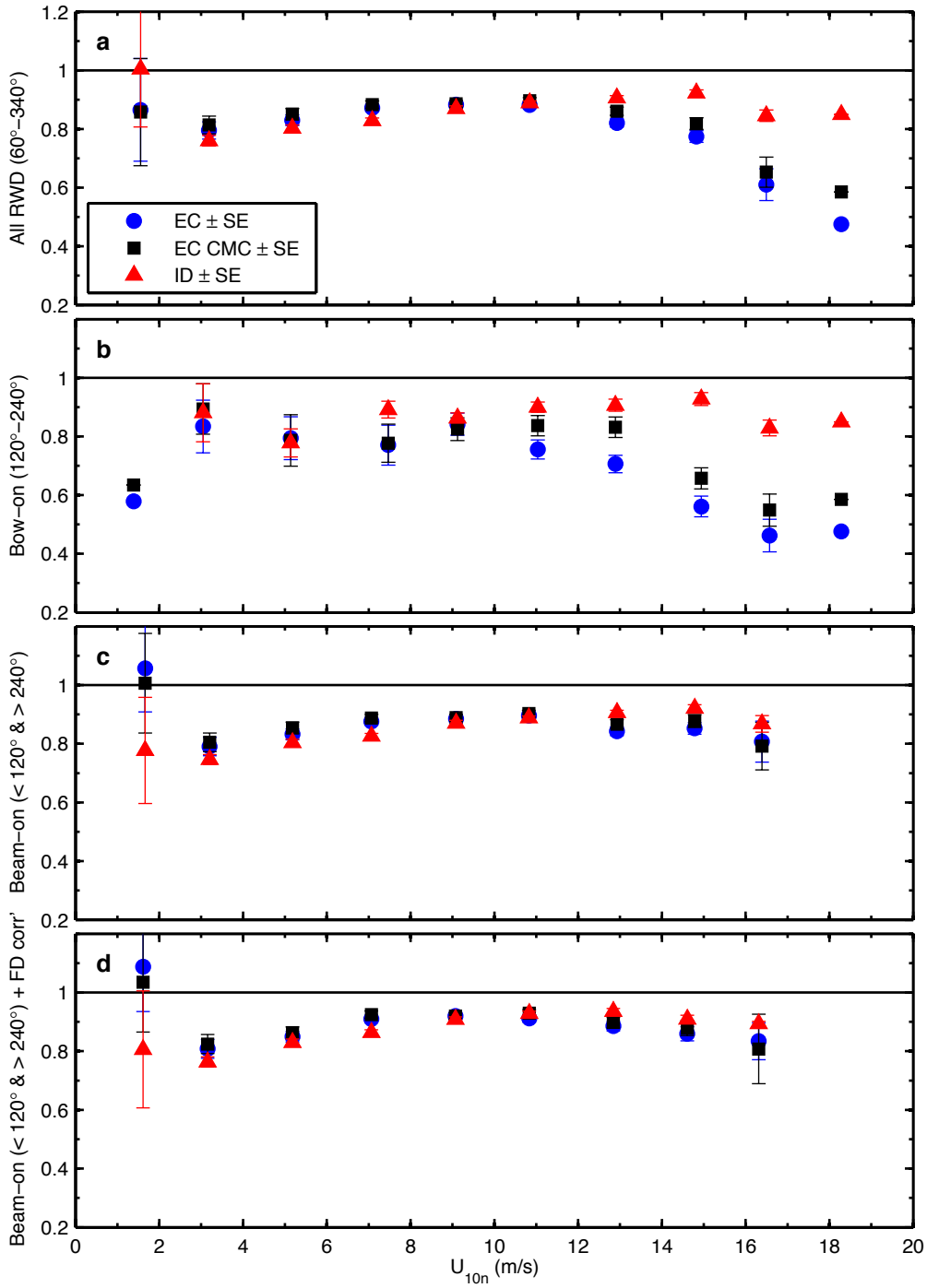

Figure 7.5. As per Figure 7.3 with relative wind direction limits determined from analysis of platform motion: a) 60°–340° (n = 3028), b) 120°-240° (n = 285) and < 120° & > 240°, without (c, n = 2743) and with (d, n = 2731) the CFD modeling derived wind speed correction.

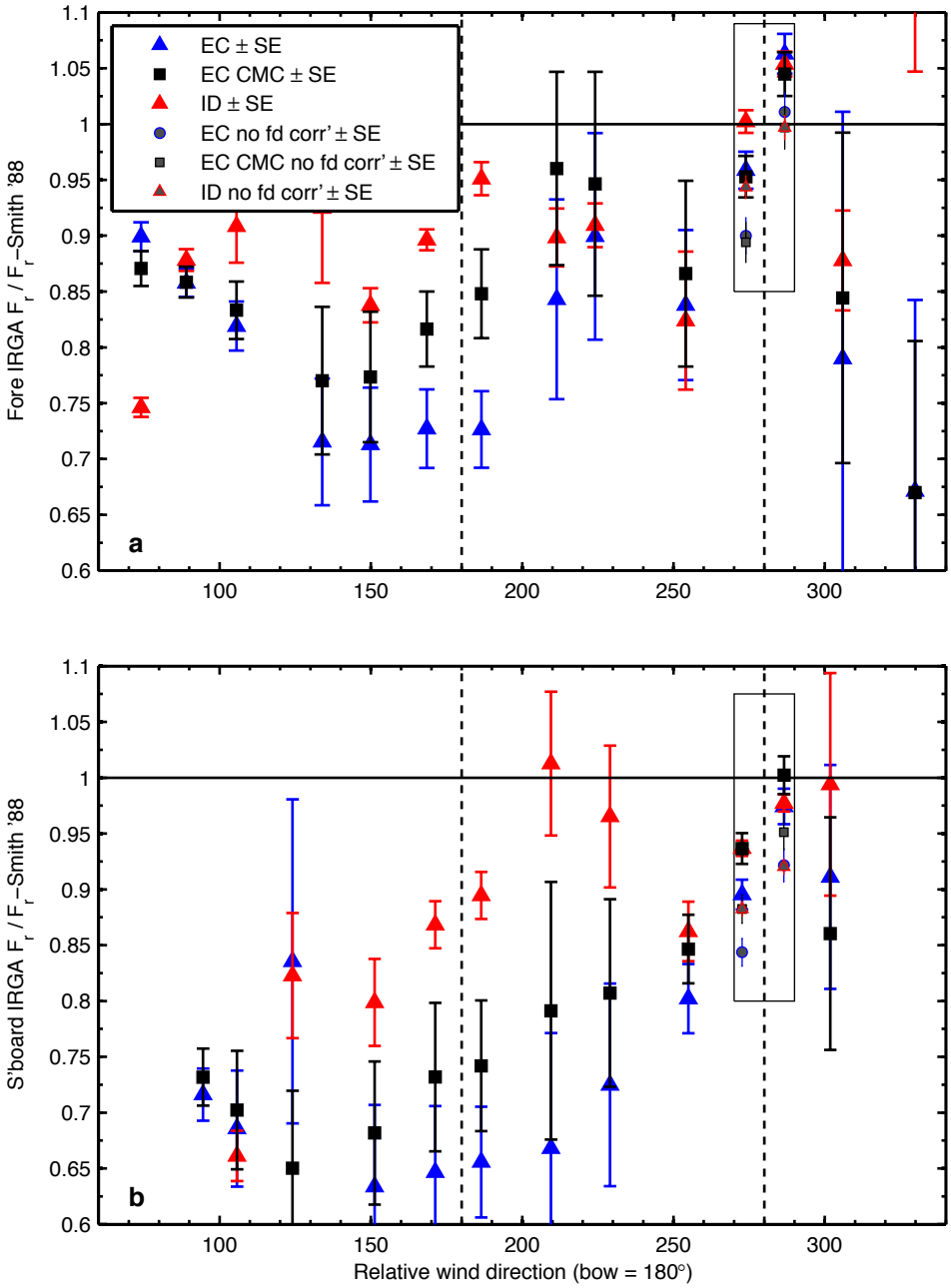

Figure 7.6. Variation of latent heat fluxes measured during HiWASE with relative wind direction. Measurements are separated into those measured with the fore IRGA (a, n = 1452) and the starboard IRGA (b, n = 1194). Results as indicated in the key are divided by a bulk latent heat flux (Smith, 1988) and binned by relative wind direction (bin width = 20°). Measurements made at wind speeds outside the range $6 \le U_{10n} \le 16$ m.s^{-1}, when the ship was steaming (speed over ground > 2 m.s^{-1}) and outlier values (ratios outside [0 2]) have been removed from the analysis. The dashed lines indicate the bow-on and nominal starboard beam-on directions. Box indicates those relative wind directions for which the CFD derived -8% wind speed adjustment was determined, and data are shown with and without ("no fd corr'") the adjustment.

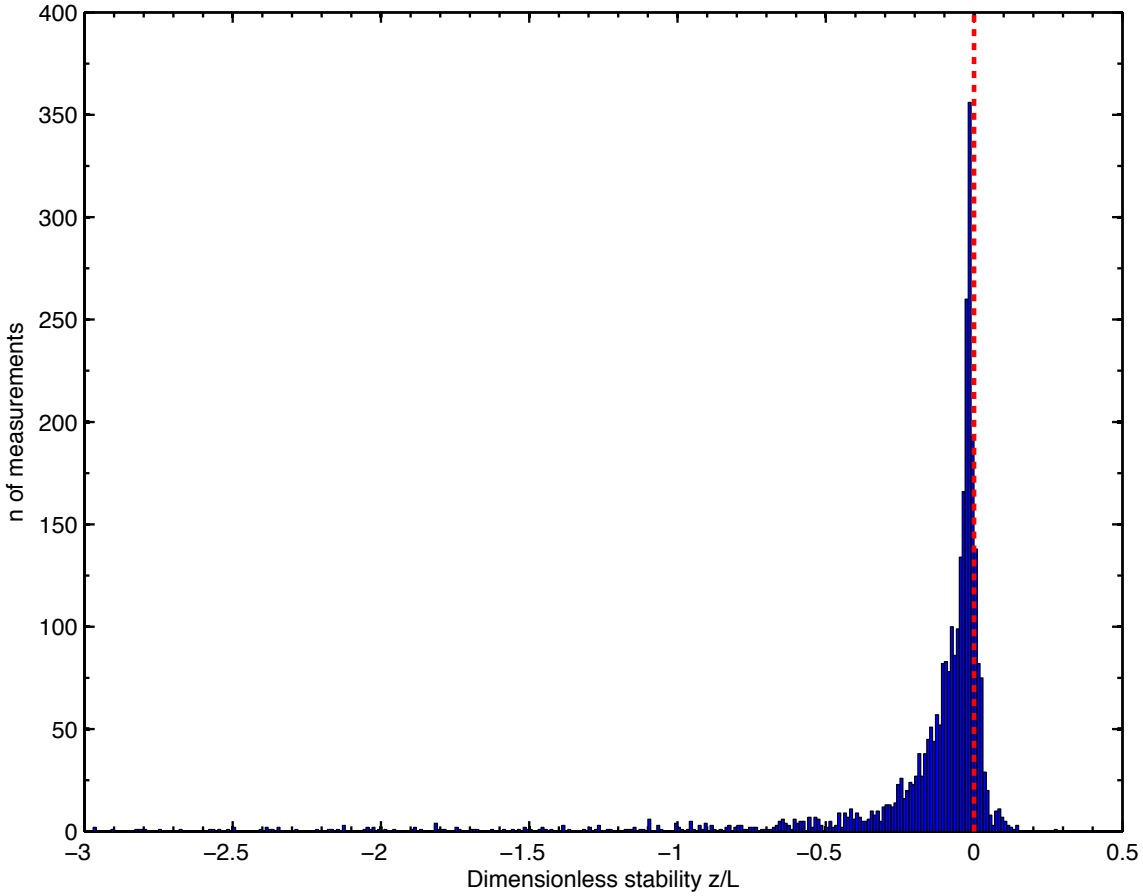

Figure 7.7. Histogram of HiWASE dimensionless stability determined from bulk flux estimates at relative wind directions less than 120° and greater than 240° (n = 2951). The red dashed line indicates neutral stability. 19 measurements with dimensionless stabilities less than -3 are not shown.

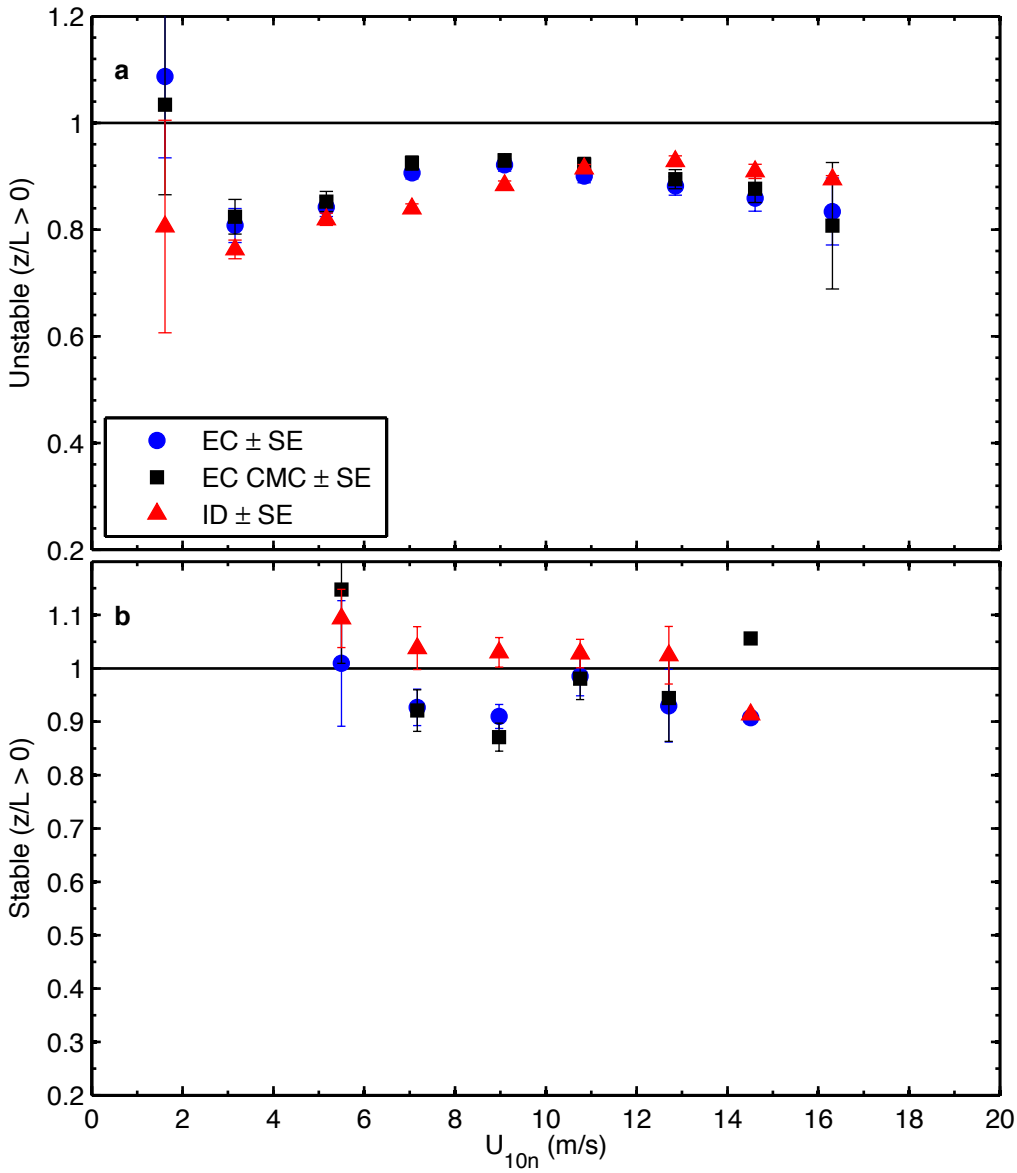

Figure 7.8. Ratios of HiWASE latent heat flux measurements to a bulk estimate (Smith, 1988). Measurement techniques are as indicated in the key. Ratios are binned by U_{10n} (bin width = 2 m.s^{-1}). Measurements obtained at relative wind directions < 120° & > 240° under unstable (**a**, n = 2418) and stable (**b**, n = 313) atmospheric conditions. Starboard beam-on (280 ± 10°) measurements have the CFD derived -8% wind speed adjustment. Measurements made when the ship was steaming (speed over ground > 2 m.s^{-1}) and outlier ratios (ratio outside the range 0-2) have been removed from the analysis.

7.4.2 Sensible heat flux

It is not currently possible to use sonic anemometers to measure sensible heat fluxes, F_T, with the ID technique due to poor sensor performance at the high frequencies required (e.g.: Dupuis et al., 2003).

7.4.2.a. Previous experimental results

As for humidity, a dimensionless transfer coefficient is defined for temperature. Termed the Stanton number, the heat flux coefficient, C_T, is defined as:

$$C_T = {-F_T} \Big/ {c_p U_{10n} \left(\theta - T_{SST}\right)} \tag{7.2}$$

where c_p is the specific heat of air at constant pressure, θ is the potential temperature of air at the measurement height and T_{SST} is the sea surface temperature. A selection of heat transfer coefficients from previous experiments is shown in Table 7.2. The EC sensible heat flux measurements of Smith (1980) were summarized by Smith (1988) to give an estimated value for the heat flux coefficient of $C_T = 1.0 \times 10^{-3}$. The coefficient estimates of Smith (1980) displayed a dependence on atmospheric stability. For unstable atmospheric conditions ($z/L < 0$), the estimate was $C_T = 1.1 \times 10^{-3}$ whilst for stable atmospheric conditions ($z/L > 0$), the coefficient was $C_T = 0.83 \times 10^{-3}$. The transfer coefficient was found to be approximately constant with wind speed. These measurements were obtained from a tied down, well-exposed tower in approximately 60 m of water. An experiment using both tower and ship based measurements found a similar value for unstable conditions of $C_T = 1.13 \times 10^{-3}$ (Large and Pond, 1982). The wind speed range in this experiment was 4-25 m.s^{-1}, and a small wind speed dependence was noted for wind speeds above 10 m.s^{-1}, but there was considerable scatter in the measurements. For stable conditions, Large and Pond (1982) also determined a lower coefficient: $C_T = 0.66 \times 10^{-3}$.

A more recent experiment utilizing EC measurements from a research vessel found a similar value for C_T with no significant dependence on wind speed for winds of up to 19 m.s^{-1} (Pedreros et al., 2003). Unlike most other experiments, stable fluxes ($C_T = 1.34 \times 10^{-3}$) were found to be larger than unstable fluxes ($C_T = 1.01 \times 10^{-3}$).

However, the uncertainty in the stable coefficient value was very large, $\pm\ 0.45 \times 10^{-3}$, and so this result must be treated with caution.

7.4.2.b. HiWASE results

The HiWASE EC sensible heat flux measurements were compared with the bulk flux estimate of Smith (1988). The resulting ratios binned by wind speed and separated into representative relative wind directions are shown in Figure 7.9. The same set of measurements used to examine the latent heat flux (Section 7.4.1) was used in the analysis, with the additional removal of outlier ratios (ratios outside the range 0-2). For averages over all wind directions, HiWASE EC sensible heat fluxes agree with the Smith (1988) estimate to within ±10% for wind speeds up to 16 $m.s^{-1}$ (a, Figure 7.9). Note that the two highest wind speed bins at approximately 16.5 $m.s^{-1}$ and 18 $m.s^{-1}$ consist of 4 and 1 measurement respectively.

The bow-on EC fluxes are biased low relative to the bulk estimate, though are highly scattered due to the relatively small (n = 54) number of measurements (b, Figure 7.9). The CMC results in measurements biased high relative to the bulk estimate at wind speeds below 17 $m.s^{-1}$, suggesting that a significant proportion of the bow-on flux is within the wave scale. As for the other HiWASE EC fluxes, the accuracy of the bow-on EC sensible heat fluxes is questionable.

Starboard beam-on CMC measurements are biased slightly high relative to the bulk estimate, and display a slight negative trend with wind speed (c, Figure 7.9). The bias and the negative trend with wind speed are reduced slightly by the CMC. For all relative wind directions away from the *Polarfront's* bow (winds between 60°-120° and 240°-340°), the EC and CMC fluxes are similar, with a slight positive bias relative to the bulk estimate and no clear trend with wind speed (d, Figure 7.9). The mean of the measurements is similar to the results obtained by Smith (1980) in unstable conditions.

The EC sensible heat fluxes show a similar dependence on relative wind direction to the EC latent heat fluxes, biased low for winds onto or near the *Polarfront's* bows (Figure 7.10). As for latent heat fluxes, the starboard beam-on measurements are biased slightly higher than the port beam measurements. The similar dependence of the latent heat and sensible heat fluxes shows that both scalars are, as expected, similarly affected by flow distortion. Again we can conclude that the overall effect of flow distortion on the scalar measurements is small.

The CMC removes some of the low bias of the bow-on flux measurements, suggesting that part of the bias is due to signal at the wave scale frequencies and may be the result of platform motion. The CMC measurements are highly variable for bow-on wind directions. However, even for the beam-on measurements, the CMC does not reduce the measurement variability. The mean effect of the CMC on the beam-on measurements is small, despite the large wave scale signal observed in the beam-on temperature cospectra in Chapter 6. The beam-on temperature wave scale signal included both a positive (upwards) and a negative peak, and hence removing both with the CMC may result in little change to the mean flux.

7.4.2.c. Atmospheric stability

For the majority of sensible heat flux measurements, the atmospheric conditions were unstable (Figure 7.11). The HiWASE mean heat transfer coefficient for both unstable and stable conditions is shown in Table 7.2. As for the humidity coefficient (Section 7.4.1), these should be treated as preliminary values. For stable conditions, the EC measurements are biased high (except for one bin with a small number (n = 4) of measurements). This is an unexpected effect, different from the results of Smith (1980) and Large and Pond (1982) who both observed lower fluxes in stable conditions. However, an increase in sensible heat flux under stable conditions was observed in the more recent ship based EC experiments reported by Pedreros et al., (2003).

As was discussed in Section 7.4.1, in stable conditions the surface layer may be below the sensor height, invalidating the assumptions required for flux measurement. As for the latent heat fluxes, the effect of stability on the mean sensible heat flux results is relatively small, and the stable measurements have not been removed from the analysis.

Table 7.2 Heat transfer coefficients determined during HiWASE and in previous open ocean experiments. Uncertainties are standard deviation. Where known, the number of measurements, wind speed range, and atmospheric conditions used to determine the coefficient are given. The HiWASE results (shown in d, Figure 7.9, and Figure 7.11) and the bulk coefficient used in Figure 7.9, Figure 7.10 and Figure 7.11 are highlighted.

Reference	**Experiment**	$C_T \times 10^{-3}$	**Atmos' stability**	**Wind speed range (m.s^{-1})**	***n***
HiWASE	**Ship based EC**	**1.07 ± 0.37** **1.24 ± 0.42**	**Unstable** **Stable**	**1.4-15.6** **5.3-13.7**	**1922** **225**
Smith, (1988)	**Restates result of Smith, 1980**	**1.0**	**Neutral**	**-**	**-**
Smith, (1980)	Tower (tied down) based EC	1.0 1.1 0.83	Neutral Unstable Stable	6-22	73 32 39
Pedreros et al., (2003)	Ship based EC	1.01 ± 0.20 1.34 ± 0.45	Unstable Stable	1-19 4-18	234 34
DeCosmo et al., (1996)	North Sea fixed platform EC	1.14 ± 0.35	Neutral	6-23	133
Large and Pond, (1982)	Tower and ship based EC and ID	1.13 ± ~0.1 0.66 ± ~0.1	Unstable Stable	4-25 6-20	179 124

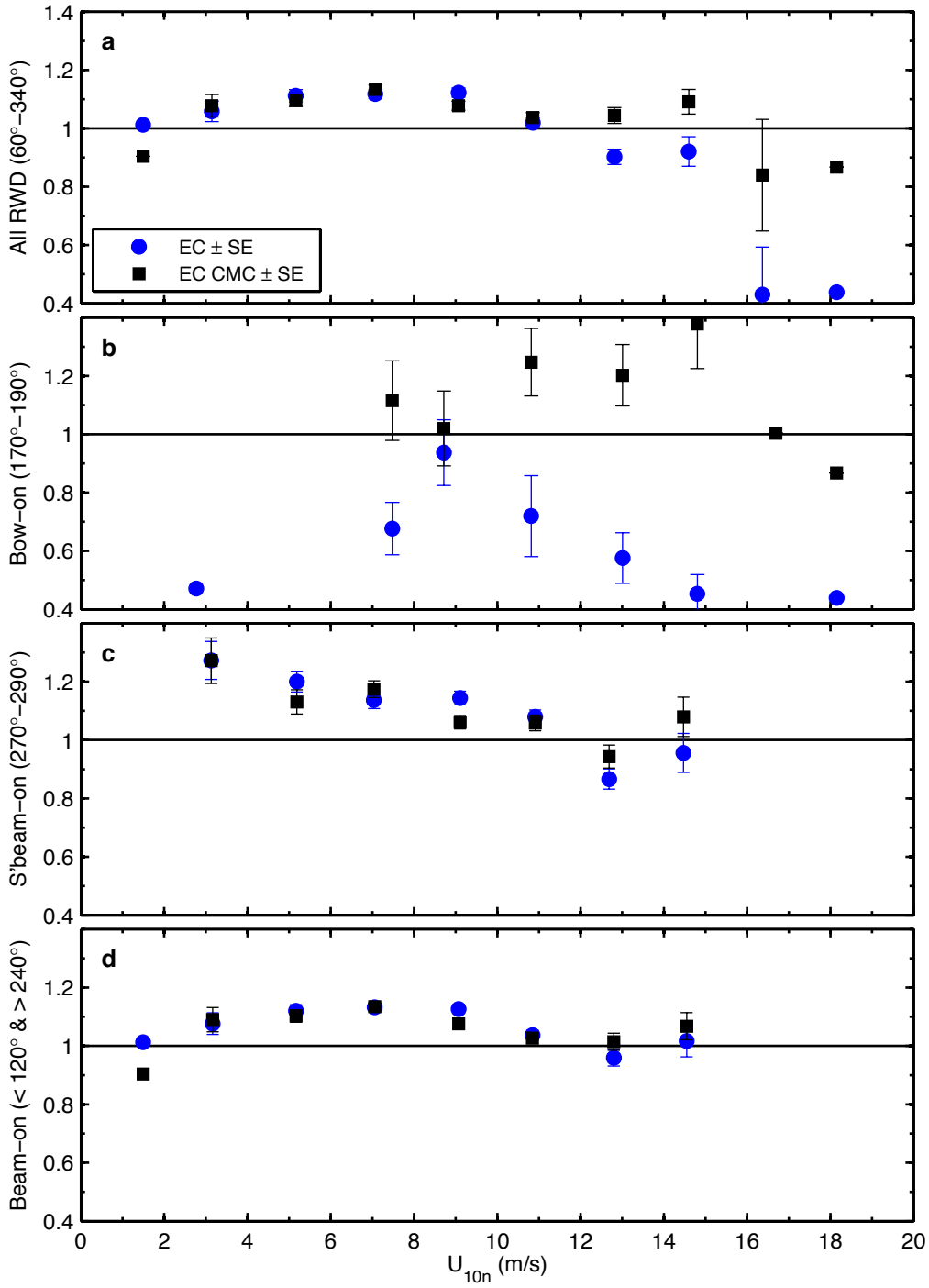

Figure 7.9. Ratios of HiWASE sensible heat flux measurements to a bulk estimate (Smith, 1988). Measurement techniques are as indicated in the key. Ratios are binned by U_{10n} (bin width = 2 m.s^{-1}). Measurements are shown for four representative relative wind directions, a) 60°–340° (n = 2313), b) 170°-190° (n = 54), c) 270°–290° (n = 900), and d) < 120° & > 240° (n = 2147). Starboard beam-on measurements have the CFD derived -8% wind speed adjustment. Measurements made when the ship was steaming (speed over ground > 2 m.s^{-1}) and outlier ratios (fluxes less than 1 W.m^{-2} or ratio outside the range 0-2) have been removed from the analysis.

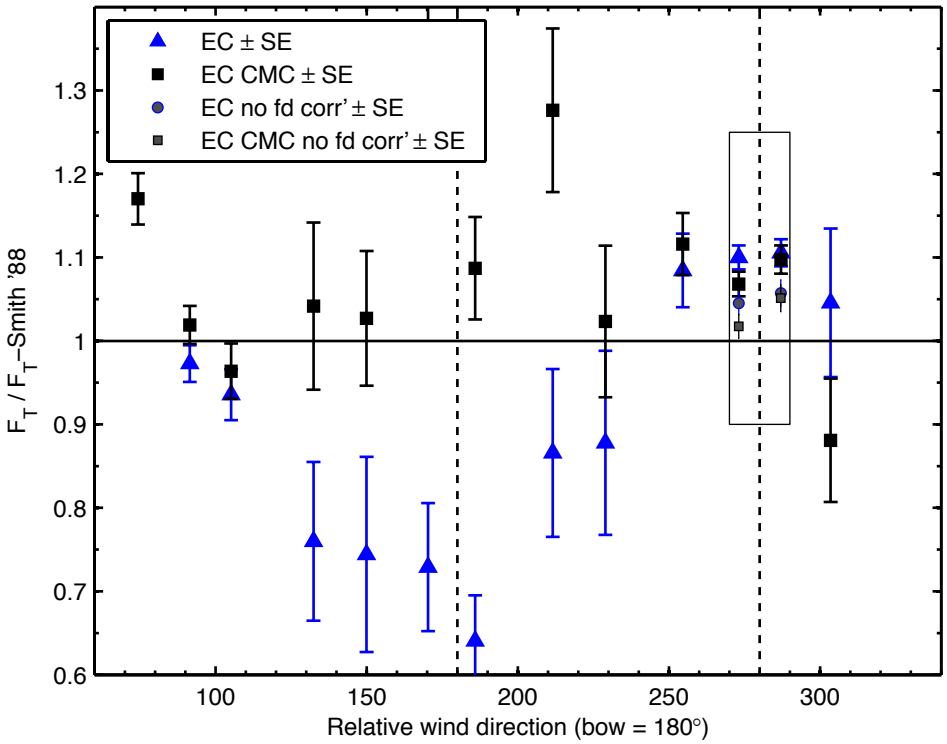

Figure 7.10. Variation of sensible heat fluxes measured during HiWASE with relative wind direction. Results (n = 1972) as indicated in the key are divided by a bulk sensible heat flux (Smith, 1988) and binned by relative wind direction (bin width = 20°). Measurements made at wind speeds outside the range $6 \le U_{10n} \le 16$ m.s^{-1} (n = 455), when the ship was steaming (speed over ground > 2 m.s^{-1}) and outlier values (ratios outside the range 0-2, n = 859) have been removed from the analysis. The dashed lines indicate the bow-on and nominal starboard beam-on directions. Box indicates those relative wind directions for which the CFD derived -8% wind speed adjustment was determined, and data are shown with and without ("no fd corr'") the adjustment.

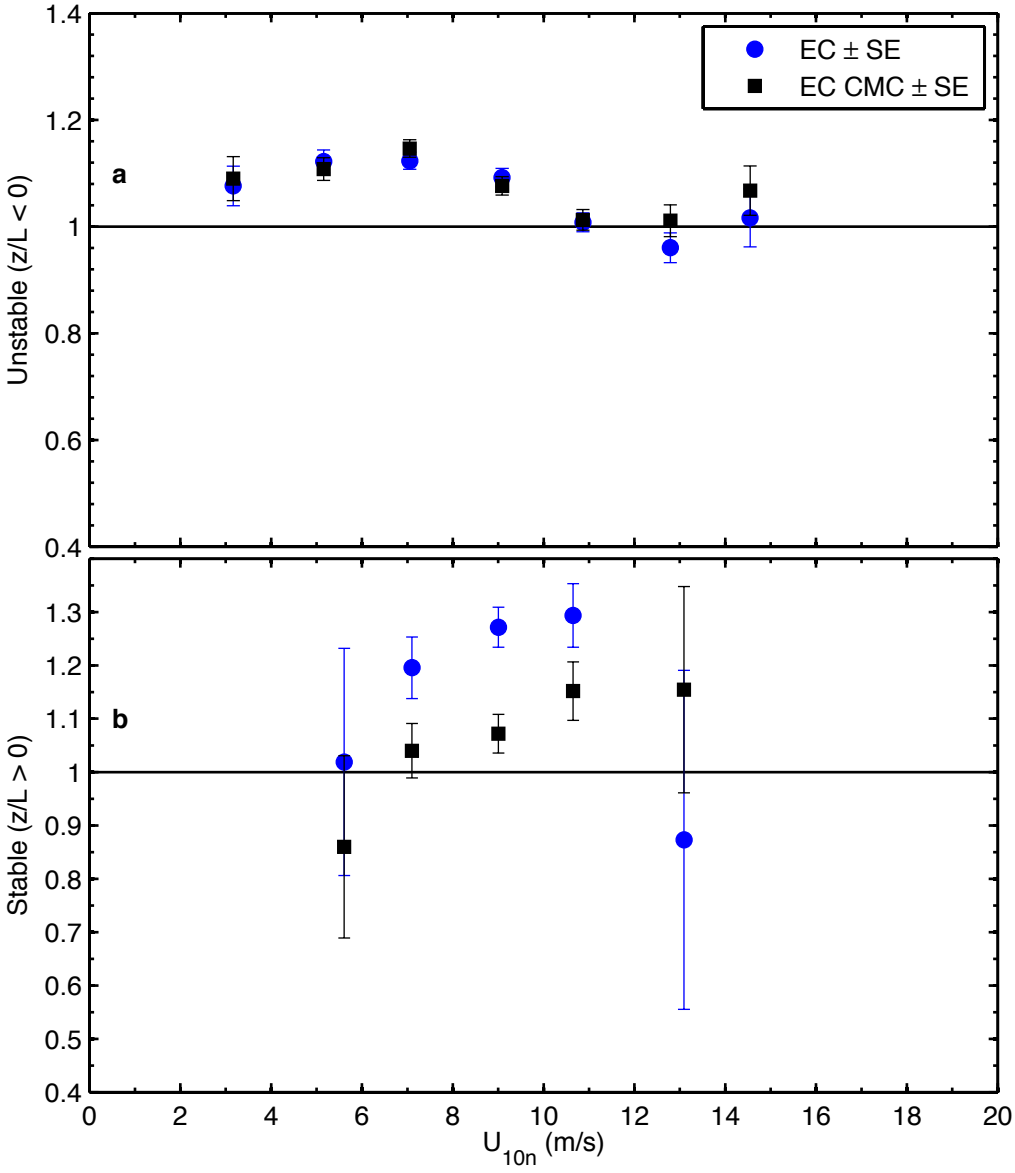

Figure 7.11. Ratios of HiWASE sensible heat flux measurements to a bulk estimate (Smith, 1988). Measurement techniques are as indicated in the key. Ratios are binned by U_{10n} (bin width = 2 m.s^{-1}). Measurements were obtained at relative wind directions < 120° & > 240°, under unstable (a, n = 1922) and stable (b, n = 225) atmospheric conditions. Starboard beam-on (280 ± 10°) measurements have the CFD derived -8% wind speed adjustment. Measurements made when the ship was steaming (speed over ground > 2 m.s^{-1}) and outlier ratios (fluxes less than 1 W.m^{-2} or ratio outside the range 0-2) have been removed from the analysis.

7.5. Effect of flow distortion on CO_2 flux

Whilst it is not currently possible to measure air-sea CO_2 fluxes using the ID technique (Section 1.3.1), the flow distortion analysis carried out for momentum, sensible heat and latent heat fluxes can be used to estimate the effects of flow distortion on the CO_2 flux. In particular, the EC latent heat fluxes serve as a proxy for the EC CO_2 flux measurements as the same sensors are used to measure both scalar fluxes.

The momentum flux results (Section 7.3) demonstrate the significant, relative wind direction dependent impact of flow distortion on the vector fluxes measured with both the ID and EC techniques. They also demonstrate the successful correction of flow distortion with CFD modeling. The CFD corrected bow-on ID drag coefficients are in good agreement with bulk estimates for wind speeds of 7-23 $m.s^{-1}$ (b, Figure 7.1). It is therefore assumed that the CFD corrected, bow-on ID momentum flux measurements do not have any significant error resulting from flow distortion.

The CFD modeling determined that winds onto the *Polarfront's* starboard beam were biased high by 8%. If this bias is corrected for, the starboard beam ID drag coefficients are in very close agreement with the bow-on measurements and the bulk estimates (d, Figure 7.1), suggesting that the CFD modeling has successfully determined the effects of flow distortion for the starboard beam-on momentum flux measurements.

Scalar flux measurements are expected to be less affected by flow distortion than the momentum flux (e.g.: Pedreros et al., 2003). CFD corrected, bow-on ID latent heat fluxes (Section 7.4.1) are relatively constant with wind speed, and are within the range of values determined by previous experiments (b, Figure 7.3). As for the momentum flux, it is assumed that these measurements do not have a significant flow distortion error.

The starboard beam-on EC and ID latent heat fluxes are biased high (by approximately 9%) relative to the bow-on ID fluxes, and the port beam-on EC and ID fluxes are biased low by a similar amount (Figure 7.4). For the latent heat flux measurements from all acceptable relative wind directions, including the highly variable bow-on (120°-240°) measurements (a, Figure 7.3), the EC latent heat flux measurements are biased low relative to the ID measurements by 5-6%. As for the latent heat fluxes, the EC sensible heat flux (Section 7.4.2) measurements are biased

high for winds onto the starboard beam and low for winds onto the port beam (Figure 7.10). The similarity of the apparent flow distortion effects on the latent heat and sensible heat EC measurements supports the use of the EC latent heat flux measurements as a proxy for the CO_2 flux measurements.

The impact of flow distortion on the vertical wind fluctuations, and the resulting effect on scalar eddy covariance measurements is assumed to affect the HiWASE CO_2 flux measurements in the same way as it affects the latent heat flux measurements. The latent heat flux results from all acceptable relative wind directions (a, Figure 7.3) suggest that flow distortion leads to a bias in the EC gas transfer velocities of approximately -5%. The ratio of the EC latent heat flux to a bulk estimate varies strongly with relative wind direction and this effect is similar in the CMC measurements, suggesting it is not due to platform motion effects. The range of variation of this ratio with wind direction allows the uncertainty in the HiWASE EC gas transfer velocities fluxes due to flow distortion to be estimated as ± 9%. The estimated overall error in the CO_2 flux measurements from flow distortion is small compared to other sources such as platform motion (Chapter 6) or humidity cross-sensitivity (Chapter 3).

8. Summary, future work and conclusions

8.1. Summary

8.1.1 HiWASE experiment data

The gas transfer velocity measurements analysed in this thesis were obtained as part of the HiWASE experiment, described in detail in Chapter 2. The measurements were made onboard the ocean weathership *Polarfront* at Station Mike (66 N 2 E) in the North Atlantic from September 2006 to December 2009. Direct, eddy covariance measurements of the momentum, latent heat, sensible heat and CO_2 flux were made using the autonomous "AutoFlux" system. AutoFlux was also used to obtain measurements of latent heat and momentum flux with the inertial dissipation technique. In addition, underway ΔpCO_2 and comprehensive meteorological and seastate measurement were made.

The HiWASE project resulted in 3938 direct gas transfer velocity measurements obtained with a high (> 40 μatm) ΔpCO_2. This is the largest set of open ocean direct transfer velocity measurements reported to date. The measurements include data obtained at 20-minute mean wind speeds up to 19.6 $m.s^{-1}$, significantly higher than in previous experiments.

8.1.2 Sources of flux measurement error

There are numerous sources of potential error that affect air-sea EC CO_2 flux measurement. This thesis has addressed 5 principal errors: humidity cross-sensitivity resulting from hygroscopic particle contamination; platform motion; flow distortion; IRGA sensor head deformation and density dilution resulting from temperature and humidity variations. The impact of these on the HiWASE measurements was examined in detail in Chapters 3, 4, 5, 6 and 7. Other sources of error are discussed in Section 5.6. These principal sources of error are summarized below and in Table 8.1. Note that these sources of error are not unique to the HiWASE experiment.

8.1.2.a. Humidity cross-sensitivity

The fast response CO_2 concentration measurements used to determine the gas transfer velocities during HiWASE were made with open path IRGAs. The initial measurements were subject to a large (> 100%) high bias. The HiWASE measurements

supported the theory (Kohsiek, 2000) that this large measurement error results from a cross-sensitivity to humidity, caused by hygroscopic particles contaminating the exposed sensor lens. This error has affected air-sea EC CO_2 flux measurements made with open path instruments since the measurements were first made at the end of the 1970s.

A similarity theory based correction, termed the PKT correction, was developed and applied to the HiWASE data, resulting in realistic gas transfer velocity results (Chapter 3; Prytherch et al., 2010a). The correction was tested by applying it to the independent sonic temperature measurements. These measurements have a bias relative to air temperature measurements that is dependent on humidity. The sonic temperature flux was corrected with the PKT correction in a manner analogous to CO_2, and shown to agree well in the mean with the air temperature flux. For measurements made with relative wind directions away from the *Polarfront's* bows, the mean agreement was very good for both positive and negative fluxes, demonstrating that the PKT correction works regardless of flux direction.

The PKT correction allows open path sensors to be used for air-sea CO_2 flux measurement, significantly increasing the number of measurements that are available for analysis by the wider community.

8.1.2.b. Platform motion and flow distortion

EC measurements from moving platforms require the platform motion to be removed from the wind vector prior to flux calculation. Following application of a standard platform motion correction method (Chapter 6; Edson et al., 1998), a significant signal remained in the HiWASE cospectra at the frequencies associated with platform motion (here termed the "wave scale signal"). This signal has been observed in other experiments from both fixed/tied down (e.g.: Smith, 1980) and moving (e.g.: McGillis et al., 2001a) platforms, but has not previously been quantified.

It remains uncertain what proportion of the wave scale signal apparent in the HiWASE measurements is due to incomplete platform motion correction, and what proportion is a real signal caused by wind-wave interactions (see the discussion in Chapter 6.3.3). A correction, termed the CMC, that removes the residual wave scale signal and hence obtains an upper bound on the possible error that may result, was described in Chapter 6.4.5. Two versions of the correction were found to give similar results, suggesting that the correction is successfully removing the wave scale signal. As

previously shown in Chapter 6.4.5, applying the CMC to the HiWASE measurements decreases the binned gas transfer velocities by approximately 20-50%, depending on wind speed.

The presence of a large structure such as a ship modifies the airflow passing over that structure and affects any flux measurement made in its vicinity. The airflow over the *Polarfront* was modeled using CFD and the results used to determine a correction for the HiWASE ID flux measurements (Chapter 7). EC and ID latent heat fluxes were compared and used to estimate the effects of flow distortion on the HiWASE CO_2 flux measurements, determining a bias of -5% and an uncertainty of ± 9% (Chapter 7.5).

Both platform motion and flow distortion related errors have been shown to be strongly dependent on relative wind direction, making their effects challenging to separate. A relative wind direction dependence has not previously been examined in experiments determining the gas transfer velocity from EC measurements, but was extensively investigated here in Chapters 6 and 7. The wave scale signal for bow-on winds was substantially larger than for beam-on winds. Whilst the effect of flow distortion on bow-on scalar EC flux measurements was expected to be relatively small, EC measurements made with winds onto or near the *Polarfront's* bows (120°-240°, bow-on = 180°) were found to be more variable than beam-on measurements, and had a physically unrealistic wind speed dependence. The *Polarfront's* operations at Station Mike have it going bow-on to the wind in rougher conditions for a given wind speed. Thus, either increased error from the greater vertical motion experienced at the foremast (where the instruments are located), or an increased real wind wave interaction signal, may contribute to the greater variability in the bow-on measurements.

8.1.2.c. IRGA sensor head deformation

The LICOR 7500 open path IRGAs used in HiWASE to measure H_2O and CO_2 concentration are subject to measurement error caused by platform motion. The movement of the platform and the resulting accelerations across the sensor slightly deform the sensor head, leading to an appreciable signal when the sensor is sealed ("shrouded") from the environment. In HiWASE this error is corrected using a previously published method that relates the shrouded "null" measurements to the MotionPak acceleration measurements (Chapter 5.5; Yelland et al., 2009).

Application of the correction reduces the standard error of the binned gas transfer velocities by approximately 7%. At higher wind speeds (> 12 $m.s^{-1}$) the

correction leads to changes in the gas transfer to wind speed relationship of greater than 100%. It is not currently possible to quantify the uncertainty from sensor head deformation that remains in the measurements following correction. A more precise, laboratory based correction procedure is planned as future work (Section 8.2.2).

8.1.2.d. Density dilution

Dilution due to the presence of humidity or temperature fluxes affects all gas concentration measurements (Webb et al., 1980). A direct correction method is used in HiWASE to convert CO_2 and H_2O concentration measurements to mixing ratios (Chapter 4.2.2). The mixing ratio measurements were compared with those obtained from the standard Webb et al. (1980) correction method and found to have good agreement (bias of less than 2%), though there was significant variability between the two methods, (26% σ). It has previously been shown that correcting the density dilution is a source of considerable noise in EC gas flux measurements, contributing 45% or more of the uncertainty in direct CO_2 flux measurements (McGillis et al., 2001a).

Table 8.1. Main sources of flux measurement error addressed in this thesis.

Error	**Thesis chapter**	**Affected flux variable**	**Error dependent on:**	**Bias (uncertainty) in *k***	**Correction**
Hygroscopic particle contamination	3	CO_2 concentration	Humidity	> 100%	PKT method
Platform motion	6	Wind vector	RWD Wind speed Seastate	Estimated 20-50%	Bound by CMC
Flow distortion	7	Wind vector	RWD	-5% (± 9%)	-
IRGA sensor head deformation	5.5	CO_2 and H_2O concentration	Wind speed Seastate	> 100% at high (>12 $m.s^{-1}$) winds	Yelland et al. (2009) method.
Density dilution	4.2.2	CO_2 concentration	Humidity flux Temperature flux	> 100%	Direct method

8.1.3 *Gas transfer results from the "classical" approach*

Most previous experimental results have found the parameterisation of the air-sea gas transfer velocity to have either a quadratic or cubic dependence on wind speed. The various parameterisations differ significantly, by approximately 50 % at wind speeds of 7 $m.s^{-1}$, and by 100% at wind speeds of 15 $m.s^{-1}$. The differences result from some unknown combination of experimental bias, measurement uncertainty, and the dependence of gas transfer on physical forcings other than wind speed, such as seastate and bubble mediated transfer (Chapter 1).

The HiWASE PKT corrected CO_2 flux measurements, and the gas transfer velocities derived from them, are presented in Chapter 4. For clarity in the following discussion, this set of 3938, PKT corrected gas transfer measurements will be termed the GRL measurements (as they are the ones published in Prytherch et al., 2010b). With the exception of the PKT correction, which was tested against an independent data set as described above, and the sensor head deformation correction, the GRL measurements have been obtained and quality controlled in a similar ("classic") fashion to previous experiments. In particular: measurements were accepted from a similarly wide range of relative wind directions to maximize the number of measurements; the same ship motion correction algorithms were applied; and the same assumption is made that the wave scale signal (which is also seen in other studies) is real rather than fully or partly erroneous.

Most previous experiments have presented gas transfer velocities binned by wind speed in 1 $m.s^{-1}$ wide bins. This was also the approach taken in Prytherch et al. (2010b). As shown in Chapter 4, binning in 2 $m.s^{-1}$ instead of 1 $m.s^{-1}$ wide bins does not significantly change the fit to the GRL measurements reported in Prytherch et al. (2010b), and significantly reduces the scatter in the high wind speed bins. As it is the higher wind speed measurements that are of particular interest here, the fit to the GRL measurements averaged in 2 $m.s^{-1}$ wide bins is preferred.

Removal of periods when the *Polarfront* was steaming (SOG > 2 $m.s^{-1}$, n = 545) was shown to reduce the binned gas transfer velocities in the mean, though it did not significantly change the wind speed dependence (Chapter 4). To maximize the number of measurements available for analysis, particularly at high wind speeds, the steaming periods were not removed from the GRL measurements.

As previously stated in Chapter 4 and repeated here, a least squares fit to the GRL measurements over the wind speed range $0 \leq U_{10n} \leq 20$ $m.s^{-1}$, binned in 2 $m.s^{-1}$

wide bins and using the functional form $k = a + bU_{10n}^{n}$, results in an approximately cubic dependence of gas transfer on wind speed (blue solid line, Figure 8.1):

$$k_{660} = -0.51 + 0.095U_{10n}^{2.7} \quad (8.1)$$

This relationship is higher than most previously determined parameterisations and has a dependence on wind speed similar to the cubic dependence of the EC measurements reported by McGillis et al., (2001a). Factors affecting low wind speed fluxes, such as surfactants or buoyancy, were not investigated during HiWASE. It is therefore uncertain whether the slightly negative intercept of Eqn. (8.1) is due to low signal to noise and measurement uncertainty, or some real physical effect.

8.1.4 Analysis of the wave scale signal

The HiWASE gas transfer velocities calculated with the CMC provide a bound on the possible error resulting from incomplete platform motion correction. The set of 3803 CMC corrected measurements will be referred to here as the CMC measurements.

There are 794 "bow-on" (RWD 120°-240°, bow = 180°) measurements in the HiWASE data, and many of these measurements are at high wind speeds (> 16 m.s^{-1}, n = 37). As shown in Chapter 6, removal of the "bow-on" measurements decreases the gas transfer velocities at moderate wind speeds ($7 \le U_{10n} \le 14$ m.s^{-1}) whilst increasing them at high winds ($U_{10n} \ge 14$ m.s^{-1}), resulting in an increase in the wind speed dependence from cubic to approximately quartic. Due to the uncertainty in the cause of the greater wave scale signal in the "bow-on" measurements, and to maximize the number of high wind speed measurements in the analysis, the "bow-on" measurements are retained in both the GRL and CMC sets.

As discussed above and in Chapter 4, measurements made during periods when the *Polarfront* was steaming (SOG > 2 m.s^{-1}) increase the binned gas transfer velocities. This offset is presumably a result of an increased wave scale signal and hence, will be removed by the CMC. Ship steaming periods have been retained in both the GRL and CMC sets.

Despite the large mean change in transfer velocity that results from the correction, the dependence of the CMC measurements on wind speed is still approximately cubic. A least squares fit to the CMC measurements over the wind speed

range $2 \le U_{10n} \le 20$ m.s^{-1}, binned in 2 m.s^{-1} wide bins, results in (red solid line, Figure 8.1):

$$k_{660} = -0.09 + 0.02U_{10n}^{3.1} \tag{8.2}$$

The wind speed dependence of this relationship is similar to the cubic dependence obtained by McGillis et al. (2001a) for wind speeds above about 5 m.s^{-1}.

8.1.5 Reduced wind speed range

The greatest uncertainty in existing parameterisations of gas transfer velocity is at high wind speeds where there is a paucity of previous measurements. In the HiWASE data, there are 61 GRL measurements and 43 CMC measurements at wind speeds greater than 16 m.s^{-1}. Whilst it is these high wind speed measurements that are of the greatest interest they are also the most scattered. In addition, there is significant scatter in the measurements within the lowest wind speed bin (centred on 1 m.s^{-1}). A least squares fit to binned measurements in the wind speed range $2 \le U_{10n} \le 16$ m.s^{-1} will remove any bias that may result from the uncertain high wind measurements, and additionally obtains a fit to measurements over a similar wind speed range to that of previous experiments (e.g.: McGillis et al., 2001a). For the GRL measurements, the resulting reduced wind speed range fit is $k_{660} = -6.4 + 0.521U_{10n}^{2.0}$ (r^2 = 0.99; blue dashed line, Figure 8.1). For the CMC measurements, the reduced wind speed range fit is $k_{660} = 2.85 + 0.002U_{10n}^{4.0}$ (r^2 = 0.99; red dashed line, Figure 8.1).

As shown in Figure 8.1, despite the different exponents, the reduced wind speed range relationships closely overlie the fits to the data sets over the full wind speed range. The quadratic and quartic exponents obtained with the reduced wind speed range are strongly influenced by the highest wind speed bin (at approximately 15 m.s^{-1}). This again demonstrates the need for high wind speed measurements in order to determine the most appropriate form of the gas transfer velocity relationship. Whilst the high wind speed measurements obtained in HiWASE are very scattered, we have no particular reason to doubt them. In addition, the uncertainties due to motion correction, ship steaming and head deformation correction (Chapter 5.5) are all expected to affect the measured cospectra at the wave scale. As such, any resulting bias from these sources will be removed by the CMC. If these errors dominated the high wind speed flux measurements, then use of the CMC would result in very large changes. However, the

percentage difference in the gas transfer relationship resulting from the CMC decreases with wind speed. Hence, the preferred HiWASE gas transfer relationships are those stated in Eqn. (8.1) and (8.2).

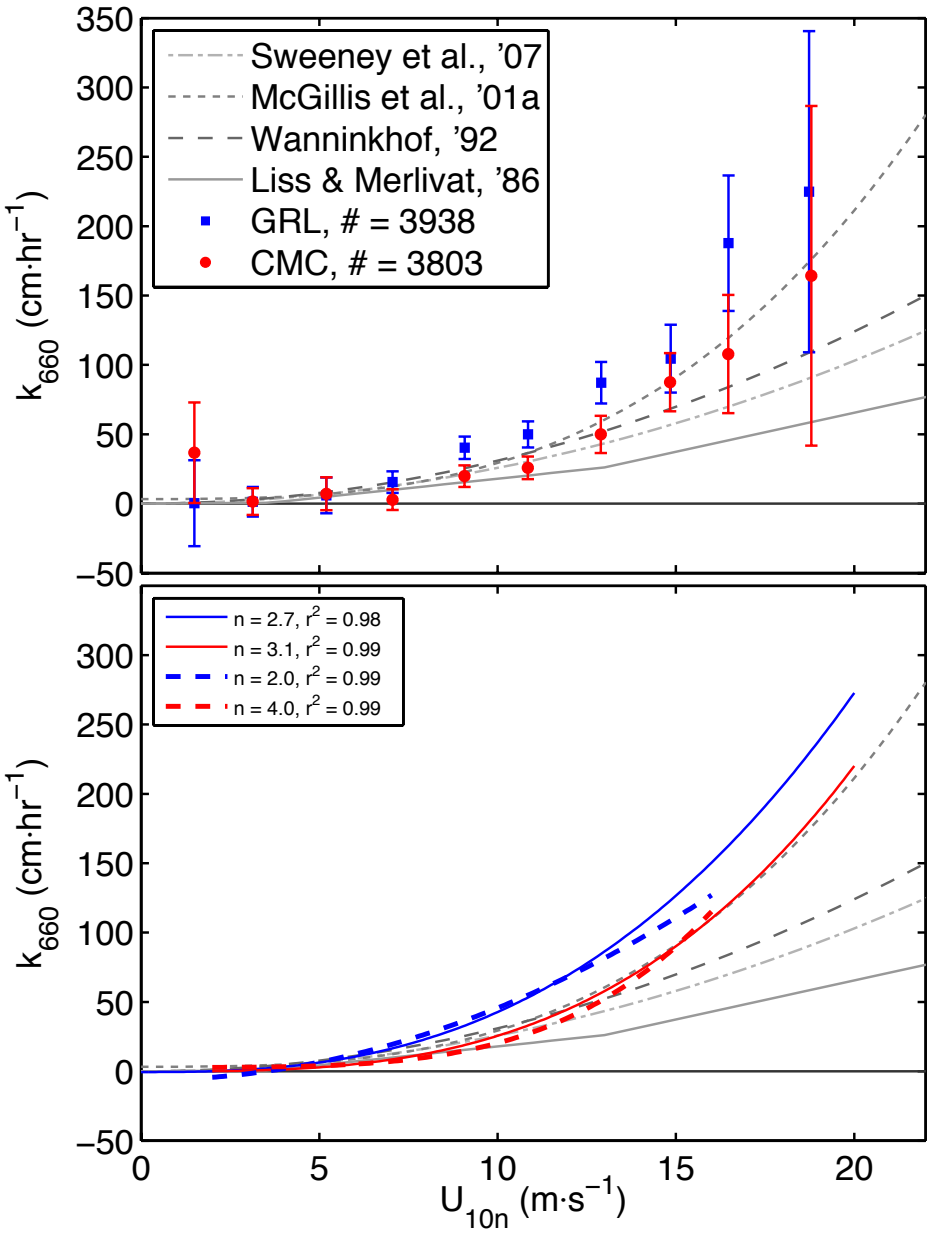

Figure 8.1. Upper plot: transfer velocities (k_{660}) for the GRL and CMC HiWASE data, averaged against the 10 m neutral wind speed (U_{10n}) in 2 m.s^{-1} wide bins. Error bars show the standard error of the mean. Also shown are four gas transfer relationships from previous experiments as specified in the key: note that these relationships are extrapolated at the higher wind speeds. Lower plot: least squares fits to the binned data. The key indicates the exponent determined for the fit, and the correlation. Dashed lines indicate a fit to data over a limited range of wind speeds ($2 \le U_{10n} \le 16$ m.s^{-1}).

8.2. Future work

The comprehensive measurements made during HiWASE provide a unique opportunity to investigate the relationship between air-sea fluxes and seastate. Following the completion of the HiWASE project in December 2009, the AutoFlux system was installed onboard *RRS James Clark Ross* as part of the Waves, Aerosols and Gas Exchange Study (WAGES). An initial examination of the influence of seastate on gas transfer is presented in Appendix D. Suggestions for future investigations of this relationship and other ideas for improvements to future air-sea flux experiments resulting from the work in this thesis are described here.

8.2.1 Seastate

This study has shown that the wave scale signal is a large source of uncertainty in EC flux measurements from moving platforms. To fully investigate seastate dependence in air-sea fluxes it will be necessary to determine the cause of this signal. When a ship is steaming a phase change will occur in the ship response to the waves. If the wave scale signal in the spectra is due to platform motion correction, the phase of the signal will also change. If the signal is due to real wind wave interactions, then it will be unchanged. The phase change will increase with ship speed. EC flux measurements obtained during WAGES and previously onboard *RRS Discovery* will have an increased number of measurements at moderate to high ship speeds compared with the data set obtained onboard *Polarfront* (since *Polarfront* was rarely on passage). Flux measurements from these experiments will be examined to investigate the cause of the wave scale signal.

An initial analysis of the seastate measurements obtained from the SBWR and WAVEX radar has shown that they can be used to determine the contribution of wind sea and swell to the wave field (pers. comm. T. Palmer, NOCS, 2011). The seastate measurements will be used to investigate whether air-sea fluxes vary predictably with rising or falling winds or sea-state development, and whether air-sea fluxes vary with the presence or absence of swell.

In the longer term, investigations from a fixed, well-exposed tower, such as that used in the experiment reported by Smith (1980) could be used to investigate the source of the wave scale signal. Smith (1980) observed wave scale signals, but did not quantify the observations. A large set of measurements from such an experiment would allow the wave signal to be quantified and related to wind speed and/or seastate. This type of

experiment could also be performed from an existing platform such as *FLIP*, though the expected wind speed range and conditions would not be ideal.

8.2.2 Flux measurements

The results presented in this thesis suggest several areas for improvement in CO_2 flux measurement that could be implemented in WAGES and other air-sea experiments. EC CO_2 flux measurements have been shown to be strongly dependent on sensor head deformation at high wind speeds (Chapter 5.5). The effect for a particular sensor was shown not to vary significantly with time. A more sophisticated correction could therefore be obtained for each IRGA from laboratory tests prior to and post deployment.

CFD modeling of the airflow over *Polarfront* from additional relative wind directions to those already modeled will allow a more thorough investigation of flow distortion effects and the resulting uncertainty in the HiWASE flux measurements. The CFD flow distortion modeling (Chapter 7) will also be performed for *RRS James Clark Ross*. The appropriate relative wind directions to model will be determined from the *Ross*' operations.

The fast response pressure sensor used in HiWASE had a low precision relative to the likely size of turbulent or heave related fluctuations. The likely impact of this was shown to be small (Chapter 5.3). However, installation of a higher precision pressure sensor is planned during WAGES. This will allow the effect of pressure fluctuations on the CO_2 flux measurements to be quantified.

The effect of diurnal warming on the HiWASE CO_2 flux measurements was estimated to be small for moderate or high wind speeds (Chapter 5.6). Day and night periods were determined from the time stamp of the measurements. At low wind speeds the effect may be more significant. A more thorough investigation of heating effects, using the shortwave radiation measurements obtained during HiWASE and WAGES, could be pursued.

The use of bulk or ID latent heat fluxes, rather than EC latent heat fluxes in the PKT correction, was briefly examined in this study (Chapter 3.9). The use of the bulk and ID fluxes did not result in a mean change, but did reduce the scatter of the results and increased the number of measurements available for analysis. The EC latent heat fluxes were used since there remains some uncertainty over the most appropriate bulk formula for the latent heat flux. Further work will include analysis of the full HiWASE heat and momentum data set (rather than the CO_2 subset), and will determine a) an

improved bulk formula and b) if use of the bulk or ID latent heat fluxes is more appropriate for correcting the cross-sensitivity error.

The temperature measurements obtained with the Sonic were found to exhibit a wave scale signal (Appendix E). The cause of this signal, whether measurement error due to instrument motion or a real signal resulting from vertical movement of the sensor through the temperature profile, remains uncertain. Shrouding of the Sonic, in a similar way to that used on the IRGAs, may allow the cause of this signal to be determined.

8.2.3 Other gas fluxes

Newly developed sensors may allow EC measurements to be made of the air-sea flux of DMS and methane. The methane sensor requires testing, but may prove reliable enough to be deployed in long-term experiments as an addition to the other sensors currently used in the AutoFlux system. Bubble mediated transfer is predicted to be dependent on gas solubility. Hence, flux measurements of less soluble gases such as methane or DMS should have a different gas transfer velocity dependence on wind speed. Coincident flux measurements of multiple gases at moderate to high wind speeds may allow the contribution of bubble-mediated transfer to trace gas flux to be better quantified.

8.3. Conclusions and implications

This thesis has described a gas transfer velocity wind speed relationship obtained from the largest (to date) set of direct open ocean CO_2 flux measurements, including measurements at higher wind speeds than previously reported. There remains uncertainty over the cause of the wave scale signal seen in the HiWASE measurements and in the results of previous experiments from both fixed and moving platforms. As such, the observed dependence of gas transfer velocity on wind speed is given in Eqn. (8.1) and Eqn. (8.2). The two relationships represent bounds on the possible error resulting from either none, or the entire wave scale signal being due to incomplete platform motion correction.

The HiWASE transfer velocity measurements are highly scattered, and are subject to numerous sources of uncertainty. Some of these uncertainties are specific to particular experimental equipment (e.g.: the head deformation of the LI-7500 IRGA). However, most of these uncertainties apply equally to other direct measurements of the air-sea transfer velocity made during previous studies. The dependence of gas transfer on wind speed observed in the HiWASE measurements is approximately cubic. This strong dependence has been shown to be robust: it is not reduced by removal of the wave scale signal (Chapter 6); selection by relative wind direction (Chapter 6); binning choices or removal of ship-steaming measurements (Chapter 4). These measurements support the argument that the open ocean transfer velocity dependence on wind speed is stronger than quadratic and so may imply a significant role for wave breaking and bubble mediated exchange in gas transfer. This makes the applicability of methods such as DTE that use a simple Schmidt number relationship to relate the transfer velocity of one gas to another problematic at higher wind speeds (Asher et al., 1998).

As discussed in Prytherch et al. (2010b), a stronger nonlinear dependence of gas transfer on wind speed increases the errors in CO_2 fluxes derived from time/space averaged wind fields. Thus the assumption of a Rayleigh distribution of wind speeds can cause significant overestimation of the global flux when calculated using global wind products (Wanninkhof et al., 2002). In addition, wind products differ in the mean wind speed by over 1 $m.s^{-1}$, leading to differences in the global flux of 43% based on a quadratic wind speed dependence for gas transfer velocity, and 71% for a cubic dependence (Wanninkhof et al., 2009).

This thesis has made significant progress in determining the air-sea gas transfer velocity for CO_2 across a greater range of wind speeds than previous studies. However, it has also demonstrated the many sources of uncertainty that apply to direct flux measurements from moving platforms. The challenge that remains is to address the outstanding uncertainties and provide a definitive characterisation of the open ocean gas transfer dependence on both wind speed and seastate/whitecapping.

Appendix A. Chemistry

The flux, F_{CO_2}, of CO_2 across the air – sea interface is commonly parameterised in terms of the fugacity or partial pressure difference across the boundary:

$$F_{CO_2} = kK_0(f_{co_2w} - f_{co_2a}) \tag{A1}$$

where k is the transfer velocity, K_0 is the solubility of CO_2 in seawater (mol.kg^{-1}.atm^{-1}) and the fugacity, f_{CO_2} (atm), is determined in the surface water, w, and air, a.

The fugacity of a gas constituent is the partial pressure of that constituent, i.e.: p_{CO_2} (atm), corrected for non-ideality of the gas with respect to its molecular interactions with air or water:

$$f_{co_2} = p_{co_2} \exp[(B_{11} + 2\partial_{12})P / RT] \tag{A2}$$

where B_{11} $\left(= 1636.75 + 12.0408T - 0.0327957T^2 + 3.16528 \times 10^{-5}T^3\right)$ and ∂_{12} $\left(= 57.7 - 0.118T\right)$ are coefficients specific to CO_2, T is air temperature (K), P is air pressure (atm) and R is the gas constant. The exponential component of the right hand side of Eqn. (A2) is often referred to as the fugacity coefficient. For CO_2 the fugacity and partial pressure are usually very similar in magnitude, differing by less than 0.5% in the typical natural temperature range (Weiss, 1974).

The solubility of CO_2 in seawater depends on both the temperature and salinity, S, of the water (Weiss, 1974):

$$\begin{aligned} K_0 = \exp[&(-60.2409 + 9345.17 / T + 23.3585 \ln(T / 100) \\ &+ S(0.023517 - 0.00023656T + 0.00000047036T^2)] \end{aligned} \tag{A3}$$

Solubility is sometimes reported in units of mol.m^{-3}.atm^{-1}, which can be approximated by multiplying by the density of seawater (approximately 1026 kg.m^{-3}). Alternatively it may be in units of mol.litre^{-1}.atm^{-1}.

Airside measurements of CO_2 are often reported as mole fractions, X_{CO2}, (parts per million, ppm) in dry air. The relationship of mole fraction to partial pressure is:

$$p_{co_2} = (P - p_{H_2O})X_{co_2} \tag{A4}$$

where p_{H2O} is the saturation water vapor pressure (atm).

Partial pressure (atm) of CO_2 is converted to c, mass mixing ratio ($kg.kg^{-1}$) via:

$$p_{CO_2} = c\left[\frac{m_a}{m_{CO_2}}\right]p_a \qquad \text{(A5)}$$

where m_a and m_{CO_2} are the molecular weights of dry air (28.9542 g) and CO_2 (44 g) respectively, and p_a is the partial pressure of dry air.

Appendix B. MotionPak Hardware and HiWASE pre-processing

M. J Yelland and R. W. Pascal.

MotionPak Hardware

The MotionPak (MP) is oriented so that the connectors point aft (see Fig. C.1, from MP spec sheet). The output from the rate gyros goes through a filter (as recommended by the manufacturer), which inverts the sign (see Fig. C.2). The acceleration channels also go through a similar filter as recommended but our arrangement has a current to voltage output (so that we can scale the range ourselves), which inverts the sign again. In other words, the acceleration channels have same sign as would be expected from the MotionPak manual diagram whereas the rates have the opposite sign.

The output filters are single pole low pass, with R values of 52,000 ohms and capacitor of 0.1 uF. Cut off frequency of the filter is 1/(2*pi*R*C) i.e. about 30 Hz. The filter causes negligible phase shift at the frequencies of interest, e.g. a phase shift of less than 2 degrees at 1 Hz and less than 0.2 degrees at 0.1 Hz. The 100 Hz output from the MP goes through the filter and is then input into the R3, which also samples at 100 Hz but performs block averaging to output all data at 20 Hz.

In order to synchronise the data from all fast response sensors, an electronic circuit (housed with the MP) is used to generate an asymmetric square wave signal of period 20 seconds. This signal is fed into the analogue input ports of the R3 and the Licors. Delays in opening the comms port for the sensors, and hence difference in delays between the start of data acquisition for each sensors, were typically around 1 second, but could be up to 5 seconds. The sync signal was used to align the data streams without having to resort to lagged correlation techniques (which would maximise the correlation of errors in the raw signals). Internal processing in the Licor delays the output of the data by 0.185 seconds. This is allowed for when syncing the Licor data with that from the R3.

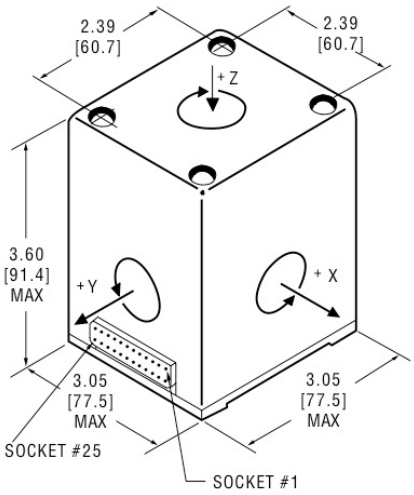

Figure C.1. MotionPak schematic indicating axes orientation.

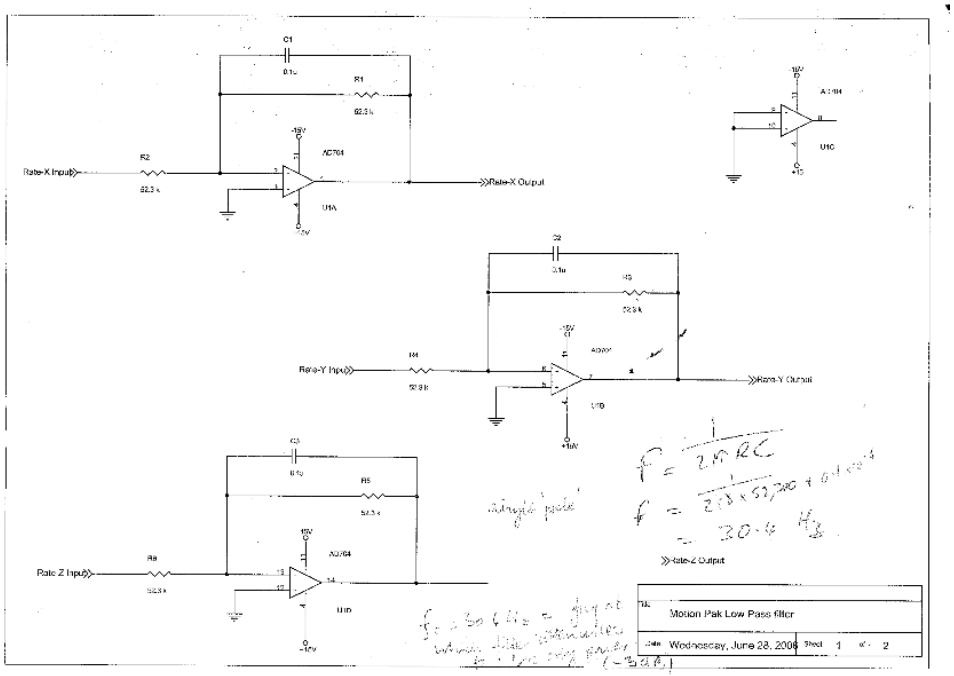

Figure C.2. The MP output filter.

Frame of reference - MotionPak axes definition.

The R3 u,v,w axes are as defined in the manual. We rotate them in to the ship's frame of reference so that;
aft to forwards is positive
starboard to port is positive
upwards is positive

In Jeff Hare's motion correction scripts, the MP data (rates in deg/s and accelerations in g) needs to be in the frame of reference defined by;

accx : to forward is positive
accy : to port is positive
accz : upwards is positive
ratex : port up is positive phi
ratey : bow down is positive theta
ratez : bow to port is positive psi (right-handed)

The MP is oriented so that the connectors point aft so x and y-axes need to be swapped. The outputs go through the filters described above, with the results that the acceleration channels have same sign as would be expected from the MP diagram (Fig. C.1) whereas the rates have the opposite sign. So the MP output is;
AccX : to starboard is positive
AccY : to aft is positive
AccZ : downwards is positive
RateX : bow down is positive phi
RateY : port up is positive theta
RateZ : bow to port is positive psi (right-handed)

To convert MP output into the frame required by the motion scripts;
ratex = RateY/57.2957795; x and y axes are swapped.
ratey = RateX/57.2957795; x and y axes are swapped.
ratez = RateZ/57.2957795;
accx = -AccY*gravity; ; x and y axes are swapped AND there is a sign change.
accy = -AccX*gravity; ; x and y axes are swapped AND there is a sign change
accz = -AccZ*gravity; sign change

EC pre-processing (post-cruise).

Raw R3 data are converted to ASCII format by Robin Pascal using a CVI program "raw2ascii". This also checks the sync signals of the R3 and Licor files to determine the offset between the R3/Licor data streams. This information is output to a daily text file called R3dddpf(2).txt.
A series of UNIX scripts are then run. These call a suite of in-house FORTRAN programs called "pexec". The pexec programs are computationally extremely slow. In

addition. the scripts are very inefficient in that they carry out a lot of now redundant computational steps. It takes at least 10 days to run the pre-processing on 100 days of data. A number of output files are produced for each hour of data so this also leads to problems with data storage (e.g. crashing the GPFS file system...). Finally, only rather old Unix operating systems can run pexec so at some point we won't be able to run these scripts at all. In short, the pre-processing is the weak link in the analysis and urgently needs to be updated to use Matlab for example.
A summary of the (non-redundant) functions of the scripts is given below.

scrp1.raw - reads in raw ASCII Licor and R3 files, converts H_2O from mmol/m^3 to mg/m^3. Uses the information in the daily R3dddpf.txt sync file to see which data stream started first and trim the start of that file so the sync signals are aligned. The 0.185-second Licor delay is accounted for.

scrp2.merge - checks the lengths of the R3 and Licor files and chops the end off whichever file is larger. Uses pjoin.F to merge the two files together without the need for interpolation/extrapolation.

scrp3.nav - takes the merged file and rotates the measured wind speed components into the MP frame of reference, accounting for any small yaw offsets between the two sensors. Merges on ship speed and heading from daily navigation file. This now checks, and allows for, for any lag between the navigation and fast response data streams by maximising the covariance between rate of change of compass heading with the rateZ measurement from the MP gyro. As expected from the offsets seen in the sync signal in the R3 and Licor data, the lag was typically about 1 second, but was occasionally up to 5 seconds.

scrp4.filtMOTcor - This is now redundant - it was used to apply a head deformation correction to the Licor data.

scrp5.pnoaa - applies Jeff Hare's matlab motion correction scripts as described in "Initial Processing" chapter. Some early work was done looking at tuning of the filters, but in the end we decided to stick with the filters used by Jeff Hare. The winds are then corrected for platform motions as measured by the MP. Note that some data were

processed using Miller's matlab scripts too. These had different filters but the end results were the same.

scrp5a.20minfiles - This splits the 58 minute long files into 3 slightly overlapping files of 23.5 minutes (i.e. 20 minute files plus an extra 2048 data at the start and end which can be removed in case transients are produced by any filtering performed subsequently).

scrp6.rot - rotates motion-corrected wind speeds into along-,cross- and vertical wind speed in the true wind speed frame of reference (i.e. earth frame). The motion corrected winds are still winds relative to the ship (or MP) so ship speed over the ground is taken into account.

scrp7.dat - outputs data in matlab format for input to the flux processing programs.

AutoFlux and near-real time processing.

The AutoFlux system is discussed in Yelland et al (2009) and is described briefly here. The AutoFlux system on *Polarfront* logs all data to a single UNIX workstation, with the exception of the images from the digital cameras (although these are stored on the backup RAID) and the raw and spectral data from the WAVEX (only mean parameters such as Hz and Tz are logged to AutoFlux).
The whole system is powered via an un-interruptible power supply. If a significant power failure occurs the system is shut down cleanly and when power returns all systems are automatically re-started and the processing programs are launched. Sampling occurs on an hourly basis and all programs are "overseen" by program monitoring software that re-launches any program if it crashes or hangs. Summary flux results, basic information from all data streams and housekeeping information were sent to NOC automatically via IRIDIUM once per day. Data from these messages are displayed under the project web pages at http://www.noc.soton.ac.uk/ooc/CRUISES/HiWASE/OBS/data_ intro.php. This allowed the systems to be monitored remotely. The 2-way IRIDIUM link also allowed fault-finding and solving to be carried out remotely.
Data are acquired to hourly files using programs written in CVI, with each data stream (mean met, navigation, R3, Licor1, Licor2, CLASP, etc) being logged to a separate file.

All data are time stamped with the system time which in turn is kept in sync with the GPS time embedded in the ship's navigation data stream. The fast response sensors were initially sampled for the first 54.6 minutes of each hour, i.e. 65,636 samples at 20 Hz, later processed in 64 sections of 1024 samples (51.2 seconds) each. In September 2009 the sample length was increased to 58.3 minutes (70,000 samples). The remaining minute or so of each hour was used by the CVI acquisition programs to produce variance spectra of the different variables for each of the 64 sections.

After the end of each hour a number of UNIX scripts are run which call various pexec programs to do the initial data processing. Again, each data stream is processed in turn with basic QC being applied and the data written to separate hourly pexec files. Finally, various parameters from the different data streams data streams are merged together and the true wind speed and direction (corrected for ship speed and direction) and the ID fluxes area calculated for each of the 64 sections in the hourly file. The flux data have basic QC applied before being averaged into 20-minute values. Flux results are therefore produced within an hour of the end of the sampling period. Around 0100 GMT each day the summary files are produced and sent via IRIDIUM to NOC.

A full description of the ID flux calculation can be found in Yelland et al. (1994), Yelland, (1997), Yelland et al. (1998) and Taylor and Yelland, (2000).

Appendix C. PKT correction MATLAB code

```
% PKT method for correcting humidity cross-sensitivity in
% open-path IR CO2 analysers,
% from Prytherch et al, 2010a.
% Code by Peter K Taylor and John Prytherch, NOCS.


% Input:
% mixrat = Fast response H2O mixing ratio (kg/kg).
% rh = Fast response relative humidity (%).
% mrh = mean relative humidity (%).
% mco2 = molecular weight of CO2 (gm).
% mixco2 = Fast response CO2 mixing ratio (kg/kg).
% ustar = friction velocity (m.s-1).
% qstar = H2O flux, normalised by ustar (kg/m^3).
% Wind vector for eddy covariance calculation
% ============================================================
% Calculate RH - q relationship
% ============================================================
% Sort mixrat and rh before determining fit.
[P,S,MU] = polyfit(mixrat,rh,1); % Approximately linear
% relationship.
drh_by_dq = P(1)/MU(2);
% ============================================================
% Detrend CO2 mixing ratio with respect to RH
% ============================================================
% Sort rh and mixco2 before determining fit.
[P,S,MU] = polyfit(rh,mixco2,1); %  calculate the polynomial
slope = P(1) / MU(2);
rhhat = (rh-MU(1))/MU(2);
response = (P(1).*rhhat);
mixco2 = mixco2 - response; % CO2 mixing ratio with RH trend removed
% ============================================================
% Calculate detrended CO2 flux
% ============================================================
% Use eddy covariance to calculate the flux of the
% detrended CO2 (cflux: kg/(m^2.s)) and hence cstar (cflux/ustar: kg/m^3).
dc_by_dq = cstar/qstar;
dc_by_drh = dc_by_dq / drh_by_dq; % determine c*/RH* ratio
% (Equ 2, Prytherch et al, 2010a)

cflux = cflux * 1000 / mco2; % mols/(m2.s)
cflux = cflux*60*60*24*365; % mols/(m2 yr)
% ============================================================
% Iterate CO2 till flux convergence or 10 iterations or flux > 1000
% ============================================================
cfluxold = cflux+2;
loop = 0;
while (abs(cflux - cfluxold) > 1 && loop < 10 && ...
        abs(cflux) < 1000 ); % begin loop
    loop = loop + 1;
    cfluxold = cflux;
    mixco2nu = mixco2 + ((rh - mrh) .* dc_by_drh)/2; % adjust
    %     gradient of CO2 mixing ratio with respect to humidity
    % (Equ 2, Prytherch et al, 2010a).

        % Use eddy correlation methods to recalculate cstar
    %     and cflux from the adjusted CO2 mixing ratio.
    dc_by_dq = cstar/qstar;
    dc_by_drh = dc_by_dq / drh_by_dq; % new c*/rh* ratio

    cflux = cflux * 1000 / mco2; % mols/(m2.s)
    cflux = cflux*60*60*24*365; % mols/(m2 yr)
end
```

Appendix D. A preliminary look at seastate

The comprehensive measurements made during HiWASE provide a unique opportunity to investigate the relationship between air-sea fluxes and seastate. An initial examination of the influence of seastate on gas transfer is presented here.

The whitecap measurements obtained onboard *Polarfront* (Chapter 2.2) have been found to have a dependence on both wind speed and significant steepness, *SS*. A preliminary fit of the whitecap fraction, *W* (%), to the measurements over the wind speed range $1.5 \le U_{10n} \le 23$ m.s^{-1}, and the steepness range 0.022 to 0.056, is given by (pers. comm., Dr Ben I Moat, NOCS, 2011):

$$W(U_{10n}) = 8.29 \times 10^{-4}(U_{10n} - 2.19)^3 \tag{D.1}$$

$$W(U_{10n}, SS) = W(U_{10n}) \times (-0.262 + 33.368 \times SS) \tag{D.2}$$

This preliminary result can be used to derive a model of gas transfer with a dependence on both wind speed and seastate. *SS* is defined as:

$$SS = {2\pi Hs}\big/{gTz^2} \tag{D.3}$$

where the significant wave height *Hs* (m) and the zero-upcrossing slope *Tz,* can be related to the fetch, *X* (km) through relationships obtained from JONSWAP observations for developing seas (Tucker and Pitt, 2001):

$$Hs = 0.0163 X^{0.5} U_{10n} \tag{D.4}$$

$$Tz = 0.47 X^{0.33} U_{10n}^{0.34} \tag{D.5}$$

As a first step, we will investigate the dependence of gas transfer on fetch through the simple seastate dependent gas transfer model of Woolf (2005). This so-called "hybrid" model assumes that the total air-sea gas transfer velocity is a sum of non-wave breaking, k_0, and wave breaking, k_b, transfer terms:

$$k = k_0 + k_b \tag{D.6}$$

As in Woolf (2005) and Woolf (1997), for the non-wave breaking transfer contribution we will use the relationship determined by Jähne et al. (1987b) from laboratory measurements:

$$k_0 = 1.57 \times 10^{-4} u_* \left(600 / Sc \right)^{0.5} \quad \text{(D.7)}$$

with u_* determined from the drag coefficient relationship of Large and Pond (1981). Note that k_0 in Eqn. (D.7) is in units of m.s^{-1}. The wave breaking term is assumed to be proportional to W:

$$k_b = 8.5W \quad \text{(D.8)}$$

The coefficient in Eqn. (D.8) was determined by Woolf (1997) through theoretical calculations of bubble-mediated transfer, and is thought appropriate for CO_2 in water at 20°C. Note that k_b in Eqn. (D.8) is in cm.hr^{-1}. Woolf (2005) further develops this model by representing W as proportional to the wind friction velocity u_* multiplied by the significant wave height Hs, with a (using Woolf's terminology) "convenient" coefficient of proportionality.

For a range of representative fetches, the gas transfer velocities predicted by this "hybrid" model (Eqns. (D.6), (D.7) and (D.8)), incorporating the steepness dependence of the *Polarfront* whitecap observations (Eqns. (D.1) to (D.5)), are shown in the top panel of Figure D.1. The gas transfer velocity in this model increases with decreasing fetch, in contrast to the increasing gas transfer with increasing fetch of the Woolf (2005) model (Figure 1.9). The JONSWAP measurements, which are used to derive the relationship between significant steepness and fetch (Eqns. (D.4) and (D.5)) show that shorter fetches (and hence younger waves) lead to steeper waves. The Woolf (2005) model also relies on JONSWAP measurements to determine the relationship between fetch and wave height, but the form of the model means that the whitecap fraction increases with larger, less steep (more developed) waves. It should be noted that the relationship between wave breaking and wave steepness or development is still very much an area of debate.

The GRL and CMC measurements are similar to the relationship predicted by this simple wave steepness model for a fetch of 1 km or less. Since Station Mike is an

open ocean site, this implies that the seastate is limited by duration, not fetch (e.g.: Taylor and Yelland, 2001 appendix).

For the HiWASE measurements, the mean *SS* is 0.029 ± 0.008 (σ). The maximum *SS* is 0.059 and the minimum is 0.005. Instead of converting the steepness relationship into a fetch relationship, the HiWASE *SS* and wind speed measurements can be used to determine *W* directly from Eqns. (D.1) and (D.2), and then used with the hybrid model (Eqns. (D.6), (D.7) and (D.8)) to predict individual gas transfer velocities (lower panel, Figure D.1) for the periods during which there are corresponding direct transfer velocity measurements. These predictions are significantly lower than the HiWASE transfer velocity measurements. If the coefficient in Eqn. (D.8) is increased heuristically from 8.5 to 40, then the model predictions are similar to the HiWASE results.

This preliminary examination of the seastate dependence of gas transfer has demonstrated the uncertainty that exists both over the influence of bubbles and whitecapping on gas transfer, and of the uncertainty in the dependence of wave breaking on various seastate parameters. The seastate and flux measurements obtained during HiWASE provide a unique dataset that will be used to investigate these relationships further in the future.

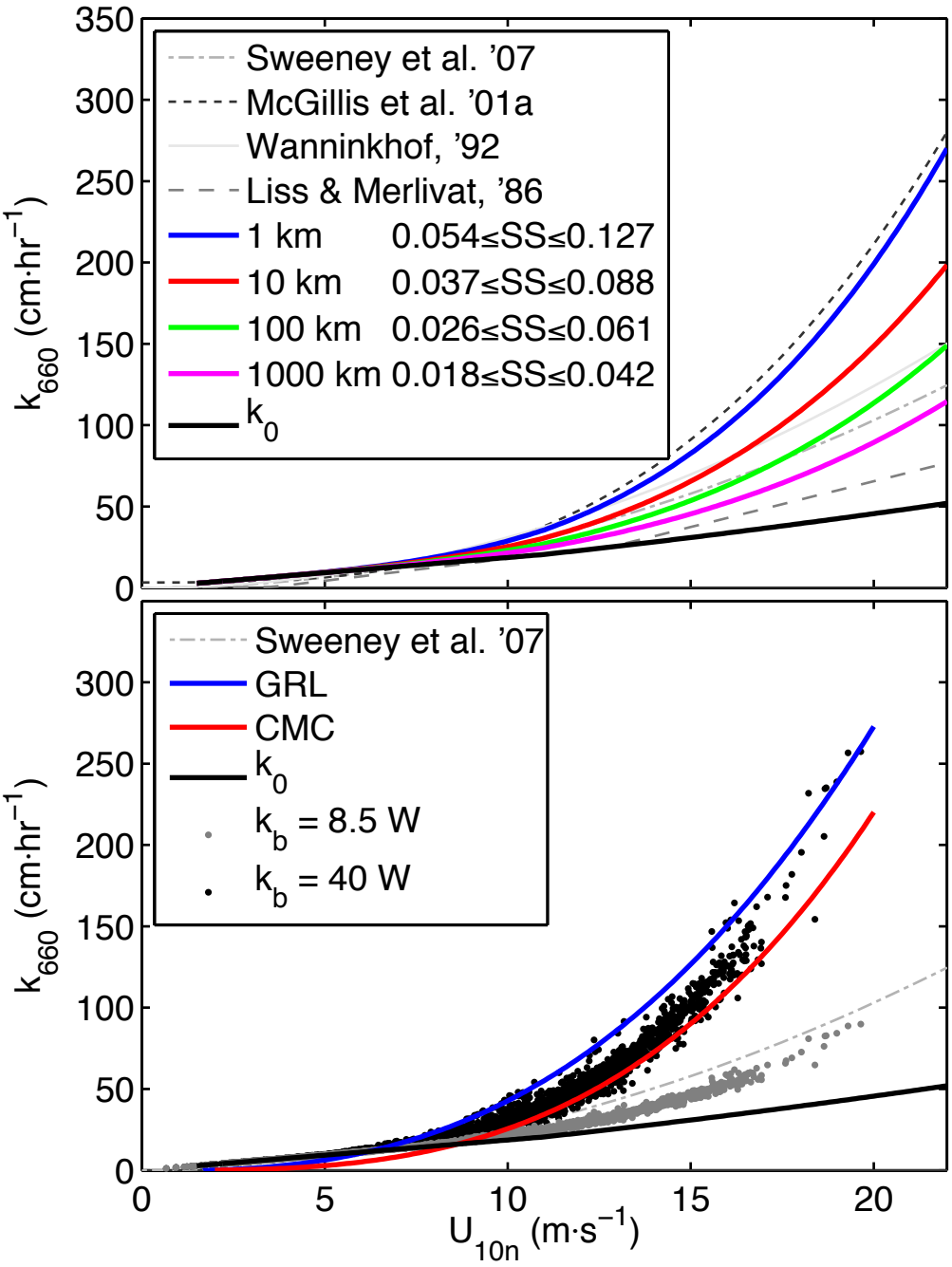

Figure D.1. Upper plot: transfer velocities (k_{660}) determined from the *Polarfront* significant steepness to whitecapping relationship and the Woolf (2005) hybrid model. Results are shown for a range of representative fetches, related to steepness through the JONSWAP measurements. Also shown are four gas transfer relationships from previous experiments as specified in the key: note that these relationships are extrapolated at the higher wind speeds. Lower plot: individual transfer velocities (n = 3918) determined from the *Polarfront* hybrid model. 20 outliers (SS > 10) have been removed. Also shown are the HiWASE gas transfer relationships.

Appendix E. Sensor movement through air column

The HiWASE air temperature variance spectra, measured using fast response instrumentation, show a strong peak at approximately 0.2 Hz (e.g.: Figure 6.9). The air temperature measurements are derived from measurements of speed of sound obtained by the Sonic. The Sonic's internal processing automatically converts the speed of sound measurements to "sonic" temperature, similar to virtual temperature (Kaimal and Gaynor, 1991). The sonic temperature is converted to air temperature on a point-by-point basis using 20 Hz measurements of humidity obtained from the IRGAs (Chapter 4). The 0.2 Hz peak in the air temperature spectra is not caused by IRGA head deformation effects (Chapter 5.5) since a 0.2 Hz signal of similar magnitude is present in the sonic temperature spectra.

There are several possible explanations for the wave scale signal in the temperature spectra. The signal may be caused by movement of the sensor vertically through the air column; it may be due to instrument error caused by vibration or other movement of the Sonic's transducers resulting from wind or platform motion; it may result from measurement error caused by cross wind variation correlated with platform motion; or it could be due to real wave scale fluctuations in temperature caused by wind-wave interactions. These possible causes will be discussed below.

Whilst vibration of the Sonic's transducers could conceivably introduce high frequency noise to the temperature spectra (e.g.: the signal at approximately 5 Hz seen in Figure 6.14), the function of the sonic is not thought to be affected by relatively low frequency movement at wave scale frequencies. Sonic anemometers determine temperature through measurement of the speed of sound through air (e.g.: Kaimal and Gaynor, 1991). The measurement of speed of sound is subject to error from wind speeds normal to the axis of measurement, termed the "crosswind effect". For a three-axis anemometer such as the Gill R3 used during HiWASE, the temperature measurement is an average of the three axis measurements of speed of sound, and can be corrected for the crosswind effect. The correction makes use of the simultaneous measurements of wind velocity to remove the crosswind fluctuations from the temperature measurement (Gill Instruments R3 and R3A user manual). The correction is applied automatically by the internal, hardwired processing of the R3 Sonic. This was confirmed by the manufacturer (pers. comm., Simon Walsh, Gill Instruments Ltd, 2011). Despite this assurance from the manufacturer, the crosswind correction was applied manually to the

temperature measurements to see if it reduced the 0.2 Hz spike. However, the 0.2 Hz spike was typically increased by a small amount (~ 5%). The crosswind correction also removes error in the temperature measurement caused by platform motion induced vibration of the anemometer sensor head.

The wave scale signal in the temperature spectra may therefore be caused by motion of the instrument vertically through the air column and temperature profile. The MotionPak accelerometer measurements can be integrated to obtain a platform displacement vector for the *Polarfront*. Variance spectra of the platform displacements are shown in Figure E.1. The displacement spectra show low frequency signals from ship heading changes, and a vertical motion signal at around 0.1 Hz. The vertical displacement measurements, combined with estimates of the surface layer profiles at Station Mike, can be used to estimate whether the wave scale variation in the temperature spectra could plausibly be explained by vertical sensor motion through the profile.

Measurements of surface layer profiles of temperature and other atmospheric constituents were not made during HiWASE. The profiles can be estimated using Monin-Obukhov Similarity Theory (MOST), parameterisations of the bulk transfer coefficients of momentum (Smith, 1980), temperature and humidity (Smith, 1988), and measurements of the mean wind speed, air temperature, humidity, SST and sea level pressure.

Due to processing commitments, platform displacements have only been obtained for measurement periods in 2006. From these measurements, a wind speed range of $10 \leq U_{10n} \leq 15$ m.s^{-1} was chosen for the analysis. As previously shown bow-on winds are associated with greater vertical motion at the *Polarfront's* foremast (Figure E.1). Of the measurements made during bow-on (± 20°, n = 13) winds, the maximum vertical platform displacement was ± 4.7 m and the standard deviation of the vertical displacement was 1.1 m. For measurements made during beam-on (10° aft of starboard beam, ± 20°, n = 82) winds, the maximum vertical platform displacement was ± 3.2 m and the standard deviation of the vertical displacement was 0.8 m. The mean atmospheric and oceanographic conditions were calculated and used to estimate the air temperature, humidity and wind speed profiles from similarity relationships.

To represent the range of vertical motion experienced at the *Polarfront's* foremast, differences in temperature, humidity and wind speed were estimated from the profiles using vertical displacements of ± 1.5 m and ± 0.5 m. The profile for CO_2 was

estimated by assuming that the CO_2 profile gradient was equal to the H_2O gradient, scaled with the ratio of the mixing ratios of the two constituents. To estimate the variance caused by vertical motion through the air column a sine function, scaled to give the same variance in z, was applied to profile values for each variable. A sine function was used to give a simple approximation of the wave-induced motion through the profiles.

The spectral energy density of a constituent *x* can be approximated from measurement of variance via:

$$S_x(f) = \frac{E_x(f)}{\Delta f} \tag{6.9}$$

where Δf is the width of the frequency band and $E_x(f)$ is the discrete spectral energy at frequency *f*, equivalent to twice the variance explained by fluctuations of frequency *f*.

The estimates of vertical motion induced temperature variance for ± 1.5 m and ± 0.5 m vertical displacements are added to the "base" variance (obtained from an interpolation between the spectral values at 0.05 Hz and 0.3 Hz) and compared to the averaged temperature variance spectra for the two different relative wind directions in Figure E.2.

The estimate of profiling variance in *u* for large (1.5 m) ship motion is similar to the size of the wave scale signal in the spectra. The estimate of increased variance for smaller motion (0.5 m) is much smaller than the peak of the beam-on wave scale variance. For humidity mixing ratio, the wave scale signal is very small and is significantly overestimated by the profiling estimate for large motion. The profiling estimate for air temperature with large range of motion is the right order of magnitude as the wave scale signal, but again the estimate for smaller range of motion is significantly smaller than either the bow-on or beam-on wave scale signal in the spectra. The estimates of CO_2 variance are several orders of magnitude larger than the measured spectra, suggesting that the CO_2 gradient is too small to accurately estimate with the approximate method used here.

It might be expected that application of the head deformation correction (Chapter 5.5) might reduce any wave scale signal in the CO_2 and H_2O spectra. For the variance spectra shown in Figure E.2, this correction has not been applied. However, the change in spectral level at the wave scale resulting from the correction is minor, and does not change the overall appearance of Figure E.2.

The method for estimating profiling variance is very sensitive to the choices made in simulating the wave motion (sine function) and the appropriate range of motion. It may also be overestimating the variance, as all the variance is concentrated in one frequency band, whereas in reality it would be spread over the range of frequencies covered by ship motion. Since the humidity (and CO_2) spectra do not display the same size peak as that estimated by the sine wave method, the large 0.2 Hz peak in the temperature variance spectra is unlikely to be due to profiling effects. The cause of the signal therefore remains unknown.

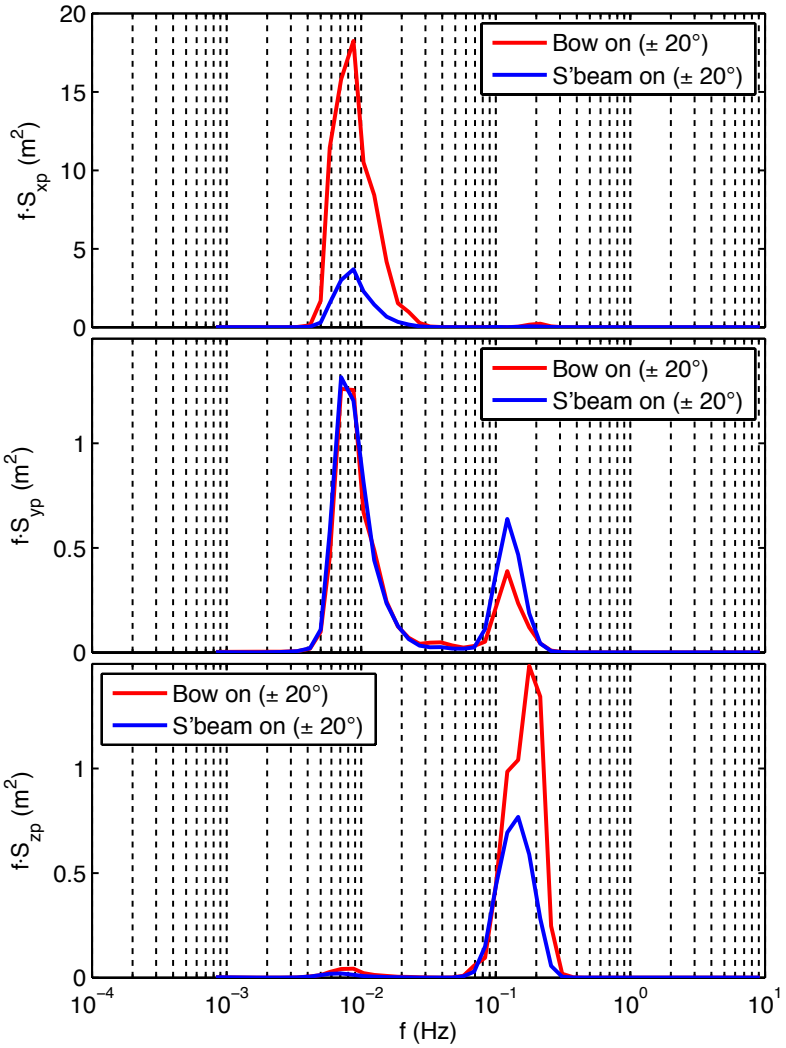

Figure E.1. Averaged platform displacement spectra in the fore-aft (*xp*), port-starboard (*yp*) and vertical (*zp*) directions. Spectra are averages of 306 observational periods with mean wind speed in the range $10 < U_{10n} < 15$ m.s^{-1} and are separated by relative wind direction into bow-on (± 20°. $n = 23$) and 10° aft of starboard beam-on (± 20°. $n = 152$) sets.

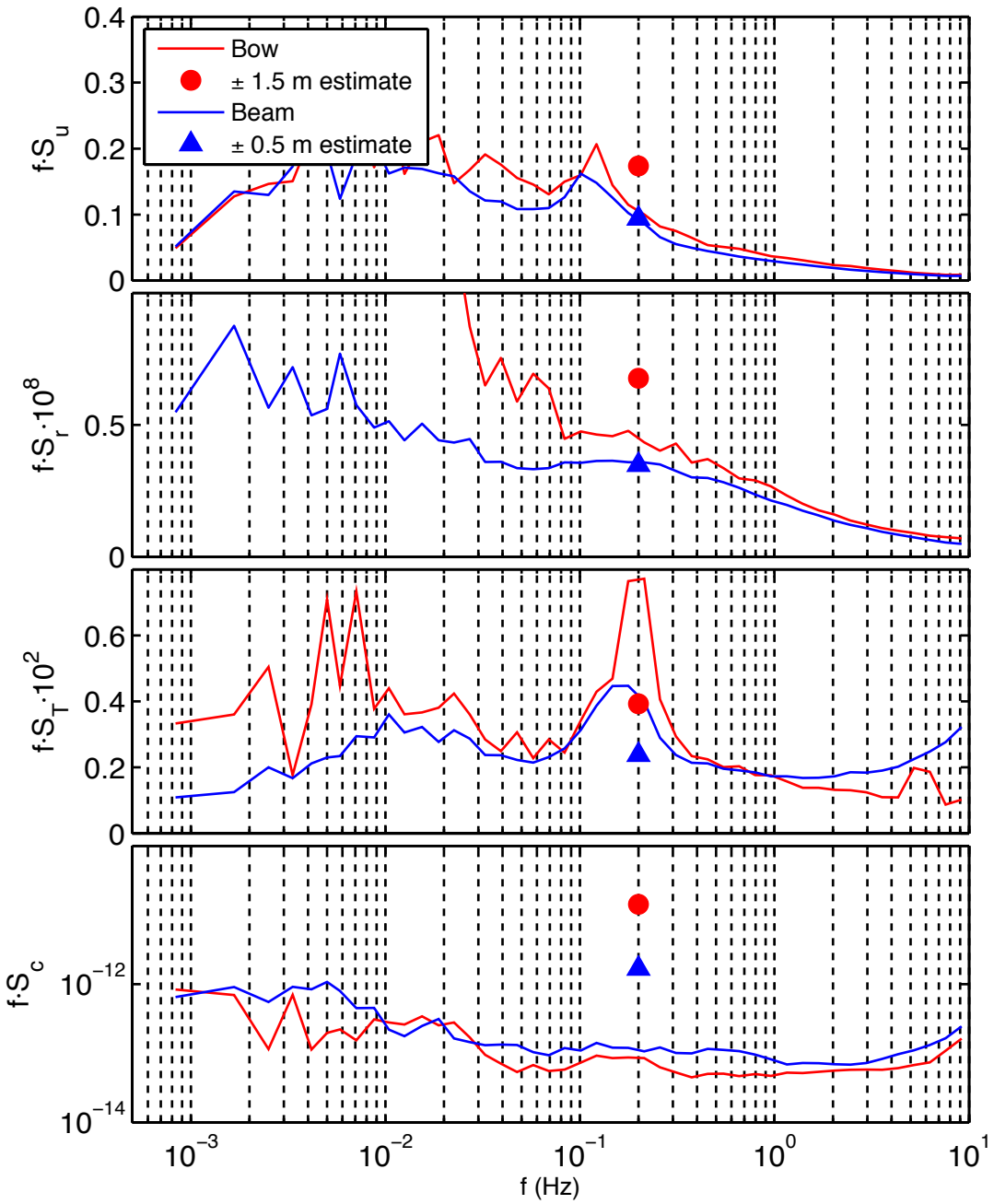

Figure E.2. Spectral energy of variables measured during HiWASE in 2006. Measurements are obtained at wind speeds $10 \leq U_{10n} \leq 15$ divided by relative wind direction into bow-on (± 20°, n = 13) and 10° aft of starboard beam-on (± 20°, n= 82). The along wind spectra has been corrected for platform motion. The estimates of bow-on and beam-on variance are obtained from profile estimates in the boundary layer at two representative height differences.

Glossary

$\bar{}$	-	Time average.
$\_'$	-	Fluctuating component of a variable.
CD_{10n}	-	Drag coefficient normalised to a 10 m measurement height and neutral atmospheric conditions.
C_{n0}	$mols.m^{-3}$	Concentration of gas species *n* at the air-water interface.
C_{na}	$mols.m^{-3}$	Concentration of gas species *n* in the bulk air.
C_{nw}	$mols.m^{-3}$	Concentration of gas species *n* in the bulk water.
C_a	$mols.m^{-3}$ or $kg.^{m-3}$	Concentration of *a*.
C_E	-	Humidity transfer coefficient (Dalton number).
C_T	-	Heat flux coefficient (Stanton number).
c	$kg.kg^{-1}$	CO_2 mass mixing ratio.
c_p	$J.kg^{-1}.K^{-1}$	Specific heat capacity of air.
E_x	x^2	Discrete spectral energy of *x*.
F_n	$mols.m^{-2}.s^{-1}$	Mass flux of gas species *n*.
FT_x	-	Fourier transform of *x*.
f	Hz	Frequency.
f_{nd}	-	Non-dimensional frequency ($f_{nd} = f \times z / U_{rel}$).
f_p	Hz	Wave spectra peak frequency.
fn_a	atm	Fugacity of gas species *n* in the bulk air.
fn_w	atm	Fugacity of gas species *n* in the bulk water.
$f(g)$	-	Fugacity coefficient.
$G_{w'x'}$	-	Cross spectrum of *w* and *x*.
g	$m.s^{-2}$	Acceleration due to gravity.
h	m	Mixed layer depth.
Hs	m	Significant wave height.
K	-	Kolmogorov constant (1.53 – 1.68).
K_{0n}	$mol.m^{-3}.atm^{-1}$	Solubility of gas species *n*.
k_x	$cmhr^{-1}$	Gas transfer velocity normalised to Schmidt number *x*.
L	m	Obukhov length.
L_{vap}	$J.kg^{-1}$	Latent heat of evaporation of water.

m_a	kg	Molecular mass of dry air.
m_v	kg	Molecular mass of water vapor.
M	m	Vector distance from anemometer to platform centre of gravity.
n		Schmidt number exponent.
P	atm	Air pressure.
px_a	atm	Partial pressure of gas species x in the bulk air.
px_w	atm	Partial pressure of gas species x in the bulk water.
p_{H2O}	atm	Saturation water vapor pressure.
q	$kg.kg^{-1}$	Specific humidity.
r	$kg.kg^{-1}$	H_2O mass mixing ratio
R	$atm.m^3.mols^{-3}.K^{-1}$ or $J.K^{-1}.kg^{-1}$	Universal gas constant.
R_{xy}	-	Correlation coefficient of components x and y.
R	m	Motion package to anemometer position vector.
RH	%	Relative humidity.
Sc	-	Schmidt number.
S_x	$x^2.f^{-1}$	Power spectral density of turbulent variable x.
$S_{x\times w}$	-	Cospectra of turbulent variable x and w.
S	m	Vector distance from MotioPak to platform centre of gravity.
$<S^2>$	-	Mean square slope of the wave field.
SS	-	Significant wave steepness.
s	-	Scalar quantity.
T	K	Air temperature.
T_v	K	Virtual temperature.
T_s	K	Sonic temperature.
T_{SST}	K	Sea surface temperature.
t	s	Time.
T_w	K	Water temperature.
T_{per}	s	Length of averaging period.
Tz	-	Zero upcrossing slope.
T	°	Vector rotation matrix.

U	$m.s^{-1}$	Mean wind speed.
U_z	$m.s^{-1}$	Mean wind speed at a height z above the surface.
U_n	$m.s^{-1}$	Mean wind speed corrected to neutral atmospheric stability.
U_{rel}	$m.s^{-1}$	Relative wind speed.
U_{true}	$m.s^{-1}$	True wind speed.
$\mathbf{U}_{mot}$	$m.s^{-1}$	Translational velocity vector of the motion package.
$\mathbf{U}_{obs}$	$m.s^{-1}$	Wind velocity vector in the observational platform frame.
$\mathbf{U}_{true}$	$m.s^{-1}$	Wind velocity vector in the Earth (reference) frame.
u_*	$m.s^{-1}$	Friction velocity.
u	$m.s^{-1}$	Alongwind component of wind vector.
V	m^3	Air volume.
v	$m.s^{-1}$	Crosswind component of wind vector.
w	$m.s^{-1}$	Vertical component of wind vector.
W	%	Fractional whitecap coverage.
X	km	Fetch.
X_n		Mole fraction of constituent n.
xp	m	Platform displacement in fore-aft direction.
x_*	-	Scale variable, $\overline{x'w'} / u_*$.
$\ddot{x}_{obs}$	$m.s^{-2}$	Measured platform acceleration in the bow-stern direction.
$\ddot{y}_{obs}$	$m.s^{-2}$	Measured platform acceleration in the port-starboard direction.
yp	m	Platform displacement in port-starboard direction.
zp	m	Platform displacement in vertical direction.
z	m	Height above air-sea interface.
z_0	m	Aerodynamic roughness length.
z_a	m	Air-side interfacial layer thickness.
z_w	m	Water-side interfacial layer thickness.
α	$atm.m^3mol^{-1}$	Henry's Law constant.
α_{on}		Otswald solubility coefficient for gas species n.
ΔpCO_2	atm	Air-sea partial pressure difference.
δ_{na}	$m^2.s^{-1}$	Diffusivity of the gas species n in air.

δ_{nw}	$m^2.s^{-1}$	Diffusivity of the gas species *n* in water.
ε	$m^2.s^{-2}$	Dissipation rate of turbulent energy.
θ	K	Potential temperature.
θ	°	Pitch.
κ	m^{-1}	Wavenumber.
κ_v	-	The von Karman constant (0.4).
ν_w	$m^2.s^{-1}$	Kinematic seawater viscosity.
v_s	$m.s^{-1}$	Speed of sound.
v	$m.s^{-1}$	Crosswind component of wind vector.
ρ_a	$kg.m^{-3}$	Dry air density.
ρ_v	$kg.m^{-3}$	Moist air density.
σ_x	*x*	Standard deviation of component *x*.
τ	$kg.m^{-1}.s^{-2}$	Surface wind stress.
τ_i	s	Integral time scale.
υ_p	$m.s^{-1}$	Wave phase speed.
ϕ_ε	-	Dissipation function.
ϕ_x	-	Vertical non-dimensional gradient of quantity *x*.
ϕ	°	Roll.
ψ	°	Yaw.
$\mathbf{\Omega}_{obs}$	°	Angular velocity vector in the platform frame.

References

Anguelova, M. D. & Webster, F. (2006), Whitecap coverage from satellite measurements: A first step toward modeling the variability of oceanic whitecaps. J. Geophys. Res.-Oceans, 111, C03017, doi:10.1029/2005JC003158.

Asher, W. (2009), The effects of experimental uncertainty in parameterizing air-sea gas exchange using tracer experiment data. Atmos. Chem. Phys., 9, 131-139.

Asher, W., Edson, J., McGillis, W., Wanninkhof, R., Ho, D. T. & Litchendorf, T. (2002), Fractional area whitecap coverage and air-sea gas transfer velocities measured during GasEx-98, in Gas Transfer at Water Surfaces, Geophys. Monogr. Ser., vol. 127, ed. by M. A. Donelan et al., pp. 199-203, AGU, Washington, D. C.

Asher, W. E. & Wanninkhof, R. (1998a), The effect of bubble-mediated gas transfer on purposeful dual-gaseous tracer experiments. J. Geophys. Res.-Oceans, 103, 10555-10560.

Asher, W. E. & Wanninkhof, R. (1998b), Transient tracers and air-sea gas transfer. Journal of J. Geophys. Res., 103, 15939-15958.

Asher, W., Karle, L., Higgins, B., Farley, P., Monahan, E. & Leifer, I. (1996), The influence of bubble plumes on air-seawater gas transfer velocities. J. Geophys. Res.-Oceans, 101, 12027-12041.

Auble, D. & Meyers, T. (1992), An open path, fast response infrared absorption gas analyzer for H_2O and CO_2. Boundary-layer meteorology, 59, 243-256.

Baldocchi, D. (2003), Assessing the eddy covariance technique for evaluating carbon dioxide exchange rates of ecosystems: past, present and future. Global Change Biology, 9, 479-492.

Bender, M. L., Kinter, S., Cassar, N. & Wanninkhof, R. (2011), Evaluating gas transfer velocity parameterizations using upper ocean radon distributions. J. Geophys. Res.-Oceans, 116, C02010, doi:10.1029/2009JC005805.

Billesbach, D. (2010), Estimating uncertainties in individual eddy covariance flux measurements: A comparison of methods and a proposed new method. Agricultural and Forest Meteorology, 151, 394-405.

Bock, E., Hara, T., Frew, N. & McGillis, W. (1999), Relationship between air sea gas transfer and short wind waves. J. Geophys. Res.-Oceans, 104, 25-25.

Bogucki, D., Carr, E., Drennan, W., Woiceshyn, P., Hara, T. & Schmeltz, M. (2010), Preliminary and novel estimates of CO_2 gas transfer using a satellite scatterometer during the 2001GasEx experiment. International Journal of Remote Sensing, 31, 75-92.

Broecker, H. C. & Siems, W. (1984), The role of bubbles for gas transfer from water to air at higher windspeeds. Experiments in the wind-wave facility in Hamburg. in Gas Transfer at Water Surfaces, ed. by G. H. Jirka and W. Brutsaert, pp. 229-238, D. Reidel, Norwell, Mass.

Broecker, W. S. & Peng, T. (1982), Tracers in the sea, Lamont-Doherty Geological Observatory, Columbia University.

Broecker, W. S. & Peng, T. H. (1974), Gas exchange rates between air and sea. Tellus, 26, l-35.

Broecker, W. S., Ledwell, J. R., Takahashi, T., Weiss, R., Merlivat, L., Memery, L., Peng, T. H., Jahne, B. & Munnich, K. O. (1986), Isotopic versus micro-meteorologic ocean CO_2 fluxes: a serious conflict, J. Geophys. Res., 91(C9), 10517–10527.

Broecker, W. S., Peng, T. H., Ostlund, G. & Stuiver, M. (1985), The distribution of bomb radiocarbon in the ocean. J. Geophys. Res., 90(C4), 6953-6970.

Brooks, I. M., Yelland, M. J., Upstill-Goddard, R. C. & 48 co-authors, (2009), Physical exchanges at the air-sea interface: UK-SOLAS Field Measurements, Bull. Am. Met. Soc., 90 (5), 629-644, doi: 10.1175/2008BAMS2578.1.

Brooks, I. M, (2008), Spatially Distributed Measurements of Platform Motion for the Correction of Ship-Based Turbulent Fluxes. J. Atmos. Oceanic Technol., 25 (11) 2007-2017.

Brumley, B. & Jirka, G. (1988), Air water transfer of slightly soluble gases – turbulence, interfacial processes and conceptual models. Physicochem Hydrodyn, 10, 295-319.

Burba, G. G. & Anderson, D. J. (2007), Introduction to the Eddy Covariance Method: General Guidelines and Conventional Workflow. LI-COR Biosciences.

Burba, G. G., McDermitt, D. K., Grelle, A., Anderson, D. J. & Xu, L. (2008), Addressing the influence of instrument surface heat exchange on the measurements of CO_2 flux from open-path gas analyzers. Glob. Change Biol. 14, 1854–1876, doi: 10.1111/j.1365-2486.2008.01606.x.

Businger, J. (1986), Evaluation of the accuracy with which dry deposition can be measured with current micrometeorological techniques. J. Clim. Appl. Meteorol, 25, 1100–1124.

Callaghan, A. & White, M. (2009), Automated Processing of Sea Surface Images for the Determination of Whitecap Coverage. J. Atmos. Oceanic Tech., 26, 383-394.

Carter, D. J. T. (1982), Prediction of wave height and period for a constant wind velocity using the JONSWAP (Joint North Sea Wave Project) results. Ocean Engineering, 9, 17-33.

Clayson, C. A. (1997), Intercomparison between a WS Ocean Systems Ltd Mk IV Shipborne Wave Recorder (SWR) and a Datawell Waverider (WR) deployed from DNMI Ship "Polarfront" during March-April 1997. Southampton Oceanography Research and Consultancy Report.

Csanady, G. (1990), The role of breaking wavelets in air-sea gas transfer. J. Geophys. Res.-Oceans, 95, 749-759.

Danckwerts, P. (1951), Significance of liquid-film coefficients in gas absorption. Industrial & Engineering Chemistry 43 (6), 1460-1467.

D'Asaro, E. & McNeil, C. (2007), Air-sea gas exchange at extreme wind speeds measured by autonomous oceanographic floats. Journal of Marine Systems, 66, 92-109.

DeCosmo, J., Katsaros, K., Smith, S., Anderson, R., Oost, W., Bumke, K. & Chadwick, H. (1996), Air‐sea exchange of water vapor and sensible heat: The Humidity Exchange Over the Sea (HEXOS) results, J. Geophys. Res., 101(C5), 12001-12016.

Deleonibus, P. (1971), Momentum flux and wave spectra observations from an ocean tower. J. Geophys. Res, 76, 6506-6527.

Drennan, W., Kahma, K. & Donelan, M. (1999), On momentum flux and velocity spectra over waves. Boundary-Layer Meteorology, 92, 489-515.

Drennan, W., Taylor, P. & Yelland, M. (2005), Parameterizing the sea surface roughness. J. Phys. Oceanogr., 35, 835-848.

Dupuis, H., Taylor, P., Weill, A. & Katsaros, K. (1997), Inertial dissipation method applied to derive turbulent fluxes over the ocean during the Surface of the Ocean, Fluxes and Interactions with the Atmosphere/Atlantic Stratocumulus Transition Experiment (SOFIA/ASTEX) and Structure des Echanges Mer-Atmosphere, Proprietes des Heterogeneites Oceaniques: Recherche Experimentale (SEMAPHORE) experiments with low to moderate wind speeds. J. Geophys. Res, 102, 21115-21129.

Dupuis, H., Guerin, C., Hauser, D., Weill, A., Nacass, P., Drennan, W. M., Cloché, S. & Graber, H. C. (2003), Impact of flow distortion corrections on turbulent fluxes estimated by the inertial dissipation method during the FETCH experiment on R/V L'Atalante. J. Geophys. Res.-Oceans, *108*(C3), 8064, doi:10.1029/2001JC001075.

Edson, J., Fairall, C., Mestayer, P. & Larsen, S. (1991), A study of the inertial-dissipation method for computing air-sea fluxes. J. Geophys. Res, 96, 10689-10,711.

Edson, J. B., Hinton, A. A., Prada, K. E., Hare, J. E. & Fairall, C. W. (1998), Direct covariance flux estimates from mobile platforms at sea. J. Atmos. Oceanic. Tech., 15, 547-562.

Edson, J. B., Zappa, C. J., Ware, J. A., McGillis, W. R. & Hare, J. E. (2004), Scalar flux profile relationships over the open ocean. J. Geophys. Res., 109 C08S09, doi:10.1029/2003JC001960.

Edson, J. B., Fairall, C. W., Bariteau, L., Zappa, C. J., Cifuentes-Lorenzen, A., McGillis, W. R. Pezoa, S., Hare, J. E. & Helmig, D. (2011), Direct covariance measurements of CO_2 gas transfer velocity during the 2008 Southern Ocean Gas Exchange Experiement: wind speed dependency. Submitted to the J. Geophys. Res..

Fairall, C., Bradley, E., Rogers, D., Edson, J. & Young, G. (1996), Bulk parameterization of air-sea fluxes for tropical ocean-global atmosphere coupled-ocean atmosphere response experiment. J. Geophys. Res., 101, 3747–3764.

Fairall, C. W., Hare, J. E., Edson, J. B. & McGillis, W. (2000), Parameterization and Micrometeorological Measurement of Air–Sea Gas Transfer. Bound.-Lay. Meteorol., 96, 63-106.

Farmer, D., McNeil, C. & Johnson, B. (1993), Evidence for the importance of bubbles in increasing air–sea gas flux. Nature, 361, 620-623.

Feely, R., Wanninkhof, R., Milburn, H., Cosca, C. & Stapp, M. (1998), A new automated underway system for making high precision pCO_2 measurements onboard research ships. Analytica Chimica Acta, 377, 185-191.

Foken, T. & Wichura, B. (1996), Tools for quality assessment of surface-based flux measurements 1. Agr Forest Meteorol, 78, 83-105.

Friehe, C. & Schmitt, K. (1976), Parameterization of air-sea interface fluxes of sensible heat and moisture by the bulk aerodynamic formulas. J. Phys. Oceanogr., 6, 801-809.

Frew, N. M., Bock, E. J., Schimpf, U., Hara, T., Haußecker, H., Edson, J. B., McGillis, W. R., Nelson, R. K., Mckenna, S. P. & Uz, B. M. (2004), Air-sea gas transfer: Its dependence on wind stress, small-scale roughness, and surface films. J. Geophys. Res, 109, 1–23.

Fujitani, T. (1981), Direct measurement of turbulent fluxes over the sea during AMTEX. Pap. Meteor. Geophys., 32, 119-134.

Geernaert, G. L. (1990), Bulk parameterizations for the wind stress and heat fluxes, in Surface Waves and Fluxes Vol. 1, ed. by G. L. Geernaert and W. J. Plant, pp. 91-172, Kluwer, Dordrecht.

Gill Instruments Ltd, (2004), Omnidirectional (R3) and asymmetric (R3A) Research Ultrasonic Anemometer User Manual, 78pp.

Hare, J. E., Persson, P. O., Fairall, C. W. & Edson, J. (1999), Behavior of Charnock's relationship for high wind conditions. Paper presented at 13th Conference on Boundary Layers and Turbulence, Am. Meteorol. Soc., Dallas, Tex., 10–15 Jan. 1999.

Hare, J., Fairall, C., McGillis, W., Edson, J., Ward, B. & Wanninkhof, R. (2004), Evaluation of the National Oceanic and Atmospheric Administration/Coupled-Ocean Atmospheric Response Experiment (NOAA/COARE) air-sea gas transfer parameterization using GasEx data. J. Geophys. Res..-Oceans, 109, C08S11.

Harriott, P. (1962), A random eddy modification of the penetration theory. Chemical Engineering Science, 17, 149-154.

Hasse, L. (1990), On the mechanism of gas exchange at the airsea interface. Tellus B, 42, 250-253.

Haußecker, H. & Jähne, B. (1995), In situ measurements of the air-sea gas transfer rate during the MBL/COOP West Coast Experiment, in *Air-Water Gas Transfer*. Selected papers from the Third International Symposium on Air-Water Gas transfer, 24-27 July 1995, Heidelberg University, eds. B. Jahne & E.C. Monahan, AEON Verlag & Studio, Hanau, 801-808.

Ho, D. T., Law, C. S., Smith, M. J., Schlosser, P., Harvey, M., & Hill, P. (2006), Measurements of airsea gas exchange at high wind speeds in the Southern Ocean: Implications for global parameterizations, Geophys. Res. Lett., 33, L16611.

Holmén, K. & Liss, P. (1984), Models for air–water gas transfer: an experimental investigation. Tellus B, 36, 92-100.

Hristov, T., Miller, S. & Friehe, C. (2003), Dynamical coupling of wind and ocean waves through wave-induced air flow. Nature, 422, 55-58.

Huebert, B. J., Blomquist, B. W., Yang, M. X., Archer, S. D., Nightingale, P. D., Yelland, M. J., Stephens, J., Pascal, R. W. & Moat, B. I. (2010), Linearity of DMS transfer coefficient with both friction velocity and wind speed in the moderate wind speed range. Geophys. Res. Lett., 37, L01605.

Iwata, T., Yoshikawa, K., Higuchi, Y., Yamashita, T., Kato, S. & Ohtaki, E. (2005), The spectral density technique for the determination of CO_2 flux over the ocean. Boundary-Layer Meteorology, 117, 511-523.

Jacobs, C., Kohsiek, W. I. M. & Oost, W. A. (1999), Airsea fluxes and transfer velocity of CO_2 over the North Sea: results from ASGAMAGE. Tellus B, 51, 629-641.

Jacobs, C., Nightingale, P., Upstill-Goddard, R., Kjeld, J. F., Larsen, S. & Oost, W. (2002a), Comparison of the deliberate tracer method and eddy covariance measurements to determine the air/sea transfer velocity of CO_2, in Gas Transfer at Water Surfaces, Geophys. Monogr. Ser., 127, edited by M. A. Donelan, et al., pp225 - 231, AGU, Washington D. C.

Jacobs, C., Kjeld, J. F., Nightingale, P., Upstill-Goddard, R., Larsen, S. & Oost, W. (2002b), Possible errors in CO_2 air-sea transfer velocity from deliberate tracer releases and eddy covariance measurements due to near-surface concentration gradients, J. Geophys. Res., 107 (C9): 3128, doi:10.1029/2001JC000983.

Jähne, B. & Haußecker, H. (1998), Air-water gas exchange. Annual Review of Fluid Mechanics, 30, 443-468.

Jähne, B., Heinz, G. & Dietrich, W. (1987a), Measurement of the diffusion coefficients of sparingly soluble gases in water with a modified Barrer method, J. Geophys. Res., 92, 10,767-10,776.

Jähne, B., Münnich, K., Bösinger, R., Dutzi, A., Huber, W. & Libner, P. (1987b), On the parameters influencing air-water gas exchange. J. Geophys. Res, 92, 1937-1950.

Janssen, P. (1999), On the effect of ocean waves on the kinetic energy balance and consequences for the inertial dissipation technique. J. Phys. Oceanogr., 29, 530-534.

Janssen, P. (2001), Comments on "on the effect of ocean waves on the kinetic energy balance and consequences for the inertial dissipation technique" - Reply. J. Phys. Oceanogr., 31, 2537-2544.

Jeffery, C., Woolf, D., Robinson, I. & Donlon, C. (2007), One-dimensional modelling of convective CO_2 exchange in the Tropical Atlantic. Ocean Modelling, 19, 161-182.

Jeffery, C., Robinson, I., Woolf, D. & Donlon, C. (2008), The response to phase-dependent wind stress and cloud fraction of the diurnal cycle of SST and air–sea CO_2 exchange. Ocean Modelling, 23, 33-48.

Jeffery, C. D., Robinson, I. S. & Woolf, D. K. (2010), Tuning a physically-based model of the air–sea gas transfer velocity. Ocean Modelling, 31, 28-35.

Johnson, M. (2010), A numerical scheme to calculate temperature and salinity dependent air-water transfer velocities for any gas. Ocean Sci. Discuss., 7, 251-290.

Kaimal, J. C. & J. E. Gaynor (1991), Another look at sonic thermometry. Boundary-Layer Meteorol. 56, 401–410.

Kaimal, J. C., Izumi, Y. J. Wyngaard, C. & Cote, R. (1972), Spectral characteristics of surface-layer turbulence, Quart. J. Roy. Met. Soc., 98 (417), 563-589.

Kohsiek, W. (2000), Water Vapor Cross-Sensitivity of Open Path H_2O/CO_2 Sensors. J. Atmo. Ocean. Tech., 17, 299-311.

Kondo, F. & Tsukamoto, O. (2007), Air-sea CO_2 flux by eddy covariance technique in the equatorial Indian Ocean. J. Oceanogr., 63, 449-456.

Kraus, E. B. & Businger, J. A. (1994), Atmosphere-Ocean Interaction, Oxford University Press US, 362pp.

Large, W. & Pond, S. (1981), Open ocean momentum flux measurements in moderate to strong winds. J. Phys. Oceanogr, 11, 324–336.

Large, W. & Pond, S. (1982), Sensible and latent heat flux measurements over the ocean. J. Phys. Oceanogr, 12, 464–482.

Lange, B., Johnson, H., Larsen, S., Hojstrup, J., Kofoed-Hansen, H. & Yelland, M. (2004), On detection of a wave age dependency for the sea surface roughness. J. Phys. Oceanogr., 34, 1441-1458.

Leuning, R. (2007), The correct form of the Webb, Pearman and Leuning equation for eddy fluxes of trace gases in steady and non-steady state, horizontally homogeneous flows. Boundary-Layer Meteorology, 123, 263-267.

Leuning, R., & King, K. M. (1992), Comparison of eddy-covariance measurements of CO_2 fluxes by open-path and closed-path CO_2 analyzers, Boundary-Layer Meteorol., 59 (3), 297-311.

LI-COR Biosciences, (2004), LI-7500 Instruction manual, 155pp.

Liss, P. S. (1983), Gas transfer: Experiments and Chemical Implications, in Air-Sea Exchange of Gases and Particles, eds. Liss, P. S. & Slinn, W. G. N., pp. 241-289, D Reidel Pub Co, Holland.

Liss, P. S., & Merivat, L. (1986), Air–sea gas exchange rates: introduction and synthesis, in The Role of Air–Sea Exchange in Geochemical Cycling, ed. P. Buat-Menard, pp. 113-129, D. Reidel, Dordrecht and Boston.

Liu, H. (2005), An alternative approach for CO_2 flux correction caused by heat and water vapour transfer. Boundary-layer meteorology, 115, 151-168.

Liu, W. T., Katsaros, K. B. & Businger, J. A. (1979), Bulk Parameterization of Air-Sea Exchanges of Heat and Water Vapor Including the Molecular Constraints at the Interface. J. Atmos. Sci., 36, 1722-1735.

Lumley, J. L. & Panoksky, H. A. (1964), The structure of atmospheric turbulence. Interscience, 239pp.

Marandino, C., De Bruyn, W., Miller, S. & Saltzman, E. (2007), Eddy correlation measurements of the air/sea flux of dimethylsulfide over the North Pacific Ocean. J. Geophys. Res., 112, D03301, doi:10.1029/2006JD007293.

McGillis, W. R., Edson, J. B., Zappa, C. J., Ware, J. D., Mckenna, S. P., Terray, E. A., Hare, J. E., Fairall, C. W., Drennan, W., Donelan, M., Degrandpre, M. D., Wanninkhof, R. & Feely, R. A. (2004), Air-sea CO_2 exchange in the equatorial Pacific. J. Geophys. Res.-Oceans, 109, C08S02, doi:10.1029/2003JC002256.

McGillis, W. R., Edson, J. B., Hare, J. E. & Fairall, C. W. (2001a), Direct covariance air-sea CO_2 fluxes. J. Geophys. Res.-Oceans, 106, 16729-16745.

McGillis, W. R., Edson, J. B. Ware, J. D., Dacey, J. W. H., J. E. Hare, J. E. & Fairall, C. W. & Wanninkhof, R. (2001b), Carbon dioxide flux techniques performed during GasEx-98, Mar. Chem., 75, 267–280.

McNeil, C. & D'Asaro, E. (2007), Parameterization of air-sea gas fluxes at extreme wind speeds. Journal of Marine Systems, 66, 110-121.

McVeigh, P. (2009) Micrometeorological and CO_2 fluxes in the coastal environment. PhD Thesis, National University of Ireland, Galway, 192pp.

Miller, S. D., Marandino, C. & Saltzman, E. S. (2010), Ship-based measurement of air-sea CO_2 exchange by eddy covariance. J. Geophys. Res.-Atmos., 115, D02304.

Miller, S., Marandino, C., De Bruyn, W. & Saltzman, E. S. (2009), Air-sea gas exchange of CO_2 and DMS in the North Atlantic by eddy covariance. Geophys. Res. Lett., 36, L15816.

Miller, S. D., Hristov, T. S., Edson, J. B. & Friehe, C. A. (2008), Platform Motion Effects on Measurements of Turbulence and Air–Sea Exchange over the Open Ocean. J. Atmos. Oceanic Tech, 25, 1683.

Memery, L. & Merlivat, L. (1985), Modelling of gas flux through bubbles at the air-water interface. Tellus 37B, 4-5, 272-285.

Moat, B. I., & Yelland, M. J. (2009), Airflow distortion of anemometer sites on the OWS *Polarfront*, National Oceanography Centre, Southampton, UK, Internal Document, No. 14. Unpublished manuscript.

Moat, B. I., Yelland, M. J., Pascal, R. W. & Prytherch, J. (2010), Metadata for the HiWASE instrumentation deployed on the OWS *Polarfront* between September 2006 and December 2009. National Oceanography Centre, Southampton, UK, Internal Document, No. 17. Unpublished manuscript.

Monahan, E. C. (1971), Oceanic whitecaps, J. Phys. Oceanogr., 1, 139-144.

Monahan, E. & Muircheartaigh, I. (1980), Optimal power-law description of oceanic whitecap coverage dependence on wind speed. J. Phys. Oceanogr., 10, 2094-2099.

Monahan, E. C. & Spillane, M. C. (1984), The role of oceanic whitecaps in air-sea gas exchange, in Gas Transfer at Water Surfaces, ed. by G. H. Jirka & W. Brutsaert, pp. 495-504, D. Reidel, Norwell, Mass.

Naegler, T., Ciais, P., Rodgers, K. & Levin, I. (2006), Excess radiocarbon constraints on air-sea gas exchange and the uptake of CO_2 by the oceans. Geophys. Res. Lett., 33, L11802.

Nightingale, P., Liss, P. & Schlosser, P. (2000a), Measurements of air-sea gas transfer during an open ocean algal bloom. Geophys. Res. Lett., 27, 2117-2120.

Nightingale, P., Malin, G., Law, C., Watson, A., Liss, P., Liddicoat, M., Boutin, J. & Upstill-Goddard, R. (2000b), In situ evaluation of air-sea gas exchange parameterizations using novel conservative and volatile tracers. Global Biogeochem. Cy., 14, 373–387.

Nilsson, E. O., Rutgersson, A. & Sullivan, P. P. (2010), Flux Attenuation due to Sensor Displacement over Sea. J. Atmos. Oceanic Tech., 27, 856-868.

Ocampo-Torres, F. J., Donelan, M. A., Merzi, N. & Jia, F. (1994), Laboratory measurements of mass transfer of carbon dioxide and water vapour for smooth and rough flow conditions. Tellus B, 46, 16-32.

Oost, W. A. (1998), ASGAMAGE Final Report, KNMI Scientific Report; 99-04. Royal Netherlands Meteorological Institute, De Bilt.

Oost, W. A., Fairall, C. W., Edson, J. B., Smith, S. D., Anderson, R. J., Wills, J. A. B., Katsaros, K. B. & Decosmo, J. (1994), Flow distortion calculations and their application in HEXMAX. J. Atmos. Oceanic Tech., 11, 366-386.

Pedreros, R., Dardier, G., Dupuis, H., Graber, H. C., Drennan, W. M., Weill, A., Guérin, C. & Nacass, P. (2003), Momentum and heat fluxes via the eddy correlation method on the R/V L'Atalante and an ASIS buoy. J. Geophys. Res.-Oceans, *108*, 3339, doi:10.1029/2002JC001449.

Peng, T. H., Broecker, W. S., Mathieu, G. G., Li, Y. H. & Bainbridge, A. E. (1979), Radon evasion rates in the Atlantic and Pacific Oceans as determined during the GEOSECS program. J. Geophys. Res., *84*(C5), 2471–2486, doi:10.1029/JC084iC05p02471.

Pierrot, D., Neill, C., Sullivan, K., Castle, R., Wanninkhof, R., Lüger, H., Johannessen, T., Olsen, A., Feely, R.A. & Cosca, C.E. (2009), Recommendations for autonomous underway pCO_2 measuring systems and data-reduction routines, Deep-Sea Res. II, 56, 512-522.

Pierson Jr, W. & Moskowitz, L. (1964), A proposed spectral form for fully developed wind seas based on the similarity theory of SA Kitaigorodskii. J. Geophys. Res., 69, 5181-5190.

Pitt, E. (1991), A new empirically-based correction procedure for shipborne wave recorder data. Applied ocean research, 13, 162-174.

Popinet, S., Smith, M. & Stevens, C. (2004), Experimental and numerical study of the turbulence characteristics of airflow around a research vessel. J. Atmos. Oceanic Tech., 21, 1575-1589.

Prytherch, J., Yelland, M. J., Pascal, R. W., Moat, B. I., Skjelvan, I. & Neill, C. C. (2010a), Direct measurements of the CO_2 flux over the ocean: Development of a novel method. Geophys. Res. Lett., 37, L03607, doi:10.1029/2009GL041482.

Prytherch, J., Yelland, M. J., Pascal, R. W., Moat, B. I., Skjelvan, I. & Srokosz, M. A. (2010b), Open ocean gas transfer velocity derived from long-term direct measurements of the CO_2 flux, Geophys. Res. Lett., 37, L23607, doi:10.1029/2010GL045597.

Prytherch, J., Yelland, M. J. & Pascal, R. W. (2010c), HiWASE: instrument alignments, National Oceanography Centre, Southampton, UK, Internal Document, No. 18. Unpublished manuscript.

Prytherch, J., Farrar, J. T. & Weller, B. A. (2011), Observations and Models of the Diurnal Warm Layer, In prep.

Robertson, J. & Watson, A. (1992), Thermal skin effect of the surface ocean and its implications for CO_2 uptake, Nature 358, 738-740.

Schulz, E., Sanderson, B. & Bradley, E. (2005), Motion correction for shipborne turbulence sensors. J. Atmos. Oceanic Tech., 22, 55-69.

Smith, S. (1988), Coefficients for sea surface wind stress, heat flux, and wind profiles as a function of wind speed and temperature. J. Geophys. Res., 93, 15467-15472.

Smith, S. (1980), Wind stress and heat flux over the ocean in gale force winds. J. Phys. Oceanogr., 10, 709–726.

Smith, S. D. & Jones, E. P. (1985), Evidence for wind-pumping of air-sea exchange based on direct measurements of CO_2 fluxes. J. Geophys. Res,. 90, 869-875.

Smith, S. D. & Jones, E. P. (1986), Isotopic and micrometeorological ocean CO_2 fluxes: different time and space scales. J. Geophys. Res., 91(C9), 529-532.

Song, X., Friehe, C. & Hu, D. (1996), Ship-board measurements and estimations of air-sea fluxes in the western tropical pacific during TOGA COARE. Boundary-layer meteorology, 81, 373-397.

Stull, R. B. (1988), An Introduction to Boundary Layer Meteorology, Springer, UK, 670pp.

Sweeney, C., Gloor, E., Jacobson, A. R., Key, R. M., Mckinley, G., Sarmiento, J. L. & Wanninkhof, R. (2007), Constraining global air-sea gas exchange for CO_2 with recent bomb 14C measurements. Global Biogeochem. Cy., 21, GB2015.

Takahashi, T., Sutherland, S., Wanninkhof, R., Sweeney, C., Feely, R., Chipman, D., Hales, B., Friederich, G., Chavez, F. & Sabine, C. (2009), Climatological mean and decadal change in surface ocean pCO_2, and net sea-air CO_2 flux over the global oceans. Deep-Sea Res. Pt. II: Topical Studies in Oceanography, 56, 554-577.

Takahashi, T., Sutherland, S. C., Sweeney, C., Poisson, A., Metzl, N., Tilbrook, B., Bates, N., Wanninkhof, R., Feely, R. A., Sabine, C., Olafsson, J. & Nojiri, Y. (2002), Global sea-air CO_2 flux based on climatological surface ocean pCO_2, and seasonal biological and temperature effects. Deep-Sea Res. Pt. II, 49, 1601-1622.

Taylor, P. & Yelland, M. (2001a), The dependence of sea surface roughness on the height and steepness of the waves. J. Phys. Oceanogr., 31, 572-590.

Taylor, P. K. & Yelland, M. J. (2001), Comments on 'On the Effect of Ocean Waves on the Kinetic Energy Balance and Consequences for the Inertial Dissipation Technique'. J. Phys. Oceanogr., 31, 2532-2536.

Taylor, P. K. & Yelland, M. J. (2000), On the apparent "imbalance" term in the turbulent kinetic energy budget. J. Atmos. Oceanic Tech., 17, 82-89.

Tsukamoto, O., Takahashi, S., Kono, T., Yamashita, E., Murata, A. & Ishida, H. (2004), Eddy covariance CO_2 flux measurements over open ocean Presented at the 13th Symposium on the Interaction of the Sea and Atmosphere, Portland, Oregon, 8-13 August, (http://ams.confex.com/ams/pdfpapers/78014.pdf).

Tucker, M. J. & Pitt, E. G. (2001), Waves in ocean engineering, Elsevier Science Ltd.

Turk, D., Zappa, C. J., Meinen, C. S., Christian, J. R., Ho, D. T., Dickson, A. G., & McGillis, W. R. (2010), Rain impacts on CO_2 exchange in the western equatorial Pacific Ocean. Geophys. Res. Lett., 37, L23610, doi:10.1029/2010GL045520.

Wanninkhof, R. (1992), Relationship between Wind-Speed and Gas-Exchange over the Ocean. J. Geophys. Res.-Oceans, 97, 7373-7382.

Wanninkhof, R. & McGillis, W. (1999), A cubic relationship between air-sea CO_2 exchange and wind speed. Geophys. Res. Lett., 26, 1889-1892.

Wanninkhof, R. & Thoning, K. (1993), Measurement of fugacity of CO_2 in surface water using continuous and discrete sampling methods. Marine Chemistry, 44, 189-204.

Wanninkhof, R., Asher, W. E., Ho, D. T., Sweeney, C. & McGillis, W. R. (2009), Advances in Quantifying Air-Sea Gas Exchange and Environmental Forcing. Annu. Rev. Mar. Sci., 1, 213-244.

Wanninkhof, R., Sullivan, K. & Top, Z. (2004), Air-sea gas transfer in the Southern Ocean. J. Geophys. Res., 109, C08S19, doi:10.1029/2003JC001767.

Wanninkhof, R., Doney, S. & Takahashi, T. (2002), The effect of using time-averaged winds on regional air-sea CO_2 fluxes. in Gas Transfer at Water Surfaces, Geophys. Monogr. Ser., vol. 127, ed. by M. A. Donelan et al., AGU, Washington, D. C., pp. 351-356.

Wanninkhof, R., Asher, W., Weppernig, R., Chen, H., Schlosser, P., Langdon, C. & Sambrotto, R. (1993), Gas transfer experiment on Georges Bank using two volatile deliberate tracers. J. Geophys. Res., 98, 20237-20248.

Wanninkhof, R., Ledwell, J. R. & Broecker, W. S. (1985), Gas-Exchange Wind-Speed Relation Measured with Sulfur-Hexafluoride on a Lake. Science, 227, 1224-1226.

Ward, B., Wanninkhof, R., Mcgillis, W., Jessup, A., Degrandpre, M., Hare, J. & Edson, J. (2004), Biases in the air-sea flux of CO_2 resulting from ocean surface temperature gradients. J. Geophys. Res, 109, C08S08, doi:10.1029/2003JC001800.

Watson, A. J., Upstill-Goddard, R. C. & Liss, P. S. (1991), Air–sea gas exchange in rough and stormy seas measured by a dual-tracer technique. Nature, 349, 145-147.

Webb, E. K., Pearman, G. I. & Leuning, R. (1980), Correction of flux measurements for density effects due to heat and water vapour transfer. Q. J. Roy. Meteor. Soc., 106, 85-100.

Weiss, R. F. (1974), Carbon dioxide in water and seawater: the solubility of a non-ideal gas. Mar. Chem, 2, 203–215.

Weiss, A., Kuss, J., Peters, G. & Schneider, B. (2007), Evaluating transfer velocity-wind speed relationship using a long-term series of direct eddy correlation CO_2 flux measurements. J. Marine Sys., 66, 130-139.

Wesely, M. L. (1986), Response to "Isotopic Versus Micrometeorologic Ocean CO_2 Fluxes: A Serious Conflict", by W. Broecker et al., J. Geophys. Res., 91, 10533-10535.

Wesely, M. L., Cook, D. R., Hart, R. L. & Williams, R. M. (1982), Air-sea exchange of CO_2 and evidence for enhanced upward fluxes. J. Geophys. Res., 87, 8827-8832.

Woolf, D. K. (1993), Bubbles and the air-sea transfer velocity of gases. Atmosphere Ocean, 31, 517-540.

Woolf, D. K. (1997), Bubbles and their role in gas exchange, in The Sea Surface and Global Change, ed. by P. S. Liss and R. A. Duce, Cambridge Univ. Press, Cambridge, pp. 173-205.

Woolf, D. K. (2005), Parameterization of gas transfer velocities and sea-state-dependent wave breaking, Tellus B, 57, 87-94.

Wu, J. (2000), Bubbles produced by breaking waves in fresh and salt waters, J. Phys. Oceangr., 30(7), 1809-1813.

Wyngaard, J. (1973), On surface-layer turbulence, in Workshop on Micrometeorology, ed. by D. A. Haugen, Amer. Meteor. Soc., Boston, 101-149.

Wyngaard, J., Coté, O. & Izumi, Y. (1971), Local Free Convection, Similarity, and the Budgets of Shear Stress and Heat Flux. J. Atmos. Sciences 28, 1171-1182.

Yelland, M. J. (1997), Wind stress over the open ocean, Ph.D. Thesis, University of Southampton, Department of Oceanography.

Yelland, M. J. & Pascal, R. W. (2010), OWS *Polarfront* Cruise P162, 09 Sep-04 Oct 2006. HiWASE mobilisation and shakedown cruise. National Oceanography Centre, Southampton, UK, Cruise Report, No. 33.

Yelland, M. & Taylor, P. K. (1996), Wind Stress Measurements from the Open Ocean. J. Phys. Oceanogr., 26, 541-558.

Yelland, M., Pascal, R., Taylor, P. & Moat, B. (2009), AutoFlux: an autonomous system for the direct measurement of the air-sea fluxes of CO_2, heat and momentum. J. Operation. Oceanogr., 2009, 15-23.

Yelland, M. J., Moat, B. I., Pascal, R. W. & Berry, D. I. (2002), CFD model estimates of the airflow distortion over research ships and the impact on momentum flux measurements. J. Atmos. Oceanic Tech., 19 (10), 1477-1499.

Yelland, M. J., Moat, B. I., Taylor, P. K., Pascal, R. W., Hutchings, J. & Cornell, V. C. (1998), Wind Stress Measurements from the Open Ocean Corrected for Airflow Distortion by the Ship. J. Phys. Oceanogr., 28, 1511-1526.

Yelland, M. J., Taylor, P. K., Consterdine, I. E. & Smith, M. H. (1994), The use of the inertial dissipation technique for shipboard wind stress determination. J. Atmos. Oceanic Tech., 11(4), 1093 – 1108.

Zappa, C., Asher, W. & Jessup, A. (2001), Microscale wave breaking and air-water gas transfer. J. Geophys. Res., 106, 9385-9391.

Zappa, C. J., Asher, W. E., Jessup, A. T., Klinke, J. & Long, S. R. (2004), Microbreaking and the enhancement of air-water transfer velocity. J. Geophys. Res., 109 C08S16, doi:10.1029/2003JC001897.